Simulating waves in the solar atmosphere with MHD

Franz Georg Fuchs

Dissertation presented for the degree
of Philosophiae Doctor

Center of Mathematics for Applications (CMA)
University of Oslo
2009

© Franz Georg Fuchs, 2009

Series of dissertations submitted to the
Faculty of Mathematics and Natural Sciences, University of Oslo
Nr. 877

ISSN 1501-7710

All rights reserved. No part of this publication may be
reproduced or transmitted, in any form or by any means, without permission.

Cover: Inger Sandved Anfinsen.
Printed in Norway: AiT e-dit AS, Oslo, 2009.

Produced in co-operation with Unipub AS.
The thesis is produced by Unipub AS merely in connection with the
thesis defence. Kindly direct all inquiries regarding the thesis to the copyright
holder or the unit which grants the doctorate.

Unipub AS is owned by
The University Foundation for Student Life (SiO)

Acknowledgements

In the three years of writing my Ph.D. I had the opportunity to work together with highly gifted people. I am very grateful for the wise counsel and inspired instruction of my principle supervisor Prof. Dr. Kenneth H. Karlsen and my second supervisor Prof. Dr. Nils H. Risebro. Their superior analytical skills and guidance were of vital importance to this Ph.D. They continuously supported me throughout the whole three years. In addition, I had the chance to work together with Dr. Siddhartha Mishra who has had a clear vision for this project from day one, and who has provided me with help whenever I needed it. I would also like to thank all of my other co-authors, namely Dr. Knut Waagan and Dr. Andrew D. McMurry. Knut Waagan for his valuable contributions to this thesis and Andrew McMurry for giving me great insight to physical phenomena and for his stunning programming skills. Last but not least, I have to thank the administration, first and foremost the director of the CMA, Prof. Dr. Ragnar Winther, and Helge Galdal for providing a flawless working environment.

Franz Georg Fuchs, Oslo, April 2009

Table of Contents

1 Introduction

This thesis deals with the simulation of energy transfer in the solar atmosphere, modeled by the equations of magneto-hydrodynamics (MHD) with a gravity source term, and suitable initial and boundary conditions. The equations of ideal MHD describe the evolution of macroscopic plasmas, and arise in many other contexts in astrophysics, and electrical and aerospace engineering. The ideal MHD equations are a system of conservation laws in multiple dimensions. The system is hyperbolic but not strictly hyperbolic, and the solution structure is highly complex due to the presence of compound and intermediate shocks, contact discontinuities, and genuinely multi-dimensional waves. Standard finite volume methods are found to be unstable in multiple dimensions in space. One possible reason is the role of the divergence constraint.

Given the complexity of the full MHD system, we consider the magnetic induction equations as a model. Although linear, the induction equations lead to similar difficulties in the discretization. A non-standard form of these equations, involving a source term proportional to the divergence, is found to be symmetrizable. This term is discretized by suitable, energy stable finite volume schemes. The key to obtain a stable scheme is a novel upwind discretization of the source term. Furthermore, we consider the full MHD system, and discretize a modified form of the equations (including a source term proportional to the divergence). We derive stable schemes based on splitting the system into an extended Euler part and the magnetic induction equations (with a source term). The extended Euler system is discretized with suitable HLL-type approximate Riemann solvers, whereas the magnetic induction equations are approximated with the above mentioned upwind scheme. The combination leads to a numerically robust scheme for approximating the solutions of the ideal MHD equations.

Next, we extend this approach to the Godunov-Powell form of the ideal MHD equations. This form is entropy symmetrizable as well as Galilean invariant. We design suitable approximate Riemann solvers and discretize the Godunov-Powell source term in an upwinded manner. In addition, high order positivity preserving ENO and WENO reconstructions are presented. Numerical experiments, illustrating the accuracy and stability of the resulting schemes, particularly on fine meshes, are presented.

Another part of this thesis employs the finite volume framework for the ideal MHD equations to simulate energy transfer in the solar atmosphere. A two dimensional model

with appropriate steady states is considered. Suitable, non-reflecting boundary conditions are discussed in detail. However, the key to obtain a robust scheme is to balance the gravity source with the numerical flux and the Godunov-Powell source. The resulting high order well-balanced schemes are tested on realistic configurations and are found to resolve the complex physical phenomena quite well.

We begin this introduction with a brief description of the physical background needed for understanding the modelling of the solar atmosphere.

1.1 Energy transfer mechanisms in the solar atmosphere

The Sun is a main sequence star in the center of our solar system. It provides light, heat and other forms of energy to Earth and comprises about 99% of the total mass in the solar system. The Sun's radius is about 7×10^5 kilometers, approximately 109 times Earth's radius, see [2] and [3]. Figure 1.1 shows a schematic view of the Sun.

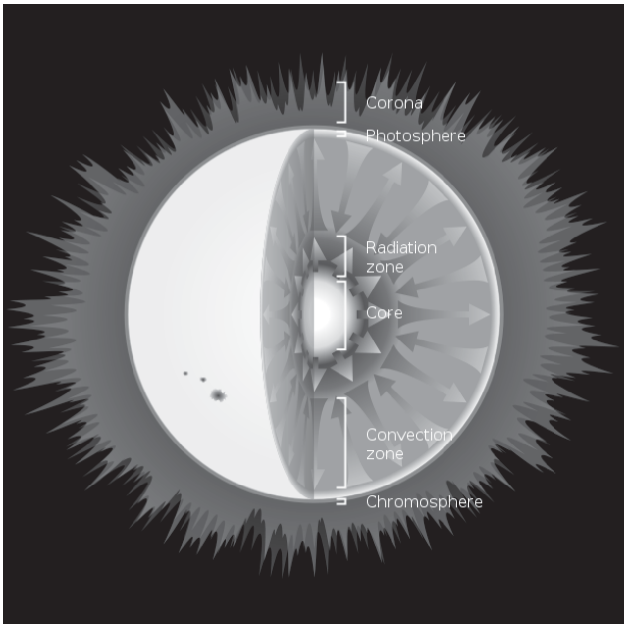

Figure 1.1: Schematic view of the Sun. Source: [5].

Like most other stars, the Sun is made up mostly of atoms of the chemical element hydrogen. About 94% of the atoms are hydrogen, 5.9% helium, and the remaining 0.1% consist mainly of the elements oxygen, carbon, neon, nitrogen, magnesium, iron and silicon. But hydrogen is the lightest of all elements, and so it accounts for only about 72% of the mass, while helium makes up around 26%.

The inner layers of the Sun, and most of its atmosphere, consist of plasma. Plasma is a partially ionized gas, in which a certain proportion of electrons are free rather than being bound to an atom or a molecule. The degree of this ionization is the proportion of atoms which have lost (or gained) electrons, and is controlled mostly by the temperature. As the temperature increases, more and more atoms become ionized, and the atoms that are ionized lose more and more electrons. The highest part of the solar atmosphere, called the corona, has a temperature of about 4×10^6K and is therefore strongly ionized.

The energy of the Sun comes from nuclear fusion reactions that occur deep inside the Sun's core. As described earlier, most of the atoms inside the Sun are positive ions of the most common form of hydrogen. Thus, most of the Sun consists of single protons and independent electrons. Because nuclei have a positive charge, they tend to repel one another, but the core's temperature and density are high enough to force nuclei together. In the most common fusion process in the Sun, the so-called proton-proton chain, the final nucleus after the fusion consists of two protons and two neutrons, a nucleus of the most common form of helium. The mass of this nucleus is slightly less than the mass of the four protons from which it forms. The lost mass is converted into energy. The amount of energy can be calculated from the physicist Albert Einstein's famous equation $E = mc^2$. In this equation, the symbol E represents the energy, m the mass that is covered, and c the speed of light. This energy is released in high-energy photons (gamma rays) which are absorbed in only a few millimeters of solar plasma and then re-emitted again in random direction and at slightly lower energy. It takes a long time for radiation to reach the Sun's surface. Statistically a photon takes between 10^4 and 10^5 years to leave the Sun. At the transparent "surface" of the photosphere, the photons escape as visible light. Each gamma ray in the Sun's core is converted into several million visible light photons before escaping into space. The additionally released neutrinos in the core react very rarely with matter, unlike photons, so almost all are able to escape the Sun immediately.

1.1.1 Zones of the Sun

The Sun is generally divided into the core, the radiative zone, the convective zone, the photosphere, and the atmosphere. The heliosphere, which may be considered the tenuous outer atmosphere of the Sun, extends outward past the orbit of Pluto to the heliopause, where it forms a sharp shock front with the interstellar medium, see figure 1.2.

The core extends from the center of the Sun about one-fourth of the way to the surface. The core has about 2% of the Sun's volume, but it contains almost half the Sun's mass. Its maximum temperature is more than 1.5×10^7 K and its density reaches $1.5 \times 10^7 \frac{g}{m^3}$, approximately 150 times the density of water on Earth. The high temperature and density of the core result in immense pressure, i.e., about 2×10^{11} times Earth's atmospheric pressure at sea level. The core's pressure supports all the overlying gas, preventing the Sun from collapsing. Almost all the fusion in the Sun takes place in the core.

Surrounding the core is a huge spherical shell, known as the radiative zone. The outer boundary of this zone is 70% of the way to the solar surface. The radiative zone makes up 32% of the Sun's volume and 48% of its mass. The radiative zone gets its name from the fact that energy travels through it mainly by radiation. Photons emerging from the core pass through stable layers of gas. But they scatter from the dense particles of gas so

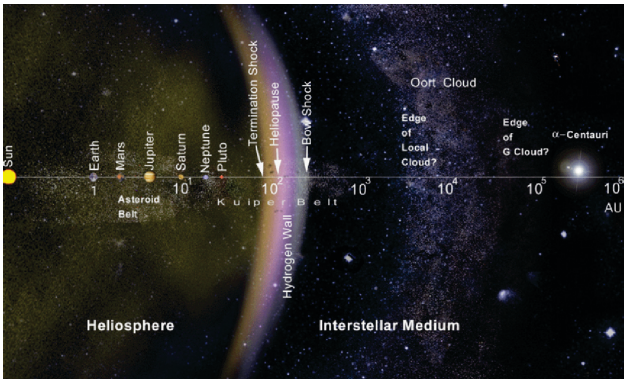

Figure 1.2: The tenuous outer atmosphere of the Sun, the solar wind, forms a sharp shock front with the interstellar medium. Source: [6].

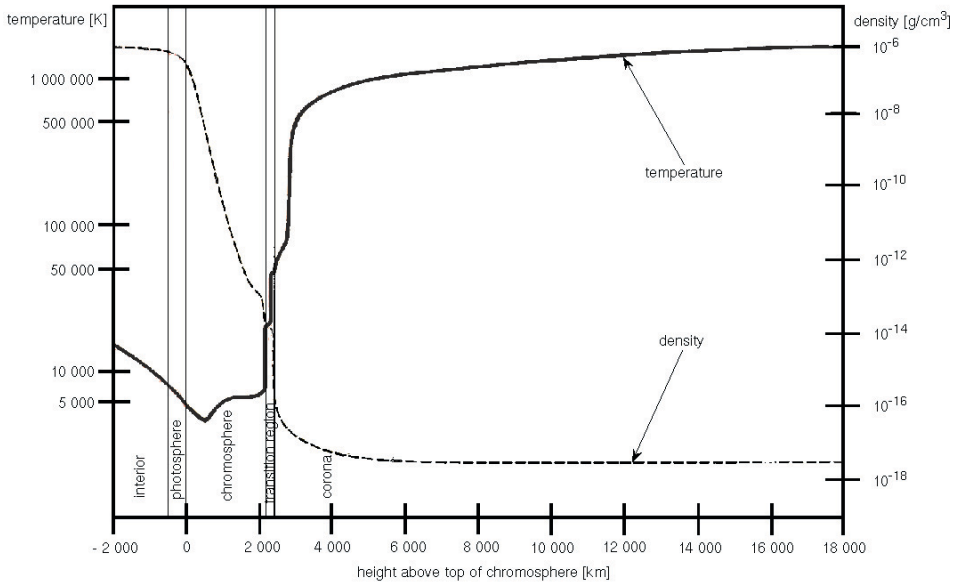

Figure 1.3: This figure shows the temperature and density distribution in the outer zones of the Sun. The x-axis shows the height above the top of the photosphere in km. On the left y-axis we find the temperature in Kelvin and on the right is the density in gram per cubic centimeter. Source: "The Solar Results From Skylab" on [1].

often that an individual photon takes statistically 10^5 years to pass through the zone.

The highest level of the solar interior, the convection zone, extends from the radiative zone to the Sun's surface. This zone consists of the "boiling" convection cells. It makes up about 66% of the Sun's volume but only slightly around 2% of its mass. At the top of the zone, the density is near zero, and the temperature is about 6×10^3 K. The convection cells "boil" to the surface because photons that spread outward from the radiative zone heat them.

The lowest layer of the atmosphere is called the photosphere. The density in the lower part of the photosphere is becoming low enough for the plasma to become transparent at most frequencies of light, so that radiation can escape from the Sun. The photosphere is about 500 km thick. Astronomers often refer to this part as the Sun's surface, since this is the part where the Sun becomes transparent. The photosphere consists of numerous granules, which are the tops of granulation cells. These granulation cells are caused by convection currents of the plasma within the convection zone and produce magnetic north and south poles all over the surface of the Sun.

The next zone upwards is the chromosphere. As shown in figure 1.3, the coolest layer of the Sun is a temperature minimum region about 500 km above the photosphere, with a temperature of about 4×10^3 K. For reasons not fully understood, the temperature rises after this minimum up to about 10^4 K and is therefore hotter than that of the photosphere. The most common feature in the chromosphere are spike-shaped structures called spicules. The density of the chromosphere drops exponentially from 10^{-7} to $10^{-13} \frac{g}{m^3}$, see figure 1.3.

The temperature of the chromosphere is about 2×10^4 K, and the corona is hotter than 5×10^5 K, see figure 1.3. Between the two zones is a region of intermediate temperatures, known as the transition region. This region receives much of its energy from the overlying corona. The transition region is not fixed in space. In models, this region moves up and down in the atmosphere every time a wave from below hits it. The thickness of the transition region is a few hundred to a few thousand kilometers.

For the described structures in the Sun's atmosphere the magnetic field of the Sun plays an important role. The influence of the magnetic field on the plasma depends on the ratio of the magnetic pressure to the gas pressure. Above the photosphere, the magnetic pressure dominates the gas pressure and thus, we expect magnetic fields to play an important role for the plasma motion in the Sun.

1.1.2 The magnetic field

The magnetic field of the Sun is generated by a physical process called the **solar dynamo**. The big plasma motions in the Sun are the following two.

i) The Sun rotates more rapidly at the equator than at higher latitudes, illustrated in figure 1.4.

ii) The inner parts of the Sun rotate more rapidly than the surface.

These different movements of the plasma cause shear stresses, especially at the tachocline, a transition layer between the radiative zone and the convection zone. Since the Sun is a very good electrical conductor (The ability of the positive and negative charges in a

plasma to move relative to each other makes the plasma electrically conductive.), these shear stresses produce a circular electrical current which, according to Ampere's law, produce a magnetic field. The detailed mechanism of the solar dynamo is not known, and is the subject of current research, in which simulations like in the chapters 5, 6 and 7 play an important role in order to understand the physical processes in the Sun.

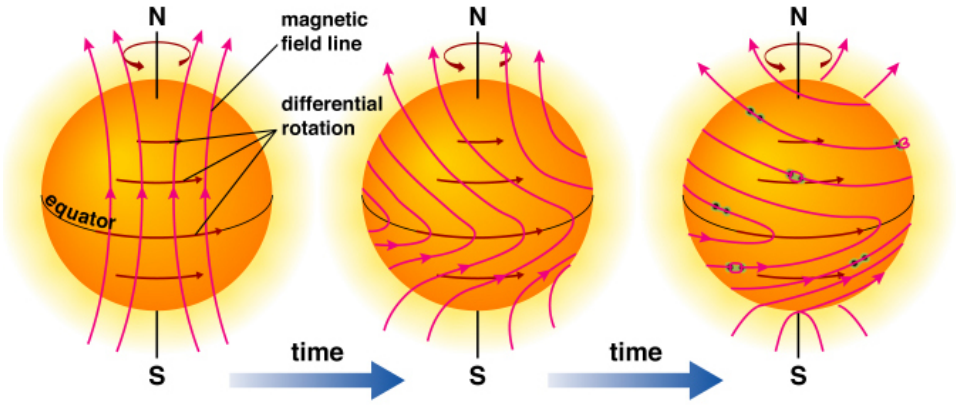

Figure 1.4: The solar cycle. The differences in rotational speed stretch the magnetic field lines. Source: [4].

In the photosphere and below the magnetic pressure is much smaller than the gas pressure (figure 1.3), and the magnetic field is pushed around by the gas. This means that the magnetic field becomes concentrated in the downflow regions at the edges of the convection cells. The typical strength of the Sun's magnetic field is only about twice that of the Earth's field. But when the Sun's magnetic field becomes highly concentrated in these small downflow regions, the field strength is around 10^3 times as great as the typical strength. Above the photosphere the magnetic pressure becomes equal and then larger than the gas pressure, and the magnetic field spreads out. In these regions where the plasma is dominated by the magnetic pressure, the field lines guide ions and electrons into the space above the sunspots. Vibrations, caused by the field being pushed around by convection, are transmitted along the field, with growing amplitude as the gas density drops. All these processes create a variety of features on the Sun's surface and in its atmosphere, the part that we can see, ranging from relatively cool, dark structures known as sunspots to spectacular eruptions called flares and coronal mass ejections.

An important feature of the solar atmosphere is that the temperature decrease from the core is reversed in the outer atmosphere, see figure 1.3. The heating of the atmosphere is only just now becoming understood, using data from modern solar observation satellites, and particularly from the results of numerical modeling. But the above description of the Sun implies that the simulation of the entire solar atmosphere is extremely complicated, and involves multiple physical models. Hence, we concentrate on a part of the atmosphere that includes the chromosphere. One of the important energy carri-

ers in the solar atmosphere are convection generated waves from the inner layers of the sun. They transport and deposit energy in the overlaying chromospheric and coronal plasmas. The waves interact with complex magnetic fields generated by the plasma, and these interactions affect the qualitative as well as the quantitative features of the energy transfer. One of the most important models for simulating the processes in the solar chromosphere are the so-called **magneto-hydrodynamic (MHD) equations**, together with a gravitational source term.

1.2 Magneto-hydrodynamic equations (MHD)

The MHD equations are used in many interesting problems in astrophysics, solar physics, and electrical and aerospace engineering, including the simulation of the processes in the solar atmosphere. In these models, the variables of interest are the mass density of the plasma ρ, the velocity field $\mathbf{u} = (u_1, u_2, u_3)^T$, the magnetic field $\mathbf{B} = (B_1, B_2, B_3)^T$, the pressure p, and the total energy E. These unknowns follow certain physical conservation or balance laws (see [66] for details).

1.2.1 Derivation of the MHD equations

The derivation of the ideal MHD equations in three spacial dimensions is described below.

i) **Conservation of mass**: Mass of a plasma is conserved, resulting in the standard conservation of mass, namely

$$\rho_t + \mathrm{div}(\rho \mathbf{u}) = 0.$$

ii) **Faraday's law**: The magnetic flux across a surface $\mathbf{S}$ bounded by a curve $\delta\mathbf{S}$ is given by Faraday's law

$$-\frac{d}{dt}\int_S \mathbf{B}\cdot\mathbf{dS} = \int_{\delta S} E\cdot dl.$$

By using Stokes theorem and the fact that the electric field in a co-moving frame is zero at infinite conductivity, Faraday's law leads to

$$\mathbf{B}_t + \mathrm{curl}(\mathbf{B}\times\mathbf{u}) = -\mathbf{u}(\mathrm{div}\mathbf{B}). \tag{1.2.1}$$

The above equation is termed the **magnetic induction equation** and can also be written in the following divergence form,

$$\mathbf{B}_t + \mathrm{div}(\mathbf{u}\otimes\mathbf{B} - \mathbf{B}\otimes\mathbf{u}) = -\mathbf{u}(\mathrm{div}\mathbf{B}).$$

iii) **Conservation of momentum**: In differential form, the conservation of momentum is

$$(\rho\mathbf{u})_t + \mathrm{div}(\rho\mathbf{u}\otimes\mathbf{u} + p\mathcal{I}) = \mathbf{J}\times\mathbf{B} - \rho g\mathbf{e_n},$$

where $\mathbf{J}$ denotes the current density and $\mathcal{I}$ the 3×3 identity matrix. The action of **gravity** enters the equation for the momentum via a source term, where g is

the constant acceleration due to gravity in the direction $\mathbf{e_n}$. The **Lorentz force**, exerted by the magnetic field, is given by $\mathbf{J} \times \mathbf{B}$. Under the assumptions of ideal MHD, **Ampere's law** expresses the current density as

$$\mathbf{J} = \text{curl}(\mathbf{B}).$$

Using standard vector identities results in the following semi-conservative form,

$$(\rho\mathbf{u})_t + \text{div}\left(\rho\mathbf{u}\otimes\mathbf{u} + (p + \frac{1}{2}\mathbf{B}^2)\mathcal{I} - \mathbf{B}\otimes\mathbf{B}\right) = -\mathbf{B}(\text{div}\mathbf{B}) - \rho g\mathbf{e_n}.$$

iv) **Conservation of energy**: Defining the hydrodynamic energy of an ideal gas as

$$E^{\text{hd}} = \frac{p}{\gamma - 1} + \frac{1}{2}\rho\mathbf{u}^2,$$

and using the conservation of this energy results in

$$E^{\text{hd}}_t + \text{div}((E^{\text{hd}} + p)\mathbf{u}) = \mathbf{J}\cdot(\mathbf{B}\times\mathbf{u}).$$

The right hand side represents the change in energy due to the magnetic field. By using standard vector identities and **Ampere's law**, we obtain

$$\mathbf{J}\cdot(\mathbf{B}\times\mathbf{u}) = (\mathbf{B}\cdot\frac{\partial\mathbf{B}}{\partial t} - (\mathbf{u}\cdot\mathbf{B})(\text{div}\mathbf{B}) - \text{div}(\mathbf{B}\cdot\mathbf{B})\mathbf{u} - (\mathbf{u}\cdot\mathbf{B})\mathbf{B}).$$

Defining the **total energy of the plasma** as $E = E^{\text{hd}} + \frac{1}{2}\mathbf{B}^2$, energy conservation takes the form

$$E_t + \text{div}((E + p + \frac{1}{2}\mathbf{B}^2)\mathbf{u} - (\mathbf{u}\cdot\mathbf{B})\mathbf{B}) = -(\mathbf{u}\cdot\mathbf{B})(\text{div}\mathbf{B}).$$

Finally, since our model accounts for the action of gravity, we have to add a source term, leading to

$$E_t + \text{div}((E + p + \frac{1}{2}\mathbf{B}^2)\mathbf{u} - (\mathbf{u}\cdot\mathbf{B})\mathbf{B}) = -(\mathbf{u}\cdot\mathbf{B})(\text{div}\mathbf{B}) - \rho g(\mathbf{u}\cdot\mathbf{e_n}),$$

where g is the constant acceleration due to gravity in the direction $\mathbf{e_n}$.

Combining all the above balance laws leads to the following semi-conservative form of the ideal MHD equations,

$$\begin{aligned}
\rho_t + \text{div}(\rho\mathbf{u}) &= 0,\\
(\rho\mathbf{u})_t + \text{div}(\rho\mathbf{u}\otimes\mathbf{u} + (p + \frac{1}{2}|\mathbf{B}|^2)I - \mathbf{B}\otimes\mathbf{B}) &= -\mathbf{B}(\text{div}\mathbf{B}) - \rho g\mathbf{e_n},\\
\mathbf{B}_t + \text{div}(\mathbf{u}\otimes\mathbf{B} - \mathbf{B}\otimes\mathbf{u}) &= -\mathbf{u}(\text{div}\mathbf{B}),\\
E_t + \text{div}((E + p + \frac{1}{2}|\mathbf{B}|^2)\mathbf{u} - (\mathbf{u}\cdot\mathbf{B})\mathbf{B}) &= -(\mathbf{u}\cdot\mathbf{B})(\text{div}\mathbf{B}) - \rho g(\mathbf{u}\cdot\mathbf{e_n}).
\end{aligned} \tag{1.2.2}$$

Neglecting the gravity ($g = 0$), the above semi-conservative form is also called the **Godunov-Powell form** of the MHD equations, and the source on the right-hand side of (1.2.2) is called the **Godunov-Powell source term**. Magnetic monopoles have not been observed in nature, although their existence has been hypothesized in a number of quantum regimes by both the unified field theory and the string theory. Hence, it is common to assume that the magnetic field is solenoidal, i.e., it satisfies the divergence constraint,

$$\mathrm{div}(\mathbf{B}) \equiv 0. \tag{1.2.3}$$

Under this constraint, the Godunov-Powell source terms in (1.2.2) is zero, and the constraint is explicitly added to the equations to obtain the following conservative standard form of the ideal MHD equations,

$$\begin{aligned}
\rho_t + \mathrm{div}(\rho\mathbf{u}) &= 0,\\
(\rho\mathbf{u})_t + \mathrm{div}(\rho\mathbf{u}\otimes\mathbf{u} + (p+\frac{1}{2}|\mathbf{B}|^2)I - \mathbf{B}\otimes\mathbf{B}) &= -\rho g\mathbf{e_n},\\
\mathbf{B}_t + \mathrm{div}(\mathbf{u}\otimes\mathbf{B} - \mathbf{B}\otimes\mathbf{u}) &= 0,\\
E_t + \mathrm{div}((E+p+\frac{1}{2}|\mathbf{B}|^2)\mathbf{u} - (\mathbf{u}\cdot\mathbf{B})\mathbf{B}) &= -\rho g(\mathbf{u}\cdot\mathbf{e_n}),\\
\mathrm{div}\mathbf{B} &= 0.
\end{aligned} \tag{1.2.4}$$

Taking divergence on both sides of the magnetic induction equation (1.2.1) yields,

$$(\mathrm{div}\mathbf{B})_t + \mathrm{div}(\mathbf{u}(\mathrm{div}\mathbf{B})) = 0. \tag{1.2.5}$$

This means that any solenoidal initial magnetic field remains divergence free. Hence, for smooth solutions, the semi-conservative form (1.2.2) is equivalent to the standard form (1.2.4), if the initial magnetic field is divergence free.

With $g = 0$, the equations of ideal MHD (1.2.4) are an example of a system of conservation laws in multiple dimensions of the from

$$q_t + f(q)_x + g(q)_y + h(q)_z = 0.$$

These PDEs of the hyperbolic type are widely used for modeling phenomena in acoustics, gas dynamics, elastodynamics, and bio-mechanics. In the physical derivation, hyperbolic PDEs arise typically from problems involving wave motion or the transport of certain substances, by assuming that a certain quantity is conserved. Conservation means that the rate of change of the total amount of a substance contained in a domain Ω is equal to the flux of that substance across the boundary of the same domain Ω.

In order to investigate the structure of a general hyperbolic partial differential equation in one space dimension, i.e.,

$$\frac{\partial}{\partial t}q(x,t) + \frac{\partial}{\partial x}f(q(x,t)) = 0, \tag{1.2.6}$$

one has to analyze the local wave structure by linearizing the equations around a certain state

$$V_t + A(V)V_x = 0, \quad A = f' = f_V,$$

where $A(V)$ is the matrix Jacobian.

1.2.2 Linear hyperbolic equations

The easiest case of the hyperbolic conservation law (1.2.6) is, when the flux function f is linear, i.e.,

$$q_t + Aq_x = 0, \quad A \in \mathbb{R}^{m\times m}. \tag{1.2.7}$$

The equation (1.2.7) is called **hyperbolic** if A is diagonalizable with real eigenvalues. For a linear hyperbolic PDE there exist eigenvalues $\lambda_1 \leq ... \leq \lambda_m$ and a complete set of eigenvectors $r^1, ..., r^m \in \mathbb{R}^m$, such that $R = [r^1|...|r^m]$ is non-singular. By multiplying (1.2.7) with R^{-1}, we can rewrite this linear system as

$$R^{-1}q_t + R^{-1}ARR^{-1}q_x = 0.$$

Introducing the so-called **characteristic variables** $w(x,t) := R^{-1}q(x,t)$ we can rewrite the linear equation as

$$w_t + \Lambda w_x = 0,$$

where $\Lambda = \text{diag}(\lambda^1, ..., \lambda^m)$. Using the characteristic variables, we can see that the linear system decouples into m independent advection equations

$$w^p_t + \lambda^p w^p_x = 0, p = 1, ..., m.$$

Now we can solve the linear system (1.2.7) together with the initial condition $q(x,0) = \overset{\circ}{q}(x)$. The solution consists of m "waves " traveling at characteristic speeds λ^p

$$q(x,t) = \sum_p w^p(x,t)r^p = \sum_p \overset{\circ}{w}{}^p(x - \lambda^p t)r^p.$$

Let us now investigate the hyperbolic structure of the linearized ideal MHD equations (1.2.4).

1.2.3 The characteristic structure of ideal MHD

Consider the equation (1.2.4) in the x-direction. The equations in x-direction can be written down in the following from

$$\mathbf{W}_t + \mathbf{f}(\mathbf{W})_x = 0, \tag{1.2.8}$$

where

$$\mathbf{W} = (\rho, \rho u_1, \rho u_2, \rho u_3, B_1, B_2, B_3, E)^T,$$

is the vector of conserved variables, and the flux f is given by

$$\mathbf{f}(\mathbf{W}) = \begin{pmatrix} \rho \\ \rho u_1^2 + \tilde{p} \\ \rho u_1 u_2 - B_1 B_2 \\ \rho u_1 u_3 - B_1 B_3 \\ 0 \\ u_1 B_2 - u_2 B_1 \\ u_1 B_3 - u_3 B_1 \\ (E + \tilde{p})u_1 - B_1(u_1 B_1 + u_2 B_2 + u_3 B_3) \end{pmatrix},$$

where we have defined

$$\tilde{p} = p + \frac{B_1^2 + B_2^2 + B_3^2}{2}. \tag{1.2.9}$$

The divergence constraint in one space dimension forces the magnetic field in x direction (B_1) to be constant in space and time, and thus act only as a parameter in the equations. Defining the vector of primitive variables,

$$V = \{\rho, u_1, u_2, u_3, B_1, B_2, B_3, p\},$$

the system (1.2.4) reduces to the following quasilinear form in one dimension,

$$V_t + A_1(V)V_x = 0. \tag{1.2.10}$$

The expression for the Jacobian matrix A_1 is

$$A_1 = \begin{pmatrix} u_1 & p & 0 & 0 & 0 & 0 & 0 & 0 \\ 0 & u_1 & 0 & 0 & -\frac{B_1}{\rho} & -\frac{B_2}{\rho} & -\frac{B_3}{\rho} & \frac{1}{\rho} \\ 0 & 0 & u_1 & 0 & -\frac{B_2}{\rho} & -\frac{B_1}{\rho} & 0 & 0 \\ 0 & 0 & 0 & u_1 & -\frac{B_3}{\rho} & 0 & -\frac{B_1}{\rho} & 0 \\ 0 & 0 & 0 & 0 & 0 & 0 & 0 & 0 \\ 0 & B_2 & -B_1 & 0 & -u_2 & u_1 & 0 & 0 \\ 0 & B_3 & 0 & -B_1 & -u_3 & 0 & u_1 & 0 \\ 0 & \gamma p & 0 & 0 & (\gamma-1)\mathbf{u}\cdot\mathbf{B} & 0 & 0 & u_1 \end{pmatrix}, \tag{1.2.11}$$

see for example [68]. Since the fifth row is zero, the matrix is evidently singular. This leads to a zero eigenvalue, and we expect that this leads to problems in simulating the equations. This zero eigenvalue is related to the fact that in one space dimension the evolution equation for B_1 is $(B_1)_t = 0$, and it is therefore common to remove the fifth column and row (and hence remove B_1 as a variable). On the other hand, using the primitive form (1.2.2) of the MHD equations, we get the following Jacobian matrix

$$A_1' = \begin{pmatrix} u_1 & p & 0 & 0 & 0 & 0 & 0 & 0 \\ 0 & u_1 & 0 & 0 & -\frac{B_1}{\rho} & -\frac{B_2}{\rho} & -\frac{B_3}{\rho} & \frac{1}{\rho} \\ 0 & 0 & u_1 & 0 & -\frac{B_2}{\rho} & -\frac{B_1}{\rho} & 0 & 0 \\ 0 & 0 & 0 & u_1 & -\frac{B_3}{\rho} & 0 & -\frac{B_1}{\rho} & 0 \\ 0 & 0 & 0 & 0 & u_1 & 0 & 0 & 0 \\ 0 & B_2 & -B_1 & 0 & -u_2 & u_1 & 0 & 0 \\ 0 & B_3 & 0 & -B_1 & -u_3 & 0 & u_1 & 0 \\ 0 & \gamma p & 0 & 0 & (\gamma-1)\mathbf{u}\cdot\mathbf{B} & 0 & 0 & u_1 \end{pmatrix}. \tag{1.2.12}$$

In the following, we will work with this Jacobian matrix A_1'. Defining the sound speed

$$a^2 = \frac{\gamma p}{\rho} \quad \text{and} \quad b_{1,2,3} = \frac{B_{1,2,3}}{\sqrt{\rho}},$$
$$b^2 = b_1^2 + b_2^2 + b_3^2, \quad b_\perp^2 = b_2^2 + b_3^2,$$

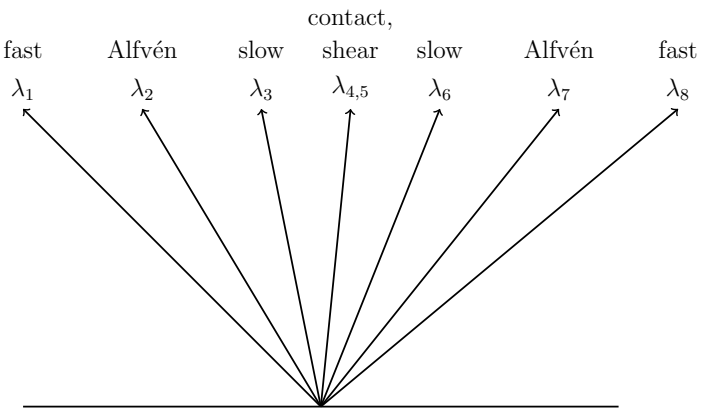

Figure 1.5: Eigenstructure of the MHD equations.

the eigenvalues of A_1' read

$$\begin{gathered}\lambda_1 = u_1 - c_f, \quad \lambda_2 = u_1 - b_1, \quad \lambda_3 = u_1 - c_s, \quad \lambda_4 = \lambda_5 = u_1, \\ \lambda_6 = u_1 + c_s, \quad \lambda_7 = u_1 + b_1, \quad \lambda_8 = u_1 + c_f,\end{gathered} \tag{1.2.13}$$

where c_f and c_s are given by

$$\begin{aligned}c_f^2 &= \frac{1}{2}\left(a^2 + b^2 + \sqrt{\left(a^2+b^2\right)^2 - 4a^2b_1^2}\right), \\ c_s^2 &= \frac{1}{2}\left(a^2 + b^2 - \sqrt{\left(a^2+b^2\right)^2 - 4a^2b_1^2}\right).\end{aligned} \tag{1.2.14}$$

As all eigenvalues are real, the system is hyperbolic. The eigenvalues are ordered by $\lambda_1 \leq ... \leq \lambda_8$ as $c_s \leq b_1 \leq c_f$, see figure 1.5. The waves corresponding to λ_1 and λ_8 are called fast waves, the ones corresponding to λ_3 and λ_6 slow waves, those corresponding to λ_2 and λ_7 Alfvén waves, the wave associated with λ_4 is called a contact wave, the wave corresponding to λ_5 is called a shear wave. However, the equations of ideal MHD are nonlinear. This introduces a lot of additional interesting phenomena. Let us start by studying the simplest nonlinear PDE.

1.2.4 Nonlinear Systems

The easiest nonlinear equation is the so-called **Burgers' Equation**

$$q_t + \left(\frac{1}{2}q^2\right)_x = 0. \tag{1.2.15}$$

Even with initially smooth conditions, the solutions to this equation can develop discontinuities in finite time. These discontinuities are called **shocks**. Additionally, the solution can contain **rarefaction waves**. The name rarefaction comes from the fact that the

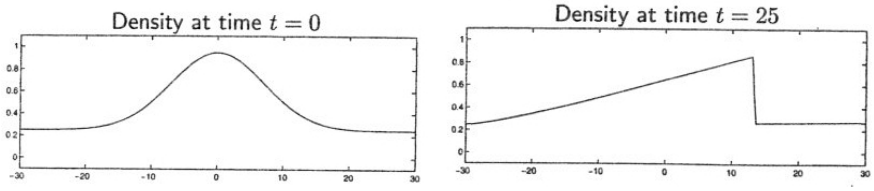

(a) Initial condition. (b) Solution at $t = 25$.

Figure 1.6: The nonlinear Burgers equation. A shock and a rarefaction wave can be seen in (b).

density q becomes more rarefied as the density increases smoothly. Figure 1.6 shows a schematic behavior of the solutions to the Burgers' equation.

Since solutions develop discontinuities, we have to define weak solutions. Following [50], we define

Definition 1.2.1 (Weak solution)**.** *The function $q(x,t)$ is a* **weak solution** *of the conservation law,*

$$\frac{\partial}{\partial t}q(x,t) + \frac{\partial}{\partial x}f(q(x,t)) = 0, \tag{1.2.16}$$

with given initial data $\overset{\circ}{q}(x)$ if the following condition holds

$$\int_0^\infty \int_\infty^\infty q\phi_t + f(q)\phi_x dxdt = -\int_0^\infty \overset{\circ}{q}(x)\phi(x,0)dx \tag{1.2.17}$$

for all continuously differentiable functions ϕ with compact support.

It can be shown that any weak solution also satisfies the integral form of the conservation law, i.e.,

$$\frac{d}{dt}\int_{x_1}^{x_2} q(x,t)dx = f(q(x_1,t)) - f(q(x_2,t)), \forall x_1, x_2 \in \mathbb{R}, \tag{1.2.18}$$

and vice versa, [50].

In general, the weak solution to a conservation law is not necessarily unique. In order to regain uniqueness, it is reasonable to look at a so-called **entropy function** $\eta(q)$. This is motivated from the second law of thermodynamics, stating that the entropy of an isolated system, which is not in equilibrium, will tend to increase over time.

Definition 1.2.2 (Entropy inequality)**.** *A weak solution q satisfies the* **entropy inequality** *if*

$$\int_0^\infty \int_\infty^\infty \eta(q)\phi_t + \psi(q)\phi_x dxdt \leq -\int_0^\infty \eta(\overset{\circ}{q}(x))\phi(x,0)dx \tag{1.2.19}$$

for all $\phi \in C_0^1(\mathbb{R}\times\mathbb{R})$ with $\phi(x,t) \geq 0\ \forall x,t$. Furthermore, an entropy function is **admissible** *if and only if*

$$\eta_q^T f_q = \psi_q^T. \tag{1.2.20}$$

The weak entropy inequality chooses the physically relevant solution among all the weak solutions.

In the linear case of a hyperbolic system of m equations, we know that for a solution there are at any point x exactly m waves passing by at different speeds, and we observe a superposition of these waves. In the nonlinear case, these waves are constantly interacting with each other, and in addition they deform separately. These problems cannot be solved analytically in general, and therefore we will look at special situations. We will introduce several concepts in order to classify the nonlinear hyperbolic PDEs.

Shock waves and Hugoniot loci

In this section, we will describe isolated shock waves separating two constant states (q_L, q_R). The relation that must hold across a shock and its speed of propagation comes from the fact that across *any* shock the so-called **Rankine-Hugoniot condition** must be satisfied. It is simply derived from applying the integral form of the conservation law to the region of the jump.

Let q^* be any fixed state. Then all states q that can be connected to q^* by a shock with speed s have to satisfy the **Rankine-Hugoniot condition**

$$s(q^* - q) = f(q^*) - f(q), \quad q^* \in \{q_L, q_R\}. \tag{1.2.21}$$

Remark 1.2.1. *In the linear case ($f(q) = Aq$) this means solving*

$$A(q^* - q) = s(q^* - q),$$

and therefore $q^* - q$ must be an eigenvector of the matrix A, and the propagation speed s of the discontinuity is the corresponding eigenvalue λ.

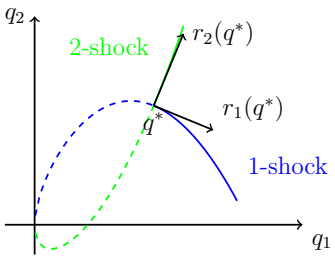

Figure 1.7: Hugoniot Loci.

In the linear case, the states connected to a state q^* by a shock will be straight lines. In the general case, we can draw all the states q that can be connected to q^* by shock wave, by solving the Rankine-Hugoniot condition in the state space. This set of states is called a **Hugoniot locus**. Figure 1.7 shows one example for the Hugoniot loci of a 2×2 system.

Simple Waves and Rarefactions

Another important case is to investigate solutions that are smoothly varying, but which also have the property of being associated with only one characteristic family of the system.

Definition 1.2.3 (Integral curve of a vector field)**.** *A smooth curve $\tilde{q}(\xi), \xi \in \mathbb{R}$ in state space is called* **integral curve of the vector field** *r_p, if*

$$\tilde{q}'(\xi) \parallel r_p(q(\xi)), \tag{1.2.22}$$

for all ξ. Figure 1.8 shows a typical integral curve for a 2×2 system.

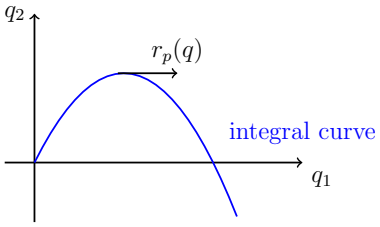

Figure 1.8: Integral curve.

A **simple wave** is a special solution to a conservation law with

$$q(x,t) = \tilde{q}(\xi(x,t)), \tag{1.2.23}$$

where $\tilde{q}(\xi)$ is an integral curve (ξ smooth).

A **centered rarefaction wave** is a special case of a simple wave in a genuinely nonlinear field, in which $\xi(x,t) = x/t$. This means that the solution is constant on rays through the origin, having the form

$$q(x,t) = \begin{cases} q_L & \text{if } x/t \leq \lambda_p(q_L), \\ \tilde{q}(x/t) & \text{if } \lambda_p(q_L) \geq x/t \leq \lambda_p(q_R), \\ q_R & \text{if } x/t \geq \lambda_p(q_R), \end{cases} \tag{1.2.24}$$

where λ_p is the pth eigenvalue.

The tendency of a simple wave to spread/steepen is given by the variation of the eigenvector along the integral curve, i.e.,

$$\frac{d}{d\xi}\lambda_p(\tilde{q}(\xi)) = \nabla\lambda_p(\tilde{q}(\xi)) \cdot \tilde{q}'(\xi).$$

This can be used to define the following.

Definition 1.2.4. *The pth field is called*

- **genuinely nonlinear**, *if*

$$\nabla\lambda_p(q) \cdot r_p(q) \neq 0, \quad \forall q,$$

- *and* **linearly degenerate**, *if*

$$\nabla\lambda_p(q) \cdot r_p(q) \equiv 0, \quad \forall q.$$

The property of genuine non-linearity insures that characteristics are always compressing or expanding as q varies.

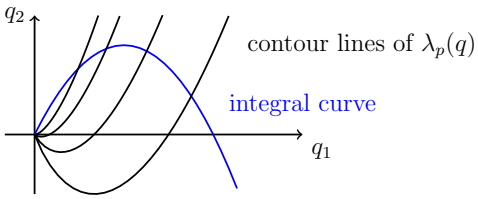

Figure 1.9: Integral curves and contour lines.

Non-strict hyperbolicity and non-convexity

The property of hyperbolicity means that all the eigenvalues are real (and we have a full set of eigenvectors). However, we can further divide hyperbolicity into three different cases. Let $f : \mathbb{R}^m \to \mathbb{R}^m$.

Strict hyperbolicity means that the Jacobian of the flux f' has distinct eigenvalues for all $q \in \mathbb{R}^m$. Therefore the geometric multiplicity equals the algebraic multiplicity and we have distinct eigenvectors forming a basis of $\mathbb{R}^m$. It can be shown, using the implicit-function theorem, that the Riemann problem can be uniquely solved for any q_L, q_R that are sufficiently close together [50].

The system is called **non-strictly** hyperbolic if not all eigenvalues of f' are distinct, but the geometric multiplicity still equals the algebraic multiplicity. Suppose q_0 is the point where the system is non-strictly hyperbolic, and there is an eigenspace with infinitely many directions that are eigenvectors. It is possible for infinitely many integral curves or Hugoniot loci to coalesce at such a point, called the **umbilic point**. This can lead to over/under-compressive shocks, where more/less characteristics are impinging on the shock, [50, 70].

A system is said to be **weakly** hyperbolic, if the eigenvalues of f' are real, but the geometric multiplicity is smaller than the algebraic multiplicity. This means, we have a defective matrix, and there is no full set of m linearly independent eigenvectors. This is, however, still close to hyperbolic theory (a small perturbation of the matrix leads to a full set of eigenvectors), but in addition we get singular shocks/delta shocks.

A further difficulty is the case of a **non-convex** flux function f. A flux function is non-convex if it is neither genuinely nonlinear nor linearly degenerate. In order to get a

valid entropy solution in this case, one can use the so-called **convex-hull construction** leading to **compound shocks**, [50]. A compound shock is basically a shock followed immediately by a rarefaction wave.

Let us now investigate the nonlinear structure of the ideal MHD equations (1.2.4).

1.2.5 Nonlinear structure of ideal MHD

For the ideal MHD equations, the eigenvalues (1.2.13) are not always distinctm and the system is therefore not strictly hyperbolic. We still have that the geometric multiplicity equals the algebraic multiplicity, and hence, the matrix is not defective, see section 1.2.4. This non-strict hyperbolicity is a formidable obstacle to the development of mathematical theory and numerical methods for MHD.

The non-strict hyperbolicity leads to the following degenerate cases displayed in the figure 1.10.

- $b_1 = 0, b_\perp \neq 0$. In this case
  - the fast waves are acoustic waves, and
  - the slow waves and Alfvén waves combine to shear waves.
- $b_1 = 0, b_\perp = 0$. Although this degeneracy is a special case of the first one, we mention it separately since we expect to have this degeneracy. This case is the hydrodynamic limit of the MHD equations, and therefore the MHD equations degenerate to the Euler equations.
- $b_1 < a, b_\perp = 0$. In this case, the fast waves are regular acoustic waves.
- $b_1 > a, b_\perp = 0$. Here, the slow waves are regular acoustic waves.
- $b_1 = a, b_\perp = 0$. This case is the so-called triple umbilic point.

In a general direction $\mathbf{n} \in \mathbb{R}^3, \|\mathbf{n}\|_2 = 1$ the eigenvalues of the equations (1.2.2) are given by ([12])

$$\lambda_{1,8} = \mathbf{u}\cdot\mathbf{n} \mp c_f, \lambda_{2,7} = \mathbf{u}\cdot\mathbf{n} \mp \mathbf{b}\cdot\mathbf{n}, \lambda_{3,6} = \mathbf{u}\cdot\mathbf{n} \mp c_s, \lambda_{4,5} = \mathbf{u}\cdot\mathbf{n}.$$

It is well known that the eigenvectors of (1.2.10) have to be scaled properly in order to be well-defined, see [68]. Here, we present these orthonormal set of **entropy scaled** eigenvectors described in [12], using the symmetric form of the MHD equations. Using the notation of [12, 68], we introduce the following normalizing factors,

$$\alpha_f^2 = \frac{a^2 - c_s^2}{c_f^2 - c_s^2}, \quad \alpha_s^2 = \frac{c_f^2 - a^2}{c_f^2 - c_s^2}.$$

Note that $\alpha_f^2 + \alpha_s^2 = 1$. Furthermore, we denote with $\mathbf{n}^\perp$ a unit vector orthogonal to $\mathbf{n}$, lying in the plane spanned by $\mathbf{n}$ and $\mathbf{b}$. Then, the right eigenvector corresponding to the contact wave λ_4 is given by

$$r_e = \sqrt{\frac{\gamma - 1}{\gamma}}(\sqrt{\rho}, \mathbf{0}, \mathbf{0}, 0)^T,$$

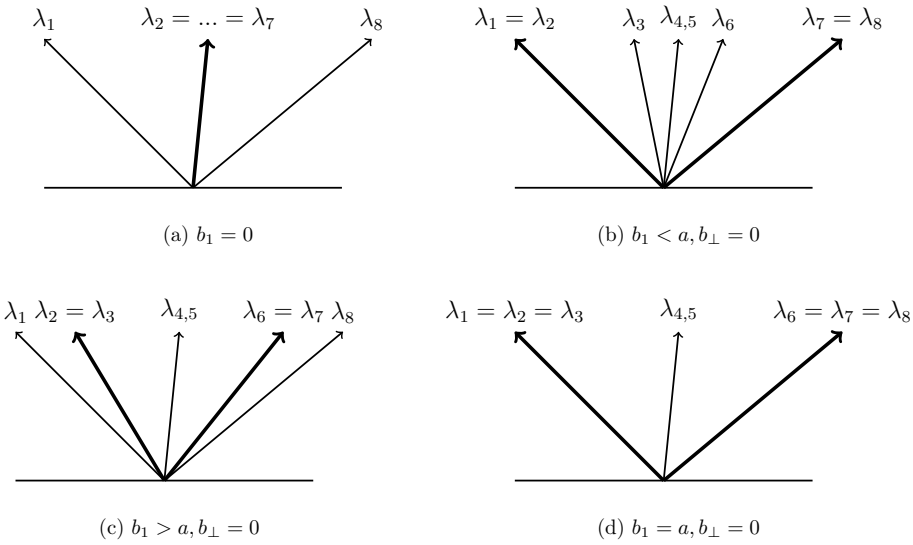

(a) $b_1 = 0$ (b) $b_1 < a, b_\perp = 0$

(c) $b_1 > a, b_\perp = 0$ (d) $b_1 = a, b_\perp = 0$

Figure 1.10: Degenerate cases for ideal MHD.

and the eigenvector corresponding to the shear wave λ_5 is

$$r_s = \sqrt{\frac{1}{\gamma}}(0, \mathbf{0}, a\mathbf{n}, 0)^T.$$

The eigenvectors corresponding to the Alfvén waves λ_2 and λ_7 are given by

$$r_A^{\pm} = \sqrt{\frac{1}{2}}\left(0, \pm\frac{\sqrt{p}}{\rho}(\mathbf{n}^\perp \times \mathbf{n}), \sqrt{\frac{p}{\rho}}(\mathbf{n}^\perp \times \mathbf{n}), 0\right)^T,$$

where r_A^+ corresponds to λ_2. The eigenvectors corresponding to the fast and slow waves read,

$$r_f^{\pm} = \sqrt{\frac{1}{2\gamma}}\begin{pmatrix} \alpha_f\sqrt{\rho} \\ \mp\frac{\alpha_f a^2 \mathbf{n} + \alpha_s a((\mathbf{b}\mathbf{n}^\perp)\mathbf{n} - (b\mathbf{n})\mathbf{n}^\perp)}{\sqrt{\rho}c_f} \\ \alpha_s a\mathbf{n}^\perp \\ \alpha_f\sqrt{\rho}a^2 \end{pmatrix}, \quad r_s^{\pm} = \sqrt{\frac{1}{2\gamma}}\begin{pmatrix} \alpha_s\sqrt{\rho} \\ \mp\mathrm{sgn}(\mathbf{b}\cdot\mathbf{n})\frac{\alpha_s a(\mathbf{b}\cdot\mathbf{n})\mathbf{n} + \alpha_f c_f^2 \mathbf{n}^\perp}{\sqrt{\rho}c_f} \\ -\alpha_f a\mathbf{n}^\perp \\ \alpha_s\sqrt{\rho}a^2 \end{pmatrix}.$$

The normalization factors α_f and α_s are not well-defined at the triple point where $b_1 = a$ and $b_\perp = 0$. In this case, we use the fact that $\alpha_f^2 + \alpha_s^2 = 1$ and define $\alpha_f = \alpha_s = 1/\sqrt{2}$. In the papers of the chapters 3, 4 and 5 we use a Roe-solver based on these eigenvectors. Since this solver is based on the symmetric form of the equations, the matrix of the left eigenvectors is given by $L = R^T$.

The eigenvalue analysis ([68, 12]) of the standard form (1.2.4) (semi-conservative form (1.2.2)) shows that the system is hyperbolic but not strictly hyperbolic. Solutions are

typically complicated and contain interesting discontinuities like shock waves, contact discontinuities, compound and intermediate shocks. Even for "simple" initial value problems, such as the Riemann problem, we do not have existence or well-posedness results. Since it is not possible to find analytic solutions to the MHD equations in general, we have to use numerical simulations as our main tool for studying the solutions of these equations.

1.2.6 Finite Volume Schemes

In order to approximate the solution to a conservation law in the domain $x \in [x_l, x_r]$, we first divide the domain into cells. For simplicity, the domain is discretized by a uniform grid with the grid spacing Δx. We set $x_i = x_l + i\Delta x$ and $I_i = [x_{i-1/2}, x_{i+1/2})$. The cell average of the unknown vector q at time t^n is denoted by Q_i^n. Any good numerical method for conservation laws is based on the integral form of the equations [50], i.e.,

$$\frac{d}{dt}\int_{x_{i-1/2}}^{x_{i+1/2}} q(x,t)dx + f(q(x_{i+1/2},t)) - f(q(x_{i-1/2},t)) = 0.$$

These methods are known as Godunov-type schemes, see figure 1.11, and are based on the so called **REA** algorithm, i.e., we iterate the following procedure

- given cell averages at some time level,
- **R**econstruct cell averages by piecewise polynomials,
- **E**volve the local Riemann problems (exactly or approximately),
- **A**verage the evolved solution at the next time level.

The resulting fully discrete form of the scheme is

$$Q_i^{n+1} = Q_i^n - \frac{\Delta t}{\Delta x}\Big(F(Q_i^n, Q_{i+1}^n) - F(Q_{i-1}^n, Q_i^n)\Big).$$

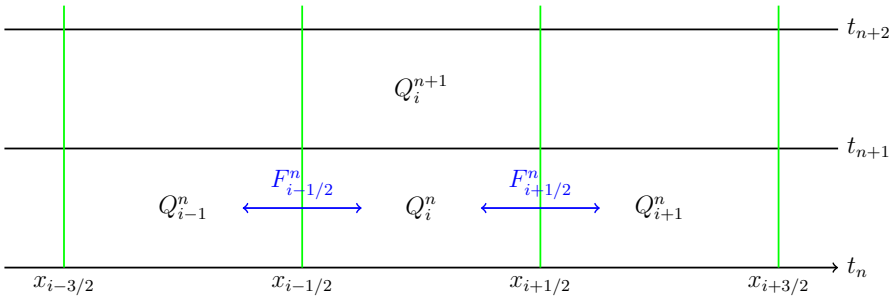

Figure 1.11: Finite Volume scheme.

One essential requirement for a numerical method convergence, i.e., the numerical solution should converge to the true solution of the differential equation as we refine the grid. Generally, this requites the following two conditions

- **Consistency**: The numerical flux should approximate the integral

$$F^n_{i+1/2} = F(Q^n_i, Q^n_{i+1}) \approx \frac{1}{\Delta t}\int_{t_n}^{t_{n+1}} f(q(x_{i+1/2}, t))dt.$$

- **Stability**: For a method to be stable, there have to be estimates (in a suitable norm) leading to a bound on the solution.

For a two point flux we have the following two conditions for **consistency**. For any constant $\bar{q} \in \mathbb{R}$ we have,

$$F(\bar{q}, \bar{q}) = f(\bar{q}) \text{ and } |F(Q^n_i, Q^n_{i+1}) - f(\bar{q})| \leq L \max(|Q^n_i - \bar{q}|, |Q^n_{i+1} - \bar{q}|), \tag{1.2.25}$$

for some constant L. For a method to be **stable**, we requite the following necessary condition.

Definition 1.2.5 (CFL-condition)**.** *A numerical method can be convergent only if its numerical domain of dependence contains the true domain of dependence of the PDE, at least in the limit as $\Delta t, \Delta x$ go to zero.*

For FV schemes we have typically the following restriction on the size of the time step

$$\max_i |\lambda^n_i| \frac{\Delta t^n}{\Delta x} \leq \mathrm{c}, \tag{1.2.26}$$

where λ^n_i is the largest eigenvalue of the flux f, and the constant c is the CFL-number of the numerical method.

The following theorem states the importance of the method being based on the conservative form, see [50].

Theorem 1.2.1 (Lax-Wendroff theorem)**.** *Consider a sequence of grids indexed by $j = 1, 2, ...$ with mesh parameters $\Delta t^{(j)}, \Delta x^{(j)} \to 0$ as $j \to \infty$. Let $Q^{(j)}(x, t)$ denote the numerical approximation computed with a consistent and conservative method on the jth grid. Suppose that $Q^{(j)}$ converges to a function q as $j \to \infty$, i.e.,*

$$\|Q^{(j)} - q\|_q \to 0, \text{ as } j \to \infty, \tag{1.2.27}$$

where $\|\cdot\|_q$ is the usual norm in L^q. Then $q(x, t)$ is a weak solution of the conservation law.

One way to derive solvers for hyperbolic conservation laws is to use **linearized Riemann solvers**. This means that instead of solving the local Riemann problems

$$\begin{aligned} q_t + f(q)_x &= 0, \\ q(x, 0) &= \begin{cases} Q^n_{i-1} & \text{, if } \quad x < 0, \\ Q^n_i & \text{, if } \quad x > 0, \end{cases} \end{aligned}$$

we linearize around some state ([67])

$$\begin{aligned} q_t + A_{i-1/2} q_x &= 0, \\ q(x, 0) &= \begin{cases} Q^n_{i-1} & \text{, if } \quad x < 0, \\ Q^n_i & \text{, if } \quad x > 0, \end{cases} \end{aligned}$$

where $A_{i-1/2}$ has to be

- hyperbolic (diagonalizable with real eigenvalues),
- and consistent, i.e., $A_{i-1/2} \to f'(\bar{q})$ as $Q^n_{j-1}, Q^n_j \to \bar{q}$.

There exist many possibilities for doing so. One possibility is to use

$$A_{i-1/2} = \frac{1}{2}\left(f'(Q^n_{i-1}) + f'(Q^n_i)\right),$$

but this is not hyperbolic in general. In order to have a hyperbolic matrix, one chooses

$$A_{i-1/2} = f'\left(\mu(Q^n_{i-1}, Q^n_i)\right).$$

Here μ is any average one can think of, but the two most commonly use are the arithmetic average and the Roe average, if it is available.

Now we are left with a linear system, and we know how to solve this. We decompose into waves,

$$Q^n_i - Q^n_{i-1} = \sum_{p=1}^{m} \alpha^p_{i-1/2} r^p_{i-1/2},$$

where the wave strength is given by $\alpha^p_{i-1/2} = l^p_{j-1/2} \cdot (Q^n_j - Q^n_{i-1})$. Now the numerical flux can be written as

$$f(Q^n_{i-1}, Q^n_i) = \frac{1}{2}\Big(f(Q^n_{i-1}) + f(Q^n_i) - \sum_p \alpha^p_{i-1/2}|\lambda_p| r^p_{i-1/2}\Big).$$

This approach is used in the **Roe-type solvers**. However, in general one has to use an **entropy fix**, see for instance [39]. Another possibility is to use **HLL-type solvers** ([50]) named after Harten, Lax and van Leer. They resolve only a certain number of waves and are in general nonlinear.

Both these approaches are limited to first order. In order to gain formally higher order schemes, one has to use an appropriate polynomial reconstruction in the above described **REA** algorithm. This has to be done in such a way that we do not introduce oscillations. In addition, an appropriate Runge-Kutta time-stepping has to be used to have the same order in space and time, see [50]. Popular methods include the ENO reconstruction ([40]) and the WENO reconstruction ([72]).

We start by summarizing the results of some standard first order finite volume schemes for the approximation of the solutions of the ideal MHD equations in one dimension.

1.2.7 Finite Volume schemes for MHD in one dimension

Some of the standard ways to determine the numerical fluxes include HLL-type solvers, like the ones described in [36, 59], and Roe-solvers, see [67]. A Roe-average for the ideal MHD equations was developed in [24]. A special form of the Roe solver based on entropy variables, proposed and tested in [12], will be used in some numerical experiments in this dissertation.

The main problem with Roe solvers is that they can result in negative pressures and densities. Among all HLL-type solvers for MHD, the two-wave solvers based on wave

speeds suggested in [28] are the simplest to implement. They are provably positive (in the sense that the pressure and density in the solution are positive) and entropy stable but are too dissipative in most test problems. Three-wave HLL solvers based on heuristic considerations have been developed in [53] and [36]. The solver of [36] is also provably positive. A positivity preserving five wave solver for MHD was developed in [59]. Recently, three-, five- and seven-wave approximate Riemann solvers have been designed in [20]. These solvers are proved to be positive. A thorough comparison of different HLL solvers has been reported in [58, 73].

Table 1.1 shows a comparison of three different schemes for the standard one dimen-

error(ρ) [%]	HLL	HLL3	Roe
100	4.44	3.35	2.42
200	2.87	1.95	1.23
400	1.88	1.22	0.73
800	1.13	0.64	0.30
1600	0.62	0.28	0.10

error(B_2) [%]	HLL	HLL3	Roe
100	3.32	2.75	1.89
200	2.04	1.56	0.85
400	1.29	0.97	0.50
800	0.75	0.51	0.18
1600	0.38	0.23	0.09

Table 1.1: Relative errors in L^1 of the density ρ (left) and B_2 (right) at time $t = 0.5$ for the Brio-Wu shock tube for various meshes.

sional Brio-Wu shock tube, given by the initial data

$$(\rho, \rho\mathbf{u}, p, \mathbf{B}) = \begin{cases} (1.0, +1.0, 0, 0, 0, 0.7, 0, 1.0), & \text{if } x < 0.5, \\ (0.3, -0.3, 0, 0, 0, 0.7, 0, 0.2), & \text{otherwise.} \end{cases}$$

The computational domain is $(x, t) \in [0, 1.5] \times [0, 0.5]$ with Neumann boundary conditions. Two solvers are of the HLL-type, resolving two (HLL) and three (HLL3) waves of the Riemann fan, and we also present the results for the Roe-solver. All standard schemes do very well (see figure 1.12 for a comparison) on the Brio-Wu test-case and converge at the expected first order rate.

However, any realistic modeling of physical phenomena, such as the wave propagation in the solar atmosphere that we are interested in, is based on the MHD equations in multiple dimensions. Therefore, we will describe the results of some standard numerical schemes for approximating the solutions of MHD in multiple spacial dimensions.

1.2.8 Finite Volume schemes for MHD in multiple dimensions

Consider the ideal MHD equations (1.2.4) in the domain $\mathbf{D} = [X_L, X_R] \times [Y_L, Y_R] \times [Z_L, Z_R]$. For simplicity, we consider a uniform grid in space with mesh points given by $x_i = i\Delta x$, $y_j = j\Delta y$, and $z_k = k\Delta z$, where Δx, Δy, and Δz are the mesh sizes in the x, y, and z direction respectively ([50]). Let the Δt^n denote the time step at the n-th time level $t^n = \sum_{m<n} \Delta t^m$, and let the cell average at t^n be denoted by $U^n_{i,j,k}$. The time step Δt^n is determined by a suitable CFL condition.

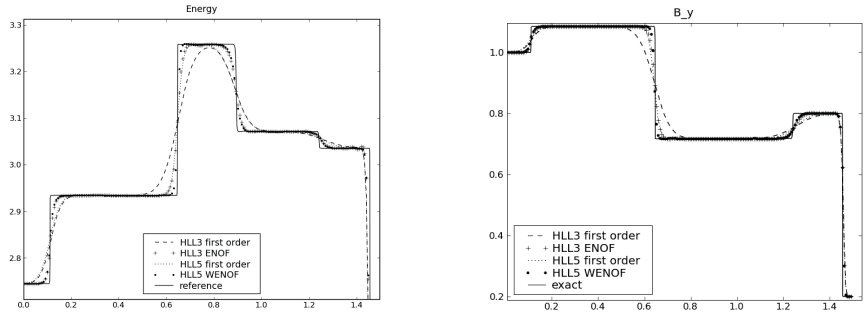

Figure 1.12: Results for the Brio-Wu shock tube with 200 grid points at $t = 0.5$. Reference solution is the H_5W scheme with 3200 grid points. Left: Energy. Right: Magnetic field component B_2.

With this notation, a general first order finite volume scheme reads

$$\begin{aligned} U^{n+1}_{i,j,k} = U^n_{i,j,k} &- \frac{\Delta t^n}{\Delta x}\left(F(U^n_{i,j,k}, U^n_{i+1,j,k}) - F(U^n_{i-1,j,k}, U^n_{i,j,k})\right) \\ &- \frac{\Delta t^n}{\Delta y}\left(G(U^n_{i,j,k}, U^n_{i,j+1,k}) - G(U^n_{i,j-1,k}, U^n_{i,j,k})\right) \\ &- \frac{\Delta t^n}{\Delta z}\left(H(U^n_{i,j,k}, U^n_{i,j,k+1}) - H(U^n_{i,j,k-1}, U^n_{i,j,k})\right), \end{aligned} \tag{1.2.28}$$

where F, G, and H are numerical fluxes consistent with the directional fluxes f, g, and h respectively.

$\max(p)$	HLL	HLL3	Roe
100×100	4.00	4.41	5.27
200×200	4.74	4.94	5.39
400×400	5.11	5.21	5.88
800×800	–	–	–
1600×1600	–	–	–

$\|\mathrm{div}(B)\|_{L^1}$	HLL	HLL3	Roe
100×100	1.92	2.81	7.77
200×200	1.77	2.93	6.94
400×400	1.47	2.60	5.64
800×800	–	–	–
1600×1600	–	–	–

Table 1.2: Maximum pressure (left) and the L^1 norm of the standard discrete divergence operator (right) at time $t = \pi$ for the Orszag-Tang vortex, for different schemes using a $M \times M$ grid.

Table 1.2 presents the results for a standard test-case, the so-called Orszag-Tang vortex. Here "-" means that the corresponding solver crashed due to negative pressure before it could reach the final time $t = \pi$. The Orszag-Tang vortex is a well-known benchmark test for two dimensional schemes for the MHD equations (see [80]). For this problem, the initial data are given by

$$\begin{aligned} &(\rho, \rho u_1, \rho u_2, \rho u_3, B_1, B_2, B_3, p) \\ &\qquad = \left(\gamma^2, -\rho\sin(y), \rho\sin(x), 0, -\sin(y), \sin(2x), 0, \gamma\right). \end{aligned} \tag{1.2.29}$$

The computational domain is $(\mathbf{x}, t) \in [0, 2\pi]^2 \times [0, \pi]$ with periodic boundary conditions.

Looking at table 1.2, we find that the three standard solvers (HLL, HLL3, and Roe) crash at a mesh size of 800×800 and higher, although the L^1 norm of the standard discrete divergence operator decreases with refining the mesh. Since there is no reference solution for the Orszag-Tang vortex, it is quite common to use the maximum pressure as a measure for dissipation. Less dissipation means higher maximum pressure. We observe in table 1.2 that all the schemes get less and less dissipative as the mesh is refined, until they crash due to negative pressure for fine enough meshes. The same behavior is seen in other standard test-cases we have tested, including the Cloud-Shock interaction and the Rotor problem, see chapter 3.

We want to investigate the observed instabilities here. One of the possible reasons for these crashes is linked to the divergence constraint. The transition from one space dimension to multiple dimensions is not trivial due to the singular matrix obtained from restriction to one space dimension, see 1.2.11. The divergence constraint (1.2.3) in one dimension implies that the normal magnetic field must be a constant in space. HLL-type solvers like the ones described in [36, 59] use this information in their definitions of speeds and states. For multi-dimensional MHD, the magnetic field in each normal direction is no longer constant. Consequently, there is no straightforward way of how to extend the HLL-solvers based on the standard form (1.2.4) to multiple dimensions. One possible solution however, consists of using an average of the normal magnetic field across each interface in the expressions. This somewhat arbitrary choice may destroy the stability properties of the solvers. In the community of numerical simulations of the solutions to the MHD equations, there has been considerable attention to the numerical treatment of the divergence constraint. We will continue with a short summary of those results.

The divergence constraint

It is well-known that the treatment of the divergence constraint $\mathrm{div}\mathbf{B} = 0$ is a highly non-trivial aspect. Standard finite volume schemes will generate divergence errors, and these can induce instabilities, see [80]. Tóth puts it very nicely in [80]: "There is a big difference between the view of theorists, who would generally insist that $\mathrm{div}\mathbf{B}$ should be exactly zero, and practitioners of numerical MHD, who usually take a more pragmatic approach, and are satisfied with $\mathrm{div}\mathbf{B}$ converging to zero as the grid resolution Δx and the time step Δt approach zero. The justification for the latter approach is simple: none of the numerical values agree to the analytical solution exactly, so why should one insist that a specific combination of them, namely some numerical representation of $\mathrm{div}\mathbf{B}$ should be equal to the analytic value, i.e., zero. Ideally, one would like to have that particular representation to be zero, which ensures that no unphysical effects arise. The usual example for such an unphysical effect is acceleration of the plasma parallel to the field lines (even if the unphysical force vanishes with increasing grid resolution, it may be quite a nuisance when an equilibrium flow is to be modeled). For conservative shock-capturing methods, however, it is impossible to define a particular discrete constraint on the magnetic field that would avoid all unphysical effects. In particular, I prove in Appendix A that a scheme cannot satisfy both the numerical conservation of momentum and the requirement that the discretized acceleration due to the Lorentz force should be

exactly perpendicular to the magnetic field in every grid cell. Due to these difficulties, the usual practice is to choose some simple discretization of div$\mathbf{B}$, but it should be clear that the choice is always somewhat arbitrary."

A popular method to remove divergence is the projection method of [22]. In this method the non-solenoidal approximate magnetic field is corrected at each time step by using an elliptic solver. Let $\mathbf{B}^*$ be the magnetic field provided by some solver at time t^{n+1}. Using the well known unique decomposition of a vector field into a curl and a gradient we can write this field as

$$\mathbf{B}^* = \nabla \times \mathbf{A} + \nabla\phi.$$

Thus, by solving the Poisson equation

$$\nabla^2\phi = \nabla \cdot \mathbf{B}^*,$$

we can correct the magnetic field to have zero divergence by

$$\mathbf{B}^{n+1} = \mathbf{B}^* - \nabla\phi.$$

The method leads to solenoidal fields but is computationally expensive on account of the elliptic solver. Also, it depends on some discretization of the divergence operator div$\mathbf{B}$. The solution is projected to have zero div$\mathbf{B}$ for one such operator, while the norm of the divergence might still be large using another discretization of the divergence, at least for solutions containing shocks. This somewhat ad hoc method has other stability issues discussed in [70, 80].

Another method for divergence cleaning consists in staggering the discretizations of the velocity and magnetic field. This can be used to design methods leading to a (discrete) divergence free magnetic field. Variants of this method have been proposed in [30, 26, 11, 70, 71] and references therein. Staggering of the variables leads to complications when parallelizing the method and in designing variable grid methods. Unstaggered variants of this approach have been proposed in [77, 78, 57]. A thorough comparison of divergence cleaning methods was performed in [80]. Another potential problem with both the staggering and projection techniques lies in their numerical stability. In chapter 3 we provide examples where the projection method is quite stable on coarse meshes but exhibits instabilities when the mesh was refined. We have also observed similar behavior for some of the staggered mesh methods.

A third alternative for divergence cleaning was proposed in [65] and consists of discretizing the semi-conservative Godunov-Powell form (1.2.2). Note that (1.2.5) suggests the initial divergence errors will be transported out of the domain by the flow. We believe that this approach is the most natural since it uses the form obtained from first principles. Furthermore, this is the only way to symmetrize the equations of MHD. In addition, the Godunov-Powell source term makes the equations Galilean invariant. For zero divergence it is equivalent to the standard form. In [65, 66], a linearized solver is used to define numerical fluxes and a simple centered discretization is proposed for the Godunov-Powell source term in (1.2.2). However, in the paper presented in chapter 2 we have constructed a simple test case showing that a centered discretization of the Godunov-Powell source term can lead to numerical instabilities, even for the simple case of the linear magnetic induction equation (1.2.1), see figure 1.13.

This concludes the discussion of the numerical results available in literature. In all the papers we emphasize the importance of the Godunov-Powell source term for numerical simulations. Despite their formal equivalence, the two forms, (1.2.4) and (1.2.2), differ in some respects.

i) We believe that it is more natural to consider and discretize the semi-conservative form (1.2.2), since the derivation from **first principles** gives (1.2.2).

ii) Furthermore, (1.2.2) is **Galilean invariant**, whereas the standard form (1.2.4) is not.

iii) From a mathematical perspective, the semi-conservative form (1.2.2) was shown to be **symmetrized by the physical entropy** in [35], leading to **stability estimates** [12]. The standard form (1.2.4) is not symmetrizable.

This thesis consists of 6 papers, and we begin by summarizing the results of the first paper.

1.3 A stable upwind scheme for the induction equations

The linear magnetic induction equation (1.2.1) can be seen as a simple model equation for MHD where we already know the velocity field. In this article (see chapter 2) we design a numerical scheme which handles the divergence constraint in a suitable manner. We design and analyze an upwind scheme based on the symmetrized version of the equations (hence using the Godunov-Powell source term) in the non-conservative form. The scheme is shown to converge to a weak solution of the equations due to an energy bound for which the symmetization is essential. Furthermore, the discrete divergence produced by the scheme is shown to be bounded. We report several numerical experiments that show that the stable upwind scheme of this paper is robust. In order to show that it is necessary to use a proper upwinding of the Powell source term we constructed the following initial data for the induction equation (1.2.1).

$$\mathbf{u}(x,y,t=0)=(1,2), \quad \text{and} \quad B_1(x,y,t=0)=B_2(x,y,t=0)=\begin{cases}2 & \text{if } x>y,\\ 0 & \text{otherwise.}\end{cases} \tag{1.3.1}$$

Since $\mathbf{u}$ is constant, the exact solution of equation (1.2.1) is

$$\mathbf{B}(x,y,t)=\mathbf{B}_0(x-t,y-2t).$$

We can see from the results shown in figure 1.13 that the divergence preserving scheme developed by Torrilhon and Fey ([77]) seems to be more accurate than the scheme using a proper upwinding of the Godunov-Powell source term, at the expense of some oscillations, as the solutions generated with the divergence preserving scheme are not total variation diminishing (TVD), even in this simple case of constant velocity fields. The naive upwind scheme (no Godunov-Powell source) gives a solution similar to the scheme that uses

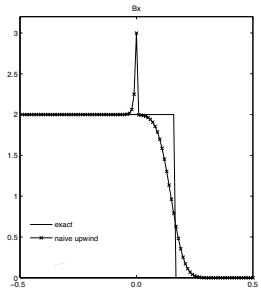

(a) standard (naive) upwind scheme without Godunov-Powell source

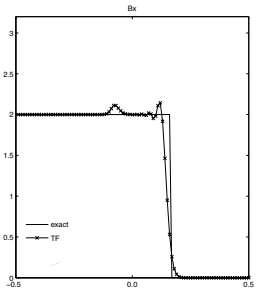

(b) divergence preserving scheme without Godunov-Powell source

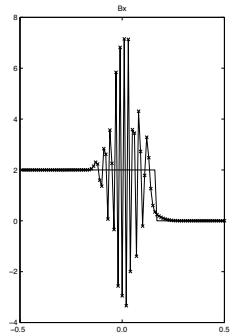

(c) standard upwind scheme with central discretization of the Godunov-Powell source term

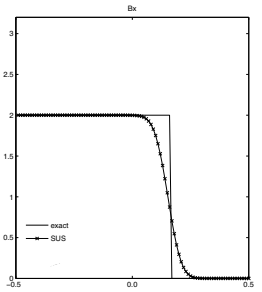

(d) stable upwind scheme with upwinded Godunov-Powell source

Figure 1.13: Approximations of $B_1(x,0), t = 0.3$, initial data given by (1.3.1).

a proper upwinded Godunov-Powell source term, but it has one pronounced spike or overshoot. The scheme using the central evaluation of the Powell source term is seen to be unstable. This example shows that the Godunov-Powell source term has to be introduced as well as upwinded in some manner in order to get stable results. The scheme developed in this paper relies on an implicit upwinding due to the use of the Friedrichs form.

The difficulties for the induction equation only occur in multiple dimensions, similar to the problems observed for standard solvers for MHD in section 1.2.8. In paper II we use the knowledge about the induction equation in order to derive more stable finite volume schemes for the MHD equations. This is achieved by splitting the MHD equations into a fluid part and a magnetic part and using the stable solver derived in paper I for the magnetic part.

1.4 MHD solver using a partial Godunov-Powell source

The magnetic induction equation is a simple model problem for MHD and has similar numerical difficulties as the equations of MHD. It is **non-strict hyperbolic** and the **divergence constraint has to be handled carefully**. Given our experience with the induction equation, we expect that it is also not only necessary to introduce and discretize the Godunov-Powell source term, but also that we need to use a proper upwinding of this term. Therefore, we derived a splitting based finite volume scheme for the ideal MHD equations (see chapter 3) based on the way the equations are actually derived from first physical principles, where MHD consists of the coupling between the Euler equations with source terms and the induction equation, see section 1.2.1.

$$
\begin{array}{lcll}
\rho_t & + & \mathrm{div}(\rho\mathbf{u}) & = 0 \\
(\rho\mathbf{u})_t & + & \mathrm{div}\left(\rho\mathbf{u}\otimes\mathbf{u} + p\mathcal{I}\right) & = \mathbf{J}\times\mathbf{B} \\
E_t^{\mathrm{hd}} & + & \mathrm{div}\left((E^{\mathrm{hd}}+p)\mathbf{u}\right) & = \mathbf{J}\cdot(\mathbf{B}\times\mathbf{u}) \\
 & & & \\
\mathbf{B}_t & + & \mathrm{div}\left(\mathbf{u}\otimes\mathbf{B} - \mathbf{B}\otimes\mathbf{u}\right) & = -\mathbf{u}\mathrm{div}(\mathbf{B}) \\
 & & \mathrm{div}(\mathbf{B}) = 0 &
\end{array}
$$

From this form of the equations the feedback loop of plasma motion triggering the magnetic field which in turn triggers some plasma motion, is easy to see.

Both the Euler equations and the induction equation are very well known, and therefore, we can use specialized solvers for each part of the MHD equations in a splitting approach. In the article presented in chapter 3 we designed finite volume schemes for the equations of ideal magnetohydrodynamics, based on splitting these equations into a fluid part and a magnetic induction part. The fluid part leads to an extended Euler system with magnetic forces as source terms. Solutions of the Riemann problem for these set of equations are approximated by suitable two and three wave HLL solvers. The magnetic part is modeled by the magnetic induction equations which are approximated using stable upwind schemes devised in the paper of chapter 2. These two sets of schemes can be combined either component by component, or by using an operator splitting procedure to obtain a finite volume scheme for the MHD equations. Since only the induction equation

uses the Godunov-Powell source term, the numerical schemes approximate the following set of equations

$$\begin{aligned} \rho_t + \operatorname{div}(\rho \mathbf{u}) &= 0, \\ (\rho \mathbf{u})_t + \operatorname{div}(\rho \mathbf{u} \otimes \mathbf{u} + (p + \frac{1}{2}|\mathbf{B}|^2) I - \mathbf{B} \otimes \mathbf{B}) &= 0, \\ E_t + \operatorname{div}((E + p + \frac{1}{2}|\mathbf{B}|^2)\mathbf{u} - (\mathbf{u} \cdot \mathbf{B})\mathbf{B}) &= 0, \\ \mathbf{B}_t + \operatorname{div}(\mathbf{u} \otimes \mathbf{B} - \mathbf{B} \otimes \mathbf{u}) &= -\mathbf{u}(\operatorname{div}\mathbf{B}), \end{aligned} \tag{1.4.1}$$

and hence use only a "partial" Godunov-Powell source term. The resulting schemes are simple to design and implement. These schemes are compared with existing HLL type and Roe type schemes for MHD equations in a series of numerical experiments. These tests reveal that the proposed schemes are robust and have a greater numerical resolution than HLL type solvers, particularly in several space dimensions. In fact, the numerical resolution is comparable to that of the Roe scheme on most test problems, with the computational cost being at the level of a HLL type solver. Furthermore, the schemes are remarkably stable even at very fine mesh resolutions and handle the divergence constraint efficiently with low divergence errors.

Here, we will present the results for the Orszag-Tang vortex (equation (1.2.29)) for the splitting based solvers. We present numerical results with different schemes in Figure 1.14 and Table 1.2. Even though the initial data are smooth, the solution develops discontinuities in form of shocks along the diagonals, together with a vortex in the center of the domain. The solution has a rich structure consisting of shocks, vortices, and other interesting smooth regions. The issues with any numerical scheme are resolution of the shocks as well as the central vortex. Another issue is that of control of divergence in some discrete norm. In fact, it is widely believed that lack of divergence control can lead to negative pressures and hence crashes in this test case. So ensuring stability of the solver, particularly at fine mesh resolutions is a challenge. There is no accepted reference solution in this case, and many papers have used the maximum pressure as a measure of accuracy of a scheme. We will compare the splitting based solvers with standard first order finite volume schemes for MHD equations.

- **HLL**. Two wave HLL-type solver for full MHD, see [28].
- **HLL3**. HLL-type solver for full MHD resolving three waves designed in [53].
- **Roe**. Roe solver based on adding symmetric diffusion in the entropy variables, in the spirit of [42] for Navier-Stokes equations and [12] for Euler equations.
- **HLL/SUS**.Splitting solver based on a two wave solver for the extended Euler equations and the stable upwind scheme for the induction equation.
- **HLLC/SUS**. Same as HLL/SUS but resolves the contact wave in addition.
- **HLLC/TF**. Same solver as HLLC/SUS for the extended Euler equations but uses a divergence preserving scheme for the induction equation (see [77]).

- **HLLC/LxF**. Same solver as HLLC/SUS for the extended Euler equations but uses the Lax-Friedrichs scheme for the induction equation.

We plot the pressure on a 100×100 mesh in Figure 1.14 and compare HLL, HLL/SUS, HLL3 and HLLC/SUS schemes for qualitative behavior. As shown in Figure 1.14, the

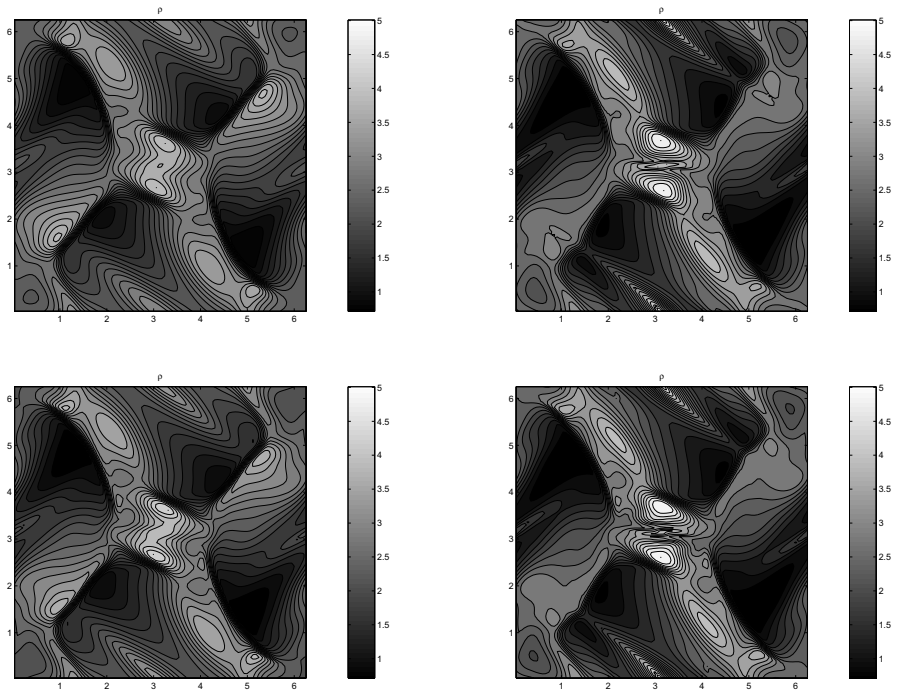

Figure 1.14: This figure shows the pressure computed with (from top left to bottom right): HLL2, HLL/SUS, HLL3 and HLLC/SUS on a 100×100 mesh at time $t = \pi$.

differences of the different schemes is clearly seen. In particular, the HLL scheme is very dissipative and the central vortex is not well resolved. Even the HLL3 scheme is quite dissipative and the shocks along the diagonal are smeared. On the other hand, the schemes based on splitting resolve the shocks very well. The central vortex is resolved by both the HLL/SUS and the HLLC/SUS scheme, and the shocks are much sharper than the features computed by the HLL3 solver for the full MHD equations. A thorough quantitative comparison is provided by considering the maximum pressures in Table 1.2 for different mesh resolutions. From table 1.3, we find that at relatively coarse mesh resolutions (up to 400×400 mesh points), the splitting solvers have much higher resolutions (measured in terms of maximum pressure) than the standard HLL and HLL3 solvers. In fact, even the HLL/SUS leads to sharper resolution of the solution than the more expensive HLL3 solver. Similarly, both the splitting solvers compare very well with the Roe solver. In

M	HLL	HLL3	HLL/SUS	HLLC/SUS	HLLC/LxF	Roe
100	4.00	4.41	4.94	5.04	4.61	5.27
200	4.74	4.94	5.39	5.41	4.71	5.39
400	5.11	5.21	5.79	5.81	5.00	5.88
800	–	–	6.05	6.07	5.26	–
1600	–	–	6.21	6.22	5.52	–

M	HLL	HLL3	HLL/SUS	HLLC/SUS	HLLC/LxF	Roe
100	1.92	2.81	4.17	4.28	0.00	7.77
200	1.77	2.93	3.23	3.32	0.00	6.94
400	1.47	2.60	2.46	2.50	0.00	5.64
800	–	–	1.85	1.87	0.00	–
1600	–	–	1.38	1.39	0.00	–

Table 1.3: Maximum pressure (top) and the L^1 norm of the divergence (bottom) at time $t = \pi$ for the Orszag-Tang vortex, for different schemes using a $M \times M$ grid.

fact, the HLLC/SUS leads to almost the same maximum pressure as the Roe solver. It should be added that the computational cost of the Roe solver is considerably higher than the HLLC/SUS solver.

One would expect that this high accuracy of the splitting based solvers should come at a price of reduced stability. On the contrary, table 1.3 shows that the splitting based solvers of this paper do not crash even for 1600×1600 mesh points and show increased resolution on these very fine meshes. On the other hand, the standard HLL, HLL3 and Roe solvers crashed on 800×800 and finer meshes due to instabilities. Thus on this test problem, the splitting based HLL solvers are at least as accurate as the Roe solver and more accurate than the HLL solvers and are far more stable.

Seeing the big success of introducing and discretizing the (partial) Godunov-Powell source term in the induction equation of the MHD equations, we expect a similar improvement for finite volume methods using the full Godunov-Powell source. The full Godunov-Powell source term, coming from the derivation from physical principles, symmetrizes the ideal MHD equation and makes them Galilean invariant, whereas the partial Godunov-Powell source term does not. Therefore, we derive an HLL-type solver, by discretizing the full source term in an appropriate way.

1.5 MHD solver using the full Godunov-Powell source

The next step was to design a stable and high order accurate finite volume schemes for the ideal MHD equations in multiple dimensions, see chapter 4. The finite volume schemes are based on three- and five-wave approximate Riemann solvers of the HLL-type, with the novelty that we allow for the magnetic field to vary. This is achieved by considering the semi-conservative Godunov-Powell form of the MHD equations (1.2.2). The Godunov-Powell source term is discretized in an upwind manner by utilizing the structure of the HLL-type solvers. Second order versions of the ENO- and WENO-type are proposed, together with suitable modifications to preserve positive pressure and density. The first

and second order schemes are tested on a suite of numerical experiments demonstrating a very satisfactory resolution and stability even on very fine meshes.

Again, we present the results for the Orszag-Tang vortex, see (1.2.29). We test a total of six schemes:

H_3	First order with the HLL three-wave solver,
H_5	first order with the HLL five-wave solver,
H_3E	second order with HLL three-wave solver and ENO reconstruction,
H_3W	second order with HLL three-wave solver and WENO reconstruction,
H_5E	second order with HLL five-wave solver and ENO reconstruction,
H_5W	second order with HLL five-wave solver and WENO reconstruction.

All the second order schemes use a positivity preserving modification described in chapter 5.

We compute with all the six schemes and present the computed pressure at the final time on a 200×200 mesh in figure 1.15. Both the first order H_3 and H_5 schemes are stable but dissipative. The shocks are smeared, and the central vortex is not resolved. The H_5 scheme is better at approximating the solution than the H_3 scheme. The second order schemes resolve the solution far better. The resolution of the shocks with the second order schemes is very impressive. The smooth regions are also resolved quite accurately. We computed a solution using the H_5W scheme on a 4000×4000 mesh using a parallelized version of the FV-code. Figure 1.16 shows the pressure. We observe that the H_5W scheme at this very fine mesh is stable and resolves the shocks as well as the central current sheet very well. Furthermore, it looks like we reached mesh convergence at these kind of fine meshes.

We also computed the well-known cloud-shock interaction (for details see chapter 5 in three dimensions. Figure 1.17 shows the results on a $200 \times 200 \times 200$ mesh using a parallelized version of the FV-code. Just as in the two dimensional case, a bow shock is created as the shock wave hits the cloud of high density from the left. We can see that the H_5W solver resolves the bow-shock very well.

In the next step, we want to apply our knowledge of simulating the ideal MHD equations to simulating wave propagation in the solar atmosphere. This means we will derive solvers using a cleverly upwinded Godunov-Powell source term in order to devise stable numerical schemes for approximating the solutions of the MHD equations with a gravity source term.

1.6 Simulating wave propagation in solar atmosphere

After developing accurate and stable schemes for the ideal MHD equations, we want to apply this knowledge to simulate real wave propagation in the stratified solar atmosphere, see section 1.1. The problem of modeling wave propagation in idealized stellar atmospheres has received considerable attention in the solar physics and astrophysics communities in recent years (see [69, 18] and references therein). A typical situation of interest is to model how convection generated waves from the inner layers of the Sun transport and deposit energy in the overlaying chromospheric and coronal plasmas. The waves interact

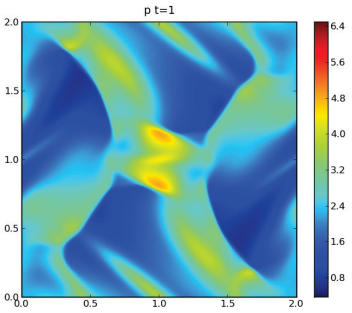

(a) H_3

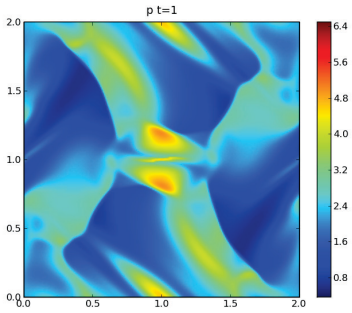

(b) H_5

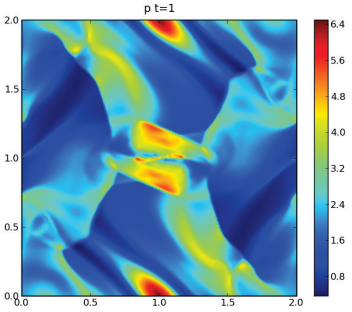

(c) H_3E

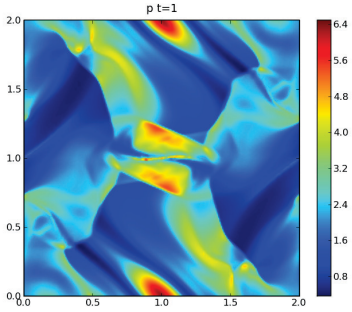

(d) H_5E

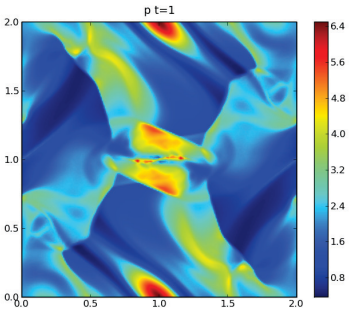

(e) H_3W

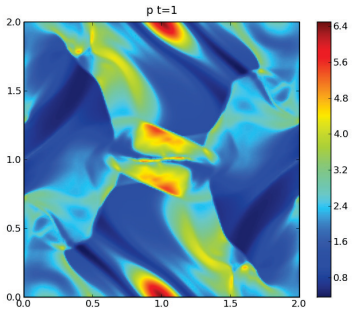

(f) H_5W

Figure 1.15: Pressure for the Orszag-Tang vortex on a 200×200 mesh at time $t = 1$ scaled to the extrema of the pressure in the reference solution.

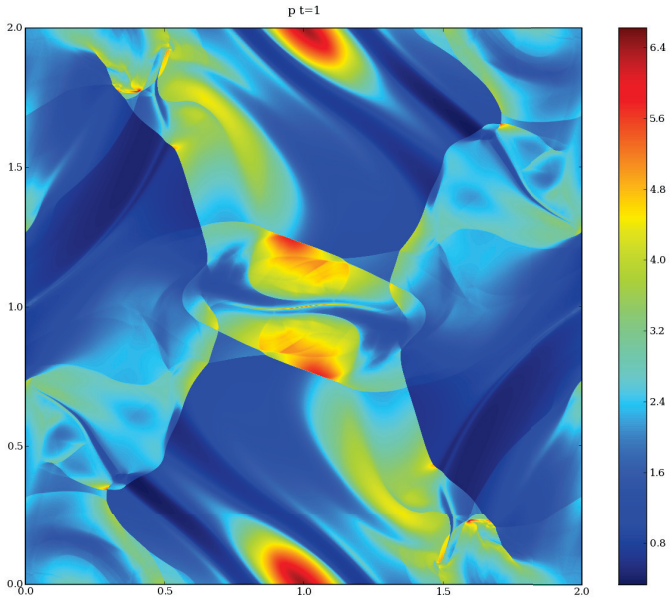

Figure 1.16: This figure shows the computed pressure for the Orszag-Tang vortex using the H_5W scheme on a 4000×4000 mesh at time $t = \pi$.

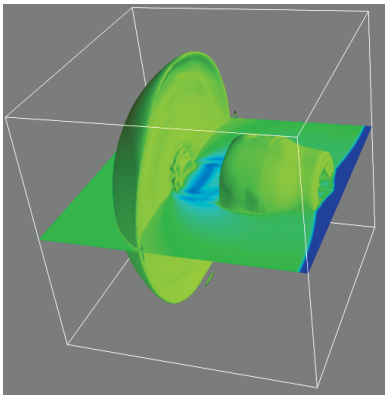

Figure 1.17: This figure shows the computed pressure for the cloud-shock interaction using the H_5W scheme on a $200 \times 200 \times 200$ mesh after the shock has hit the cloud.

with complex magnetic fields generated by the plasma, and these interactions affect the qualitative as well as quantitative features of the energy transfer.

Since we want to simulate waves in a regime where density has an exponential structure (see the chromosphere in figure 1.3), we have to include the additional physical effect of gravity. This means we look at equations of ideal magnetohydrodynamics with the gravity source (1.2.2). We specify steady states, i.e., stationary solutions, that are of interest, as they will serve as a background for the propagation of waves.

Hydrodynamic steady state

Assuming that the velocity $\mathbf{u}$ and the magnetic field $\mathbf{B}$ are zero, a simple calculation leads to the following steady state,

$$\mathbf{u} \equiv \mathbf{0}, \quad \bar{\mathbf{B}} \equiv \mathbf{0}, \quad \rho(x,y) = \rho_0 e^{-\frac{y}{H}}, \quad p(x,y) = p_0 e^{-\frac{y}{H}}, \tag{1.6.1}$$

where the scale height H is given by $H = \frac{p_0}{g\rho_0}$, and p_0 and ρ_0 are the values of the pressure and density at the bottom boundary of the domain. Note that the hydrostatic balance due to gravity implies that the pressure and the density decay exponentially in the vertical direction. Since we are modeling the chromosphere of the Sun, see figure 1.3, this is exactly what we expect from a good model. Hence, very low pressures and densities can be found at the top of the domain of interest.

Magnetic steady state

The hydrodynamic steady state assumes that the magnetic field is zero, but any realistic description of solar plasmas cannot ignore the magnetic fields. The effects of the magnetic field play a crucial role in the energy transfer, see for instance [18]. Steady states with non-zero magnetic fields are easy to determine once the momentum balance in (1.2.4) is rewritten as,

$$(\rho\mathbf{u})_t + \operatorname{div}(\rho\mathbf{u} \otimes \mathbf{u} + pI) = \operatorname{curl}(\mathbf{B}) \times \mathbf{B} - \rho g \mathbf{e_2}.$$

The above equation displays the role of the Lorentz force explicitly in the momentum balance. Under the assumption that the velocity field is set to zero, the following magnetic steady states are easy to obtain,

$$\begin{aligned} \mathbf{u} \equiv \mathbf{0}, \quad \operatorname{div}(\mathbf{B}) \equiv \mathbf{0}, \quad \operatorname{curl}(\mathbf{B}) \equiv 0, \\ \rho(x,y) = \rho_0 e^{-\frac{y}{H}}, \quad p(x,y) = p_0 e^{-\frac{y}{H}}. \end{aligned} \tag{1.6.2}$$

Again, the exponential decay of the density is exactly what we expect from a good model, since we are modeling the chromosphere of the Sun, see figure 1.3. The above conditions require that the magnetic field is both divergence free and curl free, i.e., $\mathbf{B}$ is a force free magnetic field. It is easy to obtain closed form solutions of such magnetic fields in terms of harmonic functions (see chapters 5, 6 and 7). Note that the conditions on steady magnetic fields are quite general, implying that there is a rich variety of magnetic steady states satisfying (1.6.2). The next step is to have a model for wave propagation.

Wave propagation

The propagation of waves is modeled as a perturbation of the steady state background described above. This is done by sending in a sinusoidal (in time) sequence of waves from the bottom boundary. These waves propagate across the domain, until they exit at the top bondary. The waves are modeled by the following boundary conditions for the normal velocity at the bottom (choosing the z-direction as the direction the gravity force is acting)

$$u_3(x, y, z = 0, t) = c \sin(2\pi a t)\, \chi_{[x_1,x_2]\times[y_1,y_2]}, \tag{1.6.3}$$

where c is the amplitude and a the frequency of the wave. So the boundary conditions act like a piston in the area $[x_1, x_2] \times [y_1, y_2]$.

In the article presented in chapter 5 we implemented and compared both HLL and Roe type approximate solvers on a series of test problems. The gravity source term was discretized by a method of fractional steps that preserved positivity. Boundary conditions of the characteristic type and Neumann type were adapted to this model. The key step was to introduce a novel mass balance for the boundary conditions.

Numerical results for **hydrodynamic** waves (see figure 1.18) showed that the Roe solver together with balanced characteristic type boundary conditions was most effective in computing waves. HLL three wave solvers were also quite effective in this case.

Computations in the presence of **complex magnetic fields**, however, led to a different story. For the wave propagation, characteristic type boundary conditions were observed to be unstable on fine meshes. Similarly, both the highly accurate Roe solver as well as the more dissipative HLL2 solver were unstable. The combination of HLL3G/HLL3R solvers together with modified Neumann type boundary conditions gave the best results. However, the results were not as accurate as the hydrodynamic case.

One possibility to overcome these difficulties is to use higher order schemes of the ENO/WENO type to increase accuracy and reduce numerical errors. However, the computations presented in chapter 5 suggest caution - the more accurate Roe solver failed to be stable. Therefore, we need to use higher order schemes based on nonlinear HLL type solvers like HLL3G and HLL3R.

In the case of wave propagation without magnetic fields the article presented in chapter 6 deals with these finite volume schemes, based on HLL-solvers and an ENO-WENO second order interpolation. Figure 1.19 shows the significant gain of accuracy by applying a WENO type second order. The HLL solvers and ENO-WENO second order interpolation were found to be robust and accurate at computing the waves. The key ingredient was a proper choice of non-reflecting and balanced Neumann type extrapolated boundary conditions. The schemes, particularly at second order resolve both the steady states and the propagating waves quite accurately.

Another possible cause of the instabilities observed in the article of chapter 5 might be the discretization of the divergence constraint. As reported before, it is not clear that divergence errors are responsible for the instabilities, and it is difficult to impose boundary conditions with schemes that preserve discrete forms of divergence. Due to our experience with the ideal MHD equations, we expect that an upwinded discretization of the Godunov-Powell source term increases the stability of the scheme.

Some of the errors are due to lack of well-balancing of the source term, i.e, failure

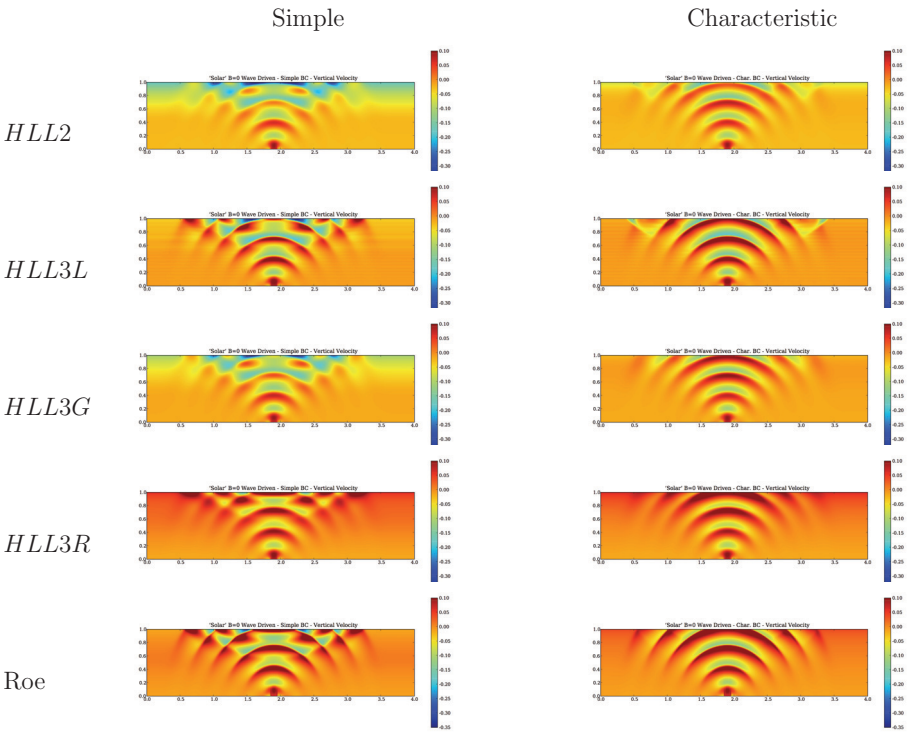

Figure 1.18: $u_1(x, z, 1.8)$ calculated with grid size 400×100, left column: simple boundary conditions, right column: balanced characteristic boundary conditions.

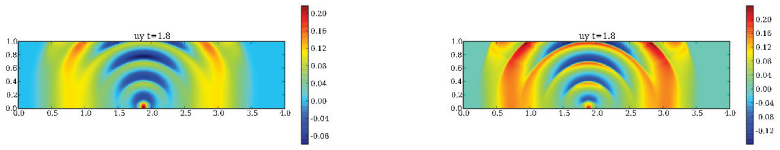

(a) HLL first order

(b) WENO second order

Figure 1.19: Comparison of the approximate u_2 obtained from the first order HLL scheme and a second order WENO scheme on a 400×100 mesh at time $t = 1.8$.

to preserve a discrete version of the magneto-hydrodynamic steady state (1.6.2) exactly. We need to adapt existing procedures for well-balancing sources (see [7]) to the case of stratified flows. These issues are addressed in the next and final paper.

1.6.1 Well-balanced scheme for wave propagation

In order to be able to successfully simulate the wave perturbation for the magnetic steady state background (1.6.2) or to simulate really small perturbations ($c = \mathcal{O}(10^{-3})$) of the steady state, we need to develop well-balanced solvers.

In the paper of chapter 7 we consider numerical simulations of wave propagation in an idealized stellar atmosphere. The configuration is modeled by considering a modified MHD system based on the Godunov-Powell form of the ideal MHD equations, together with an embedded steady magnetic field. The resulting equations are balance laws with gravity source terms and background magnetic fields, playing the role of coefficients.

The system is simulated by finite volume schemes based on HLL three wave approximate Riemann solvers and upwind discretizations of the Godunov-Powell source term. The scheme is well-balanced by using local hydrostatic reconstructions of the density and pressure and a suitable discretization of the gravity source term. Second order accurate schemes are designed by suitable minmod and WENO reconstructions. The reconstructions are performed in terms of **equilibrium** variables to ensure well-balancing.

The resulting schemes are high order accurate, stable and well-balanced. They are validated on a large suite of numerical experiments. The underlying physical phenomena are quite complex and involve multiple scales and parameters.

Table 1.4 shows a comparison of how well the un-balanced and well-balanced schemes preserve the steady state 1.6.2. The table clearly shows that the well-balanced schemes

L^1-error in p	H_3	H_3W	$H_{3\mathrm{WB}}$	$H_{3\mathrm{WB}}M$	$H_{3\mathrm{WB}}W$
100x25	3.5e+2	6.3e+0	9.8e-20	2.5e-18	7.9e-17
200x50	1.2e+2	8.2e-1	1.6e-18	3.6e-18	4.1e-16
400x100	4.9e+1	1.0e-1	2.8e-18	3.5e-18	2.6e-15
800x200	2.2e+1	1.3e-2	4.6e-18	1.4e-17	2.0e-14

Table 1.4: Percentage relative L^1 errors in p for different schemes on different meshes. Left un-balanced schemes. Right well-balanced schemes

preserve the steady state to machine precision whereas the **unbalanced schemes** lead to large errors. The errors in both sets of schemes are comparable to the errors in preserving the hydrodynamic steady state. Hence, it is not possible to use **unbalanced schemes** for approximating perturbations of steady states.

The well-balanced schemes perform very well, and are able to resolve very small perturbations as well as the complex physics to a high degree of accuracy. Figure 1.6.1 shows the numerical results for these well-balanced schemes with a very small perturbation ($c = 3e^{-3}$) to test the well-balancing properties of the schemes. The parallel and perpendicular components (to the direction of the magnetic field) of the velocity field at a resolution of 800×200 points are shown in figure 1.6.1. All the three schemes are able to capture the small perturbations quite accurately. The first order scheme is dissipative,

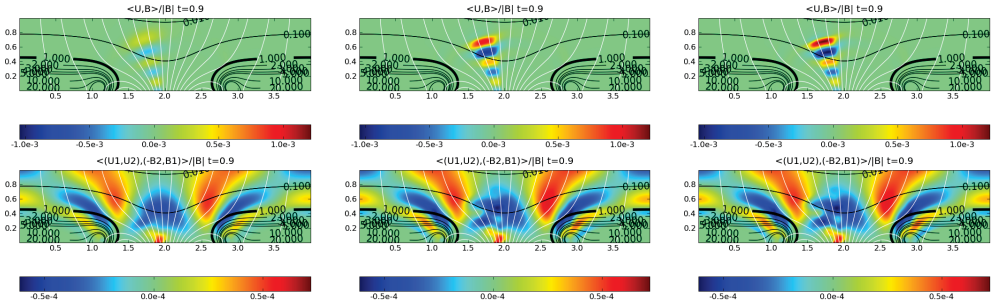

Figure 1.20: Results for the strong magnetic background with small wave perturbations ($c = 3e^{-3}$) at $t = 0.9$ on a 800×200 mesh. The magnetic field-lines are shown in white and the β-lines in black. The top row shows the speed in the direction of the magnetic field-lines and the bottom row shows the speed perpendicular to the magnetic field-lines. left column: $H_{3\mathrm{WB}}$, middle column: $H_{3\mathrm{WB}}M$, right column: $H_{3\mathrm{WB}}W$.

but the minmod and WENO schemes compute much sharper wave fronts. Compared to the hydrodynamic wave propagation model, the waves in the direction of the magnetic field are much more focused by the magnetic field. This is to be expected, as the magnetic field is strong. The Lorentz-force prohibits the plasma more and more to move perpendicular to the magnetic field, as the magnetic field dominates more and more. The highly accurate numerical resolution of the complex phenomena at very small amplitudes illustrates the robustness of the well-balanced schemes.

1.7 Concluding remarks

In this thesis we have devised numerical methods for simulating the equations of ideal magnetohydrodynamics (MHD). The methods are shown to be accurate and highly stable. We have emphasized the importance of the Godunov-Powell source term for numerical methods. It is necessary to keep the Godunov-Powell source from the derivation of first physical principles as well as to discretize it in an appropriate "up-winded" manner. In the second part of the thesis we constructed well-balanced finite volume methods for simulating waves in the solar atmosphere. The model we used is very close to the real conditions in the solar atmosphere, including the effect of gravity. Again, the numerical methods are stable and produce very accurate results. Future projects include employing those schemes on more realistic three dimensional configurations with background magnetic fields and perturbations given by observed data.

2

Stable Upwind Schemes for the Magnetic Induction Equation

F. G. Fuchs, K.H. Karlsen, S. Mishra, N.H. Risebro
M2AN, February 2009

Keywords: Conservation laws, Induction equation, Divergence constraint, Upwinded Source terms

Abstract

We consider the magnetic induction equation for the evolution of a magnetic field in a plasma where the velocity is given. The aim is to design a numerical scheme which also handles the divergence constraint in a suitable manner. We design and analyze an upwind scheme based on the symmetrized version of the equations in the non-conservative form. The scheme is shown to converge to a weak solution of the equations. Furthermore, the discrete divergence produced by the scheme is shown to be bounded. We report several numerical experiments that show that the stable upwind scheme of this paper is robust.

2.1 Introduction

2.1.1 The Model

In this paper, we study the magnetic induction equation

$$\partial_t \mathbf{B} + \mathrm{curl}(\mathbf{B} \times \mathbf{u}) = 0, \tag{2.1.1}$$

where the unknown $\mathbf{B} = \mathbf{B}(\mathbf{x}, t) \in \mathbb{R}^3$ describes the magnetic field of a plasma in three space dimensions with coordinate $\mathbf{x} = (x, y, z)$. The above equation models the evolution of the magnetic field in the plasma which is moving with a prescribed velocity field $\mathbf{u}(\mathbf{x}, t)$. An immediate consequence of (2.1.1) is that the divergence of $\mathbf{B}$ is preserved in time, i.e.,

$$\partial_t \left(\mathrm{div}\mathbf{B}\right) = 0. \tag{2.1.2}$$

Thus if the divergence is initially zero, it remains so.

The equation (2.1.1) is augmented with suitable initial and boundary conditions. In this paper, we focus on the Cauchy problem with the initial conditions

$$\mathbf{B}(\mathbf{x}, 0) = \mathbf{B}_0(\mathbf{x}), \quad \mathbf{x} \in \mathbb{R}^3.$$

If we write $\mathbf{B} = (B^1, B^2, B^3)^t$ and $\mathbf{u} = (u^1, u^2, u^3)^t$, (2.1.1) reads

$$\begin{aligned}
\partial_t B^1 - \partial_y \left(u^1 B^2 - u^2 B^1\right) + \partial_z \left(u^3 B^1 - u^1 B^3\right) &= 0, \\
\partial_t B^2 + \partial_x \left(u^1 B^2 - u^2 B^1\right) - \partial_z \left(u^2 B^3 - u^3 B^2\right) &= 0, \\
\partial_t B^3 - \partial_x \left(u^3 B^1 - u^1 B^3\right) + \partial_y \left(u^2 B^3 - u^3 B^2\right) &= 0.
\end{aligned}$$

For vectors $\mathbf{a}$ and $\mathbf{b}$ we use the notation

$$\mathbf{a} \otimes \mathbf{b} = \begin{pmatrix} a^1 b^1 & a^1 b^2 & a^1 b^3 \\ a^2 b^1 & a^2 b^2 & a^2 b^3 \\ a^3 b^1 & a^3 b^2 & a^3 b^3 \end{pmatrix}.$$

Then we can rewrite (2.1.1) in conservative form

$$\partial_t \mathbf{B} + \operatorname{div} (\mathbf{u} \otimes \mathbf{B} - \mathbf{B} \otimes \mathbf{u}) = 0, \tag{2.1.3}$$

where the divergence of the matrix is the vector obtained by taking the divergence of the rows. The equation (2.1.1) can be derived from the full Maxwell's equations for electromagnetic fields by using the standard Lorentz transformations and the assumptions that the electric field at rest for a plasma is zero and that the plasma is a perfect conductor (so that we neglect the viscous terms). The details of the derivation of (2.1.1) can be found in any standard book on electrodynamics, for example [43]. One of the key issues in the design of numerical schemes for (2.1.1) is to handle the divergence constraint (2.1.2), i.e., to ensure that some discrete version of (2.1.2) holds at least approximately.

Equation (2.1.1) arises in a wide variety of contexts in the electrodynamics of plasmas. One important application is the equations of magnetohydrodynamics (MHD). MHD models the motion of a plasma in a magnetic field. In this case, the Euler equations of compressible gas dynamics are coupled with (2.1.1), see [64] for details. Numerical methods for MHD must address the divergence constraint, and several methods have been proposed in order to handle this constraint. These methods are in turn based on methods which preserve some discrete form of the divergence of $\mathbf{B}$.

In general, good numerical schemes for (2.1.1) is a step in the design of efficient numerical schemes for MHD, and a good motivation for studying (2.1.1) numerically. Our aim in this paper is to design, analyze and implement a simple upwind scheme for (2.1.1) and show that it is stable for very general initial data and velocity fields. In addition, the scheme also keeps divergence errors bounded and leads to sharp resolution of discontinuities. We start with a description of the continuous problem.

2.1.2 The continuous problem

In general, (2.1.1) is a system of linear conservation laws in three dimensions, it is hyperbolic, but not strictly hyperbolic.

In order to show existence of solutions to (2.1.1), we need to derive á priori estimates. The standard procedure for hyperbolic equations in multi space dimensions is to symmetrize the system and derive an energy estimate. In order to do this we introduce the operator

$$\mathbf{a}\cdot\nabla = a^1\partial_x + a^2\partial_y + a^3\partial_z,$$

and write

$$\begin{aligned}\mathrm{curl}(\mathbf{B}\times\mathbf{u}) &= \mathbf{B}\mathrm{div}\mathbf{u} - \mathbf{u}\mathrm{div}\mathbf{B} + (\mathbf{u}\cdot\nabla)\,\mathbf{B} - (\mathbf{B}\cdot\nabla)\,\mathbf{u}\\ &= \left(u^1\mathbf{B}\right)_x + \left(u^2\mathbf{B}\right)_y + \left(u^3\mathbf{B}\right)_z - \mathbf{u}\mathrm{div}\mathbf{B} - (\mathbf{B}\cdot\nabla)\mathbf{u}.\end{aligned}$$

Thus (2.1.1) can also be recast as

$$\partial_t\mathbf{B} + \left(u^1\mathbf{B}\right)_x + \left(u^2\mathbf{B}\right)_y + \left(u^3\mathbf{B}\right)_z = \mathbf{u}\mathrm{div}\mathbf{B} + (\mathbf{B}\cdot\nabla)\mathbf{u}.$$

Then we see that a simple way to symmetrize (2.1.1) is to add a "source" term: (which is supposed to be zero anyway!) $-\mathbf{u}\mathrm{div}\mathbf{B}$, resulting in

$$\partial_t\mathbf{B} + \mathrm{curl}(\mathbf{B}\times\mathbf{u}) = -\mathbf{u}\mathrm{div}\mathbf{B}. \tag{2.1.4}$$

Rewriting this, we find

$$\begin{aligned}\partial_t\mathbf{B} + (\mathbf{u}\cdot\nabla)\,\mathbf{B} &= -\mathbf{B}(\mathrm{div}\mathbf{u}) + (\mathbf{B}\cdot\nabla)\mathbf{u}\\ &= M(D\mathbf{u})\mathbf{B},\end{aligned} \tag{2.1.5}$$

where the matrix $M(D\mathbf{u})$ is given by

$$M(D\mathbf{u}) = \begin{pmatrix} -\partial_y u^2 - \partial_z u^3 & \partial_y u^1 & \partial_z u^1 \\ \partial_x u^2 & -\partial_x u^1 - \partial_z u^3 & +\partial_z u^2 \\ \partial_x u^3 & \partial_y u^3 & -\partial_x u^1 - \partial_y u^2 \end{pmatrix}.$$

The above source term was first introduced for the non-linear MHD equations by Godunov in [35], see also [65, 12]. This strategy of using a source term to handle constraints is very general and can be used for similar hyperbolic models involving other restrictions.

Let us write (2.1.4) as

$$\partial_t\mathbf{B} + \partial_x\left(u^1\mathbf{B}\right) + \partial_y\left(u^2\mathbf{B}\right) + \partial_z\left(u^3\mathbf{B}\right) = (\mathbf{B}\cdot\nabla)\mathbf{u}. \tag{2.1.6}$$

Introducing the matrices $A^i = u^i I$ for $i = 1, 2, 3$, and

$$C = -\begin{pmatrix} \partial_x u^1 & \partial_y u^1 & \partial_z u^1 \\ \partial_x u^2 & \partial_y u^2 & \partial_z u^2 \\ \partial_x u^3 & \partial_y u^3 & \partial_z u^1 \end{pmatrix},$$

we may further rewrite (2.1.6) as

$$\partial_t\mathbf{B} + \partial_x\left(A^1\mathbf{B}\right) + \partial_y\left(A^2\mathbf{B}\right) + \partial_z\left(A^3\mathbf{B}\right) + C\mathbf{B} = 0.$$

This system is symmetric in the sense of Friedrichs (the matrices A^i are symmetric). Regarding the functions u^1, u^2 and u^3 we assume that they are "sufficiently differentiable",

i.e., whenever a derivative of u^i is appearing in our calculations, we assume that this is a continuous and bounded function. Of course, this means that the matrices A^i are also sufficiently smooth.

Observe that the above system is a special case of the more general problem

$$\partial_t \mathbf{v} + \sum_{i=1}^{d} \Theta^i(\mathbf{x},t)\partial_{x_i}\mathbf{v} = \Gamma(\mathbf{x},t)\mathbf{v} + \mathbf{f}(\mathbf{x},t), \qquad \mathbf{v}(\mathbf{x},0) = \mathbf{v}_0(\mathbf{x}), \tag{2.1.7}$$

where the $d \times d$ matrices $\Theta^1, \dots, \Theta^d$,and B depend smoothly on $\mathbf{x}$ and t. We recall that the system (2.1.7) is Friedrichs symmetric if there exists a matrix $S_0(\mathbf{x},t) \in C^\infty(\mathbb{R}^d \times \mathbb{R})$ that is symmetric and uniformly positive definite, and the matrices

$$S_0(\mathbf{x},t)\Theta^1(\mathbf{x},t), \dots, S_0(\mathbf{x},t)\Theta^d(\mathbf{x},t)$$

are symmetric for all $(\mathbf{x},t)$ (see [13]). To analyze (2.1.7) one uses pseudo-differential calculus. We have the following well-posedness result, see [13, Theorem 2.6].

Theorem 2.1.1. *Suppose* (2.1.7) *has smooth coefficients and is Friedrichs symmetrizable. Fix $T > 0$ and $s > 1$. Assume that $f \in L^2(0,T;H^s(\mathbb{R}^d))$ and $v_0 \in H^s(\mathbb{R}^d)$. Then there exists a unique (weak) solution $\mathbf{v} \in C([0,T];H^s(\mathbb{R}^d)) \cap C^1([0,T];H^{s-1}(\mathbb{R}^d))$ of the Cauchy problem* (2.1.7)*. Moreover, there exists a constant, which is independent of the vector v, such that for any $t \in [0,T]$*

$$\|\mathbf{v}(\cdot,t)\|^2_{H^s(\mathbb{R}^d)} \le C\left(\|\mathbf{v}_0\|^2_{H^s(\mathbb{R}^d)} + \int_0^t \|\mathbf{f}(\cdot,\tau)\|^2_{H^s(\mathbb{R}^d)}\, d\tau\right).$$

If $\mathbf{f} \in C^\infty([0,T];H^\infty(\mathbb{R}^d))$ and $\mathbf{v}_0 \in H^\infty(\mathbb{R}^d)$, then the solution $\mathbf{v}$ belongs to $C^\infty([0,T];H^\infty(\mathbb{R}^d))$.

In the special case of a constant velocity field, the above equations decouple and reduce to

$$\partial_t \mathbf{B} + (\mathbf{u}\cdot\nabla)\,\mathbf{B} = 0,$$

and in this case we have the exact solution

$$\mathbf{B}(\mathbf{x},t) = \mathbf{B}_0(\mathbf{x} - \mathbf{u}t), \tag{2.1.8}$$

Clearly in this special case, the exact solution is actually *TVD*. In general, we do not expect the initial data to be smooth. This is particularly true in the case of MHD equations where the magnetic field can have discontinuities. As a consequence, we define weak solutions of (2.1.1) by

Definition 2.1.1 (Weak solution)**.** *For all function $\mathbf{u} \in H^1(\mathbb{R}^3)$ we call a locally integrable function $\mathbf{B}$ a weak solution of* (2.1.1) *if for all smooth test functions $\Phi \in \mathcal{C}_0^1$, the following integral identity holds,*

$$\int_0^\infty \int_{\mathbb{R}^n} \mathbf{B}\Phi_t + \mathbf{B}\,(\mathbf{u}\cdot\nabla)\,\Phi\, d\mathbf{x}\, dt = \int_{\mathbb{R}^n} \mathbf{B}_0(x)\Phi(\mathbf{x},0)\, d\mathbf{x} + \int_0^\infty \int_{\mathbb{R}^n} (\mathbf{B}\cdot\nabla)\mathbf{u}\Phi\, d\mathbf{x}\, dt. \tag{2.1.9}$$

Hence, weak solutions of (2.1.1) are defined in terms of the Friedrichs form (2.1.6). The existence of these is a consequence of Theorem 1.1.

For simplicity we will concentrate on the two-dimensional case, i.e., $\partial_z = 0$ and $u^3 = 0$. In this case (2.1.3) reads

$$\begin{aligned} &\partial_t B^1 + \partial_y \left(u^1 B^2 - u^2 B^1\right) = 0, \\ &\partial_t B^2 - \partial_x \left(u^1 B^2 - u^2 B^1\right) = 0, \end{aligned} \tag{2.1.10}$$

$$\partial_t B^3 + \partial_x \left(u^1 B^3\right) + \partial_y \left(u^2 B^3\right) = 0. \tag{2.1.11}$$

The third equation is independent of the first two, and is such that if $B^3(x, y, 0) = 0$, then also $B^3(x, y, t) = 0$. Hence we ignore (2.1.11) in the remainder of this paper.

2.1.3 Numerical Schemes

From the theory for the continuous problem, it is reasonable to require the following properties of a "good" numerical scheme for (2.1.1),

(i.) The scheme should be upwind i.e., it should be able to resolve discontinuities in the solution sharply even at first order.

(ii.) The scheme should be stable in the energy norm for a large class of initial data and velocity fields.

(iii.) In the special case of constant velocity fields, the scheme should be *TVD*.

(iv.) Discrete versions of the divergence constraint should hold, at least approximately.

We shall consider first order schemes, since higher order extensions can be made once an efficient first order scheme is available. Note that the second property is essential for proving convergence, the third is a non-oscillatory property and the control of divergence is essential for respecting the constraint on (2.1.1).

Before we continue with a technical description of some schemes, let us introduce some useful notation. As usual, Δx and Δy denotes the spatial discretization parameters, these are (small) positive numbers. For i and j in $\mathbb{Z}$, let $x_i = i\Delta x$, $y_j = j\Delta y$, $x_{i+1/2} = x_i + \Delta x/2$ and $y_{j+1/2} = y_j + \Delta y/2$. Similarly we define the temporal discretization Δt, and set $t^n = n\Delta t$ for $n \geq 0$.

For a continuous function $a(x, y)$, we set

$$a_{i,j} = a\left(x_i, y_j\right), \quad i \text{ and } j \in \mathbb{Z}/2.$$

For any quantity $\{a_{i,j}\}$ let the forward/backward differences be denoted by

$$D_x^{\pm} a_{i,j} = \pm \frac{a_{i\pm1,j} - a_{i,j}}{\Delta x}, \quad D_y^{\pm} a_{i,j} = \pm \frac{a_{i,j\pm1} - a_{i,j}}{\Delta y},$$

and the central differences

$$D_{x,y}^0 = \frac{1}{2}\left(D_{x,y}^+ + D_{x,y}^-\right).$$

We also let the discrete time derivative be denoted by

$$D_t^+ b^n = \frac{b^{n+1} - b^n}{\Delta t},$$

for any quantity $\{b^n\}_{n\geq 0}$. Furthermore, set $[a]^+ = \max\{a, 0\}$ and $[a]^- = \min\{a, 0\}$. We shall need the following identities:

$$D_x^\pm (a_i b_i) = a_i D_x^\pm b_i + b_{i\pm 1} D_x^\pm a_i \tag{2.1.12}$$

$$D_x^\pm \left((a_i)^2\right) = 2a_i D_x^\pm a_i \pm \Delta x \left(D_x^\pm a_i\right)^2 \tag{2.1.13}$$

$$\begin{aligned} D_x^0 (a_j b_j) = a_j D_x^0 (b_j) + b_j D_x^0 (a_j) \\ + \frac{\Delta x^2}{2} \left[\left(D_x^+ a_j\right)\left(D_x^- D_x^+ b_j\right) + \left(D_x^- b_j\right)\left(D_x^- D_x^+ a_j\right)\right] \end{aligned} \tag{2.1.14}$$

$$\sum_{i=I}^{J} a_i \left(D_x^+ b_i\right) = -\sum_{i=I+1}^{J} \left(D_x^- a_i\right) b_i + \frac{1}{\Delta x}\left(a_J b_{J+1} - a_I b_I\right). \tag{2.1.15}$$

We also let I_{ij} denote the rectangle $(x_{i-1/2}, x_{i+1/2}] \times (y_{j-1/2}, y_{j+1/2}]$ and $I_{i,j}^n$ the cube $I_{i,j} \times [n\Delta t, (n+1)\Delta t)$.

When solving (2.1.10) numerically, we consider piecewise constant approximations

$$\mathbf{B}_{i,j}^n \approx \frac{1}{|I_{i,j}|} \int_{I_{i,j}} \mathbf{B}(x, y, t^n)\, dxdy,$$

in the fully discrete case, and

$$\mathbf{B}_{i,j}(t) \approx \frac{1}{|I_{i,j}|} \int_{I_{i,j}} \mathbf{B}(x, y, t)\, dxdy,$$

for semi-discrete approximations. To obtain functions defined for all $\mathbf{x}$ and t, we define

$$\begin{aligned} \mathbf{B}^{\Delta t}(x, y, t) &= \sum_{i,j} \mathbf{B}_{i,j}^n \mathbf{1}_{I_{i,j}^n}(x, y, t), \quad \text{and} \\ \mathbf{B}^{\Delta x}(x, y, t) &= \sum_{i,j} \mathbf{B}_{i,j}(t) \mathbf{1}_{I_{i,j}}(x, y). \end{aligned} \tag{2.1.16}$$

where $\mathbf{1}_\Omega$ is the characteristic function of the set Ω. All the schemes for (2.1.10) which we consider can be written as

$$D_t^+ \mathbf{B}_{i,j}^n = \mathcal{F}_{i,j}\left(\mathbf{u}, \mathbf{B}^{\Delta t}(\cdot, \cdot, t^n)\right) \quad \text{or} \quad \frac{d}{dt}\mathbf{B}_{i,j}(t) = \mathcal{F}_{i,j}\left(\mathbf{u}, \mathbf{B}^{\Delta x}(\cdot, \cdot, t)\right) \tag{2.1.17}$$

for various functions $\mathcal{F}_{i,j}$.

The system (2.1.1) contains terms of the type $\partial_x(u^1 B^2)$, which we shall discretize in an upwind manner. To this end we introduce the notation,

$$D_x \{u, B\}_{i,j} = D_x^- \left(\left[u_{i+1/2,j}\right]^+ B_{i,j}\right) + D_x^+ \left(\left[u_{i-1/2,j}\right]^- B_{i,j}\right) \tag{2.1.18}$$

$$= \left[u_{j+1/2,j}\right]^{-} D_x^{+} B_{i,j} + \left[u_{i-1/2,j}\right]^{+} D_x^{-} B_{i,j} + B_{i,j} D_x^{-} u_{i+1/2,j}.$$

An analogous expression defines $D_y\{u, B\}$. If u and B are smooth functions, then

$$\partial_x (uB)(x_i, y_j) = D_x \{u, B\}_{i,j} + \mathcal{O}(\Delta x).$$

Equipped with above notation, the standard upwind scheme for (2.1.10) reads

$$\begin{aligned} D_t^{+} B_{i,j}^{1,n} &= -D_y \left\{u^2, B^{1,n}\right\}_{i,j} + D_y \left\{u^1, B^{2,n}\right\}_{i,j}, \\ D_t^{+} B_{i,j}^{2,n} &= -D_x \left\{u^1, B^{2,n}\right\}_{i,j} + D_x \left\{u^2, B^{1,n}\right\}_{i,j}. \end{aligned} \tag{2.1.19}$$

This scheme works well on many examples, but, it is not *TVD* when $\mathbf{u}$ is constant. As Example 2.3.1 and Figure 2.3.1 indicates, the scheme gives sharp oscillations near discontinuities in $\mathbf{B}$. In addition, the scheme does not have an energy estimate. Regarding the divergence constraint, the scheme does not preserve the central discrete divergence operator given by,

$$\mathrm{div}^0(\mathbf{B}_{i,j}) = D_x^0(B_{i,j}^1) + D_y^0(B_{i,j}^2).$$

In fact, the divergence errors can be very large in some numerical experiments. Since preserving the divergence constraint is a key numerical issue, several approaches have been suggested to couple upwinding of numerical schemes for (2.1.1) along with preservation/control of numerical divergence. The motivation behind most of these schemes is the need for efficient schemes for the MHD equations. A good review of divergence preserving schemes for MHD can be found in [80]. We now provide a very brief survey relevant to the situation considered here.

Projection Methods

These methods are based on the Hodge decomposition of the magnetic field. At each time step, the magnetic field obtained from (2.1.17), denoted $\tilde{\mathbf{B}}^{n+1}$, can be written as

$$\tilde{\mathbf{B}}^{n+1} = \mathrm{grad}\Psi + \mathrm{curl}\Phi \quad \Rightarrow \quad \Delta\Psi = \mathrm{div}\left(\tilde{\mathbf{B}}^{n+1}\right).$$

Solving the last equation for Ψ and then setting

$$\mathbf{B}^{n+1} = \tilde{\mathbf{B}}^{n+1} - \mathrm{grad}\Psi,$$

makes $\mathbf{B}^{n+1}$ divergence free. The computational cost of this is significant, as one needs to solve an elliptic equation at each time step. This method was proposed in [22].

Design of discrete divergence free operators/Staggering

Another strategy to control divergence errors is to use difference methods that preserve some (not necessarily div^0) discrete form of the divergence. An important contribution in

this direction is the paper of Torrilhon and Fey [77], where following scheme was proposed

$$\begin{aligned} D_t^+ B_{i,j}^{1,n} &= \frac{1}{2}\Big(D_y^- \left(\varphi_{i,j}^1 + \varphi_{i-1,j}^1 + \varphi_{i,j}^2 + \varphi_{i+1,j}^2\right) \\ &\qquad + D_y^+ \left(\varphi_{i,j}^3 + \varphi_{i+1,j}^3 + \varphi_{i,j}^4 + \varphi_{i-1,j}^4\right)\Big), \\ D_t^+ B_{i,j}^{2,n} &= -\frac{1}{2}\Big(D_x^- \left(\varphi_{i,j}^1 + \varphi_{i,j-1}^1 + \varphi_{i,j}^4 + \varphi_{i,j+1}^4\right) \\ &\qquad + D_x^+ \left(\varphi_{i,j}^2 + \varphi_{i,j-1}^2 + \varphi_{i,j}^3 + \varphi_{i,j+1}^3\right)\Big), \end{aligned} \tag{2.1.20}$$

where

$$\varphi_{i,j}^k = \omega_{i,j}^k \left(u_{i,j}^1 B_{i,j}^{2,n} - u_{i,j}^2 B_{i,j}^{1,n}\right),$$

and

$$\omega_{i,j}^k = \frac{\left[\mathbf{n}^k \cdot \mathbf{u}_{i,j}\right]^+}{\sum_{k=1}^4 \left[\mathbf{n}^k \cdot \mathbf{u}_{i,j}\right]^+},$$

$$\mathbf{n}^1 = (1,1),\ \mathbf{n}^2 = (-1,1),\ \mathbf{n}^3 = (-1,-1) \text{ and } \mathbf{n}^4 = (1,-1).$$

This scheme preserves the following discrete divergence,

$$\mathrm{div}^*(\mathbf{B}_{i,j}) = \frac{1}{4}\Big(D_x^0 \left(B_{i,j+1}^1 + 2B_{i,j}^1 + B_{i,j-1}^1\right) + D_y^0 \left(B_{i+1,j}^2 + 2B_{i,j}^2 + B_{i-1,j}^1\right)\Big).$$

If $\mathbf{B}$ is smooth, div^* differs from div^0 by $\mathcal{O}(\Delta x^2 + \Delta y^2)$, with a constant depending on the second derivatives of $\mathbf{B}$. More details on this scheme can be found in [77, 78]. In [77] this scheme is proved to be von Neumann stable if $\mathbf{u}$ is constant. However, we were unable to prove that it is stable in the energy norm when the velocity field varies in space and time. Also, the scheme is not *TVD* when the velocity field is constant, as is shown in Example 2.3.1 and Figure 2.3.1. Some numerical experiments in Section 2.3 show that even though the scheme preserves the discrete divergence div^*, the central discrete divergence div^0 is not preserved and can be large.

In [77, 78] it was remarked that the scheme (2.1.20) is equivalent to staggering the discretizations of the velocity and magnetic fields. In this approach, the velocity and magnetic fields in the x-direction are centered on the cell edges in the x-direction and the velocity and magnetic fields in the y-direction are centered on the cell-edges in the y-direction. This approach has been proposed in number a papers including [30, 11, 26, 71, 70] and details can be found in these references.

The main advantage of schemes based on this approach is the fact that some form of discrete divergence is preserved. Unfortunately, it is not possible to prove energy bounds (and hence convergence) for general non-constant velocity fields. Furthermore, these schemes can be oscillatory near discontinuities as shown in some numerical examples in this paper.

Schemes using the Godunov-Powell source term

Another common approach to controlling the divergence, at least in the context of non-linear MHD equations, is to numerically solve (2.1.4) rather than (2.1.1). This approach

was proposed by Powell in [65]. Formally, taking the divergence on both sides of (2.1.4)

$$\partial_t(\mathrm{div}(\mathbf{B})) + (\mathbf{u}\cdot\nabla)\,(\mathrm{div}\mathbf{B}) = -\,(\mathrm{div}\mathbf{u})\,(\mathrm{div}\mathbf{B})\,. \tag{2.1.21}$$

Hence, any non-zero divergence is advected along $\mathbf{u}$, and hopefully out of the computational domain.

Another key point about introducing the Godunov-Powell source term at the continuous level is to symmetrize (2.1.1) and write it in the form (2.1.6) which results in the derivation of energy estimates.

At the level of numerical schemes, one of the key issues is how to discretize the Godunov-Powell source term. It is common in the literature to use a discretization of the source term based on central differences (see, e.g., [53]).

Example 3.1 of this paper shows that such an approach might result in large oscillations in the solution and should be avoided. In [65], the author incorporates the source term into flux thus implicitly upwinding it.

Another way to upwind the Godunov-Powell source term is to discretize the Friedrichs form (2.1.6). In [16], the authors propose high order discontinuous Galerkin methods based on the "conservative" Friedrichs form (2.1.6) and show convergence results and error estimates for the scheme. They use locally divergence free basis functions, but they were unable to obtain any global divergence bound. The first order version the scheme proposed in [16] leads to an upwind discretization of the Godunov-Powell source term.

If the Friedrichs form is used as a basis for discretization of (2.1.1), one can appeal to the considerable literature that is devoted to finite volume schemes for Friedrichs systems. A notable reference in this regard is the work of Vila and Villedeau [82], and other related works of these authors. In [82], the authors analyze finite volume schemes for general Friedrichs systems and show convergence results and error estimates under very general assumptions. These results were further extended to even weaker solutions and error estimates by Jovanovič and Rohde in [44]. Thus, any finite volume scheme based on the Friedrichs form (2.1.6) falls into the framework of these papers.

Even though finite volume schemes based on the Friedrichs form (2.1.6) can be proved to converge and have error estimates for very general velocity fields, it has not been possible to derive bounds on the discrete divergence produced by these schemes. Heuristically, arguments of [65] imply that there is some control of divergence due to the fact that schemes should satisfy some discrete version of (2.1.21), and any divergence created by the scheme should be transported out of the domain. Yet, we have yet to find any rigorous proof of this fact. Even in [16], the authors were able to use local divergence free elements but were unable to control the divergence jump terms.

Another related problem with this approach, particularly in the context of the nonlinear MHD equations, is the fact that (2.1.4) is not conservative. Hence, the Rankine-Hugoniot conditions are modified by the presence of the source term and this can lead to incorrect propagation speeds for strong shocks as pointed out in [65]. Other references attesting to this fact can be found in [80]. However, the errors are quite small. In case of the linear induction equation, we were unable to find any such errors at linear contact discontinuities in our numerical experiments.

Summing up, the two most common approaches to discretization of (2.1.1) are based on staggering/preserving some form of the discrete divergence, or on introducing the

Godunov-Powell source term (the Friedrichs form of the equations). Using schemes based on staggering like in [77], one is able to preserve some form of discrete divergence exactly, but it is not possible to prove energy estimates (and hence convergence) for non-constant velocity fields. The resulting schemes can lead to oscillations near discontinuities even for constant velocity fields. On the other hand, use of the Friedrichs form or upwinding the Godunov-Powell source term leads to schemes for which we can prove energy estimates, convergence and even convergence rates. These schemes are non-oscillatory near discontinuities, at least for constant velocity fields. Yet, no rigorous control of the discrete divergence is available.

Given this, we propose a new class of finite difference schemes for (2.1.1). These schemes are based on the non-conservative form of the Friedrichs system (2.1.5). We use point values of the velocity field coupled with a upwind discretization of the transport terms. The sources in (2.1.5) are discretized by using central differences. Furthermore, we need to add some extra numerical diffusion at points where the velocity field vanishes. All these ingredients result in a scheme for which we are able to prove energy bounds, maximum principles and show that the scheme converges to a weak solution (2.1.9). In the case where the velocity field is constant, our scheme is TVD and preserves any consistent discrete divergence operator. Most crucially, the upwind scheme of this paper has bounded discrete divergence i.e., we are able to show that the standard discrete divergence div^0 produced by this scheme is bounded in L^2. Nevertheless, the resulting scheme is simple to implement.

Compared with other results, our scheme is in the spirit of schemes based on the symmetrized form of the equations. The key difference is that we discretize the non-conservative form of the symmetrized equations and have to add some extra (very small) numerical diffusion at sonic points (i.e., points where $|\mathbf{u}| = 0$). This seems to be crucial to obtain bounds on the discrete divergence. We were unable to rewrite the upwind scheme of this paper in a form that falls directly into the class of schemes analyzed in [82, 44] and hence, the general results of those papers do not apply to our scheme and the energy estimates need to proved independently. Numerical results obtained with the scheme show that the scheme is very robust, resolves the discontinuities well even at first order, and does not generate spurious oscillations around discontinuities. We are planning to use this upwind scheme for (2.1.1) in conjunction with suitable approximate Riemann solvers for the fluid part in order to design efficient splitting schemes for the MHD equations in a forthcoming paper [32].

The rest of this paper is organized as follows: in Section 2.2, we present the stable upwind scheme in two space dimensions, and prove stability and convergence. In Section 2.3, we present several numerical examples and compare the stable upwind scheme with other schemes.

2.2 A Stable upwind scheme.

For simplicity, we restrict our presentation to two spatial dimensions. As stated in the introduction, we are going to discretize the nonconservative version of the equation (2.1.5),

which in two dimensions takes the form

$$\begin{aligned}(B^1)_t + u^1(B^1)_x + u^2(B^1)_x &= -(u^2)_y B^1 + (u^1)_y B^2\\ (B^2)_t + u^1(B^2)_x + u^2(B^2)_x &= (u^2)_x B^1 - (u^1)_x B^2.\end{aligned} \tag{2.2.1}$$

Our scheme is initiated by setting

$$\mathbf{B}^0_{i,j} = \frac{1}{|I_{i,j}|}\int_{I_{i,j}} \mathbf{B}_0(x,y)\,dxdy.$$

Regarding $\mathbf{u}$, we either assume that $\mathbf{u}$ is a continuous function of x and y, or that we have given $\mathbf{u}$ as a table $\mathbf{u}_{i,j}$. The following definitions are also useful

$$M_{i,j} = \begin{pmatrix} -D^0_y u^2_{i,j} & D^0_y u^1_{i,j} \\ D^0_x u^2_{i,j} & -D^0_x u^1_{i,j}\end{pmatrix}, \tag{2.2.2}$$

and

$$(\mathbf{u}\cdot D^{\text{upw}})_{i,j} = \left[u^1_{i,j}\right]^- D^+_x + \left[u^1_{i,j}\right]^+ D^-_x + \left[u^2_{i,j}\right]^- D^+_y + \left[u^2_{i,j}\right]^+ D^-_y \tag{2.2.3}$$

$$\left(\mathbf{u}\cdot D^0\right)_{i,j} = u^1_{i,j} D^0_x + u^2_{i,j} D^0_y \tag{2.2.4}$$

$$\sigma_\delta(\mathbf{u}_{i,j})\left(\tfrac{\Delta x}{\Delta y}\right)\cdot D^2 = \sigma_\delta(u^1_{i,j})\Delta x D^+_x D^-_x + \sigma_\delta(u^2_{i,j})\Delta y D^+_y D^-_y, \tag{2.2.5}$$

where the auxiliary function σ_δ is an even smooth function such that

$$\sigma_\delta(a) = \begin{cases} \frac{\delta}{2}, & \text{if } |a| \le \delta/2,\\ 0, & \text{if } |a| \ge \delta.\end{cases}$$

Furthermore, we demand that σ is non-increasing in the interval $[0,\delta]$ and that $|\sigma'_\delta(a)| < 2$ for all a.

Then the numerical scheme in the fully discrete form is given by

$$D^+_t \mathbf{B}^n_{i,j} + (\mathbf{u}\cdot D^{\text{upw}})_{i,j}\,\mathbf{B}^n_{i,j} = M_{i,j}\mathbf{B}^n_{i,j} + \sigma_\delta(\mathbf{u}_{i,j})\left(\tfrac{\Delta x}{\Delta y}\right)\cdot D^2 \mathbf{B}^n_{i,j}, \quad (i,j)\in\mathbb{Z}^2,\ n\ge 0. \tag{2.2.6}$$

The semi-discrete version of this reads

$$\begin{aligned}\frac{d}{dt}\mathbf{B}_{i,j} + (\mathbf{u}\cdot D^{\text{upw}})_{i,j}\,\mathbf{B}_{i,j} = M_{i,j}\mathbf{B}_{i,j} + \sigma_\delta(\mathbf{u}_{i,j})\left(\tfrac{\Delta x}{\Delta y}\right)\cdot D^2\mathbf{B}_{i,j},\ t>0,\\ \mathbf{B}_{i,j}(0) = \mathbf{B}^0_{i,j}, \quad (i,j)\in\mathbb{Z}^2.\end{aligned} \tag{2.2.7}$$

The semi-discrete form is an infinite system of ordinary differential equations,

$$\frac{d}{dt}\mathbf{B} = \mathcal{F}(\mathbf{B}),$$

where we can regard $\mathbf{B}\in \ell^2\times\ell^2$, and $\mathcal{F}:\ell^2\times\ell^2\to\ell^2\times\ell^2$ is given by

$$(\mathcal{F}(\mathbf{B}))_{i,j} = -(\mathbf{u}\cdot D^{\text{upw}})_{i,j}\,\mathbf{B}_{i,j} + M_{i,j}\mathbf{B}_{i,j} + \sigma_\delta(\mathbf{u}_{i,j})\left(\tfrac{\Delta x}{\Delta y}\right)\cdot D^2\mathbf{B}_{i,j}.$$

For *fixed* Δx and Δy, it is not difficult to show that

$$\|\mathcal{F}(\mathbf{B})\|_{\ell^2\times\ell^2} \leq \frac{C}{\min\{\Delta x, \Delta y\}} \|\mathbf{B}\|_{\ell^2\times\ell^2}.$$

Therefore $\mathcal{F}$ is Lipschitz continuous, and we have existence of a differentiable solution $\mathbf{B}(t)$ at least for small t. The energy bound, Lemma 2.2.1, ensures that we do not have any blow up in finite time. Therefore there exists a differentiable solution $\mathbf{B}(t)$ of (2.2.7) for all $t > 0$.

Componententwise, (2.2.6) takes the form

$$\begin{aligned}
D_t^+ B_{i,j}^{1,n} =& - \left[u_{i,j}^1\right]^- D_x^+ \left(B_{i,j}^{1,n}\right) - \left[u_{i,j}^1\right]^+ D_x^- \left(B_{i,j}^{1,n}\right) \\
&- \left[u_{i,j}^2\right]^- D_y^+ \left(B_{i,j}^{1,n}\right) - \left[u_{i,j}^2\right]^+ D_y^- \left(B_{i,j}^{1,n}\right) \\
&- D_y^0\left(u_{i,j}^2\right) B_{i,j}^{1,n} + D_y^0\left(u_{i,j}^1\right) B_{i,j}^{2,n} \\
&+ \sigma_\delta(u_{i,j}^1)\Delta x D_x^+ D_x^- \left(B_{i,j}^{1,n}\right) + \sigma_\delta(u_{i,j}^2)\Delta y D_y^+ D_y^- \left(B_{i,j}^{1,n}\right), \\
D_t^+ B_{i,j}^{2,n} =& - \left[u_{i,j}^1\right]^- D_x^+ \left(B_{i,j}^{2,n}\right) - \left[u_{i,j}^1\right]^+ D_x^- \left(B_{i,j}^{2,n}\right) \\
&- \left[u_{i,j}^2\right]^- D_y^+ \left(B_{i,j}^{2,n}\right) - \left[u_{i,j}^2\right]^+ D_y^- \left(B_{i,j}^{2,n}\right) \\
&+ D_x^0\left(u_{i,j}^2\right) B_{i,j}^{1,n} - D_x^0\left(u_{i,j}^1\right) B_{i,j}^{2,n} \\
&+ \sigma_\delta(u_{i,j}^1)\Delta x D_x^+ D_x^- \left(B_{i,j}^{2,n}\right) + \sigma_\delta(u_{i,j}^2)\Delta y D_y^+ D_y^- \left(B_{i,j}^{2,n}\right),
\end{aligned} \tag{2.2.8}$$

We remark that the scheme is based on a upwind discretization of the nonconservative symmetric form (2.2.1). In addition, to the upwind discretization we also need to add a small amount of explicit numerical diffusion at the sonic points. This is necessary in the subsequent analysis.

Using the notation

$$|a|_\delta = |a| + \sigma_\delta(a)$$

and

$$\left(|\mathbf{u}|_\delta\left(\tfrac{\Delta x}{\Delta y}\right)\cdot D^2\right)_{i,j} = \left|u_{i,j}^1\right|_\delta \Delta x D_x^- D_x^+ + \left|u_{i,j}^2\right|_\delta \Delta y D_y^- D_y^+,$$

the scheme (2.2.6) can also be rewritten using central discrete derivatives

$$D_t^+ \mathbf{B}_{i,j}^n + \left(\mathbf{u}\cdot D^0\right)_{i,j} \mathbf{B}_{i,j}^n = M_{i,j}\mathbf{B}_{i,j} + \frac{1}{2}\left(|\mathbf{u}|_\delta\left(\tfrac{\Delta x}{\Delta y}\right)\cdot D^2\right)_{i,j} \mathbf{B}_{i,j}^n. \tag{2.2.9}$$

The semi-discrete form of this is obtained replacing D_t^+ by d/dt.

We are going to prove that both the fully discrete and the semi-discrete schemes have solutions that are bounded in both the energy and the maximum norms. In addition, we will also show that the semi-discrete scheme leads to a discrete divergence that is bounded in the L^2 norm. This is the main reason why we work with a discretization of the non-conservative form of the Friedrichs system (2.2.1).

In addition to the energy and divergence bounds, we are going to show that the scheme (2.2.8) converges to a weak solution (2.1.9) of the equation (2.1.6). To do this we need the "conservative", form i.e., the discrete form consistent with the two dimensional version of (2.1.6). Since we use point values of the coefficient $\mathbf{u}$ in our scheme this is not completely

straightforward. Using the discrete Leibnitz rule for the central differences (2.1.14), we can rewrite (2.2.8) as,

$$\begin{aligned} D_t^+ B_{i,j}^{1,n} = &-D_x^0\left(u_{i,j}^1 B_{i,j}^{1,n}\right) - D_y^0\left(u_{i,j}^2 B_{i,j}^{1,n}\right) + D_x^0\left(u_{i,j}^1\right) B_{i,j}^{1,n} + D_y^0\left(u_{i,j}^1\right) B_{i,j}^{2,n} \\ &+ \frac{1}{2}\left(|\mathbf{u}|_\delta\left(\tfrac{\Delta x}{\Delta y}\right)\cdot D^2\right)_{i,j} B_{i,j}^{1,n} \\ &+ \frac{\Delta x^2}{2}\left[\left(D_x^+ u_{i,j}^{1,n}\right)\left(D_x^- D_x^+ B_{i,j}^1\right) + \left(D_x^- B_{i,j}^{1,n}\right)\left(D_x^- D_x^+ u_{i,j}^1\right)\right] \\ &+ \frac{\Delta y^2}{2}\left[\left(D_y^+ u_{i,j}^2\right)\left(D_y^- D_y^+ B_{i,j}^{1,n}\right) + \left(D_y^- B_{i,j}^{1,n}\right)\left(D_y^- D_y^+ u_{i,j}^2\right)\right] \end{aligned} \tag{2.2.10}$$

$$\begin{aligned} D_t^+ B^{2,n} = &-D_x^0\left(u_{i,j}^1 B_{i,j}^{2,n}\right) - D_y^0\left(u_{i,j}^2 B_{i,j}^{2,n}\right) + D_x^0\left(u_{i,j}^2\right) B_{i,j}^{1,n} + D_y^0\left(u_{i,j}^2\right) B_{i,j}^{2,n} \\ &+ \frac{1}{2}\left(|\mathbf{u}|_\delta\left(\tfrac{\Delta x}{\Delta y}\right)\cdot D^2\right)_{i,j} B_{i,j}^{2,n} \\ &+ \frac{\Delta x^2}{2}\left[\left(D_x^+ u_{i,j}^1\right)\left(D_x^- D_x^+ B_{i,j}^{2,n}\right) + \left(D_x^- B_{i,j}^{2,n}\right)\left(D_x^- D_x^+ u_{i,j}^1\right)\right] \\ &+ \frac{\Delta y^2}{2}\left[\left(D_y^+ u_{i,j}^2\right)\left(D_y^- D_y^+ B_{i,j}^{2,n}\right) + \left(D_y^- B_{i,j}^{2,n}\right)\left(D_y^- D_y^+ u_{i,j}^2\right)\right] \end{aligned} \tag{2.2.11}$$

Rewritten in the above form, (2.2.8) represents a consistent discretization of (2.1.6). Note that (2.2.10) and (2.2.11), we use conservative central differences, a stabilizing diffusion term and second order error terms due to the discrete Liebnitz rule.

We have not managed to write (2.2.8) as a special case of the class of finite volume schemes that were presented and analysed in [82, 44]. The reason for this is the non-conservative form of the scheme. This is reflected in the presence of error terms in the conservative form (2.2.10) and (2.2.11) which have second derivatives in $\mathbf{B}$ multiplied by derivatives of $\mathbf{u}$, which can be of either sign. Hence, the results of [82, 44] do not apply directly to our scheme.

2.2.1 Some estimates

Now we prove that $\mathbf{B}^{\Delta t}$ satisfies some estimates which will allow us to conclude that $\left\{\mathbf{B}^{\Delta t}\right\}$ is weakly compact, and that any limit is a weak solution to (2.1.6). We start by

Lemma 2.2.1. *Let $\left\{\mathbf{B}_{i,j}^n\right\}$ satisfy the scheme (2.2.6), and Δt the following CFL-condition*

$$\Delta t \max\left\{\frac{6\left\|u^1\right\|_{L^\infty(\mathbb{R}^2)}}{\Delta x}, \frac{6\left\|u^2\right\|_{L^\infty(\mathbb{R}^2)}}{\Delta y}, 32\delta\right\} \leq \frac{1}{2}, \tag{2.2.12}$$

Then

$$\Delta x \Delta y \sum_{i,j}\left|\mathbf{B}_{i,j}^n\right|^2 \leq e^{Mn\Delta t}\Delta x\Delta y\sum_{i,j}\left|\mathbf{B}_{i,j}^0\right|^2, \tag{2.2.13}$$

where

$$M = 2\bar{M} + 4\bar{M}^2 + 6\left(\left\|\partial_x u^1\right\|_{L^\infty} + \left\|\partial_y u^2\right\|_{L^\infty}\right),$$

with

$$\bar{M} = \max_{i,j}\left\|M_{i,j}\right\|.$$

Furthermore for the solution of (2.2.7) *we have that*

$$\Delta x \Delta y \sum_{i,j} |\mathbf{B}_{i,j}(t)|^2 \leq e^{Mt} \Delta x \Delta y \sum_{i,j} \left|\mathbf{B}^0_{i,j}\right|^2, \quad t \geq 0. \tag{2.2.14}$$

Proof. We shall prove (2.2.13), the proof of (2.2.14) is simpler and uses the same basic ideas. Using the notation

$$\mathbf{B}^2 = \mathbf{B} \cdot \mathbf{B} = (B^1)^2 + (B^2)^2,$$

and the discrete chain rule, (2.1.13), we find

$$\begin{aligned} 2\mathbf{B}^n_{i,j} \cdot D^+_t \mathbf{B}^n_{i,j} = &- \left(\mathbf{u} \cdot D^{\text{upw}}\right)_{i,j} \left(\left(\mathbf{B}^n_{i,j}\right)^2\right) \\ &- \Delta x \left(-\left[u^1_{i,j}\right]^- \left(D^+_x \mathbf{B}^n_{i,j}\right)^2 + \left[u^1_{i,j}\right]^+ \left(D^-_x \mathbf{B}^n_{i,j}\right)^2\right) \\ &- \Delta y \left(-\left[u^2_{i,j}\right]^- \left(D^+_y \mathbf{B}^n_{i,j}\right)^2 + \left[u^2_{i,j}\right]^+ \left(D^-_y \mathbf{B}^n_{i,j}\right)^2\right) \\ &+ 2\mathbf{B}^n_{i,j} \cdot M_{i,j} \mathbf{B}^n_{i,j} + \mathbf{B}^n_{i,j} \cdot D^2_\delta(\mathbf{u})_{i,j} \mathbf{B}^n_{i,j}. \end{aligned} \tag{2.2.15}$$

For any quantity $Z_{i,j}$, using summation by parts

$$\begin{aligned} \sum_{i,j} Z_{i,j} \Delta x \sigma_\delta\left(u^1_{i,j}\right) D^+_x D^-_x Z_{i,j} &= -\Delta x \sum_{i,j} D^-_x \left(Z_{i,j} \sigma_\delta\left(u^1_{i,j}\right)\right) D^-_x Z_{i,j} \\ &= -\Delta x \sum_{i,j} Z_{i,j} D^-_x \left(\sigma_\delta\left(u^1_{i,j}\right)\right) D^-_x Z_{i,j} + \sigma_\delta\left(u^1_{i-1,j}\right) \left(D^-_x Z_{i,j}\right)^2 \\ &\leq -\Delta x \sum_{i,j} \sigma_\delta\left(u^1_{i-1,j}\right) \left(D^-_x Z_{i,j}\right)^2 \\ &\quad + 2 \sum_{i,j} \left|D^-_x u^1_{i,j}\right| \left(|Z_{i,j}| + |Z_{i-1,j}|\right) |Z_{i,j}| \\ &\leq -\Delta x \sum_{i,j} \sigma_\delta\left(u^1_{i,j}\right) \left(D^+_x Z_{i,j}\right)^2 + 4 \left\|\partial_x u^1\right\|_{L^\infty(\mathbb{R}^2)} \sum_{i,j} \left(Z_{i,j}\right)^2. \end{aligned}$$

Since $D^+_x D^-_x = D^-_x D^+_x$, we the term $(D^+_x Z_{i,j})^2$ can be replaced by $(D^-_x Z_{i,j})^2$ above. Therefore we have that

$$\begin{aligned} &\sum_{i,j} Z_{i,j} \Delta x \sigma_\delta\left(u^1_{i,j}\right) D^+_x D^-_x Z_{i,j} \\ &\qquad \leq -\frac{\Delta x}{2} \sum_{i,j} \sigma_\delta\left(u^1_{i,j}\right) \left(\left(D^+_x Z_{i,j}\right)^2 + \left(D^-_x Z_{i,j}\right)^2\right) + 4 \left\|\partial_x u^1\right\|_{L^\infty(\mathbb{R}^2)} \sum_{i,j} \left(Z_{i,j}\right)^2, \end{aligned}$$

and similarly

$$\begin{aligned} &\sum_{i,j} Z_{i,j} \Delta y \sigma_\delta\left(u^2_{i,j}\right) D^+_y D^-_y Z_{i,j} \\ &\qquad \leq -\frac{\Delta y}{2} \sum_{i,j} \sigma_\delta\left(u^2_{i,j}\right) \left(\left(D^+_y Z_{i,j}\right)^2 + \left(D^-_y Z_{i,j}\right)^2\right) + 4 \left\|\partial_y u^2\right\|_{L^\infty(\mathbb{R}^2)} \sum_{i,j} \left(Z_{i,j}\right)^2. \end{aligned}$$

Hence, we get

$$\sum_{i,j}\left(\mathbf{B}^n_{i,j}\cdot D^2_\delta(\mathbf{u})_{i,j}\mathbf{B}^n_{i,j}\right)\le-\sum_{i,j}\frac{\Delta x}{2}\sigma_\delta\left(u^1_{i,j}\right)\left(\left(D^+_x\mathbf{B}^n_{i,j}\right)^2+\left(D^-_x\mathbf{B}^n_{i,j}\right)^2\right)$$
$$\frac{\Delta y}{2}\sigma_\delta\left(u^2_{i,j}\right)\left(\left(D^+_y\mathbf{B}^n_{i,j}\right))^2+\left(D^-_y\mathbf{B}^n_{i,j}\right))^2\right)$$
$$+4\left(\left\|\partial_x u^1\right\|_{L^\infty(\mathbb{R}^2)}+\left\|\partial_y u^2\right\|_{L^\infty(\mathbb{R}^2)}\right)\sum_{i,j}(\mathbf{B}^n_{i,j})^2.$$

Note also that by the discrete Leibnitz rule (2.1.12), we have that for any quantity $Z_{i,j}$,

$$\sum_{i,j}\left(\mathbf{u}\cdot D^{\mathrm{upw}}\right)_{i,j}Z_{i,j}=-\sum_{i,j}Z_{i,j}\left[D^+_x\left[u^1_{i,j}\right]^+ + D^-_x\left[u^1_{i,j}\right]^- + D^+_y\left[u^2_{i,j}\right]^+ + D^-_y\left[u^2_{i,j}\right]^-\right].$$

Using this on the first term on the right in (2.2.15) we find that

$$\sum_{i,j}2\mathbf{B}^n_{i,j}D^+_t\mathbf{B}^n_{i,j}\le\left(6\left(\left\|\partial_x u^1\right\|_{L^\infty(\mathbb{R}^2)}+\left\|\partial_y u^2\right\|_{L^\infty(\mathbb{R}^2)}\right)+2\bar{M}\right)\sum_{i,j}\left(\mathbf{B}^n_{i,j}\right)^2$$
$$-\sum_{i,j}\Delta x\left(-\left[u^1_{i,j}\right]^-\left(D^+_x\mathbf{B}^n_{i,j}\right)^2+\left[u^1_{i,j}\right]^+\left(D^-_x\mathbf{B}^n_{i,j}\right)^2\right)$$
$$\Delta y\left(-\left[u^2_{i,j}\right]^-\left(D^+_y\mathbf{B}^n_{i,j}\right)^2+\left[u^2_{i,j}\right]^+\left(D^-_y\mathbf{B}^n_{i,j}\right)^2\right)$$
$$-\sum_{i,j}\frac{\Delta x}{2}\sigma_\delta\left(u^1_{i,j}\right)\left(\left(D^+_x\mathbf{B}^n_{i,j}\right)^2+\left(D^-_x\mathbf{B}^n_{i,j}\right)^2\right)$$
$$\frac{\Delta y}{2}\sigma_\delta\left(u^2_{i,j}\right)\left(\left(D^+_y\mathbf{B}^n_{i,j}\right)^2+\left(D^-_y\mathbf{B}^n_{i,j}\right))^2\right).$$

We also have that

$$D^+_t\left(\left(\mathbf{B}^n_{i,j}\right)^2\right)=2\mathbf{B}^n_{i,j}\cdot D^+_t\mathbf{B}^n_{i,j}+\Delta t\left(D^+_t\mathbf{B}^n_{i,j}\right)^2.$$

In order to balance the terms, we use the scheme (2.2.6), and the inequality

$$\left(\Delta x D^+_x D^-_x a_j\right)^2\le 2\left(\left(D^+_x a_j\right)^2+\left(D^-_x a_j\right)^2\right).$$

Then

$$\left(D^+_t\mathbf{B}^n_{i,j}\right)^2\le 2\left(\left(\mathbf{u}\cdot D^{\mathrm{upw}}\right)_{i,j}\mathbf{B}^n_{i,j}\right)^2+4\left(M_{i,j}\mathbf{B}^n_{i,j}\right)^2+4\left(D^2_\delta(\mathbf{u})_{i,j}\mathbf{B}^n_{i,j}\right)^2$$
$$\le 8\Big[\left(\left[u^1_{i,j}\right]^-\right)^2\left(D^+_x\mathbf{B}^n_{i,j}\right)^2+\left(\left[u^1_{i,j}\right]^+\right)^2\left(D^-_x\mathbf{B}^n_{i,j}\right)^2$$
$$+\left(\left[u^2_{i,j}\right]^-\right)^2\left(D^+_y\mathbf{B}^n_{i,j}\right)^2+\left(\left[u^2_{i,j}\right]^+\right)^2\left(D^-_y\mathbf{B}^n_{i,j}\right)^2\Big]$$
$$+8\left[\left(\Delta x\sigma_\delta\left(u^1_{i,j}\right)D^+_x D^-_x\mathbf{B}^n_{i,j}\right)^2+\left(\Delta y\sigma_\delta\left(u^2_{i,j}\right)D^+_y D^-_y\mathbf{B}^n_{i,j}\right)^2\right]$$
$$+4\bar{M}^2\left(\mathbf{B}^n_{i,j}\right)^2$$

$$
\begin{aligned}
&\leq 8\Big[\Big(\big[u^1_{i,j}\big]^-\Big)^2\big(D_x^+\mathbf{B}^n_{i,j}\big)^2+\Big(\big[u^1_{i,j}\big]^+\Big)^2\big(D_x^-\mathbf{B}^n_{i,j}\big)^2\\
&\qquad+\Big(\big[u^2_{i,j}\big]^-\Big)^2\big(D_y^+\mathbf{B}^n_{i,j}\big)^2+\Big(\big[u^2_{i,j}\big]^+\Big)^2\big(D_y^-\mathbf{B}^n_{i,j}\big)^2\Big]\\
&\quad+16\Big[\sigma_\delta^2\big(u^1_{i,j}\big)\Big(\big(D_x^+\mathbf{B}^n_{i,j}\big)^2+\big(D_x^-\mathbf{B}^n_{i,j}\big)^2\Big)\\
&\qquad+\sigma_\delta^2\big(u^2_{i,j}\big)\Big(\big(D_y^+\mathbf{B}^n_{i,j}\big)^2+\big(D_y^-\mathbf{B}^n_{i,j}\big)^2\Big)\Big]\\
&\quad+4\bar{M}^2\big(\mathbf{B}^n_{i,j}\big)^2.
\end{aligned}
$$

Using the above and summing over i and j,

$$
\begin{aligned}
D_t^+\sum_{i,j}\big(\mathbf{B}^n_{i,j}\big)^2 \leq \sum_{i,j}\Bigg[&\Big|\big[u^1_{i+1/2,j}\big]^-\Big|\Big(8\Delta t\Big|\big[u^1_{i+1/2,j}\big]^-\Big|-\Delta x\Big)\big(D_x^+\mathbf{B}^n_{i,j}\big)^2\\
&+\big[u^1_{i-1/2,j}\big]^+\Big(8\Delta t\big[u^1_{i-1/2,j}\big]^+-\Delta x\Big)\big(D_x^-\mathbf{B}^n_{i,j}\big)^2\\
&+\Big|\big[u^2_{i,j+1/2}\big]^-\Big|\Big(8\Delta t\Big|\big[u^2_{i,j+1/2}\big]^-\Big|-\Delta y\Big)\big(D_y^+\mathbf{B}^n_{i,j}\big)^2\\
&+\big[u^1_{i,j-1/2}\big]^+\Big(8\Delta t\big[u^2_{i,j-1/2}\big]^+-\Delta y\Big)\big(D_y^-\mathbf{B}^n_{i,j}\big)^2\\
&+\sigma_\delta\big(u^1_{i,j}\big)\Big(16\Delta t\sigma_\delta\big(u^1_{i,j}\big)-\frac{\Delta x}{2}\Big)\Big(\big(D_x^+\mathbf{B}^n_{i,j}\big)^2+\big(D_x^-\mathbf{B}^n_{i,j}\big)^2\Big)\\
&+\sigma_\delta\big(u^2_{i,j}\big)\Big(16\Delta t(\sigma_\delta\big(u^2_{i,j}\big)-\frac{\Delta y}{2}\Big)\Big(\big(D_y^+\mathbf{B}^n_{i,j}\big)^2+\big(D_y^-\mathbf{B}^n_{i,j}\big)^2\Big)\Bigg]\\
&+\big(2\bar{M}+4\bar{M}^2+6\big(\big\|\partial_x u^1\big\|_{L^\infty}+\big\|\partial_y u^2\big\|_{L^\infty}\big)\big)\sum_{i,j}\big(\mathbf{B}^n_{i,j}\big)^2\\
\leq M\sum_{i,j}&\big(\mathbf{B}^n_{i,j}\big)^2,
\end{aligned}
$$

if the CFL-condition (2.2.12) holds. Now (2.2.13) follows by the discrete Gronwall inequality. □

The CFL-condition (2.2.12) implies that the terms in front of $(D^\pm_{x,y}\mathbf{B}^n_{i,j})^2$ above are all less than $-\Delta x/2$ or $-\Delta y/2$. Therefore, as a consequence of the proof, we also get a bound on the spatial variation of $\mathbf{B}^n_{i,j}$. Set

$$
\begin{aligned}
\Upsilon^n_{i,j}=&\frac{\Delta x}{2}\Big(\Big(-\big[u^1_{i,j}\big]^-+\sigma_\delta\big(u^1_{i,j}\big)\Big)\big(D_x^+\mathbf{B}^n_{i,j}\big)^2+\Big(\big[u^1_{i,j}\big]^++\sigma_\delta\big(u^1_{i,j}\big)\Big)\big(D_x^-\mathbf{B}^n_{i,j}\big)^2\Big)\\
&+\frac{\Delta y}{2}\Big(\Big(-\big[u^2_{i,j}\big]^-+\sigma_\delta\big(u^2_{i,j}\big)\Big)\big(D_y^+\mathbf{B}^n_{i,j}\big)^2+\Big(\big[u^2_{i,j}\big]^++\sigma\big(u^2_{i,j}\big)\Big)\big(D_y^-\mathbf{B}^n_{i,j}\big)^2\Big).
\end{aligned}
$$

By (2.2.15) and (2.2.13) the following bound holds

$$\begin{aligned}\Delta t \sum_{i,j} \Upsilon_{i,j}^n &\le (M+1) \sum_{i,j} \left(\left(\mathbf{B}_{i,j}^n\right)^2 + \left(\mathbf{B}_{i,j}^{n+1}\right)^2 \right) \\ &\le 2\,(M+1)\, e^{M(n+1)\Delta t} \sum_{i,j} \left(\mathbf{B}_{i,j}^0\right)^2 .\end{aligned} \tag{2.2.16}$$

Since the scheme uses local upwinding and adds some numerical diffusion, the first part of the updating is monotone in all its arguments. More concretely, set

$$\begin{aligned}&f\left(Z_{i,j}, Z_{i-1,j}, Z_{i+1,j}, Z_{i,j-1}, Z_{i,j+1}\right) \\ &\qquad = Z_{i,j} - \Delta t \left(\mathbf{u} \cdot D^{\text{upw}}\right)_{i,j} Z_{i,j} + \Delta t D_\delta^2(\mathbf{u})_{i,j} Z_{i,j}.\end{aligned}$$

Differentiation and positivity of the coefficients σ_δ and the CFL-condition (2.2.12) show that

$$\frac{\partial f}{\partial Z_{i,j}} \ge 0, \quad \frac{\partial f}{\partial Z_{i\pm1,j}} \ge 0 \quad \text{and} \quad \frac{\partial f}{\partial Z_{i,j\pm1}} \ge 0.$$

Next, we prove a bound for the supremum norm, defined as

$$\left\|\mathbf{B}_{i,j}^n\right\|_{L^\infty} = \sup_{i,j} \left|B_{i,j}^{1,n}\right| + \sup_{i,j} \left|B_{i,j}^{2,n}\right| .$$

Lemma 2.2.2. *Let $\mathbf{B}_{i,j}^n$ be defined by the scheme* (2.2.8)*. Then*

$$\left\|\mathbf{B}_{i,j}^n\right\|_{L^\infty} \le e^{Cn\Delta t} \left\|\mathbf{B}_{i,j}^0\right\|_{L^\infty}, \tag{2.2.17}$$

where $C = \|\partial_x u^1\|_{L^\infty} + \|\partial_y u^1\|_{L^\infty} + \|\partial_x u^2\|_{L^\infty} + \|\partial_y u^2\|_{L^\infty}$.

Proof. We write (2.2.6) as

$$\begin{aligned}B_{i,j}^{1,n+1} &= f\left(B_{i,j}^{1,n}, B_{i-1,j}^{1,n}, B_{i+1,j}^{1,n}, B_{i,j-1}^{1,n}, B_{i,j+1}^{1,n}\right) \\ &\quad - \Delta t \left(D_y^0 u_{i,j}^2 B_{i,j}^{1,n} - D_y^0 u_{i,j+1/2}^1 B_{i,j}^{2,n}\right) \\ B_{i,j}^{2,n+1} &= f\left(B_{i,j}^{2,n}, B_{i-1,j}^{2,n}, B_{i+1,j}^{2,n}, B_{i,j-1}^{2,n}, B_{i,j+1}^{2,n}\right) \\ &\quad + \Delta t \left(D_y^0 u_{i+1/2,j}^2 B_{i,j}^{1,n} - D_0^y u_{i+1/2,j}^1 B_{i,j}^{2,n}\right).\end{aligned}$$

Set $\alpha^n = \sup_{i,j} |B_{i,j}^{1,n}|$ and $\beta = \sup_{i,j} |B_{i,j}^{2,n}|$. Since $f(a,a,a,a,a) = a$ and f is increasing in all its arguments, it follows that

$$\begin{aligned}\alpha^{n+1} &\le \alpha^n + \Delta t \left(\left\|\partial_y u^2\right\|_{L^\infty} \alpha^n + \left\|\partial_y u^1\right\|_{L^\infty} \beta^n\right) \\ \beta^{n+1} &\le \beta^n + \Delta t \left(\left\|\partial_x u^2\right\|_{L^\infty} \alpha^n + \left\|\partial_x u^1\right\|_{L^\infty} \beta^n\right).\end{aligned}$$

Adding these two inequalities we obtain

$$\begin{aligned}\left\|\mathbf{B}_{i,j}^{n+1}\right\|_{L^\infty} &\le \left\|\mathbf{B}_{i,j}^n\right\|_{L^\infty} + \Delta t \left(\left\|\partial_x u^2\right\|_{L^\infty} + \left\|\partial_y u^2\right\|_{L^\infty}\right) \alpha^n \\ &\quad + \Delta t \left(\left\|\partial_x u^1\right\|_{L^\infty} + \left\|\partial_y u^1\right\|_{L^\infty}\right) \beta^n \\ &\le (1 + C\Delta t) \left\|\mathbf{B}_{i,j}^n\right\|_{L^\infty} .\end{aligned}$$

Gronwall's inequality concludes the proof of the lemma. □

Remark 2.2.1. If $\mathbf{u}$ is constant, i.e., $\mathbf{u} = (u^1, u^2)$ for two constants u^1 and u^2, we can choose $\delta = 0$ in the diffusion coefficients σ_δ This follows by taking $\delta \leq \min\{|u_1|, |u_2|\}$ in the case where both u_1, u_2 are away from zero. The case where one or both of the constant velocity fields is zero leads to a single advection equation and we ignore it here. In this special case, the scheme (2.2.8) reduces to a particularly simple form,

$$\begin{aligned} D_t^+ B_{i,j}^{1,n} = &-\left[u^1\right]^- D_x^+ \left(B_{i,j}^{1,n}\right) - \left[u^1\right]^+ D_x^- \left(B_{i,j}^{1,n}\right) \\ &- \left[u^2\right]^- D_y^+ \left(B_{i,j}^{1,n}\right) - \left[u^2\right]^+ D_y^- \left(B_{i,j}^{1,n}\right), \\ D_t^+ B_{i,j}^{2,n} = &- \left[u^1\right]^- D_x^+ \left(B_{i,j}^{2,n}\right) - \left[u^1\right]^+ D_x^- \left(B_{i,j}^{2,n}\right) \\ &- \left[u^2\right]^- D_y^+ \left(B_{i,j}^{2,n}\right) - \left[u^2\right]^+ D_y^- \left(B_{i,j}^{2,n}\right). \end{aligned} \tag{2.2.18}$$

In this case, we have some additional properties. Firstly, we observe that now Lemma 2.2.1 and Lemma 2.2.2 give

$$\Delta x \Delta y \sum_{i,j} \left|\mathbf{B}_{i,j}^n\right|^2 \leq \Delta x \Delta y \sum_{i,j} \left|\mathbf{B}_{i,j}^0\right|^2, \text{ and } \left\|\mathbf{B}_{i,j}^n\right\|_{L^\infty} \leq \left\|\mathbf{B}_{i,j}^0\right\|_{L^\infty}$$

respectively. Also the operator $(\mathbf{u} \cdot D)_{i,j}$ is independent of i and j. By Harten's lemma, see [50], and the monotonicity of f

$$\left|B_{i,j}^{k,n}\right|_{B.V.} \leq \left|B_{i,j}^{k,0}\right|_{B.V.}, \text{ for } k = 1, 2, \tag{2.2.19}$$

where

$$\left|B_{i,j}^{k,n}\right|_{B.V.} = \Delta y \Delta x \sum_{i,j} \left|D_x^+ B_{i,j}^{k,n}\right| + \left|D_y^+ B_{i,j}^{k,n}\right|.$$

If $\mathbf{u}$ is constant, then we also have that if some discrete divergence of $\mathbf{B}$ initially is zero, then this will remain zero. To see this, let $\mathcal{L}\mathbf{B}_{i,j}^n$ be *any* finite linear combination of $\mathbf{B}_{i,j}^n$ for various i's and j's, i.e.,

$$(\mathcal{L}\mathbf{B}_{i,j}^n) = \sum_{m=1}^{2} \sum_{k=1}^{N} \alpha_k^m B_{i+\sigma(k), j+\kappa(k)}^{m,n},$$

where σ and κ are functions taking integer values, and α_k^m is a constant. Applying $\mathcal{L}$ to the definition of the scheme gives

$$D_t^+ \left(\mathcal{L}\mathbf{B}_{i,j}^n\right) = -(\mathbf{u} \cdot D)\left(\mathcal{L}\mathbf{B}_{i,j}^n\right).$$

In particular, if $\mathcal{L}\mathbf{B}_{i,j}^0 = 0$ then $\mathcal{L}\mathbf{B}_{i,j}^n = 0$ for $n > 0$. Since any discrete divergence is of the same type as $\mathcal{L}$, any zero initial discrete divergence will remain zero. We also remark that for constant velocity, the CFL-condition can be relaxed to

$$\Delta t \max\left\{\frac{|u^1|}{\Delta x}, \frac{|u^2|}{\Delta y}\right\} \leq \frac{1}{2}. \tag{2.2.20}$$

Hence, in the case of constant velocity fields, the scheme (2.2.8) is non-oscillatory and preserves any discrete divergence operator. These are important structural properties of the scheme and explain some of the results in the section on numerical experiments.

2.2.2 Convergence

It follows directly from the L^2 bound in Lemma 2.2.1 that that the sequence $\left\{\mathbf{B}^{\Delta t}\right\}$ is weakly compact in $L^2(\mathbb{R}^2 \times [0,T])$. By the L^2 bound we infer the existence of a function $\mathbf{B}(x,y,t)$ such that

$$\mathbf{B}^{\Delta t} \rightharpoonup \mathbf{B}, \quad \text{in } L^2(\mathbb{R}^2 \times [0,T]) \text{ as } \Delta t \to 0.$$

Theorem 2.2.1. *Let $\mathbf{B}^n$ be defined by the scheme (2.2.8), and assume that $\|\mathbf{B}_0\|_{L^2(\mathbb{R}^2)}$ is finite. If $\mathbf{u} \in C^2(\mathbb{R}^2)$ with bounded derivatives, and Δt satisfies the CFL-condition (2.2.12), then there exists a subsequence $\{\Delta t_j\}$ such that $\mathbf{B}^{\Delta t_j} \rightharpoonup \mathbf{B}$ in $L^2(\mathbb{R}^2 \times [0,T])$. Furthermore, the limit $\mathbf{B} = (B^1, B^2)$ is a weak solution of (2.1.6), with the property that*

$$\|\mathbf{B}(\cdot,T)\|_{L^2(\mathbb{R}^2)} \le C_T \|\mathbf{B}_0\|_{L^2(\mathbb{R}^2)}, \quad T \ge 0,$$

where C_T is a finite constant depending on $\mathbf{u}$ and T. The same results hold for the approximations generated by the semi-discrete scheme (2.2.7).

Proof. We must show that $\mathbf{B}$ is a weak solution, and we shall do this for the first component B^1. Identical arguments apply to B^2. To demonstrate that $\mathbf{B}$ is a weak solution of (2.1.6) we must then show that B^1 satisfies

$$\mathcal{W}_\varphi(\mathbf{B}) := \iiint\limits_{\mathbb{R}^2\times[0,\infty)} B^1\partial_t\varphi + u^1B^1\partial_x\varphi + u^2B^1\partial_y\varphi - B^1\partial_x(u^1)\varphi - B^2\partial_y(u^1)\varphi \, dxdydt + \iint_{\mathbb{R}^2} B_0^1\varphi(x,y,0)\, dxdy = 0, \quad (2.2.21)$$

for all test functions $\varphi \in C_0^\infty(\Pi)$, where $\Pi = \mathbb{R}^2 \times [0,\infty)$.

Choose a test function φ and set

$$\varphi_{i,j}^n = \frac{1}{\Delta t\Delta x\Delta y} \iiint_{I_{i,j}^n} \varphi(x,y,t)\, dxdydt.$$

In order to prove convergence to a weak solution (2.2.21), we need to work with the "conservative form" of the scheme (2.2.10).

To save space, set $\Delta = \Delta t\Delta x\Delta y$, multiply (2.2.10) by $\Delta\varphi_{i,j}^n$, sum over $n = 0, \dots, \infty$, and (i,j) in $\mathbb{Z}^2$, and sum by parts to arrive at

$$\alpha_1 + \alpha_2 + \alpha_3 + \alpha_4 + \alpha_5 + \alpha_6 + \alpha_7 + \alpha_8 + \alpha_9 + \alpha_{10} + \alpha_{11} + \alpha_{12} = 0$$

where

$$\alpha_1 = \Delta \sum_{n=1}^{\infty}\sum_{i,j} B_{i,j}^{1,n} D_t^- \varphi_{i,j}^n, \qquad \alpha_2 = \Delta x\Delta y \sum_{i,j} B_{i,j}^{1,0}\varphi_{i,j}^0,$$

$$\alpha_3 = \Delta \sum_{n=1}^{\infty}\sum_{i,j} u_{i,j}^1 B_{i,j}^1 (D_x^0\varphi_{i,j}^n), \qquad \alpha_4 = \Delta \sum_{n=1}^{\infty}\sum_{i,j} u_{i,j}^2 B_{i,j}^1 (D_y^0\varphi_{i,j}^n),$$

$$\alpha_5 = -\Delta \sum_{n=1}^{\infty} \sum_{i,j} \varphi_{i,j}^n B_{i,j}^1 (D_x^0 u_{i,j}^1), \qquad \alpha_6 = \Delta \sum_{n=1}^{\infty} \sum_{i,j} \varphi_{i,j}^n B_{i,j}^2 (D_y^0 u_{i,j}^1),$$

and

$$\begin{aligned}
\alpha_7 &= -\Delta x \Delta \sum_{n=1}^{\infty} \sum_{i,j} D_x^+ D_x^- (|u_{i,j}^1|_\delta \varphi_{i,j}^n) B_{i,j}^{1,n}, \\
\alpha_8 &= -\Delta y \Delta \sum_{n=1}^{\infty} \sum_{i,j} D_y^+ D_y^- (|u_{i,j}^2|_\delta \varphi_{i,j}^n) B_{i,j}^{1,n}, \\
\alpha_9 &= (\Delta x)^2 \Delta \sum_{n=1}^{\infty} \sum_{i,j} D_x^+ (\varphi_{i,j}^n D_x^- (u_{i,j}^1)) D_x^+ (B_{i,j}^{1,n}), \\
\alpha_{10} &= (\Delta y)^2 \Delta \sum_{n=1}^{\infty} \sum_{i,j} D_y^+ (\varphi_{i,j}^n D_y^- (u_{i,j}^2)) D_y^+ (B_{i,j}^{1,n}), \\
\alpha_{11} &= -(\Delta x)^2 \Delta \sum_{n=1}^{\infty} \sum_{i,j} \varphi_{i,j}^n D_x^+ D_x^- (u_{i,j}^1) D_x^+ (B_{i,j}^{1,n}), \\
\alpha_{12} &= (\Delta y)^2 \Delta \sum_{n=1}^{\infty} \sum_{i,j} \varphi_{i,j}^n D_y^+ D_y^- (u_{i,j}^2) D_y^+ (B_{i,j}^{1,n}).
\end{aligned}$$

We claim that since $\mathbf{B}^{\Delta t} \in L^2(\mathbb{R}^2 \times [0,T])$ for all finite T, all the terms $\alpha_7, \alpha_8, \ldots, \alpha_{12}$ vanish a $\Delta \to 0$. We can estimate α_7 and α_8 as follows,

$$\begin{aligned}
\alpha_7^2 &\le \Delta x^2 \left(\Delta \sum_{n,i,j} \left(D_x^+ D_x^- \left(\left| u_{i,j}^1 \right|_\delta \varphi_{i,j}^n \right) \right)^2 \right) \left(\Delta \sum_{n,i,j} (B_{i,j}^{1,n})^2 \right) \\
&\le C \Delta x^2 \quad \to 0, \quad \text{as} \quad \Delta x \to 0,
\end{aligned}$$

for some constant C which is independent of Δt. When we estimate $\alpha_9, \ldots, \alpha_{12}$ we have an extra Δx or Δy which can be used to "remove the discrete derivative" from $\mathbf{B}$. This is done for α_9 as

$$\begin{aligned}
\alpha_9 &\le \Delta x \sum_{n,i,j} \left| D_x^+ \left(\varphi_{i,j}^n D_x^- u_{i,j}^1 \right) \right| \left(\left| B_{i+1,j}^{1,n} \right| + \left| B_{i,j}^{1,n} \right| \right) \\
&\le \Delta x \left(\sum_{n,i,j} \left(D_x^+ \left(\varphi_{i,j}^n D_x^- u_{i,j}^1 \right) \right)^2 \right)^{1/2} \left(4 \sum_{n,i,j} \left(B_{i,j}^{1,n} \right)^2 \right)^{1/2} \\
&\le C \Delta x,
\end{aligned}$$

for some constant C which is independent of Δt.

Using that $\mathbf{B}^{\Delta t} \rightharpoonup \mathbf{B}$ as $\Delta t \to 0$ and that $\mathbf{u}$ and φ are smooth enough, we can use standard arguments to show that as $\Delta t, \Delta x, \Delta y \to 0$,

$$\alpha_1 \to \iiint_{\Pi} B^1 \partial_t \varphi \, dx dy dt, \qquad \alpha_2 \to \iint_{\mathbb{R}^2} B_0^1 \varphi(x,y,0) \, dx dy$$

$$\alpha_3 \to \iiint_\Pi u^1 B^1 \partial_x \varphi \, dxdydt, \qquad \alpha_4 \to \iiint_\Pi u^2 B^1 \partial_y \varphi \, dxdydt$$
$$\alpha_5 \to \iiint_\Pi \partial_x (u^1) B^1 \varphi \, dxdydt, \qquad \alpha_6 \to \iint_\Pi \partial_y (u^1) B^1 \varphi \, dxdydt$$

Hence, we have shown that the approximations defined by (2.2.10) and (2.2.11) converge to a weak solution of (2.1.6). □

2.2.3 Divergence Bounds

In this section, we show that we can bound the divergence of the semi-discrete scheme (2.2.7) under certain assumptions.

In order to motivate some rather long calculations, we start by considering the exact equations

$$B^1_t + u^1 B^1_x + u^2 B^1_y = -u^2_y B^1 + u^1_y B^2 \tag{2.2.22}$$
$$B^2_t + u^1 B^2_x + u^2 B^2_y = u^2_x B^1 - u^1_x B^2. \tag{2.2.23}$$

Setting $d = B^1_x + B^2_y$, differentiating the first equation with respect to x and the second with respect to y and adding yields

$$d_t + u^1 d_x + u^2 d_y = -\left(u^1_x + u^2_y\right) d. \tag{2.2.24}$$

Multiplying by $2d$, and using Leibnitz' rule (again) yields

$$d^2_t + \left(u^1 d^2\right)_x + \left(u^2 d^2\right)_y = -\left(u^1_x + u^2_y\right) d^2. \tag{2.2.25}$$

Integrating over x and y gives

$$\frac{d}{dt} \left\| d(\cdot, t) \right\|^2_{L^2(\mathbb{R}^2)} \leq \left\| \mathrm{div} \mathbf{u} \right\|_{L^\infty(\mathbb{R}^2)} \left\| d(\cdot, t) \right\|^2_{L^2(\mathbb{R}^2)}. \tag{2.2.26}$$

We wish to "replicate" this calculation for the approximations generated by the semi-discrete scheme. There are three obstacles in the way of doing so, firstly the approximations do not satisfy (2.2.22) and (2.2.23), but (2.2.7). Secondly we used Leibnitz' rule to arrive at (2.2.24), this rule do not hold exactly for the discrete differentiation operators D^0_x and D^0_y. Thirdly we used the chain rule to arrive at (2.2.24), this is not exact for discrete derivatives.

We start by considering the scheme in the form (2.2.9), which reads

$$\begin{aligned} \frac{d}{dt} B^1_{i,j} = &-u^1_{i,j} D^0_x B^1_{i,j} - u^2_{i,j} D^0_y B^1_{i,j} - \left(D^0_y u^2_{i,j}\right) B^1_{i,j} + \left(D^0_y u^1_{i,j}\right) B^2_{i,j} \\ &+ \frac{\Delta x}{2} \left|u^1_{i,j}\right|_\delta D^+_x D^-_x B^1_{i,j} + \frac{\Delta y}{2} \left|u^2_{i,j}\right|_\delta D^+_y D^-_y B^1_{i,j} \end{aligned} \tag{2.2.27}$$

$$\begin{aligned} \frac{d}{dt} B^2_{i,j} = &-u^1_{i,j} D^0_x B^2_{i,j} - u^2_{i,j} D^0_y B^2_{i,j} + \left(D^0_x u^2_{i,j}\right) B^1_{i,j} - \left(D^0_x u^1_{i,j}\right) B^2_{i,j} \\ &+ \frac{\Delta x}{2} \left|u^1_{i,j}\right|_\delta D^+_x D^-_x B^2_{i,j} + \frac{\Delta y}{2} \left|u^2_{i,j}\right|_\delta D^+_y D^-_y B^2_{i,j}. \end{aligned} \tag{2.2.28}$$

In order to replace the exact Leibnitz rule, for a smooth function $a(x)$, and a sequence $\{b_i\}$, we have

$$\begin{aligned} D^0(a_i b_i) &= b_i D^0(a_i) + \frac{1}{2}\left(a_{i+1}D^+ b_i + a_{i-1}D^- b_i\right) \\ &= b_i D^0(a_i) + \frac{1}{2}\left[\left(a_i + a_i'\Delta x + \frac{\Delta x^2}{2}a''\left(\xi_{i+1/2}\right)\right)D^+ b_i \right. \\ &\qquad \left. + \left(a_i - a_i'\Delta x + \frac{\Delta x^2}{2}a''\left(\xi_{i-1/2}\right)\right)D^- b_i\right] \\ &= a_i D^0 b_i + b_i D^0 a_i \quad \leftarrow \text{“Leibnitz part”} \\ &\quad + \underbrace{\frac{\Delta x^2}{2}a_i' D^+ D^- b_i + \frac{\Delta x^2}{4}\left(a''\left(\xi_{i+1/2}\right)D^+ b_i + a''\left(\xi_{i-1/2}\right)D^- b_i\right)}_{\text{“discrete correction”}}, \end{aligned}$$

where we use the notation $a_i = a(x_i)$, $a_i' = a'(x_i)$ and $\xi_{i\pm1/2}$ is between x_i and $x_{i\pm1}$.

We shall first apply D_x^0 to (2.2.27), D_y^0 to to (2.2.28) and add the results. The “Leibnitz” part of this will give the discrete equivalent of (2.2.26), with central differences replacing derivatives, and d replaced by

$$d_{i,j} = D_x^0 B_{i,j}^1 + D_y^0 B_{i,j}^2.$$

Concretely we get

$$\begin{aligned} \frac{d}{dt}d_{i,j} = &-u_{i,j}^1 D_x^0 d_{i,j} - u_{i,j}^2 D_y^0 d_{i,j} - \left(D_x^0 u_{i,j}^1 + D_y^0 u_{i,j}^2\right)d_{i,j} \\ &+ \text{discrete correction terms} + \text{terms from } D^+D^-. \end{aligned} \tag{2.2.29}$$

Next, we shall multiply this with $d_{i,j}$, and use the chain rule (2.1.13). In order to get a useful form of the numerical diffusion, we must convert (2.2.29) to upwind form. The formula for doing so reads

$$a_i D^0 b_i = a_i^+ D^- b_i + a_i^- D^+ b_i - \Delta x\,|a_i|\,D^+D^- b_i.$$

Consequently, the upwind form of the equation for the discrete divergence is

$$\begin{aligned} \frac{d}{dt}d_{i,j} = &-\left[u_{i,j}^1\right]^- D_x^+ d_{i,j} - \left[u_{i,j}^1\right]^+ D_x^- d_{i,j} - \left[u_{i,j}^2\right]^- D_y^+ d_{i,j} - \left[u_{i,j}^2\right]^+ D_y^- d_{i,j} \\ &- \left(D_x^0 u_{i,j}^1 + D_y^0 u_{i,j}^2\right)d_{i,j} + \underbrace{\Delta x\left|u_{i,j}^1\right| D_x^+ D_x^- d_{i,j} + \Delta y\left|u_{i,j}^2\right| D_y^+ D_y^- d_{i,j}}_{\text{“upwind diffusion”}} \\ &+ \text{discrete correction terms} + \text{terms from } D^+D^-. \end{aligned} \tag{2.2.30}$$

Now we multiply this with $2d_{i,j}$, and use the discrete chain rule (2.1.13) to get

$$\begin{aligned}\frac{d}{dt}d_{i,j}^2 = &-\left[u_{i,j}^1\right]^- D_x^+ d_{i,j}^2 - \left[u_{i,j}^1\right]^+ D_x^- d_{i,j}^2 - \left[u_{i,j}^2\right]^- D_y^+ d_{i,j}^2 - \left[u_{i,j}^2\right]^+ D_y^- d_{i,j}^2 \\ &- \left(D_x^0 u_{i,j}^1 + D_y^0 u_{i,j}^2\right) d_{i,j}^2 \\ &\left.\begin{aligned}&+\Delta x \left(\left[u_{i,j}^1\right]^- \left(D_x^+ d_{i,j}\right)^2 - \left[u_{i,j}^1\right]^+ \left(D_x^- d_{i,j}\right)^2\right) \\ &+\Delta y \left(\left[u_{i,j}^2\right]^- \left(D_y^+ d_{i,j}\right)^2 - \left[u_{i,j}^2\right]^+ \left(D_y^- d_{i,j}\right)^2\right)\end{aligned}\right\} \leftarrow \text{signed terms} \\ &+ 2d_{i,j}\left(\text{upwind diffusion} + \text{discrete correction} + \text{terms from } D^+D^-\right).\end{aligned} \tag{2.2.31}$$

The next step is summing the above equation over i and j, using partial summation and other tricks to bound the right hand side. The first four terms on the right hand side of (2.2.31) are bounded as follows

$$\begin{aligned}\left|\sum_{i,j}\left[u_{i,j}^1\right]^- D_x^+ d_{i,j}^2\right| &= \left|\sum_{i,j} D_x^-\left(\left[u_{i,j}^1\right]^-\right) d_{i,j}^2\right| \\ &\leq \left\|\partial_x u^1\right\|_{L^\infty(\mathbb{R}^2)} \sum_{i,j} d_{i,j}^2.\end{aligned}$$

The fifth term on the right side of (2.2.31) has the same type of bound. Therefore

$$\begin{aligned}\frac{d}{dt}d_{i,j}^2 \leq\ & 3\left(\left\|\partial_x u^1\right\|_{L^\infty(\mathbb{R}^2)} + \left\|\partial_y u^2\right\|_{L^\infty(\mathbb{R}^2)}\right)\sum_{i,j} d_{i,j}^2 \\ &+ \sum_{i,j}\text{signed terms} \\ &+ 2d_{i,j}\left(\text{upwind diffusion} + \text{discrete correction} + \text{terms from } D^+D^-\right).\end{aligned}$$

Next, let us tackle the "discrete correction" terms. These are terms coming from applying D^0 to the first order differences in (2.2.27) and (2.2.28). Furthermore, these are essentially of two types; a correction for D_x^0 applied to $u_{i,j}^1 D_x^0 B_{i,j}^1$, and a correction for D_x^0 applied to $\left(D_x^0 u_{i,j}^2\right) B_{i,j}^1$. Now the correction part of $D_x^0(u_{i,j}^1 D_x^0 B_{i,j}^1)$ equals

$$\frac{\Delta x^2}{2} u_{i,j}^{1,'} D_x^+ D_x^- D_x^0 B_{i,j}^1 + \frac{\Delta x^2}{4}\left(u_{i+1/2,j}^{1,''} D_x^+ D_x^0 B_{i,j}^1 + u_{i-1/2,j}^{1,''} D_x^- D_x^0 B_{i,j}^1\right). \tag{2.2.32}$$

We must multiply this by $2d_{i,j}$ and sum over i and j and bound the result. For the second term of this part of the correction we have

$$\begin{aligned}&\left|\frac{1}{4}\sum_{i,j} u_{i+1/2,j}^{1,''} 2d_{i,j}\Delta x^2 D_x^+ D_x^0 B_{i,j}^1\right| \\ &\quad\leq \frac{1}{2}\left\|\partial_x^2 u^1\right\|_{L^\infty(\mathbb{R}^2)} \sum_{i,j}|d_{i,j}|\,\frac{1}{2}\left(\left|B_{i+2,j}^1\right| + \left|B_{i+1,j}^1\right| + \left|B_{i,j}^1\right| + \left|B_{i-1,j}^1\right|\right) \\ &\quad\leq \frac{1}{2}\left\|\partial_x^2 u^1\right\|_{L^\infty(\mathbb{R}^2)}\left(\sum_{i,j} d_{i,j}^2 + \sum_{i,j}\left(B_{i,j}^1\right)^2\right)\end{aligned}$$

The sum coming from the third term in (2.2.32) has the same bound. To bound the sum coming from the first term in (2.2.32) we use summation by parts

$$\begin{aligned}
&\left|\frac{1}{2}\sum_{i,j} 2d_{i,j}u^{1,'}_{i,j}\Delta x^2 D_x^+ D_x^- D_x^0 B^1_{i,j}\right| \\
&\quad = \frac{1}{2}\left|\sum_{i,j} D_x^-\left(u^{1,'}_{i,j}d_{i,j}\right)\Delta x^2 D_x^- D_x^0 B^1_{i,j}\right| \\
&\quad = \frac{1}{2}\left|\sum_{i,j}\left(u^{1,'}_{i,j}D_x^- d_{i,j} + d_{i-1,j}D_x^- u^{1,'}_{i,j}\right)\Delta x^2 D_x^- D_x^0 B^1_{i,j}\right| \\
&\quad \leq \left\|\partial_x^2 u^1\right\|_{L^\infty(\mathbb{R}^2)}\sum_{i,j} d^2_{i,j} + \left(B^1_{i,j}\right)^2 \\
&\qquad + \frac{1}{2}\left\|\partial_x u^1\right\|_{L^\infty(\mathbb{R}^2)}\sum_{i,j}\frac{\Delta x}{4\varepsilon}\left(D_x^- B^1_{i,j}\right)^2 + \Delta x\varepsilon\left(D_x^- d_{i,j}\right)^2,
\end{aligned}$$

where ε is a positive number yet to be determined. The last term here looks threatening, but we shall look for countermeasures. Next the correction part of $D_x^0((D_x^0 u^2_{i,j})B^1_{i,j})$ is

$$\begin{aligned}
c_{i,j} := &\frac{\Delta x^2}{2}D_x^0\left(u^{2,'}_{i,j}\right)D_x^+ D_x^- B^1_{i,j} \\
&+ \frac{\Delta x^2}{4}\left(D_x^0\left(u^{2,''}_{i+1/2,j}\right)D_x^+ B^1_{i,j} + D_x^0\left(u^{2,''}_{i-1/2,j}\right)D_x^- B^1_{i,j}\right).
\end{aligned} \tag{2.2.33}$$

Now we can use Δx^2 to remove both discrete derivatives of $B^1_{i,j}$ in the first term, and one from $B^1_{i,j}$ and one from $u^{2,''}_{i,j}$ in the second term, and conclude that

$$\sum_{i,j} c_{i,j}2d_{i,j} \leq C\left\|\partial_x^2 u^2\right\|_{L^\infty(\mathbb{R}^2)}\sum_{i,j} d^2_{i,j} + \left(B^1_{i,j}\right)^2,$$

where C equals 8, and is in any case independent of Δx.

The rest of the discrete correction terms are similar to those we have bounded, and we end up with the bound

$$\begin{aligned}
&\sum_{i,j} 2d_{i,j}\,(\text{discrete correction}) \\
&\leq C\left(\left\|\partial_x^2 u^1\right\|_{L^\infty(\mathbb{R}^2)} + \left\|\partial_y^2 u^1\right\|_{L^\infty(\mathbb{R}^2)} + \left\|\partial_x^2 u^2\right\|_{L^\infty(\mathbb{R}^2)} + \left\|\partial_y^2 u^2\right\|_{L^\infty(\mathbb{R}^2)}\right) \\
&\qquad \times \sum_{i,j}\left(d^2_{i,j} + \mathbf{B}^2_{i,j}\right) \\
&\quad + C\left(\left\|\partial_x u^1\right\|_{L^\infty(\mathbb{R}^2)} + \left\|\partial_y u^1\right\|_{L^\infty(\mathbb{R}^2)} + \left\|\partial_x u^2\right\|_{L^\infty(\mathbb{R}^2)} + \left\|\partial_y u^2\right\|_{L^\infty(\mathbb{R}^2)}\right) \\
&\qquad \times \sum_{i,j}\frac{1}{\varepsilon}\left(\Delta x\left(D_x^- B^1_{i,j}\right)^2 + \Delta y\left(D_y^- B^2_{i,j}\right)^2\right) + \varepsilon\left(\Delta x\left(D_x^- d_{i,j}\right)^2 + \Delta y\left(D_y^- d_{i,j}\right)^2\right),
\end{aligned} \tag{2.2.34}$$

for some finite constant C which does not depend on Δx or Δy.

Now we bound the terms coming from the "upwind diffusion", here we must bound terms like

$$\begin{aligned}\sum_{i,j} 2d_{i,j}\Delta x \left|u^1_{i,j}\right| D^+_x D^-_x d_{i,j} &\leq -2\Delta x \sum_{i,j} D^-_x \left(\left|u^1_{i,j}\right| d_{i,j}\right) D^-_x d_{i,j} \\ &= -2\Delta x \sum_{i,j} \left|u^1_{i,j}\right| \left(D^-_x d_{i,j}\right)^2 - d_{i-1,j} D^-_x \left|u^1_{i,j}\right| D^-_x d_{i,j} \\ &\leq -2\Delta x \sum_{i,j} \left|u^1_{i,j}\right| \left(D^-_x d_{i,j}\right)^2 + 10 \left\|\partial_x u^1\right\|_{L^\infty(\mathbb{R}^2)} \sum_{i,j} d^2_{i,j}.\end{aligned}$$

Then we have that

$$\begin{aligned}&\sum_{i,j} 2d_{i,j} \,(\text{upwind diffusion}) \\ &\quad\leq -\sum_{i,j} \Delta x \left|u^1_{i,j}\right| \left(D^-_x d_{i,j}\right)^2 + \Delta y \left|u^2_{i,j}\right| \left(D^-_y d_{i,j}\right)^2 \\ &\qquad + 10 \left(\left\|\partial_x u^1\right\|_{L^\infty(\mathbb{R}^2)} + \left\|\partial_y u^2\right\|_{L^\infty(\mathbb{R}^2)}\right) \sum_{i,j} d^2_{i,j}.\end{aligned} \tag{2.2.35}$$

Then we turn to the "terms from D^+D^-". These are the result of applying D^0_x to the second order differences in (2.2.27), D^0_y to the second order differences in (2.2.28) and adding the results. We have that

$$\begin{aligned}&D^0_x \left(\frac{\Delta x}{2} \left|u^1_{i,j}\right|_\delta D^+_x D^-_x B^1_{i,j} + \frac{\Delta y}{2} \left|u^2_{i,j}\right|_\delta D^+_y D^-_y B^1_{i,j}\right) \\ &\quad= \frac{\Delta x}{2}\Bigg[\left|u^1_{i,j}\right|_\delta D^+_x D^-_x D^0_x \left(B^1_{i,j}\right) \\ &\qquad\quad + \frac{1}{2}\left(D^-_x D^+_x B^1_{i+1,j} D^+_x \left|u^1_{i,j}\right|_\delta + D^+_x D^-_x B^1_{i-1,j} D^-_x \left|u^1_{i,j}\right|_\delta\right)\Bigg] \\ &\qquad + \frac{\Delta y}{2}\Bigg[\left|u^2_{i,j}\right|_\delta D^+_y D^-_y D^0_x \left(B^1_{i,j}\right) \\ &\qquad\quad + \frac{1}{2}\left(D^-_y D^+_y B^1_{i+1,j} D^+_x \left|u^2_{i,j}\right|_\delta + D^+_y D^-_y B^1_{i-1,j} D^-_x \left|u^2_{i,j}\right|_\delta\right)\Bigg]\end{aligned}$$

and

$$\begin{aligned}&D^0_y \left(\frac{\Delta x}{2} \left|u^1_{i,j}\right|_\delta D^+_x D^-_x B^2_{i,j} + \frac{\Delta y}{2} \left|u^2_{i,j}\right|_\delta D^+_y D^-_y B^2_{i,j}\right) \\ &\quad= \frac{\Delta x}{2}\Bigg[\left|u^1_{i,j}\right|_\delta D^+_x D^-_x D^0_y \left(B^2_{i,j}\right) \\ &\qquad\quad + \frac{1}{2}\left(D^-_x D^+_x B^2_{i,j+1} D^+_y \left|u^1_{i,j}\right|_\delta + D^+_x D^-_x B^2_{i,j-1} D^-_y \left|u^1_{i,j}\right|_\delta\right)\Bigg] \\ &\qquad + \frac{\Delta y}{2}\Bigg[\left|u^2_{i,j}\right|_\delta D^+_y D^-_y D^0_y \left(B^2_{i,j}\right)\end{aligned}$$

$$+\frac{1}{2}\left(D_y^- D_y^+ B_{i,j+1}^2 D_y^+ \left|u_{i,j}^2\right|_\delta + D_y^+ D_y^- B_{i,j-1}^2 D_y^- \left|u_{i,j}^2\right|_\delta\right)\Bigg].$$

Adding these we get

$$\begin{aligned}\text{“terms from } D^+D^-\text{”} = \frac{\Delta x}{2}\left|u_{i,j}^1\right|_\delta D_x^+ D_x^- d_{i,j} + \frac{\Delta y}{2}\left|u_{i,j}^2\right|_\delta D_y^+ D_y^- d_{i,j} \\ + \text{second order corrections.}\end{aligned} \tag{2.2.36}$$

Multiplied by $2d_{i,j}$ and summed over i and j, a typical term from the “second order corrections” can be estimated as

$$\begin{aligned}&\sum_{i,j}\left(\Delta x D_x^+ D_x^- B_{i,j+1}^1 D_y^+ \left|u_{i,j}^1\right|_\delta\right) d_{i,j} \\ &\quad= -\sum_{i,j}\Delta x\left(D_x^- B_{i,j+1}^1\right) D_x^-\left(D_y^+\left|u_{i,j}^1\right|_\delta d_{i,j}\right) \\ &\quad= -\sum_{i,j}\Delta x\left(D_x^+ B_{i,j}^1\right)\left(\left(D_x^- D_y^+\left|u_{i,j}^1\right|_\delta\right) d_{i,j} + D_y^+\left|u_{i-1,j}^1\right|_\delta D_x^- d_{i,j}\right) \\ &\quad\le \left\|\partial_{xy}^2 u^1\right\|_{L^\infty(\mathbb{R}^2)}\sum_{i,j} 4\left(B_{i,j}^1\right)^2 + 2d_{i,j}^2 \\ &\qquad+ \left\|\partial_y u^1\right\|_{L^\infty(\mathbb{R}^2)}\sum_{i,j}\frac{\Delta x}{4\varepsilon}\left(D_x^+ B_{i,j}^1\right)^2 + \Delta x\varepsilon\left(D_x^- d_{i,j}\right)^2.\end{aligned}$$

Applying this to all the terms in the second order corrections, we get

$$\begin{aligned}&\sum_{i,j}(\text{second order corrections})\ 2d_{i,j} \\ &\quad\le 2\left(\left\|\partial_{xy}^2 u^1\right\|_{L^\infty(\mathbb{R}^2)} + \left\|\partial_{xx}^2 u^1\right\|_{L^\infty(\mathbb{R}^2)} + \left\|\partial_{xy}^2 u^2\right\|_{L^\infty(\mathbb{R}^2)} + \left\|\partial_{yy}^2 u^2\right\|_{L^\infty(\mathbb{R}^2)}\right) \\ &\qquad\times\sum_{i,j}\left(4\mathbf{B}_{i,j}^2 + 2d_{i,j}^2\right) \\ &\qquad+ 4\left(\left\|\partial_x u^1\right\|_{L^\infty(\mathbb{R}^2)} + \left\|\partial_y u^1\right\|_{L^\infty(\mathbb{R}^2)} + \left\|\partial_x u^2\right\|_{L^\infty(\mathbb{R}^2)} + \left\|\partial_y u^2\right\|_{L^\infty(\mathbb{R}^2)}\right) \\ &\qquad\times\sum_{i,j}\frac{1}{4\varepsilon}\left(\Delta x\left(D_x^- B_{i,j}^1\right)^2 + \Delta y\left(D_y^- B_{i,j}^2\right)^2\right) + \varepsilon\left(\Delta x\left(D_x^- d_{i,j}\right)^2 + \Delta y\left(D_y^- d_{i,j}\right)^2\right)\end{aligned} \tag{2.2.37}$$

Now the first terms on the right of (2.2.36) will save the day. When multiplied by $2d_{i,j}$, the first of these yields

$$\begin{aligned}\sum_{i,j}\Delta x\, d_{i,j}\left|u_{i,j}^1\right|_\delta D_x^+ D_x^- d_{i,j} &= -\sum_{i,j}\Delta x D_x^-\left(d_{i,j}\left|u_{i,j}^1\right|_\delta\right) D_x^- d_{i,j} \\ &= -\sum_{i,j}\Delta x\left|u_{i,j}^1\right|_\delta\left(D_x^- d_{i,j}\right)^2 + \Delta x d_{i-1,j} D_x^-\left|u_{i,j}^1\right|_\delta D_x^- d_{i,j} \\ &\le -\sum_{i,j}\Delta x\left|u_{i,j}^1\right|_\delta\left(D_x^- d_{i,j}\right)^2 + 5\left\|\partial_x u^1\right\|_{L^\infty(\mathbb{R}^2)}\sum_{i,j} d_{i,j}^2.\end{aligned}$$

Similarly we have that

$$\sum_{i,j} \Delta y\, d_{i,j} \left|u^2_{i,j}\right|_\delta D^+_y D^-_y d_{i,j} \le -\sum_{i,j} \Delta x \left|u^2_{i,j}\right|_\delta \left(D^-_y d_{i,j}\right)^2 + 4\left\|\partial_y u^2\right\| \sum_{i,j} d^2_{i,j}.$$

Collecting all our bounds, we find that there are finite constants C_ℓ, $\ell = 1, \ldots, 4$, depending only on u^1, u^2 and their first and second derivatives, such that

$$\begin{aligned}\frac{d}{dt}\sum_{i,j} d^2_{i,j} \le C_1 \sum_{i,j} d^2_{i,j} + C_2 \sum_{i,j} \mathbf{B}^2_{i,j} + C_3 \frac{1}{\varepsilon} \sum_{i,j} \Delta x \left(D^-_x B^1_{i,j}\right)^2 + \Delta y \left(D^-_y B^2_{i,j}\right)^2 \\ + \left(C_4\varepsilon - \frac{\delta}{2}\right) \sum_{i,j} \left(\Delta x \left(D^-_x d_{i,j}\right)^2 + \Delta y \left(D^-_y d_{i,j}\right)^2\right).\end{aligned}$$

Remembering that δ is a fixed positive number, we now choose ε positive, but so small that $(C_4\varepsilon - \delta/2) \le 0$. Next use the estimates (2.2.16) and (2.2.14), multiply by $\Delta x \Delta y$ and integrate over the interval $(0, t)$ to get the divergence bound:

Lemma 2.2.3. *Assume that* $\mathbf{u} \in C^2(\mathbb{R}^2)$. *Let* $\{\mathbf{B}_{i,j}(t)\}$ *be defined by* (2.2.7) *and define the discrete divergence*

$$d^n_{i,j}(t) = D^0_x\left(B^1_{i,j}(t)\right) + D^0_y\left(B^2_{i,j}(t)\right).$$

Then

$$\Delta x \Delta y \sum_{i,j} \left(d_{i,j}(t)\right)^2 \le e^{Ct}\left(\Delta x \Delta y \sum_{i,j} |d_{i,j}(0)|^2 + \Delta x \Delta y \sum_{i,j} |\mathbf{B}_{i,j}(0)|^2\right) \tag{2.2.38}$$

for some finite constant C *depending only on* δ *and on* $\mathbf{u}$ *and its derivatives up to second order.*

Remark 2.2.2. *If* the limit of the scheme; $\mathbf{B}$, has bounded first and second derivatives, *and* the approximate solution $\mathbf{B}^{\Delta x}$ has uniformly (in Δx and Δy) bounded first and second differences, then the terms hidden behind "discrete correction terms" and "terms from D^+D^-" in (2.2.29) will be $\mathcal{O}(\Delta x) + \mathcal{O}(\Delta y)$. Hence if $\operatorname{div}(\mathbf{B}(x, y, 0)) = 0$, also $\operatorname{div}(\mathbf{B}(x, y, t)) = 0$ for $t > 0$. Furthermore,

$$\operatorname{div}^0(\mathbf{B}^{\Delta x}(x, y, t)) = \mathcal{O}(\Delta x) + \mathcal{O}(\Delta y).$$

2.3 Numerical examples

In this section, we test the stable upwind scheme (SUS) (2.2.8) and compare it with other schemes. We present test cases where we compare the performance of SUS with the standard upwind scheme (2.1.19), and with the scheme of Torrilhon and Fey (2.1.20), which we henceforth refer to as the TF scheme.

2.3.1 Example 1

The first example uses

$$\mathbf{u} = (1, 2), \quad \text{and} \quad B_0^1(x, y) = B_0^2(x, y) = \begin{cases} 2 & \text{if } x > y, \\ 0 & \text{otherwise.} \end{cases} \tag{2.3.1}$$

Since $\mathbf{u}$ is constant, the exact solution is

$$\mathbf{B}(x, y, t) = \mathbf{B}_0(x - t, y - 2t).$$

As a computational domain we use $(x, y) \in [-0.5, 0.5]^2$ and Neumann boundary conditions. All schemes we tested used a CFL-number of $1/2$. In Figure 2.3.1 we show how some schemes compute the approximation at $t = 0.3$, with $\Delta x = \Delta y = 0.01$. We see

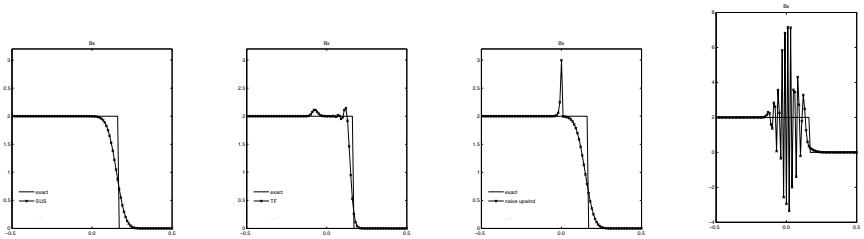

Figure 2.3.1: Approximations of $B^1(x, 0, 0.3)$, initial data given by (2.3.1).From left to right: SUS, TF, standard upwind, central Powell.

that the TF scheme seems to be more accurate than the SUS scheme, at the expense of some oscillations as the solutions generated with the TF scheme are not TVD even in this simple case of constant velocity fields. The standard upwind scheme, (2.1.19), gives a solution similar to SUS, but with one pronounced spike. The scheme called "central Powell" is the result of central evaluation of the Powell source term, and is seen to be unstable. This example shows that the Godunov-Powell source term has to be introduced as well as upwinded in some manner in order to get stable results. The SUS scheme relies on an implicit upwinding due to the use of the Friedrichs form.

2.3.2 Example 2

The goal of this example is to investigate how the discrete divergence introduced by the SUS scheme varies with Δt, as well as to compare the SUS scheme with the TF scheme.

In order to do this we choose divergence free initial data given by

$$B_0^1(x, y) = \partial_y A(x, y), \; B_0^2(x, y) = -\partial_x A(x, y), \; \text{where } A = \frac{1}{2\pi} \sin(2\pi x) \sin(2\pi y) + y - x,$$

and

$$\mathbf{u} = (1, 1) + 0.25(\cos(2\pi x) + 2\sin(2\pi y), \sin(2\pi x) + 2\cos(2\pi y)).$$

To compute approximations we use periodic boundary conditions in the domain $(x, y) \in [-0.5, 0.5]^2$ and $t \in [0, 0.5]$. Although in violation of the CFL-condition (2.2.12), both the SUS and the TF scheme use the CFL-number 1/2. Figure 2.3.2 shows how the discrete divergence(s) for both schemes vary with Δx. We have not shown div^* for the TF scheme, since this remains *very* small throughout the computation. We have used $\Delta x = \Delta y = 2^{-6}, 2^{-7}, \ldots, 2^{-11}$. From Figure 2.3.2 we see that both div^0 and div^* seem

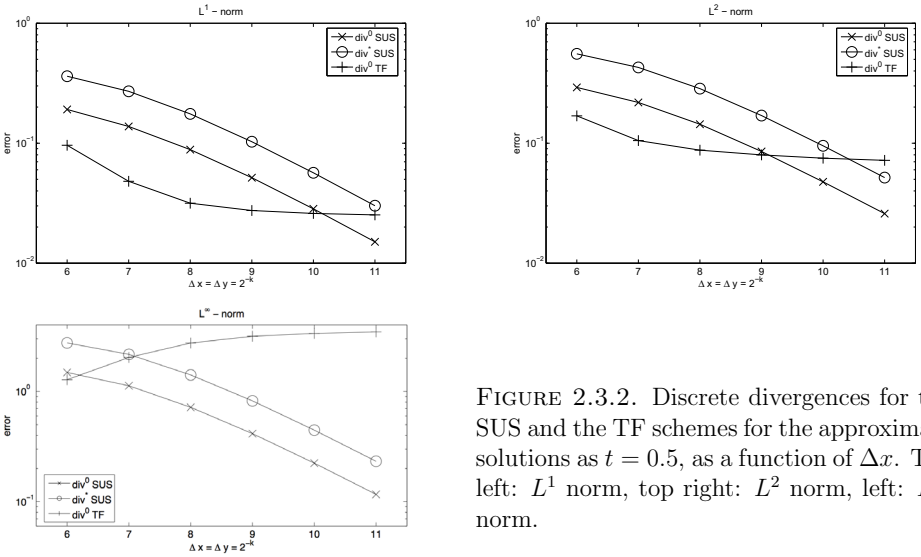

FIGURE 2.3.2. Discrete divergences for the SUS and the TF schemes for the approximate solutions as $t = 0.5$, as a function of Δx. Top left: L^1 norm, top right: L^2 norm, left: L^∞ norm.

to converge to zero for the SUS scheme at the expected first order accuracy, but div^0 does *not* seem to converge to zero for the TF scheme, although this scheme preserves div^* to machine precision. This example indicates that although a scheme preserves some discrete divergence, other discrete divergences need not be small.

Since the SUS-scheme proposed here is not conservative, it is interesting to see how much of $\mathbf{B}$ is lost. We have measured the relative conservation error defined as

$$100 \times \sum_{i=1}^{2} \frac{|\iint B^{i,\Delta t}(x, y, t) - B^{i,\Delta t}(x, y, 0)\, dxdy|}{|\iint B^{i,\Delta t}(x, y, 0)\, dxdy|}$$

	$\Delta x = 2^{-6}$	$\Delta x = 2^{-7}$	$\Delta x = 2^{-8}$	$\Delta x = 2^{-9}$	$\Delta x = 2^{-10}$	$\Delta x = 2^{-11}$
SUS	1.4577	0.7774	0.4019	0.2044	0.1031	0.0518

Table 2.3.1: Relative conservation errors for the SUS scheme.

From table 2.3.1, it is clear that although some mass is lost due to the fact that SUS scheme is not conservative, the errors are quite small and converge to zero as the mesh is refined at the expected first order of accuracy.

2.3.3 Example 3

If $\mathbf{u}(x,y) = (-y,x)$, i.e., a rotation around the origin, the solution to (2.1.3) in two space dimensions is given by

$$\mathbf{B}(\mathbf{x},t) = R(t)\mathbf{B}_0(R(-t)\mathbf{x}),$$

where $R(t)$ is a rotation matrix for a rotation with angle t. This means that $\mathbf{B}(\mathbf{x},2\pi) = \mathbf{B}_0(\mathbf{x})$, which makes comparisons between approximations and the exact solution easy. We have taken the initial data from [77],

$$\mathbf{B}_0(x,y) = 4\begin{pmatrix} -y \\ x-\frac{1}{2}\end{pmatrix} e^{-20\left((x-1/2)^2+y^2\right)}. \tag{2.3.2}$$

Note that $\operatorname{div}(\mathbf{B}_0) = 0$. We have used the computational domain $(x,y) \in \Omega = [-1,1]^2$ and Neumann boundary conditions, and compared the SUS and the TF schemes. In table 2.3.2 we show the relative L^2 errors produced by the schemes, for $\Delta x = \Delta y = 2^{-5},\ldots,2^{-10}$, where both schemes used the CFL-number 1/2. The relative error is defined as

$$e = 100 \times \frac{\left\|\mathbf{B}^{\Delta t}(\cdot,2\pi) - \mathbf{B}^{\Delta t}(\cdot,0)\right\|_{L^2(\Omega)}}{\|\mathbf{B}^{\Delta t}(\cdot,0)\|_{L^2(\Omega)}}.$$

Although we observed that the two schemes produced solutions which were different in

	$\Delta x = 2^{-5}$	$\Delta x = 2^{-6}$	$\Delta x = 2^{-7}$	$\Delta x = 2^{-8}$	$\Delta x = 2^{-9}$	$\Delta x = 2^{-10}$
SUS	79	61	42	26	15	8
TF	67	52	36	23	13	7

Table 2.3.2: Relative errors for the SUS and TF schemes with initial data given by (2.3.2).

some details, both schemes have comparable L^2 errors. Also the numerical convergence rate of both schemes is slightly less than one. Therefore, for a scheme to work reasonably well, it does not seem crucial that it preserves some discrete divergence.

2.3.4 Example 4

The analysis presented in this paper can easily be extended to a time dependent velocity filed $\mathbf{u} = \mathbf{u}(\mathbf{x},t)$. Therefore we present an example with a time dependent velocity field. This velocity field originates from a simulation of the well-known test case for magnetohydrodynamics called the "Orszag-Tang vortex", and is given as a table[1] $\mathbf{u}^n_{i,j}$.

We have used the computational domain $(x,y) \in [0,2\pi]^2$ with periodic boundary conditions, and $t \in [0,\pi]$. The initial magnetic field is

$$\mathbf{B}_0(x,y) = \begin{pmatrix} -\sin(y) \\ \sin(2x)\end{pmatrix}.$$

In this example, Δt is not constant, and the time steps are given in the table. Although $\mathbf{u}$ is initially smooth, it develops shocks after some time steps. The test used $\Delta x =$

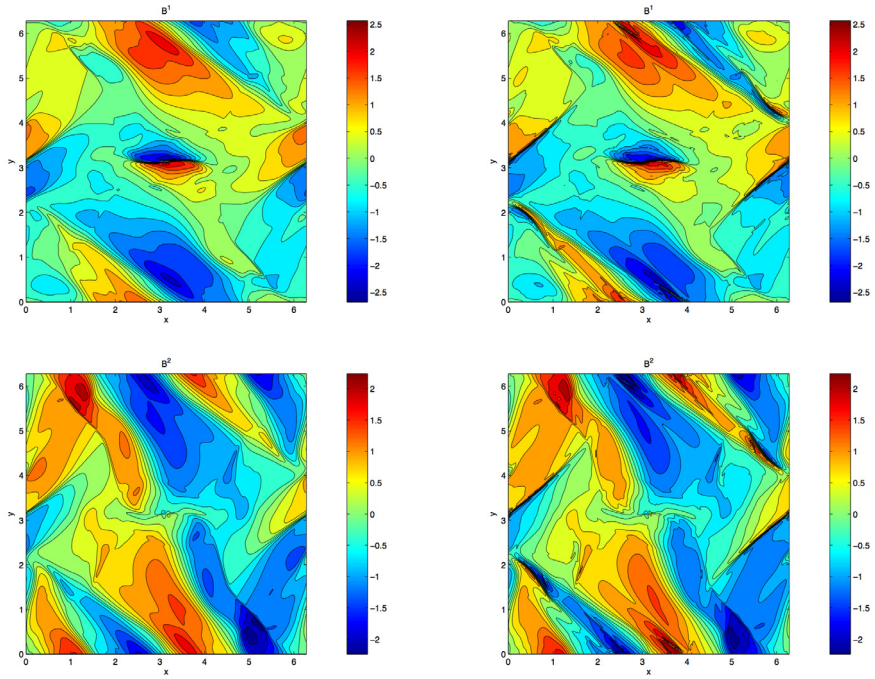

Figure 2.3.2: The approximations at $t = \pi$, left column: SUS, right column: TF.

$\Delta y = 2\pi/300$. Figure 2.3.2 shows the approximations generated by the SUS and the TF schemes for this example. The solution is complicated, with many features, but we see that the schemes produce similar results. In Figure 2.3.3 we illustrate this by plotting the approximation to B^1 along the lines $y = (122/300) \times 2\pi$ and $y = (293/300) \times 2\pi$. From this figure, we see that the TF scheme resolve discontinuities better, but since it is less stable, some of the "spikes" are numerical artifacts and reflect the lack of TVD property in the TF scheme. We should emphasize that even though our analysis requires that the velocity field u is sufficiently smooth, we have found that the SUS scheme works very well even for non-smooth velocity fields.

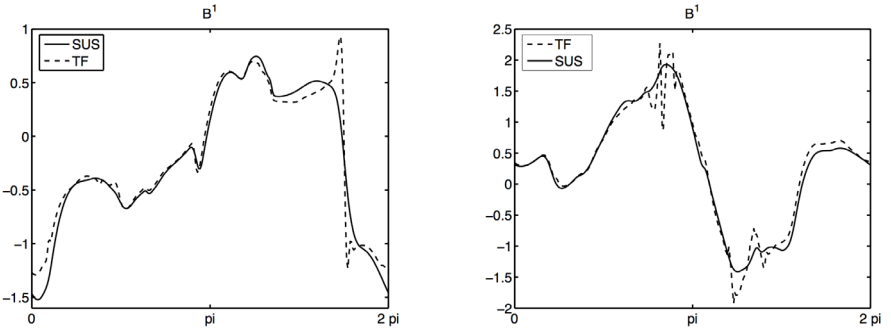

Figure 2.3.3: Left: $B^1(x, 2.54, \pi)$, right: $B^1(x, 6.13, \pi)$.

2.4 Conclusions

Based on these numerical experiments, we conclude that the stable upwind scheme (2.2.8) proposed in this paper is robust, efficient and reasonably accurate compared with other first order schemes.

Regarding divergence preservation, the divergence errors generated by the scheme are small and converge to zero with Δt. Furthermore, two different discrete forms of the divergence are of the same magnitude. On the other hand, even though the scheme of Torrilhon and Fey (2.1.20) preserves one form of discrete divergence, it does not preserve other discrete divergences. Therefore, we think that if a numerical scheme for (2.1.1) is stable, exact divergence preservation is not necessary to obtain good results.

We also remark that it is straightforward to extend our result to three space dimensions, i.e., $\mathbf{B} = (B^1, B^2, B^3)(x, y, z)$, by upwinding the Godunov-Powell source term. We plan to extend the ideas presented here both to unstructured meshes and higher orders in a forthcoming paper.

[1]This table can be downloaded from `http://folk.uio.no/~franzf/OT300x300.tar.gz`

3

Splitting based finite volume schemes for ideal MHD equations

F. G. Fuchs, S. Mishra, N.H. Risebro
Journal of Computational Physics, Volume 228, Issue 3 (February 2009), Pages 641-660

Keywords: Conservation laws, Induction equation, Divergence constraint, Upwinded Source terms, MHD

Abstract

We design finite volume schemes for the equations of ideal magnetohydrodynamics (MHD) and based on splitting these equations into a fluid part and a magnetic induction part. The fluid part leads to an extended Euler system with magnetic forces as source terms. This set of equations are approximated by suitable two and three wave HLL solvers. The magnetic part is modeled by the magnetic induction equations which are approximated using stable upwind schemes devised in a recent paper [31]. These two sets of schemes can be combined either component by component, or by using an operator splitting procedure to obtain a finite volume scheme for the MHD equations. The resulting schemes are simple to design and implement. These schemes are compared with existing HLL type and Roe type schemes for MHD equations in a series of numerical experiments. These tests reveal that the proposed schemes are robust and have a greater numerical resolution than HLL type solvers, particularly in several space dimensions. In fact, the numerical resolution is comparable to that of the Roe scheme on most test problems with the computational cost being at the level of a HLL type solver. Furthermore, the schemes are remarkably stable even at very fine mesh resolutions and handle the divergence constraint efficiently with low divergence errors.

3.1 Introduction

Many interesting problems in astrophysics, solar physics, electrical engineering and aerospace engineering are based on modeling the evolution of plasmas. Most models involve the

equations of magneto-hydro dynamics (MHD) which read

$$\begin{aligned} \rho_t + \mathrm{div}(\rho \mathbf{u}) &= 0, \\ (\rho \mathbf{u})_t + \mathrm{div}\left(\rho \mathbf{u} \otimes \mathbf{u} + \left(p + \frac{1}{2}\mathbf{B}^2\right)\mathcal{I} - \mathbf{B} \otimes \mathbf{B}\right) &= 0, \\ E_t + \mathrm{div}\left(\left(E + p + \frac{1}{2}\mathbf{B}^2\right)\mathbf{u} - (\mathbf{u}\cdot\mathbf{B})\,\mathbf{B}\right) &= 0, \\ \mathbf{B}_t + \mathrm{div}\left(\mathbf{u} \otimes \mathbf{B} - \mathbf{B} \otimes \mathbf{u}\right) &= 0, \\ \mathrm{div}\mathbf{B} &= 0, \end{aligned} \tag{3.1.1}$$

where ρ denotes the density, $\mathbf{u} = \{u^1, u^2, u^3\}$ and $\mathbf{B} = \{B^1, B^2, B^3\}$ denote the velocity and the magnetic fields respectively, p the pressure and E the total energy of the plasma. The variables are related by the following ideal gas equation of state

$$E = \frac{p}{\gamma - 1} + \frac{1}{2}\rho|\mathbf{u}|^2 + \frac{1}{2}\left|\mathbf{B}\right|^2, \tag{3.1.2}$$

with γ being the gas constant. The above system is a system of conservation laws (with a constraint) in three dimensions on the following form

$$\begin{aligned} V_t + f(V)_x + g(V)_y + h(V)_z &= 0, \\ \mathrm{div}\mathbf{B} &= 0, \end{aligned}$$

with $V = (\rho, \rho u^1, \rho u^2, \rho u^3, E, B^1, B^2, B^3)$ being the vector of conserved variables and f, g and h are the directional fluxes in the x, y and z directions respectively. The constraint that the divergence field should be solenoidal is a consequence of the fact that magnetic monopoles have not been observed in nature. A complete derivation of the MHD equations along with a description of the hypotheses on its validity is presented in [66]. We summarize the basic steps in the derivation below,

3.1.1 Derivation of the model:

We non-dimensionalize all the quantities following [66] and choose units suitably so that the permeability of the medium is set to 1. Then the equations (3.1.1) are derived from the following set of physical laws,

Conservation of mass:

The conservation of mass takes the following differential form (mass conservation for plasmas being the same as that of fluids),

$$\rho_t + \mathrm{div}(\rho \mathbf{u}) = 0. \tag{3.1.3}$$

Faraday's law:

By using Maxwell's equations, the Stokes theorem and the fact that the electric field in a co-moving frame is zero, Faraday's law for the magnetic flux across a surface $\mathbf{S}$ bounded by a curve $\delta\mathbf{S}$ is given by

$$-\frac{d}{dt}\int_S \mathbf{B}\cdot\mathbf{dS} = \int_{\delta S} E\cdot dl$$

becomes

$$\mathbf{B}_t + \mathrm{div}(\mathbf{u}\otimes\mathbf{B} - \mathbf{B}\otimes\mathbf{u}) = -\mathbf{u}(\mathrm{div}\mathbf{B}). \tag{3.1.4}$$

The right hand side is proportional to div$\mathbf{B}$ and is often omitted due to the divergence constraint. Equation (3.1.4) is referred to as the magnetic induction equation and can be considered as the special form of Maxwell equations governing the evolution of magnetic fields due to the action of a given velocity field $\mathbf{u}$.

Conservation of momentum:

In differential form, the conservation of momentum for a plasma is given by,

$$(\rho\mathbf{u})_t + \mathrm{div}(\rho\mathbf{u}\otimes\mathbf{u} + p\mathcal{I}) = \mathbf{J}\times\mathbf{B}, \tag{3.1.5}$$

where $\mathbf{J}$ denotes the current density and $\mathcal{I}$ the 3×3 identity matrix. The above equation results from the fact that the momentum of the plasma changes due to the pressure and action of the Lorentz force $\mathbf{J}\times\mathbf{B}$ exerted by the magnetic field. Under the assumptions of ideal MHD, Ampere's law expresses the current density as

$$\mathbf{J} = \mathrm{curl}(\mathbf{B}). \tag{3.1.6}$$

Use of standard vector identities results in the following "semi-conservative" form,

$$(\rho\mathbf{u})_t + \mathrm{div}\left(\rho\mathbf{u}\otimes\mathbf{u} + (p+\frac{1}{2}\mathbf{B}^2)\mathcal{I} - \mathbf{B}\otimes\mathbf{B}\right) = -\mathbf{B}(\mathrm{div}\mathbf{B}). \tag{3.1.7}$$

Due to the divergence constraint, one usually neglects the right hand side of the above equation to get the momentum conservation in (3.1.1).

Conservation of energy:

Defining the hydrodynamic energy of an ideal gas as

$$E^{\mathrm{hd}} = \frac{p}{\gamma-1} + \frac{1}{2}\rho\mathbf{u}^2,$$

and using the conservation of this energy results in

$$E^{\mathrm{hd}}_t + \mathrm{div}((E^{\mathrm{hd}}+p)\mathbf{u}) = \mathbf{J}\cdot(\mathbf{B}\times\mathbf{u}). \tag{3.1.8}$$

The right hand side represents the change in energy due to the magnetic field. Using standard vector identities and Ampere's law, we obtain

$$\mathbf{J}\cdot(\mathbf{B}\times\mathbf{u}) = (\mathbf{B}\cdot\frac{\partial\mathbf{B}}{\partial t} - (\mathbf{u}\cdot\mathbf{B})(\mathrm{div}\mathbf{B}) - \mathrm{div}(\mathbf{B}\cdot\mathbf{B})\mathbf{u} - (\mathbf{u}\cdot\mathbf{B})\mathbf{B}).$$

Defining the total energy of the plasma as $E = E^{\text{hd}} + \frac{1}{2}\mathbf{B}^2$, energy conservation takes the form

$$E_t + \text{div}((E + p + \frac{1}{2}\mathbf{B}^2)\mathbf{u} - (\mathbf{u}\cdot\mathbf{B})\mathbf{B}) = -(\mathbf{u}\cdot\mathbf{B})(\text{div}\mathbf{B}). \tag{3.1.9}$$

Using the divergence constraint results in the energy equation in (3.1.1). Combining all the above we get

$$\begin{aligned}
\rho_t + \text{div}(\rho\mathbf{u}) &= 0,\\
(\rho\mathbf{u})_t + \text{div}(\rho\mathbf{u}\otimes\mathbf{u} + (p + \frac{1}{2}|\mathbf{B}|^2)I - \mathbf{B}\otimes\mathbf{B}) &= -c_1\mathbf{B}(\text{div}\mathbf{B}),\\
E_t + \text{div}((E + p + \frac{1}{2}|\mathbf{B}|^2)\mathbf{u} - (\mathbf{u}\cdot\mathbf{B})\mathbf{B}) &= -c_1(\mathbf{u}\cdot\mathbf{B})(\text{div}\mathbf{B}),\\
\mathbf{B}_t + \text{div}(\mathbf{u}\otimes\mathbf{B} - \mathbf{B}\otimes\mathbf{u}) &= -c_2\mathbf{u}(\text{div}\mathbf{B}),
\end{aligned} \tag{3.1.10}$$

with constants $c_1 = c_2 = 1$. Note that this form of the equations is symmetrizable by the results of [35]. An explicit inclusion of the divergence constraint means taking $c_1 = c_2 = 0$, and this is the standard form of the MHD equations (3.1.1).

We remark that MHD equations can be thought of as a combination of fluid dynamics coupled with magnetic fields. In fact, the "physical" form of these equations are a combination of the fluid equations (3.1.3), (3.1.5) and (3.1.8) (with magnetic forces acting on them) and the magnetic induction equation (3.1.4). Collecting these equations, we can obtain the "physical" form

$$\begin{aligned}
\rho_t + \text{div}(\rho\mathbf{u}) &= 0,\\
(\rho\mathbf{u})_t + \text{div}(\rho\mathbf{u}\times\mathbf{u} + p\mathcal{I}) &= \mathbf{J}\times\mathbf{B},\\
E^{\text{hd}}_t + \text{div}((E^{\text{hd}} + p)\mathbf{u}) &= \mathbf{J}\cdot(\mathbf{B}\times\mathbf{u}),\\
\mathbf{B}_t + \text{div}(\mathbf{u}\otimes\mathbf{B} - \mathbf{B}\otimes\mathbf{u}) &= -\mathbf{u}(\text{div}\mathbf{B}).
\end{aligned} \tag{3.1.11}$$

This system is non-conservative. We will use this "physical" splitting of the equation into the fluid part and a magnetic part in order to design efficient finite volume schemes for (3.1.1).

As remarked earlier, the MHD equations are a system of conservation laws in three dimensions. A calculation of eigenvalues of the Jacobians (see [68] for details) shows that the equations are hyperbolic but not strictly hyperbolic. In particular, the fast, slow and Alfven waves coincide at the triple point, and this can lead to considerable difficulties in the analysis of the model. Furthermore, a naive scaling of eigenvectors leads to singularities, and the eigenvectors must be properly scaled. Well-defined eigensystems for MHD equations have been proposed in [68] and [12]. Nonlinearities in the equations result in formation of discontinuities such as shock waves and contact discontinuities. The complex structure of the equations leads to intermediate shocks and compound shocks which are difficult to analyze and simulate. A detailed description of the analytical and numerical difficulties concerning MHD equations can be found in [70].

In the absence of analytical results, the main approach in dealing with these equations has to been to devise efficient numerical schemes to approximate their solutions. For a long time finite volume methods have been the preferred means to solve conservation laws

numerically. These methods are based on approximating the integral form of the conservation law inside each cell or control volume. Numerical fluxes at each cell interface are based on either exact or approximate Riemann solvers. Higher order accuracy in space is obtained by using non-oscillatory ENO/WENO type piecewise polynomial functions. Time integration is performed by using high order stability preserving Runge-Kutta methods. A detailed account of finite volume schemes for conservation laws can be found in [50].

The crucial ingredient in the design and performance of any finite volume method is a suitable choice of the numerical flux function at cell interfaces. Usually, numerical fluxes are built either from exact or approximate solutions to Riemann problems at each cell interface. Exact solutions (even to Riemann problems) for the MHD equations are very complicated (and largely unavailable), and are therefore seldom used in numerical methods. Hence, approximate Riemann solvers for the MHD equations are widely used. These solvers are either of the Roe (linearized) or the HLL (non-linear) types. Roe solvers based on either a simple average of the Jacobians across each interface or the Roe average, see [67], can be used as approximate Riemann solvers. A Roe-average for the ideal MHD equations was developed in [24]. A special form of the Roe solver based on entropy variables, proposed and tested in [12], will be used in some numerical experiments in this paper.

The main problem with Roe solvers is that they can result in negative pressures and densities. Another issue is the high computational cost of these solvers. As a consequence, an attractive alternative has been to use HLL solvers, see [50]. These non-linear solvers are based on approximating the wave structure of the full Riemann problem by a simplified wave structure. The one dimensional form of the MHD equations result in seven waves for each Riemann problem. HLL solvers approximate the solution by fewer waves. The two-wave solvers based on wave speeds suggested in [28] are the simplest to implement. They are provably positive (in the sense that the pressure and density in the solution are positive) and entropy stable, but are too dissipative in most test problems. Three-wave HLL solvers based on heuristic considerations have been developed in [53] and [36]. The solver of [36] is also provably positive. A positivity preserving five wave solver for MHD was developed in [59]. Recently, three-, five- and seven-wave approximate Riemann solvers have been designed in [20]. These solvers are proved to be positive. A thorough comparison of different HLL solvers has been reported in [58, 73].

There is no clear choice for an ideal HLL solver. Some of the solvers are too dissipative but guarantee positive pressures and densities. Some are complicated to design and implement and can be costly in terms of computational resources, particularly in several space dimensions. The computational results indicate that the three-wave solver of [53] appears to be the least dissipative among HLL three-wave solvers, whereas the solvers of [36] and [20] are provably positivity preserving. However, none of the HLL three-wave solvers have the resolution of the Roe solver. Given the above factors, there is considerable scope for designing a simple HLL type two or three wave solver for the MHD equations which are less dissipative and hence, have more resolution than the available HLL two or three wave solvers and a resolution comparable to the Roe solver. Our main aim in this paper is to design such a HLL type solver. We would also like to point out that recent papers [58, 73] have extensively compared different HLL solvers and concluded that the

five wave solver designed in [59] is very robust and has a resolution comparable to the Roe solver.

A key issue in the design of numerical schemes for the MHD equations in several space dimensions is how to handle the divergence constraint. A standard numerical scheme is not going to satisfy a discrete version of the divergence constraint exactly, and even for smooth solutions will give divergence errors controlled by the truncation error. When the solution contains shocks, the discretization can lead to large divergence errors which may result in negative densities and pressures. There has been wide interest in designing numerical schemes which enforce, or control the divergence constraint. Popular methods include using projection onto divergence free fields, see [22], this involves solving an elliptic equation at each time step. Another popular choice is to stagger the grids or design updates which preserve some discrete divergence. An incomplete list of references dealing with this approach includes [30, 26, 11, 70, 71, 77] and references therein.

Another simple method to deal with the divergence constraint was proposed by Powell in [65]. This involves using the symmetrizable version of MHD equations (3.1.10) derived earlier this section with $c_1 = c_2 = 1$. Taking divergence of the magnetic field in (3.1.10) results in

$$(\mathrm{div}\mathbf{B})_t + \mathrm{div}(\mathbf{u}(\mathrm{div}\mathbf{B})) = 0. \tag{3.1.12}$$

Hence, any non-zero divergence introduced by a numerical discretization should be swept away from the domain by the velocity field by this approach, provided that the boundaries are absorbing. A detailed comparison of different methods for divergence cleaning is reported in [80].

The HLL or Roe solvers mentioned earlier, are not designed to handle the divergence constraint. In fact, most of them are based on a locally one dimensional form of the MHD equations which presupposes that the normal component of the magnetic field across an interface is constant. Although this assumption is valid in one dimension, one has to use some ad hoc procedure to extend the HLL solvers to multiple space dimensions. It would be desirable to design a solver that also handles the divergence constraint and can be extended to several space dimensions in a natural way. Another aim of this paper is to design a solver that addresses the divergence constraint.

The approximate Riemann solvers that we design in this paper are based on the "physical form" (3.1.11) of the MHD equations. This form suggests a natural splitting of the equations into a fluid and a magnetic part. The fluid part is the Euler equations of hydrodynamics along with Lorentz forces exerted on the fluid due to the magnetic field (3.1.5). Hence, we can use approximate Riemann solvers of the HLL type for the Euler equations, these are well known in the literature, see [76] for details. We will use both a standard HLL two-wave solver as well as a HLLC three-wave solver for the Euler equation part of (3.1.11). It is not enough to treat the hydrodynamic part only. The right hand side of the fluid equations in (3.1.11) involves magnetic forcing terms and these terms have to discretized suitably. Since the forcing terms involve derivatives, we must upwind these derivatives. Furthermore, we need to enforce conservation of the variables. In order to do so, we will work with the first three equations of (3.1.1) (the conservative form) and treat the magnetic field as a coefficient in this extended Euler system and devise suitable HLL two wave and three wave solvers for this extended system.

The magnetic field is evolved by the magnetic induction equation (3.1.4). This is a linear system and has been studied extensively, see [16, 77] and references therein. Despite being a linear system, (3.1.4) is not easy to deal with numerically. In a recent paper [31], we pointed out some of the difficulties involved in numerically approximating (3.1.4). We also developed a class of upwind schemes based on the form (3.1.4) without explicitly enforcing the divergence constraint and showed that the scheme converges and that the discrete divergence is bounded in L^2. In this paper we use the upwind schemes from [31] to approximate the magnetic part of (3.1.11).

We can also use the simple Lax-Friedrichs scheme to approximate (3.1.4). This scheme is very dissipative, but preserves a discrete version of the divergence constraint. Another class of schemes that can be used are the divergence preserving upwind schemes of [77]. When we implemented this scheme, we found that the resulting scheme for (3.1.1) was oscillatory.

Thus we emphasize that the main idea behind the schemes presented in this paper is to "split" the MHD equations into a fluid part and a magnetic part, and to use tailor made schemes for each part to devise a scheme for the full system. The choice of schemes for both the Euler part as well as the magnetic part, and the method to patch them together have to made judiciously in order to obtain a robust scheme for the MHD equations. The numerical resolution of these schemes is higher (in some cases, considerably higher) than that of HLL solvers and is comparable to the Roe solver. Furthermore, the splitting based schemes turn out to be remarkably stable at fine mesh resolutions. It is well known that computing at fine mesh resolutions results in lower numerical difffusions leading to instabilities. These instabilities can cause the pressure and density to be negative and the scheme crashes consequently. Most standard solvers for the MHD equations exhibit this behaviour. On the other hand, the splitting based schemes are quite stable and do not crash even for fine mesh resolutions. However, these schemes might still exhibit instabilites like the carbuncle phenomena which effect even very robust finite volume solvers for the Euler equations as well as MHD equations. Based on their stability as well as good resolution, simplicity of design and low computational cost, we believe that these schemes can be used as an alternative to both Roe solvers as well as HLL solvers in practical codes and do not require any extra divergence cleaning.

The rest of the paper is organized as follows:-In Section 3.2, we present both the extended Euler solver as well as the upwind schemes for the induction equation and present the approximate Riemann solver for the MHD equations. These schemes are compared with existing HLL and Roe solvers in a set of numerical experiments in both one and two space dimensions in Section 3.3 and we summarize the contents of this paper in Section 3.4.

3.2 Numerical schemes.

In this section, we design finite volume schemes based on splitting the ideal MHD equations into its fluid part and magnetic part. Consider the ideal MHD equations (3.1.1) in the domain $\mathbf{D} = [X_L, X_R] \times [Y_L, Y_R] \times [Z_L, Z_R]$. For simplicity, we consider a uniform grid in space with mesh points given by $x_i = i\Delta x$, $y_j = j\Delta y$ and $z_k = k\Delta z$ where Δx, Δy

and Δz are the mesh sizes in the x, y and z directions respectively. Let the Δt^n denote the time step at the n-th time level $t^n = \sum_{m<n} \Delta t^m$, be determined by a suitable CFL condition, and let the cell average at t^n be denoted by $U^n_{i,j,k}$.

With this notation, a general first order finite volume scheme reads

$$\begin{aligned} U^{n+1}_{i,j,k} &= V(U^n_{i-1,j,k}, U^n_{i,j-1,k}, U^n_{i,j,k-1}, U^n_{i,j,k}, U^n_{i+1,j,k}, U^n_{i,j+1,k}, U^n_{i,j,k+1}), \\ &= U^n_{i,j,k} - \frac{\Delta t^n}{\Delta x}\left(F(U^n_{i,j,k}, U^n_{i+1,j,k}) - F(U^n_{i-1,j,k}, U^n_{i,j,k})\right) \\ &\quad - \frac{\Delta t^n}{\Delta y}\left(G(U^n_{i,j,k}, U^n_{i,j+1,k}) - G(U^n_{i,j-1,k}, U^n_{i,j,k})\right) \\ &\quad - \frac{\Delta t^n}{\Delta z}\left(H(U^n_{i,j,k}, U^n_{i,j,k+1}) - H(U^n_{i,j,k-1}, U^n_{i,j,k})\right), \end{aligned} \tag{3.2.1}$$

where F, G and H are numerical fluxes consistent with the directional fluxes f, g and h respectively. The numerical fluxes will be determined by the splitting procedure outlined in the introduction.

3.2.1 Schemes for the extended Euler system:

As mentioned before, we use the natural splitting of the MHD equations and divide the equations into a hydrodynamic and a magnetic part. We start with approximate Riemann solvers for the hydrodynamic part. This amounts to considering the mass, momentum and energy equations in (3.1.1), regarding the magnetic field as a known function that is constant in t. This results in the following extended Euler equations

$$\begin{aligned} \rho_t + \operatorname{div}(\rho \mathbf{u}) &= 0, \\ (\rho \mathbf{u})_t + \operatorname{div}\left(\rho \mathbf{u} \otimes \mathbf{u} + \left(p + \frac{1}{2}\mathbf{B}^2\right)\mathcal{I} - \mathbf{B} \otimes \mathbf{B}\right) &= 0, \\ E_t + \operatorname{div}\left(\left(E + p + \frac{1}{2}\mathbf{B}^2\right)\mathbf{u} - (\mathbf{u}\cdot\mathbf{B})\mathbf{B}\right) &= 0, \end{aligned} \tag{3.2.2}$$

where the total energy E is given by the equation of state (3.1.2), and the magnetic field B is playing the role of a coefficient. This is a a hyperbolic conservation law where the fluxes depend on the location through $\mathbf{B}$,

$$U^e_t + f^e(U^e, \mathbf{B})_x + g^e(U^e, \mathbf{B})_y + h^e(U^e, \mathbf{B})_z = 0, \tag{3.2.3}$$

with $U^e = \{\rho, \rho u^1, \rho u^2, \rho u^3, E\}$ being the conserved fluid variables and f^e, g^e, h^e are the directional fluxes in (3.2.2). Defining the vector of primitive variables $V^e = [\rho, u^1, u^2, u^3, p]$, we get the following quasilinear form the equation (3.2.2)

$$V^e_t + A^{1,e}(V^e, \mathbf{B})V^e_x + A^{2,e}(V^e, \mathbf{B})V^e_y + A^{3,e}(V^e, \mathbf{B})V^e_z = S^e(V, \mathbf{B}, D\mathbf{B}),$$

with $D\mathbf{B}$ denoting the matrix of partial derivatives of $\mathbf{B}$. Consider any unit vector $\mathbf{n} = (n^1, n^2, n^3)$ and take $u_{\mathbf{n}} := \mathbf{u} \cdot \mathbf{n}$, the directional Jacobian is given by

$$A^{1,e}n^1 + A^{2,e}n^2 + A^{3,e}n^3 = A^e \cdot \mathbf{n} = \begin{pmatrix} u_{\mathbf{n}} & \rho n^1 & \rho n^2 & \rho n^3 & 0 \\ 0 & u_{\mathbf{n}} & 0 & 0 & \frac{1}{\rho}n^1 \\ 0 & 0 & u_{\mathbf{n}} & 0 & \frac{1}{\rho}n^2 \\ 0 & 0 & 0 & u_{\mathbf{n}} & \frac{1}{\rho}n^3 \\ 0 & a_1 & a_2 & a_3 & u_{\mathbf{n}} \end{pmatrix},$$

where

$$\begin{aligned} a^1 &= \gamma n^1 p + (\gamma - 1)\left(n^1(\mathbf{B}^2 - (B^1)^2) - B^1(n^2B^2 + n^3B^3)\right), \\ a^2 &= \gamma n^2 p + (\gamma - 1)\left(n^2(\mathbf{B}^2 - (B^2)^2) - B^2(n^1B^1 + n^3B^3)\right), \\ a^3 &= \gamma n^3 p + (\gamma - 1)\left(n^3(\mathbf{B}^2 - (B^3)^2) - B^3(n^1B^1 + n^2B^2)\right). \end{aligned}$$

, The eigenvalues of the directional Jacobian are

$$\lambda^{1,5} = u_{\mathbf{n}} \mp \frac{1}{\sqrt{\rho}}\sqrt{\mathbf{a} \cdot \mathbf{n}}, \quad \text{and} \quad \lambda^{2,3,4} = u_{\mathbf{n}}.$$

The two extreme eigenvalues λ^1 and λ^5 correspond to acoustic waves with the sound speed being modified due to the presence of the magnetic field. The middle eigenvalues correspond to contact discontinuities and shear waves. If $\mathbf{B} = 0$, the system reduces to the Euler equations and the matrix is non strictly hyperbolic. For $\mathbf{B} \neq 0$, the above system is only weakly hyperbolic.

For notational simplicity, denote the extended sound speed in the x-direction as

$$a^{1,e} = \frac{1}{\sqrt{\rho}}\sqrt{\gamma p + (\gamma - 1)((B^2)^2 + (B^3)^2)}.$$

Then the eigenvalues in the x-direction are given by

$$\lambda^{1,5} = u^1 \mp a^{1,e} \quad \text{and} \quad \lambda^{2,3,4} = u^1. \tag{3.2.4}$$

Our aim is to design approximate Riemann solvers of the HLL type for this extended system (3.2.2). We start with a simple two wave solver,

HLL solver

We consider the extended Euler system (3.2.2) in the x-direction. The main feature of HLL solvers, see [50], is to approximate the true Riemann solution with a wave fan containing fewer waves, all of which are moving discontinuities. Thus for fixed time t, the approximate Riemann solution of a HLL solver is a piecewise constant function of x.

We start by defining the HLL solver which approximate the Riemann solution of (3.2.2) (in general containing 5 waves) with a wave fan containing only two waves. Let $U^e_{L,R}$, $\mathbf{B}_{L,R}$ denote the conserved fluid variables and magnetic field to the left and right of an interface. Then define the left and right fluxes by,

$$f^e_L = f^e\left(U^e_L, \frac{(\mathbf{B}_L + \mathbf{B}_R)}{2}\right) \quad f^e_R = f^e\left(U^e_R, \frac{(\mathbf{B}_L + \mathbf{B}_R)}{2}\right). \tag{3.2.5}$$

Note that we freeze the magnetic field locally in time and assume it to be constant across the Riemann fan. This essentially amounts to staggering the coefficient in (3.2.2). This strategy for dealing with coefficients in conservation laws was also used in [45]. Let s_L^e and s_R^e denote the left and right wave speeds and U_*^e, f_*^e the middle state and middle flux respectively. Conservation of U^e implies that

$$f_R^e - f_*^e = s_R^e(U_R^e - U_*^e), \quad f_*^e - f_L^e = s_L^e(U_*^e - U_L^e)$$

Solving the above equations results in

$$U_*^e = \frac{f_R^e - f_L^e - s_R^e U_R^e + s_L^e U_L^e}{s_L^e - s_R^e}, \quad f_*^e = \frac{s_R^e f_L^e - s_L^e f_R^e + s_L^e s_R^e (U_R^e - U_L^e)}{s_R^e - s_L^e}. \tag{3.2.6}$$

Once the wave speed are defined, the numerical flux across the interface can be written

$$F^{e,\text{hll}} = F^e\left(U_L^e, U_R^e, \frac{(\mathbf{B}_L + \mathbf{B}_R)}{2}\right) = \begin{cases} f_L^e & \text{if} \quad s_L^e > 0 \\ f_*^e & \text{if} \quad s_L^e < 0 < s_R^e \\ f_R^e & \text{if} \quad s_R^e < 0 \end{cases}. \tag{3.2.7}$$

The wave speeds s_L^e and s_R^e are defined as in [28], let $A^{\hat{1},e}$ denote the arithmetic-average of the Jacobians $A_L^{1,e}$ and $A_R^{1,e}$, then the wave speeds are given by

$$\begin{aligned} s_L^e &= \min\left\{u_L^1 - a_L^{1,e}, \hat{u^1} - a^{\hat{1},e}\right\} \\ s_R^e &= \max\left\{u_R^1 + a_R^{1,e}, \hat{u^1} + a^{\hat{1},e}\right\} \end{aligned} \tag{3.2.8}$$

where $\hat{u^1}$ and $a^{\hat{1},e}$ are the normal velocity and the extended sound speed of the averaged Jacobian respectively. This solver is design to approximate only the outermost waves of the Riemann solutionand will not approximate contact discontinuities or shear waves very well. The choice of the wave speeds by comparing with an averaged Jacobian is an attempt to replicate the strategy of [28] of using Roe-averages to increase resolution at isolated shocks. We were unable to obtain a Roe-matrix for the extended Euler system. Furthermore, the above choice of wave speeds doesn't imply that the scheme will resolve isolated fast magnetosonic shocks exactly due to the splitting but will hopefully approximate such discontinuities with good accuracy.

HLLC solver

HLL three-wave solvers model the action of the two outer waves (as the HLL solver) as well as the contact/shear wave. Hence we must define three speeds $s_L^e \leq s_M^e \leq s_R^e$. The

approximate three wave solver and the corresponding numerical flux have the form

$$U^{e,\text{hllc}} = \begin{cases} U_L^e & \text{if} \quad s_L^e > 0, \\ U_L^{e,*} & \text{if} \quad s_L^e < 0 < s_M^e, \\ U_R^{e,*} & \text{if} \quad s_M^e < 0 < s_R^e, \\ U_R^e & \text{if} \quad s_R^e < 0, \end{cases}$$
$$F^{e,\text{hllc}} = F^{e,\text{hllc}}\left(U_L^e, U_R^e, \frac{(\mathbf{B}_L + \mathbf{B}_R)}{2}\right) = \begin{cases} f_L^e & \text{if} \quad s_L^e > 0, \\ f_L^{e,*} & \text{if} \quad s_L^e < 0 < s_M^e, \\ f_R^{e,*} & \text{if} \quad s_M^e < 0 < s_R^e, \\ f_R^e & \text{if} \quad s_R^e < 0, \end{cases} \tag{3.2.9}$$

Local conservation implies that

$$\begin{gathered} s_L^e U_L^{e,*} - f_L^{e,*} = s_L^e U_L^e - f_L^e, \quad s_M^e U_R^{e,*} - f_R^{e,*} = s_M^e U_L^{e,*} - f_L^{e,*} \\ \text{and} \quad s_R^e U_R^e - f_R^e = s_R^e U_R^{e,*} - f_R^{e,*}. \end{gathered} \tag{3.2.10}$$

Solving the above equations, we obtain the following expressions for $f_L^{e,*}$ and $f_R^{e,*}$

$$f_L^{e,*} = f_*^e - \frac{s_L^e(s_R^e - s_M^e)}{s_R^e - s_L^e}\Delta U^{e,*}, \quad f_R^{e,*} = f_*^e + \frac{s_R^e(s_M^e - s_L^e)}{s_R^e - s_L^e}\Delta U^{e,*}, \tag{3.2.11}$$

where $\Delta U^{e,*} = U_R^{e,*} - U_L^{e,*}$ and f_*^e is the middle flux of the HLL solver (3.2.6).

We follow [53] and determine the two middle states by the following simple observation

$$\Delta U^{e,*} = \alpha(U_R^e - U_L^e),$$

where α is a constant to be determined, thus the jump across the middle wave is proportional to the difference between the left and right states. The case of $\alpha = 0$ corresponds gives the HLL solver. When $\alpha = 1$, the solver gives an isolated single discontinuity. We choose s_L^e and s_R^e as the Einfeldt speeds given in (3.2.8). Since the middle wave is supposed to model the contact discontinuity, s_M^e is chosen as the corresponding velocity of the averaged Jacobian $A^{\hat{1},e}$ i.e., $s_M^e = \hat{u}^1$. Let $c_* = |a_L^{1,e} - s_M^e|$ and

$$s = \frac{\|\Delta f^e - s_M^e \Delta U^e\|}{\|\Delta U^e\|},$$

where $\Delta U^e = U_R^e - U_L^e$, $\Delta f^e = f_R^e - f_L^e$ and $\|C\| = \sum_k \left|C^k\right|$. The factor α is then defined by

$$\alpha = \max\left\{0, 1 - \frac{s}{c_*}\right\}$$

This choice of α is motivated by the following argument. Consider the quantity

$$\left\|\Delta f^e - s_M^e \Delta U^e\right\|.$$

At an isolated contact discontinuity, the above is equal to zero. Thus $\alpha = 1$ should represent this situation adequately. Similarly, if an isolated shock is present, then α should be equal to zero and

$$\left\|\Delta f^e - s_M^e \Delta U^e\right\| = c_* \left\|\Delta U^e\right\|.$$

This implies that the above linear interpolation gives the correct values of α in this regime.

It is straightforward to extend the HLL and the HLLC solvers to three dimensions. Let $F^{e,\text{hllc}}$, $G^{e,\text{hllc}}$ and $H^{e,\text{hllc}}$ be HLLC fluxes consistent with f^e, g^e and h^e and defined by (3.2.11) with the obvious modifications in the y and z directions. Let the discrete time derivative for any function b be denoted

$$D_t^+ b^n = \frac{b^{n+1} - b^n}{\Delta t},$$

and the average of two states across an interface as

$$\overline{b}_{l+1/2} = \frac{b_l + b_{l+1}}{2}.$$

Similarly we define the discrete spatial derivatives as

$$\mathcal{D}_x^{\pm} b_{i,j,k} = \pm \frac{b_{i\pm1,j,k} - b_{i,j,k}}{\Delta x},$$

with analogous definitions of $D_y^{\pm}$ and $D_z^{\pm}$. Then the HLLC scheme in three dimensions reads

$$\begin{aligned} D_t^+ U_{i,j,k}^{e,n} = &- D_x^- F^{e,\text{hllc}}\left(U_{i,j,k}^{e,n}, U_{i+1,j,k}^{e,n}, \overline{\mathbf{B}}_{i+1/2,j,k}\right) \\ &- D_y^- G^{e,\text{hllc}}\left(U_{i,j,k}^{e,n}, U_{i,j+1,k}^{e,n}, \overline{\mathbf{B}}_{i,j+1/2,k}\right) \\ &- D_z^- H^{e,\text{hllc}}\left(U_{i,j,k}^{e,n}, U_{i,j,k+1}^{e,n}, \overline{\mathbf{B}}_{i,j,k+1/2}\right) \end{aligned} \tag{3.2.12}$$

The HLL solver is extended to three space dimensions analogously.

As a shorthand notation we write

$$U_{i,j,k}^{e,n+1} = V^{e,\text{hllc}}\left(U_{\dots}^{e,n}, \mathbf{B}_{\dots}^{n}, \Delta t^n\right),$$

to indicate a single application of the HLLC scheme with a timestep Δt^n.

Remark. *The usual approach in designing a HLLC solver for Euler equations (see [76]) uses the fact that the pressure and normal velocities are constant across the middle wave and that the tangential velocities only jump across the middle wave. Plugging these assumptions into* (3.2.10) *results in a slightly different version of the HLLC solver for the extended Euler system* (3.2.2)*, with formulas similar to those obtained in [36] for the MHD equations. We have found that the numerical results with this solver are slightly more dissipative than those obtained with the solver described here.*

3.2.2 Schemes for the induction equation

The next step in this splitting procedure is to devise an efficient scheme for the induction equations (3.1.4). Rewriting the induction equation using the divergence constraint we obtain,

$$\partial_t \mathbf{B} + \text{curl}(\mathbf{B} \times \mathbf{u}) = 0, \tag{3.2.13}$$

and this implies

$$\partial_t \left(\text{div}\mathbf{B}\right) = 0. \tag{3.2.14}$$

Thus if the divergence is initially zero, it remains so and satisfies the divergence constraint in (3.1.1). The above equation is a linear hyperbolic system but not strictly hyperbolic. In general (see [31]), it is not possible to symmetrize (3.2.13) without explicitly using the divergence constraint. One way to symmetric these equations is to write them in the Godunov-Powell form (3.1.4) mentioned in the introduction. Following [31] and using standard vector identities, we can obtain the following symmetrized form of the system (3.2.13),

$$\partial_t \mathbf{B} + u^1 \partial_x (\mathbf{B}) + u^2 \partial_y (\mathbf{B}) + u^3 \partial_z (\mathbf{B}) = (\mathbf{B} \cdot \nabla)\mathbf{u} - \mathbf{B}(\mathrm{div}\mathbf{u}). \tag{3.2.15}$$

For a given smooth velocity field $\mathbf{u}$, it is easy to prove that weak solutions to the above equation exist, are unique and satisfy an energy estimate, see [31] for the relevant references. It seems essential to rewrite (3.2.13) in the symmetric form (3.2.15) in order to obtain well-posedness. Furthermore, all the above forms are equivalent if the initial divergence is zero and the solutions are sufficiently smooth.

Our aim in this section is to present efficient numerical schemes for the induction equation. The schemes should be stable in a suitable sense and not introduce too much divergence errors. Furthermore, it is obviously important that they should work effectively with the HLL Euler solvers of the last section to yield a robust scheme for the MHD equations. To simplify the presentation, we consider the induction equation in two dimensions,

$$\begin{aligned} \partial_t B^1 + \partial_y \left(u^1 B^2 - u^2 B^1 \right) = 0, \\ \partial_t B^2 - \partial_x \left(u^1 B^2 - u^2 B^1 \right) = 0. \end{aligned} \tag{3.2.16}$$

Consider a given velocity field $\mathbf{u}$ and a uniform discretization in both the x and y directions with mesh sizes Δx and Δy. We start with the following notation, for a continuous function $a(x, y)$, we set

$$a_{i,j} = a\left(x_i, y_j\right), \quad i \text{ and } j \in \mathbb{Z}/2,$$

and define and the central differences

$$D^0_{x,y} = \frac{1}{2}\left(D^+_{x,y} + D^-_{x,y}\right).$$

Furthermore, set $[a]^+ = \max\{a, 0\}$ and $[a]^- = \min\{a, 0\}$.

The Lax-Friedrichs scheme

The simplest scheme for the hyperbolic system (3.2.16) is the Lax-Friedrichs scheme. Set $\phi^n_{i,j} = B^{1,n}_{i,j} u^{2,n}_{i,j} - B^{2,n}_{i,j} u^{1,n}_{i,j}$ and define this scheme as

$$\begin{aligned} D^+_t B^{1,n}_{i,j} = \frac{1}{\Delta t} \left[\left(\frac{\Delta x}{2}\right)^2 D^+_x D^-_x \left(B^{1,n}_{i,j}\right) + \left(\frac{\Delta y}{2}\right)^2 D^+_y D^-_y \left(B^{1,n}_{i,j}\right) \right] \\ + D^0_y \left(\phi^n_{i,j}\right), \\ D^+_t B^{2,n}_{i,j} = \frac{1}{\Delta t} \left[\left(\frac{\Delta x}{2}\right)^2 D^+_x D^-_x \left(B^{2,n}_{i,j}\right) + \left(\frac{\Delta y}{2}\right)^2 D^+_y D^-_y \left(B^{2,n}_{i,j}\right) \right] \\ - D^0_x \left(\phi^n_{i,j}\right). \end{aligned} \tag{3.2.17}$$

Note that this scheme is based on using a second central difference for the flux coupled with a artificial diffusion term. In general, this scheme is too dissipative for practical applications, but if the central discrete divergence is constant, the scheme preserves this central divergence. To be concrete, let the central discrete divergence be defined as

$$d^n_{i,j} = \mathrm{div}^0(\mathbf{B}^n_{i,j}) = D^0_x(B^{1,n}_{i,j}) + D^0_y(B^{2,n}_{i,j}). \tag{3.2.18}$$

Under the Lax-Friedrichs scheme, the evolution of $d^n_{i,j}$ reads

$$d^{n+1}_{i,j} = d^n_{i,j} + \left(\frac{\Delta x}{2}\right)^2 D^+_x D^-_x \left(d^n_{i,j}\right) + \left(\frac{\Delta y}{2}\right)^2 D^+_y D^-_y \left(d^n_{i,j}\right).$$

Thus if $d^n_{i,j} = 0$, the above identity implies that $d^{n+1}_{i,j} \equiv 0$ and the scheme preserves divergence free fields.

As shorthand notation for a single application of the Lax-Friedrichs scheme we write $\mathbf{B}^{n+1}_{i,j} = W^{m,\mathrm{LxF}}(\mathbf{u}^n_{\dots}, \mathbf{B}^n_{\dots}, \Delta t^n)$.

Divergence preserving upwind schemes

As mentioned in the introduction, there exists an extensive literature devoted to devising suitable upwind schemes which preserve some form of discrete divergence in (3.2.16). We present the divergence preserving scheme of Torhillon and Fey [77] as an example. This scheme is given by

$$\begin{aligned} D^+_t B^{1,n}_{i,j} &= \frac{1}{2}\Big(D^-_y \left(\varphi^1_{i,j} + \varphi^1_{i-1,j} + \varphi^2_{i,j} + \varphi^2_{i+1,j}\right) \\ &\qquad + D^+_y \left(\varphi^3_{i,j} + \varphi^3_{i+1,j} + \varphi^4_{i,j} + \varphi^4_{i-1,j}\right)\Big), \\ D^+_t B^{2,n}_{i,j} &= -\frac{1}{2}\Big(D^-_x \left(\varphi^1_{i,j} + \varphi^1_{i,j-1} + \varphi^4_{i,j} + \varphi^4_{i,j+1}\right) \\ &\qquad + D^+_x \left(\varphi^2_{i,j} + \varphi^2_{i,j-1} + \varphi^3_{i,j} + \varphi^3_{i,j+1}\right)\Big), \end{aligned} \tag{3.2.19}$$

where

$$\varphi^k_{i,j} = \omega^k_{i,j}\left(u^1_{i,j} B^{2,n}_{i,j} - u^2_{i,j} B^{1,n}_{i,j}\right),$$

and

$$\omega^k_{i,j} = \frac{\left[\mathbf{n}^k \cdot \mathbf{u}_{i,j}\right]^+}{\sum_{k=1}^4 \left[\mathbf{n}^k \cdot \mathbf{u}_{i,j}\right]^+},$$

$$\mathbf{n}^1 = (1,1),\ \mathbf{n}^2 = (-1,1),\ \mathbf{n}^3 = (-1,-1) \text{ and } \mathbf{n}^4 = (1,-1).$$

This scheme preserves the following discrete divergence,

$$\mathrm{div}^*(\mathbf{B}_{i,j}) = \frac{1}{4}\Big(D^0_x \left(B^1_{i,j+1} + 2B^1_{i,j} + B^1_{i,j-1}\right) + D^0_y \left(B^2_{i+1,j} + 2B^2_{i,j} + B^1_{i-1,j}\right)\Big).$$

If $\mathbf{B}$ is smooth, div^* differs from div^0 by $\mathcal{O}(\Delta x^2 + \Delta y^2)$, with a constant depending on the second derivatives of $\mathbf{B}$. More details on this scheme can be found in [77, 78]. We write this scheme as $\mathbf{B}^{n+1}_{i,j} = W^{m,\mathrm{TF}}(\mathbf{u}^n_{\dots}, \mathbf{B}^n_{\dots}, \Delta t^n)$.

A stable upwind scheme

It is desirable to have a scheme which is stable in the L^2 norm, and which does not create spurious oscillations. The natural starting point to design a scheme with these properties is the Godunov-Powell form (3.1.4), and then use the symmetrized form (3.2.15). This strategy was adopted in [31] and [16]. Introduce the following notation,

$$\begin{aligned} D_x\{u,B\}_{i,j} &= D_x^-\left(\left[u_{i+1/2,j}\right]^+ B_{i,j}\right) + D_x^+\left(\left[u_{i-1/2,j}\right]^- B_{i,j}\right) \\ &= \left[u_{j+1/2,j}\right]^- D_x^+ B_{i,j} + \left[u_{i-1/2,j}\right]^+ D_x^- B_{i,j} + B_{i,j} D_x^- u_{i+1/2,j}. \end{aligned} \tag{3.2.20}$$

An analogous expression defines $D_y\{u,B\}$. If u and B are smooth functions, then

$$\partial_x(uB)(x_i,y_j) = D_x\{u,B\}_{i,j} + \mathcal{O}(\Delta x).$$

Then the stable upwind from [31] takes the form

$$\begin{aligned} D_t^+ B_{i,j}^{1,n} = &\left(D_y\left\{u^{1,n},B^{2,n}\right\}_{i,j} - D_y\left\{u^{2,n},B^{1,n}\right\}_{i,j}\right) \\ &- \left[u_{i-1/2,j}^{1,n}\right]^+ D_x^-\left(B_{i,j}^{1,n}\right) - \left[u_{i+1/2,j}^{1,n}\right]^- D_x^+\left(B_{i,j}^{1,n}\right) \\ &- \left[u_{i,j-1/2}^{1,n}\right]^+ D_y^-\left(B_{i,j}^{2,n}\right) - \left[u_{i,j+1/2}^{1,n}\right]^- D_y^+\left(B_{i,j}^{2,n}\right), \\ D_t^+ B_{i,j}^{2,n} = &-\left(D_x\left\{u^{1,n},B^{2,n}\right\}_{i,j} - D_x\left\{u^{2,n},B^{1,n}\right\}_{i,j}\right) \\ &- \left[u_{i-1/2,j}^{2,n}\right]^+ D_x^-\left(B_{i,j}^{1,n}\right) - \left[u_{i+1/2,j}^{2,n}\right]^- D_x^+\left(B_{i,j}^{1,n}\right) \\ &- \left[u_{i,j-1/2}^{2,n}\right]^+ D_y^-\left(B_{i,j}^{2,n}\right) - \left[u_{i,j+1/2}^{2,n}\right]^- D_y^+\left(B_{i,j}^{2,n}\right). \end{aligned} \tag{3.2.21}$$

Hence, the above scheme is based on upwinding the Godunov-Powell source term in (3.1.4). This scheme can also be written down in terms of the non-conservative symmetric form (3.2.15). Under the assumptions of sufficiently smooth velocity fields, it is shown to be stable in L^2 and hence converges to a weak solution of the magnetic induction equation. Furthermore, in the simple case of constant velocity fields, the above scheme is *TVD*. Numerical experiments indicating robustness of this scheme were presented in [31]. As mentioned before, the introduction of the Godunov-Powell source term results in divergence errors being transported by the velocity field, and one would like control these errors, but unfortunately we have not been able to prove that the divergence remains bounded in L^2. Nevertheless, numerical experiments indicate that the divergence generated by the scheme remaines small.

Note also that this scheme requires evaluation of the velocities at the cell interfaces. We do this by averaging, i.e.,

$$u_{i+1/2,j}^n = \frac{1}{2}\left(u_{i+1,j}^n + u_{i,j}^n\right).$$

We write this scheme as $\mathbf{B}_{i,j}^{n+1} = W^{m,\mathrm{SUS}}(\mathbf{u}_{\dots}^n, \mathbf{B}_{\dots}^n, \Delta t^n)$.

A stable "non-conservative" upwind scheme

Since the SUS-scheme of the last section did not lead to a rigorous divergence bound, the authors designed a slightly modified version of this scheme in [31] for which it was possible to establish L^2 bounds on the discrete divergence.

This upwind scheme is based on the non-conservative symmetric form (3.2.15) and hence we refer to it as the stable non-conservative upwind scheme (SUS-N). Define the auxiliary function σ_δ as an even smooth function such that

$$\sigma_\delta(a) = \begin{cases} \frac{\delta}{2}, & \text{if } |a| \leq \delta/2, \\ 0, & \text{if } |a| \geq \delta. \end{cases}$$

Furthermore, we demand that σ is non-increasing in the interval $[0, \delta]$ and that $|\sigma'_\delta(a)| < 2$ for all a. Then in two dimensions, the scheme reads

$$\begin{aligned} D_t^+ B_{i,j}^{1,n} = &- \left[u_{i,j}^{1,n}\right]^- D_x^+ \left(B_{i,j}^{1,n}\right) - \left[u_{i,j}^{1,n}\right]^+ D_x^- \left(B_{i,j}^{1,n}\right) \\ &- \left[u_{i,j}^{2,n}\right]^- D_y^+ \left(B_{i,j}^{1,n}\right) - \left[u_{i,j}^{2,n}\right]^+ D_y^- \left(B_{i,j}^{1,n}\right) \\ &- D_y^0 \left(u_{i,j}^{2,n}\right) B_{i,j}^{1,n} + D_y^0 \left(u_{i,j}^{1,n}\right) B_{i,j}^{2,n} \\ &+ \sigma_\delta(u_{i,j}^{1,n}) \Delta x D_x^+ D_x^- \left(B_{i,j}^{1,n}\right) + \sigma_\delta(u_{i,j}^{2,n}) \Delta y D_y^+ D_y^- \left(B_{i,j}^{1,n}\right), \\ D_t^+ B_{i,j}^{2,n} = &- \left[u_{i,j}^{1,n}\right]^- D_x^+ \left(B_{i,j}^{2,n}\right) - \left[u_{i,j}^{1,n}\right]^+ D_x^- \left(B_{i,j}^{2,n}\right) \\ &- \left[u_{i,j}^{2,n}\right]^- D_y^+ \left(B_{i,j}^{2,n}\right) - \left[u_{i,j}^{2,n}\right]^+ D_y^- \left(B_{i,j}^{2,n}\right) \\ &+ D_x^0 \left(u_{i,j}^{2,n}\right) B_{i,j}^{1,n} - D_x^0 \left(u_{i,j}^{1,n}\right) B_{i,j}^{2,n} \\ &+ \sigma_\delta(u_{i,j}^{1,n}) \Delta x D_x^+ D_x^- \left(B_{i,j}^{2,n}\right) + \sigma_\delta(u_{i,j}^{2,n}) \Delta y D_y^+ D_y^- \left(B_{i,j}^{2,n}\right), \end{aligned} \tag{3.2.22}$$

Note that we add a small amount of explicit numerical diffusion at the points $\mathbf{u} = 0$ in addition to upwinding the derivatives. In [31], we were able to show that the approximate solutions generated by the above scheme (3.2.22) are bounded in L^2 and the standard central discrete divergence (3.2.18) is also bounded in L^2 under the assumptions that velocity field is sufficiently smooth. Furthermore, the approximate solutions are TVD when the velocity field is constant. We write an application of a single step with this scheme as $\mathbf{B}_{i,j}^{n+1} = W^{m,\mathrm{SUS-N}}(\mathbf{u}_{\ldots}^n, \mathbf{B}_{\ldots}^n, \Delta t^n)$.

Remark. *It is straightforward extend all the above schemes to three space dimensions. For the sake of clarity we give the full three dimensional form of the SUS scheme. The extension of the other schemes to three dimensions is analogous.*

$$\begin{aligned} D_t^+ B_{i,j,k}^{1,n} = &- D_y \left\{u_{i,j,k}^{2,n}, B_{i,j,k}^{1,n}\right\} + D_y \left\{u_{i,j,k}^{1,n}, B_{i,j,k}^{2,n}\right\} \\ &- D_z \left\{u_{i,j,k}^{3,n}, B_{i,j,k}^{1,n}\right\} + D_z \left\{u_{i,j,k}^{1,n}, B_{i,j,k}^{3,n}\right\} \\ &- \left(\left[u_{i-\frac{1}{2},j,k}^{1,n}\right]^+ D_x^-(B_{i,j,k}^{1,n}) + \left[u_{i+\frac{1}{2},j,k}^{1,n}\right]^- D_x^+(B_{i,j,k}^{1,n}) \right) \\ &- \left(\left[u_{i,j-\frac{1}{2},k}^{1,n}\right]^+ D_y^-(B_{i,j,k}^{2,n}) + \left[u_{i,j+\frac{1}{2},k}^{1,n}\right]^- D_y^+(B_{i,j,k}^{2,n}) \right) \\ &- \left(\left[u_{i,j,k-\frac{1}{2}}^{1,n}\right]^+ D_z^-(B_{i,j,k}^{3,n}) + \left[u_{i,j,k+\frac{1}{2}}^{1,n}\right]^- D_z^+(B_{i,j,k}^{3,n}) \right), \end{aligned}$$

$$
\begin{aligned}
D_t^+ B_{i,j,k}^{2,n} = &-D_x\left\{u_{i,j,k}^{1,n}, B_{i,j,k}^{2,n}\right\} + D_x\left\{u_{i,j,k}^{2,n}, B_{i,j,k}^{1,n}\right\} \\
&- D_z\left\{u_{i,j,k}^{3,n}, B_{i,j,k}^{2,n}\right\} + D_z\left\{u_{i,j,k}^{2,n}, B_{i,j,k}^{3,n}\right\} \\
&- \left(\left[u_{i-\frac{1}{2},j,k}^{2,n}\right]^+ D_x^-(B_{i,j,k}^{1,n}) + \left[u_{i+\frac{1}{2},j,k}^{2,n}\right]^- D_x^+(B_{i,j,k}^{1,n})\right) \\
&- \left(\left[u_{i,j-\frac{1}{2},k}^{2,n}\right]^+ D_y^-(B_{i,j,k}^{2,n}) + \left[u_{i,j+\frac{1}{2},k}^{2,n}\right]^- D_y^+(B_{i,j,k}^{2,n})\right) \\
&- \left(\left[u_{i,j,k-\frac{1}{2}}^{2,n}\right]^+ D_z^-(B_{i,j,k}^{3,n}) + \left[u_{i,j,k+\frac{1}{2}}^{2,n}\right]^- D_z^+(B_{i,j,k}^{3,n})\right), \\
D_t^+ B_{i,j,k}^{3,n} = &-D_x\left\{u_{i,j,k}^{1,n}, B_{i,j,k}^{3,n}\right\} + D_x\left\{u_{i,j,k}^{3,n}, B_{i,j,k}^{1,n}\right\} \\
&- D_y\left\{u_{i,j,k}^{2,n}, B_{i,j,k}^{3,n}\right\} + D_y\left\{u_{i,j,k}^{3,n}, B_{i,j,k}^{2,n}\right\} \\
&- \left(\left[u_{i-\frac{1}{2},j,k}^{3,n}\right]^+ D_x^-(B_{i,j,k}^{1,n}) + \left[u_{i+\frac{1}{2},j,k}^{3,n}\right]^- D_x^+(B_{i,j,k}^{1,n})\right) \\
&- \left(\left[u_{i,j-\frac{1}{2},k}^{3,n}\right]^+ D_y^-(B_{i,j,k}^{2,n}) + \left[u_{i,j+\frac{1}{2},k}^{3,n}\right]^- D_y^+(B_{i,j,k}^{2,n})\right) \\
&- \left(\left[u_{i,j,k-\frac{1}{2}}^{3,n}\right]^+ D_z^-(B_{i,j,k}^{3,n}) + \left[u_{i,j,k+\frac{1}{2}}^{3,n}\right]^- D_z^+(B_{i,j,k}^{3,n})\right).
\end{aligned}
$$

3.2.3 Combining the schemes

In order to obtain a scheme for the full MHD equations, we can now piece together the schemes for the hydrodynamic part with the schemes for the induction equation.

This can be done either simultaneously, resulting in update formula

$$
\begin{aligned}
U_{i,j,k}^{e,n+1} &= V^{e,\text{type}_1}\left(U_{\dots}^{e,n}, \mathbf{B}_{\dots}^{n}, \Delta t^n\right), \\
\mathbf{B}_{i,j,k}^{n+1} &= W^{m,\text{type}_2}\left(\mathbf{u}_{\dots}^{n}, \mathbf{B}_{\dots}^{n}, \Delta t^n\right),
\end{aligned}
\tag{3.2.23}
$$

or sequentially, in which case we have the update formula

$$
\begin{aligned}
U_{i,j,k}^{e,n+1} &= V^{e,\text{type}_1}\left(U_{\dots}^{e,n}, \mathbf{B}_{\dots}^{n}, \Delta t^n\right), \\
\mathbf{B}_{i,j,k}^{n+1} &= W^{m,\text{type}_2}\left(\mathbf{u}_{\dots}^{n+1}, \mathbf{B}_{\dots}^{n}, \Delta t^n\right).
\end{aligned}
\tag{3.2.24}
$$

Here "type$_1$" is either "HLL" or "HLLC", and "type$_2$" is one of "LxF", "TF", "SUS" or "SUS-N". Therefore all possible combinations give 16 possible update formulas. Furthermore, we can also reverse the order in the sequential update (3.2.24) by evolving the magnetic part first, followed by the evolution of the fluid part. We found no difference in the numerical results by reversing orders in (3.2.24).

Remark. *Note that both the above schemes are consistent with the form* (3.1.10) *of the MHD equations with constants* $c_1 = 0$ *and* $c_2 = 1$. *This form is a special form of the equations which conserves mass, momentum and energy and has the Godunov-Powell source term only in the induction equations. This form is also formally equivalent to* (3.1.1) *for divergence free data.*

Remark. *The splitting schemes based on* (3.2.24) *are formally first order in both space and time. It is easy to increase the spatial accuracy by a standard ENO/WENO type non-oscillatory piecewise polynomial reconstruction. Second order formal accuracy in time can be accomplished by a Strang splitting, and further increased by using standard strong stability preserving Runge-Kutta methods.*

3.3 Numerical examples

We are going to test the splitting schemes of the last section on a variety of numerical experiments in both one and two space dimensions. These experiments have been used in the literature on numerical schemes for MHD equations as benchmark test cases to compare different methods. The key issues are both accuracy and stability. Since the schemes of this paper are first order methods, we will compare them with three standard first order finite volume schemes for MHD equations: 1) a HLL two wave solver (see [28]) for the full MHD equations which we will refer to as the HLL2 solver, 2) a HLL three wave solver for the MHD equations designed in [53], referred to HLL3 solver and 3) a Roe solver. The Roe solver that we use is based on adding symmetric diffusion in the entropy variables, in the spirit of [42] for Navier-Stokes equations and [12] for Euler equations. This Roe solver has better accuracy as well as stability compared to the standard Roe solvers used in the literature. More details about this Roe solver will be reported in a forthcoming paper. In terms of computational cost, the HLL2 solver is as costly as the HLL/SUS solver, the HLL3 solver has the same cost as the HLLC/SUS solver and the Roe solver is the most expensive. So, we will see whether the HLL/SUS and HLLC/SUS solvers do better than the HLL2 and HLL3 solvers respectively and how they compare with the Roe solver.

Remark. *With a small choice of* δ*, e.g.,* $\delta = \min\{\Delta x, \Delta y\}/2$*, we observed no difference between the SUS and the SUS-N solvers. Therefore we choose to report results using the SUS scheme only.*

We concentrate on one- and two dimensional examples, therefore we let the computational domain $[X_L, X_R] \times [Y_L, Y_R]$ be discretized uniformly in each direction leading to mesh sizes of Δx and Δy respectively. The time step is determined by the following CFL condition

$$\frac{\max\limits_{i,j} \left\{ |u^{1,n}_{i,j}| + a^{1,e,n}_{i,j}, \quad |u^{2,n}_{i,j}| + a^{2,e,n}_{i,j} \right\} \Delta t^n}{\min\{\Delta x, \Delta y\}} \leq 1,$$

where $a^{l,e,n}_{i,j}$ is the extended sound speed in the l-th direction in the cell $I_{i,j}$. We run the numerical experiments at the same CFL number of 0.45.

We use the following notation for errors, let W^M be a component of the numerical solution given by a scheme using a $M \times M$ grid, and W^R the same component of a reference solution. We define the relative error as

$$\mathfrak{RE}^p_M(W) = 100 \times \frac{\left\| W^M - W^R \right\|_p}{\left\| W^R \right\|_p},$$

where $\|\cdot\|_p$ is the discrete L^p norm. In this way we refer to e.g., $\mathfrak{RE}^1_{100}(\rho)$, denoting the relative difference in L^1 between the density calculated on a 100×100 grid and a reference density.

We have used $\gamma = 5/3$ and the simultaneous update formula (3.2.23) in all examples. We found that using the sequential update (3.2.24) gave very similar results.

3.3.1 Shock tube

We start with a one dimensional shock tube test case. The initial conditions are given by

$$\begin{aligned}\big(\rho, \rho u_1, \rho u_2, \rho u_3, B^1, B^2, B^3, p\big) \\ = \begin{cases} (1.0, +1.0, 0.0, 0.0, 0.7, 1.0, 0.0, 1.0), & \text{if } x < 0.5 \\ (0.3, -0.3, 0.0, 0.0, 0.7, 0.2, 0.0, 0.2), & \text{otherwise.} \end{cases}\end{aligned} \tag{3.3.1}$$

The computational domain is $(x, t) \in [0, 1.5] \times [0, 0.5]$ with Neumann boundary conditions. All schemes use the CFL-number 0.45. The Riemann problem has a complicated solution containing shocks, rarefactions and contact discontinuities. We test different schemes on this problem and report the results in Figure 3.3.1 and Table 3.3.1. We compute a reference solution with the standard HLL2 solver using 8000 mesh points. The results in Figure 3.3.1 compare the HLLC/LxF, HLL/SUS and HLLC/SUS schemes with 400 mesh points on this problem. As shown in this figure, all three schemes resolve the complicated solution fairly well with the HLLC/SUS scheme being the least dissipative and the HLLC/LxF being the most dissipative. Note that HLLC/LxF is much less dissipative than the standard LxF scheme for a system, since the "Euler part" is approximated with a HLL solver. Table 3.3.1 gives a more quantitative comparison of the schemes. In this

M	HLL	HLL3	HLL/SUS	HLLC/SUS	HLLC/LxF	HLLC/TF	Roe
100	4.44	3.35	4.49	3.26	3.30	3.22	2.42
200	2.87	1.95	2.65	1.90	2.08	1.86	1.23
400	1.88	1.22	1.73	1.18	1.26	1.15	0.73
800	1.13	0.64	1.02	0.62	0.73	0.61	0.30
1600	0.62	0.28	0.55	0.27	0.37	0.26	0.10

M	HLL	HLL3	HLL/SUS	HLLC/SUS	HLLC/LxF	HLLC/TF	Roe
100	3.32	2.75	3.06	2.81	3.56	2.09	1.89
200	2.04	1.56	1.77	1.55	2.14	1.25	0.85
400	1.29	0.97	1.11	0.95	1.35	0.73	0.50
800	0.75	0.51	0.60	0.48	0.74	0.40	0.18
1600	0.38	0.23	0.29	0.21	0.34	0.16	0.09

Table 3.3.1: Relative errors, $\mathfrak{RE}^1_M(\rho)$ (top) and $\mathfrak{RE}^1_M(B^2)$ (bottom), at time $t = 0.5$ for the Brio-Wu shock tube for various mesh sizes M.

table, a "–" means that the scheme crashed due to negative density or pressure. We show

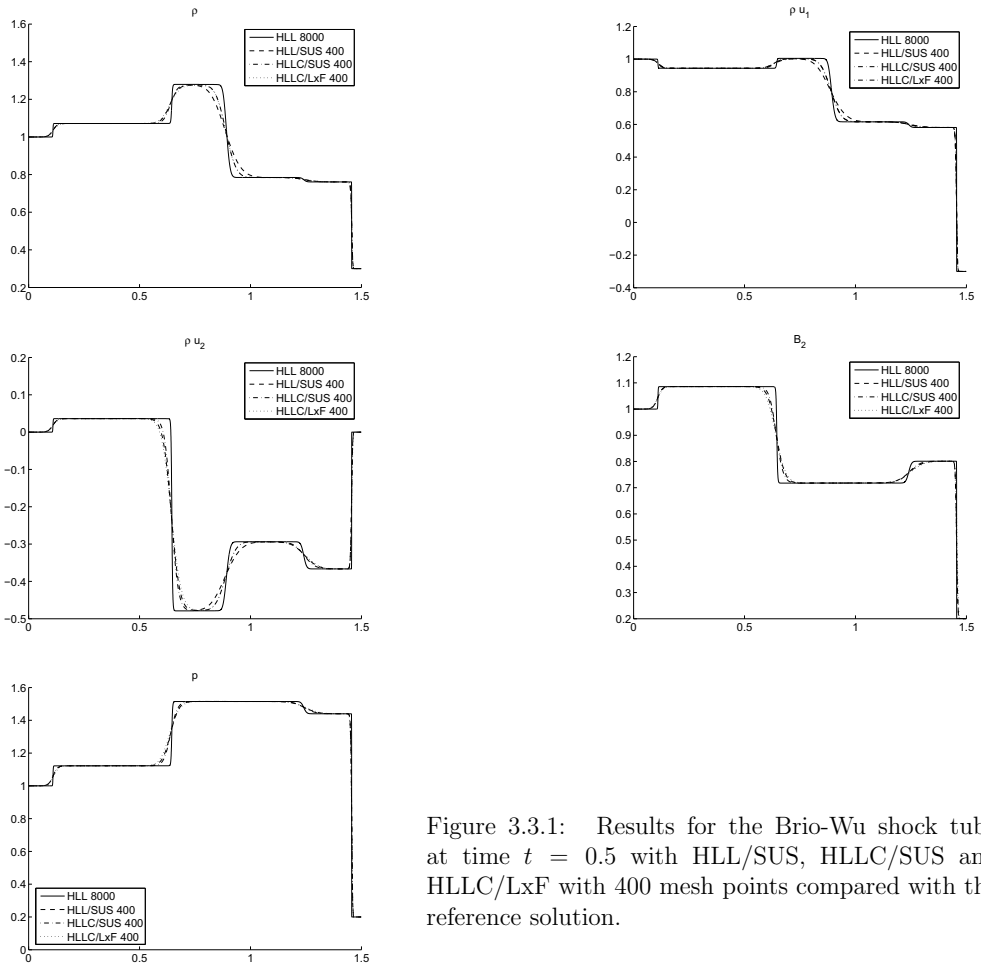

Figure 3.3.1: Results for the Brio-Wu shock tube at time $t = 0.5$ with HLL/SUS, HLLC/SUS and HLLC/LxF with 400 mesh points compared with the reference solution.

relative errors in L^1 on different meshes for both the density and a component of the magnetic field and compare the HLL, HLL3, HLL/SUS, HLLC/SUS, HLLC/LxF, HLLC/TF and Roe schemes.

From the table, all the splitting based solvers yielded reasonably small errors for this problem. Surprisingly, the errors due to the HLLC/LxF scheme are not very high and this implies that the split scheme is much less dissipative than a standard Lax-Friedrichs scheme would have been. In fact, this scheme has lower errors than the standard HLL scheme. As expected the HLLC/SUS scheme had lower errors than the HLL/SUS scheme and these errors were comparable to the HLLC scheme. The HLLC/TF had the best resolution among the splitting solvers in this case. Unfortunately, the approximate magnetic field was oscillatory. This is to be expected as in [31], we demonstrated via a numerical experiment that the TF scheme leads to oscillations around discontinuities and this might be the reason for the instabilities reported here.

Comparing the splitting schemes with the standard schemes, we see from the above table that the errors due to the HLL/SUS scheme and the HLLC/SUS scheme are comparable to those generated by the HLL scheme and HLL3 scheme respectively. For the density, the HLLC/SUS scheme has slightly greater resolution than the HLL3 scheme. Furthermore, none of the HLL two and three wave solvers presented above have the resolution comparable to the Roe solver particularly in the density variable. However, recent papers [58, 73] have reported that the HLL five wave solver has comparable accuracy as the Roe solver.

This experiment indicates that the splitting scheme are comparable to the standard HLL two-three wave schemes in one space dimension. We have performed tests with other shock tubes and obtain similar qualitative and quantitative results.

One of the key robustness criteria in one dimensional MHD is whether the numerical schemes yield approximations with positive pressure and density. It is well known that the Roe solver is not positivity preserving and the references cited in the introduction prove that the HLL2 solver and other HLL three and five solvers are proved to be positivity preserving. We are unable to provide a proof that our splitting based solvers are positivity preserving in one space dimension. However, numerical tests indicated that these solvers do preserve positive pressue and density in practice. In order to test this assertion, we present the following numerical experiment.

3.3.2 Super-fast expansion

This test problem has been used in [59] and other references therein as a test of positivity preservation for one dimensional MHD solvers. The set up is a shock tube with initial data,

$$\begin{aligned}\big(\rho, \rho u_1, \rho u_2, \rho u_3, B^1, B^2, B^3, p\big) \\ = \begin{cases} (1.0, -3.1, 0, 0, 0, 0.5, 0, 0.45), & \text{if } x < 0.5 \\ (1.0, 3.1, 0, 0, 0, 0.5, 0, 0.45), & \text{otherwise.} \end{cases}\end{aligned} \tag{3.3.2}$$

The data has been selected in such a manner that the exact solution is an expansion with fast wave mach number equal to 3.1. The solution contains very low densities and

pressures and is designed to test positivity of solvers. As expected, the HLL2 and HLL3 solvers retained positivity and the Roe solver crashed due to negative pressure. Similarly, the HLLC/LxF solver retained positivity. We present the results for the HLL/SUS and HLLC/SUS solvers in Figure 3.3.2, where we plot the logarithm of the pressure computed by the HLL/SUS and the HLLC/SUS solvers for 400 and 1600 mesh points. The figure

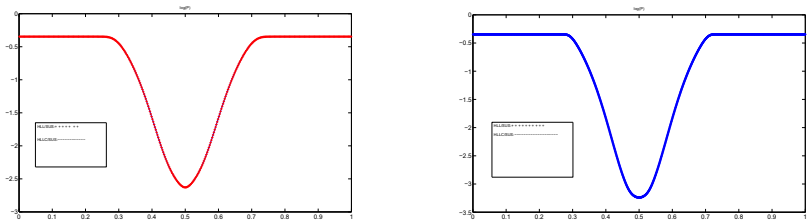

Figure 3.3.2: Numerical results for the superfast expansion problem. We show $log_{10}(P)$ at time $t = 0.2$ with both HLL/SUS and HLLC/SUS solvers. Left: 400 mesh points and Right:1600 mesh points

clearly demonstrates that both solvers retain positivity. The HLLC/TF scheme crashed due to oscillations.

This experiment doesn't prove that our HLL/SUS and HLLC/SUS schemes are positivity preserving. However, based on this and many other one dimensional numerical tests, we can conclude that these solvers are robust for one-dimensional problems. Encouraged by these results, we move on to two-dimensional test problems.

3.3.3 Orszag-Tang Vortex

The so-called Orzag-Tang vortex is a well-known benchmark test for two dimensional schemes for the MHD equations (see [80]) . For this problem, the initial data are given by

$$\begin{aligned}\big(\rho, \rho u_1, \rho u_2, \rho u_3, B^1, B^2, B^3, p\big) \\ = \big(\gamma^2, -\rho\sin(y), \rho\sin(x), 0.0, -\sin(y), \sin(2x), 0.0, \gamma\big)\,. \quad (3.3.3)\end{aligned}$$

The computational domain is $(\mathbf{x}, t) \in [0, 2\pi]^2 \times [0, \pi]$ with periodic boundary conditions. We present numerical results with different schemes in Figure 3.3.3 and Table 3.3.2.

Even though the initial data are smooth, the solution develops discontinuities in form of shocks along the diagonals, together with a vortex in the center of the domain. The solution has a rich structure consisting of shocks, vortices and other interesting smooth regions. The issues with any numerical scheme are resolution of the shocks as well as the central vortex. Another issue is that of control of divergence in some discrete norm. In fact, it is widely believed that lack of divergence control can lead to negative pressures and hence crashes in this test case. So ensuring stability of the solver, particularly at fine mesh resolutions is a challenge. There is no accepted reference solution in this case and

many papers have used the maximum pressure as a measure of accuracy and of a scheme. We plot the pressure on a 100×100 mesh in Figure 3.3.3 and compare HLL, HLL/SUS, HLL3 and HLLC/SUS schemes for qualitative behavior. As shown in Figure 3.3.3, the

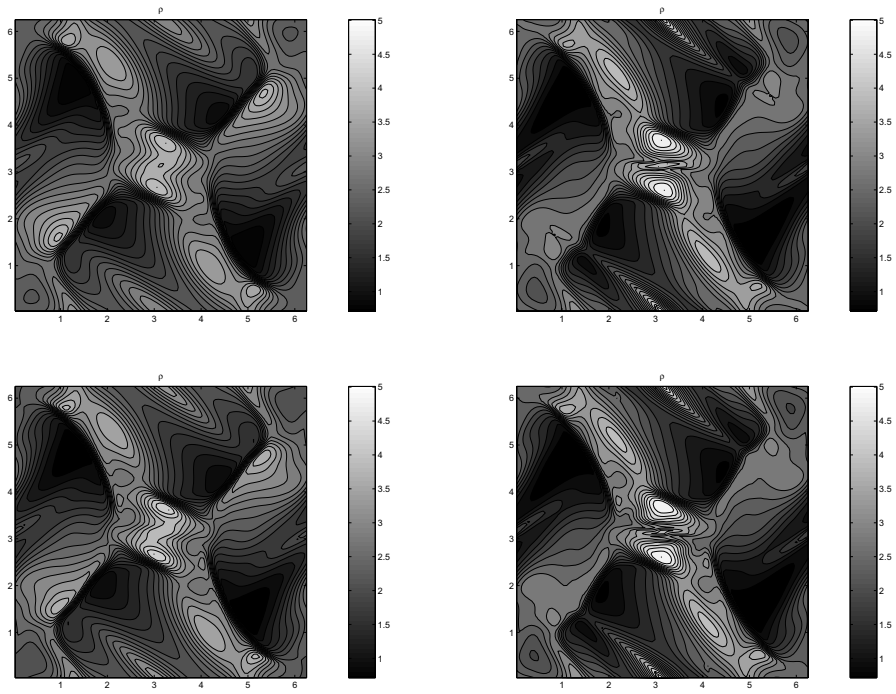

Figure 3.3.3: This figure shows the pressure computed with (from top left to bottom right): HLL2, HLL/SUS, HLL3 and HLLC/SUS on a 100×100 mesh at time $t = \pi$.

differences in resolving the solution are much more pronounced in this case. In particular, the HLL scheme is very dissipative and the central vortex is not well resolved. Even the HLL3 scheme is quite dissipative and the shocks along the diagonal are smeared. On the other hand, the schemes based on splitting resolve the shocks very well. The central vortex is resolved by both the HLL/SUS and the HLLC/SUS scheme, and the shocks are much sharper than the features computed by the HLL3 solver for the full MHD equations. A thorough quantitative comparison is provided by considering the maximum pressures in Table 3.3.2 for different mesh resolutions. From Table 3.3.2, we find that at relatively coarse mesh resolutions (upto 400×400 mesh points), the splitting solvers have much higher resolutions (measured in terms of maximum pressure) than the standard HLL and HLL3 solvers. In fact, even the HLL/SUS leads to sharper resolution of the solution than the more expensive HLL3 solver. Similarly, both the splitting solvers compare very well with the Roe solver. In fact, the HLLC/SUS leads to almost the same maximum

M	HLL	HLL(Pr)	HLL3	HLL3(Pr)	HLL/SUS	HLLC/SUS	HLLC/LxF	Roe
100	4.00	4.01	4.41	4.42	4.94	5.04	4.61	5.27
200	4.74	4.76	4.94	4.95	5.39	5.41	4.71	5.39
400	5.11	–	5.21	–	5.79	5.81	5.00	5.88
800	–	–	–	–	6.05	6.07	5.26	–
1600	–	–	–	–	6.21	6.22	5.52	–

M	HLL	HLL(Pr)	HLL3	HLL3(Pr)	HLL/SUS	HLLC/SUS	HLLC/LxF	Roe
100	1.92	0.00	2.81	0.00	4.17	4.28	0.00	7.77
200	1.77	0.00	2.93	0.00	3.23	3.32	0.00	6.94
400	1.47	–	2.60	–	2.46	2.50	0.00	5.64
800	–	–	–	–	1.85	1.87	0.00	–
1600	–	–	–	–	1.38	1.39	0.00	–

Table 3.3.2: Maximum pressure (top) and the L^1 norm of the divergence defined by (3.2.18) (bottom) at time $t = \pi$ for the Orszag-Tang vortex, for different schemes using a $M \times M$ grid.

pressure as the Roe solver. It should added that the computational cost of the Roe solver is considerably higher than the HLLC/SUS solver.

One would expect that this high accuracy of the splitting based solvers should come at a price of reduced stability. On the contrary, Table 3.3.2 shows that the splitting based solvers of this paper do not crash even for 1600×1600 mesh points and show increased resolution on these very fine meshes. On the other hand, the standard HLL, HLL3 and Roe solvers crashed on 800×800 and finer meshes due to instabilities. Thus on this test problem, the splitting based HLL solvers are at least as accurate as the Roe solver and more accurate than the HLL solvers and are far more stable.

One possible explanation of this behavior is divergence errors. We compute the standard discrete divergence (3.2.18) and show the results in Table 3.3.2. The initial data has zero divergence, but the solution has several shocks, and numerical solutions may have non-zero divergence. The standard HLL, HLL3 and Roe does not preserve the divergence constraint. The splitting based solvers have some divergence cleaning built into them since they are based on adding the Godunov-Powell source term. Yet, we observe that on coarse meshes, the HLLC/SUS scheme has larger divergence errors than the HLL3 scheme. This could be due to the periodic boundary conditions which re-introduce any non-zero divergence swept away from the domain. Observe from Table 3.3.2, that the divergence errors due to the HLL/SUS and HLLC/SUS reduce with increasing mesh resolution. In fact, the divergence error due to the HLLC/SUS is lower than the errors due to both HLL3 scheme and the Roe scheme on the 400×400 mesh. This behaviour of the divergence error might be a reason for the robustness of the splitting based solvers.

Even the HLLC/LxF scheme is fairly robust and we did not observe any crashes. The numerical resolution of the HLLC/LxF scheme is inferior to that of the HLL/SUS and the HLLC/SUS schemes in this case, even though HLLC/LxF preserve divergence. The HLLC/TF scheme crashed even on the coarse 100×100 mesh in this test case.

In order to investigate the connection between divergence errors, stability and overall

accuracy, we have tested versions of the HLL, HLL3 and Roe solvers with additional divergence "cleaning". As mentioned in the introduction, a wide variety of divergence cleaning procedures have been proposed, and their relative merits/demerits have been discussed at length, see [80] and references therein. On this particular problem, we decided to couple the HLL and HLL3 solvers with divergence cleaning by the projection method designed in [22] and described in [80]. The projection method is based on the Hodge decomposition of $\mathbf{B}$ and involves projecting $\mathbf{B}$ to a divergence free field at the end of each time step by solving a Poisson equation. We chose the central form of discrete divergence (3.2.18) and solve the resulting discrete Poisson's equation by a preconditioned conjugate gradient method suggested in [80]. The method is considerably (by several orders of magnitude) more expensive than the basic finite volume schemes as the Poisson solver is used at every time step. The resulting schemes were called HLL(Pr) and HLL3(Pr) indicating that the HLL and HLL3 solvers were coupled with projection based divergence cleaning. The quantitative results with the HLL(Pr) and HLL3(Pr) schemes are shown in table 3.3.2. As shown in this table, for coarse meshes up to 200×200 mesh – the HLL(Pr) and HLL3(Pr) keep divergence zero. But, the quality of numerical solution is very very similar to that of the HLL and HLL3 schemes. In fact, the accuracy (measured by the maximum pressure) is practically unchanged when the HLL and HLL3 solvers were equipped with divergence cleaning. This indicates that controlling divergence or preserving the divergence constraint does not increase the accuracy of the scheme. More surprisingly, the HLL(Pr) and HLL3(Pr) schemes crashed even on a 400×400 mesh at times close to $t = \pi/3$ i.e., at one-third of the final time. The results obtained just before the crash showed oscillations near the shocks, and these oscillations may have caused negative pressure. One possible explanation of the oscillations is that the Poisson solver is second order accurate and can introduce slight oscillations. Without divergence cleaning, the HLL and HLL3 solvers did not crash at this mesh resolution (although they crashed on finer meshes).

This test indicates that divergence errors are not necessarily the only cause of instabilities on multi-dimensional MHD simulations, and that divergence cleaning itself can cause instability.

Hence, from this test problem, it appears that the splitting based HLL/SUS and HLLC/SUS solvers are both more accurate (and as accurate as the Roe solver) as well as stable compared with the standard schemes.

3.3.4 Rotor Problem

This two dimensional test problem is another standard benchmark for numerical solutions of the MHD equations and was first reported in [80].

The computational domain is $(\mathbf{x}, t) \in [0,1]^2 \times [0, 0.295]$ with artificial Neumann type boundary conditions. The initial data are given by

$$\rho = \begin{cases} 10.0 & \text{if } r < 0.1, \\ 1 + 9f(r) & \text{if } 0.1 \leq r < 0.115, \\ 1.0 & \text{otherwise,} \end{cases}$$

with $r(\mathbf{x}) = |\mathbf{x} - (0.5, 0.5)|$ and

$$f(r) = \frac{23 - 200r}{3}.$$

The other variables are initially

$$\left(\rho u^1, \rho u^2\right) = \begin{cases} (-(10y-5)\rho, (10x-5)\rho) & \text{if } r < 0.1, \\ (-(10y-5)f(r)\rho, (10x-5)f(r)\rho) & \text{if } 0.1 \le r < 0.115, \\ (0.0, 0.0) & \text{otherwise,} \end{cases}$$

$$\left(\rho u^3, B^1, B^2, B^3, p\right) = \left(0.0, 2.5/\sqrt{\pi}, 0.0, 0.0, 0.5\right).$$

The initial velocity and magnetic fields are such that the variables are rotated in the domain. The pressure drops to very low values in the center, and this test case is set up in order to determine how a scheme handles low pressures. We present numerical results in Table 3.3.3 and in Figure 3.3.4. In Figure 3.3.4, we plot the pressure at the final time on

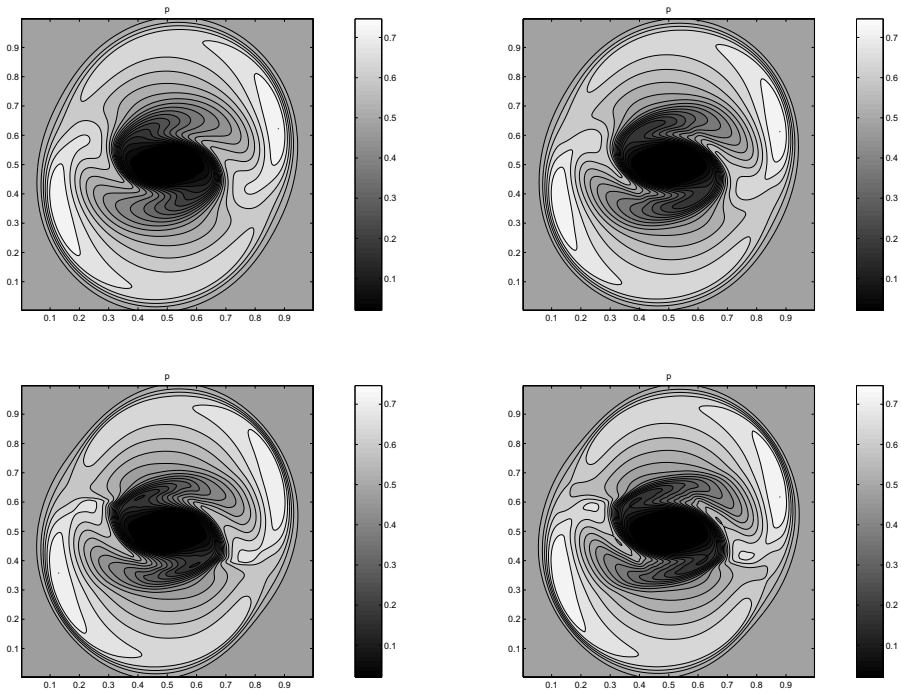

Figure 3.3.4: Pressure at $t = 0.295$ for the Rotor problem on a 200×200 mesh. Top left: HLL, top right: HLL/SUS, bottom left: HLL3, bottom right: HLLC/SUS.

a 200×200 mesh and compare the HLL, HLL3, HLL/SUS and HLLC/SUS schemes. At

this resolution, we see that the differences in the all the solvers is not as pronounced as the Orszag-Tang vortex even though the HLLC/SUS has the best resolution among the four solvers. We compute the solutions on a series of meshes and report results in Table 3.3.3. In the absence of any accepted measure of errors, we report divergence errors in the L^1 norm. From the table, we find that the HLL/SUS and HLLC/SUS solvers are stable even at the fine resolution of 1600×1600 mesh points. Despite the very low pressures, these solvers did not crash for any of the mesh resolutions that we ran in this case. On the other hand, the HLL, HLL3 and Roe solvers crashed at the resolution of 800×800 mesh points due to negative pressures. The divergence errors generated with both the HLL/SUS and HLLC/SUS schemes were quite low on this test problem. The HLLC/LxF scheme was stable but dissipative while the HLLC/TF crashed at all resolutions that we tested . To further investigate the effect of divergence errors on stability, we decided to

M	HLL	HLL2(Ps)	HLL3	HLL3(Ps)	HLL/SUS	HLLC/SUS	Roe
100	6.9e-2	6.4e-2	1.1e-1	9.7e-2	7.1e-2	7.8e-2	1.2e-1
200	6.3e-2	6.2e-2	9.3e-2	9.4e-2	5.5e-2	6.1e-2	1.0e-1
400	5.2e-2	–	7.3e-2	–	4.3e-2	4.6e-2	9.9e-2
800	–	–	–	–	3.2e-2	3.4e-2	–
1600	–	–	–	–	2.3e-2	2.5e-2	–

Table 3.3.3: The discrete divergence defined by (3.2.18) at $t = 0.295$ for the Rotor problem using a $M \times M$ grid.

test a different divergence cleaning technique (than the projection approach used for the Orszag-Tang vortex) for the HLL and HLL3 solvers. As this problem has non-reflecting boundary conditions, we can employ divergence cleaning by the Godunov-Powell source term technique [65]. We implement the discretization of the Godunov-Powell source term described in [66] where the authors used a central discretization of the divergence terms on the right hand sides of (3.1.10) and evaluated the rest of the right hand side at the given cell. The resulting HLL and HLL3 schemes together with this discretization of the source term were denoted by HLL(Ps) and HLL3(Ps), and the divergence errors are shown in Table 3.3.3. As shown in this table, the Powell source term did not affect the divergence errors much. Furthermore, both HLL(Ps) and HLL3(Ps) crashed on a 400×400 mesh. This crash was probably due to slight oscillations introduced by the source term. In [31], we showed that central discretizations of Powell source term can lead to oscillations even for the induction equation (3.1.4). This also happens for the MHD equations as shown by this test example.

3.3.5 Two-dimensional Riemann problem

This two-dimensional Riemann problem was proposed in [78] as test case to compare stability, resolution as well as divergence control. The computational domain is $(\mathbf{x}, t) \in [0, 0.8]^2 \times [0, 0.1]$ with Neumann boundary conditions. The initial conditions are given by

$$(\rho, p) = \begin{cases} (10, 15), & \text{if } x < 0.4,\ y < 0.4, \\ (1, 1/2), & \text{otherwise.} \end{cases} \tag{3.3.4}$$

Furthermore $\mathbf{B} = 1/\sqrt{2}(1,1,0)$ and $\rho\mathbf{u} = 0$.

This is a two-dimensional Riemann problem and the solution has a fairly complicated structure. In Table 3.3.4 we present the divergence errors in L^1. The most notable feature

M	HLL	HLL3	HLL/SUS	HLLC/SUS	HLLC/TF	Roe
125	2.9e-1	2.9e-1	2.9e-1	2.9e-1	5.8e-3	3.1e-1
250	2.9e-1	3.0e-1	2-9e-1	2.9e-1	4.9e-3	3.1e-1
500	3.0e-1	3.0e-1	2.9e-1	2.9e-1	3.5e-1	3.1e-1
1000	3.0e-1	3.0e-1	2.9e-1	2.9e-1	–	3.1e-1
2000	3.0e-1	3.0e-1	3.0e-1	3.0e-1	–	3.1e-1

Table 3.3.4: Two dimensional Riemann problem; the L^1 norm of the discrete divergence defined by (3.2.18), using a $M \times M$ mesh.

of this table is that the divergence does not seem to decrease under mesh refinement. However, the quality of the computed solutions does not seem to suffer from this, and we observe numerical convergence. The divergence errors are roughly the same for all schemes. That the divergence errors did not prevent a convergence is also illustrated in Figure 3.3.5, where we show the B^2 component computed for the HLLC/SUS scheme for the different mesh sizes. From this figure it is apparent that the approximations converge to some limit as the mesh size decreases. In this test case, none of the schemes other than the HLLC/TF crashed, even at 2000×2000 mesh points.

3.4 Conclusion

We have presented finite volume schemes for the ideal MHD equations. Our schemes are based on splitting the ideal MHD equations into two parts: a fluid part consisting of an extended Euler system (3.2.2) with the magnetic forces as source terms, and a magnetic part consisting of the magnetic induction equation (3.1.4) with fluid velocity driving the evolution of the magnetic field. The extended Euler equations are solved by designing HLL two wave and HLL three wave solvers with staggered magnetic fields. This form of the equations leads to an implicit upwinding of the magnetic force terms while retaining conservation of the fluid variables. The magnetic induction equation is solved by stable upwind schemes designed in a recent paper [31]. The schemes are based on adding a suitable Godunov-Powell source term and upwinding this source term. The two types of schemes are combined either simultaneously or using an operator-splitting procedure.

We have tested the schemes in a series of benchmark numerical experiments and compared them with standard HLL and Roe type approximate Riemann solvers. In the one-dimensional test cases, the HLL/SUS and the HLLC/SUS schemes are comparable in their accuracy to the standard HLL and HLL three wave solvers. The HLLC/LxF scheme was also reasonably accurate. HLLC/TF scheme was even more accurate than the HLLC/SUS scheme but the resulting approximations contained small oscillations. Although we were unable to prove that HLL/SUS and HLLC/SUS are positivity preserving in one space dimension, we present numerical evidence showing that these schemes are positivity preserving in practice.

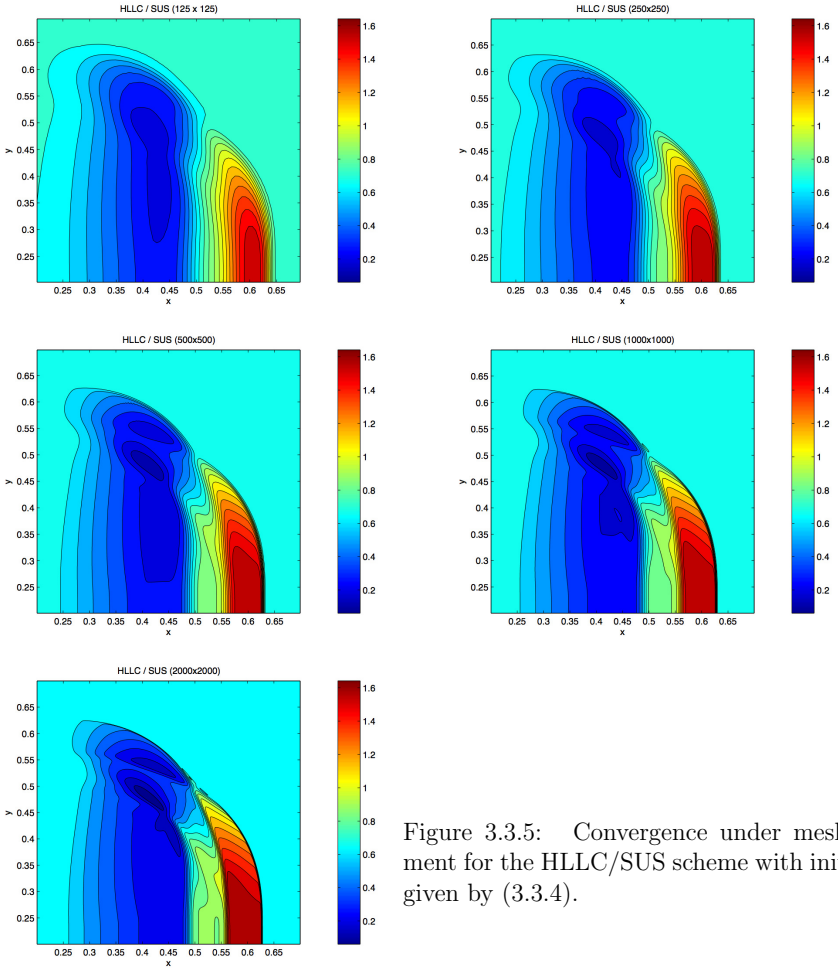

Figure 3.3.5: Convergence under mesh refinement for the HLLC/SUS scheme with initial data given by (3.3.4).

The differences between the schemes were more pronounced in the two-dimensional test cases. We observed that the splitting based HLL/SUS and HLLC/SUS schemes were more accurate than the standard HLL and HLL-three solvers on coarse meshes. In fact, the HLLC/SUS scheme was as accurate as the Roe scheme on some experiments. On fine meshes, the standard schemes crashed due to negative pressures, whereas the HLL/SUS, HLLC/SUS and HLLC/LxF scheme were stable and led to a good approximation of complex flow features. Furthermore, we also added extra divergence cleaning to the standard HLL and HLL-three solvers in form of the projection method and the discretized Godunov-Powell source term. These divergence cleaning technique did not increase the stability of the standard HLL solvers. This should be contrasted with the robustness observed for the splitting, particularly on very fine meshes.

Given the fact that the HLL/SUS and HLLC/SUS schemes are simpler to design, easier to implement, as accurate and more stable than the standard HLL three and Roee solvers, these schemes can replace existing HLL and Roe solvers in practical computations.

4

High order FV schemes for the Godunov-Powell form of the ideal MHD equations in multi-dimensions

F. G. Fuchs, A. D. McMurry, S. Mishra, N.H. Risebro, K. Waagan
preprint

Keywords: Conservation laws, MHD, divergence constraint, upwinded source terms, high-order schemes.

Abstract

We design stable and high-order accurate finite volume schemes for the ideal MHD equations in multi-dimensions. The finite volume schemes are based on three- and five-wave approximate Riemann solvers of the HLL-type, with the novelty that we allow a varying normal magnetic field. This is achieved by considering the semi-conservative Godunov-Powell form of the MHD equations. The Godunov-Powell source term is discretized in an upwind manner by utilizing the structure of the HLL-type solvers. Second-order versions of the ENO- and WENO-type are proposed, together with suitable modifications to preserve positive pressure and density. The first- and second-order schemes are tested on a suite of numerical experiments demonstrating a very satisfactory resolution and as stability even on very fine meshes.

4.1 Introduction

Many interesting problems in astrophysics, solar physics and engineering involve macroscopic plasma models and are usually described by the equations of ideal magnetohydrodynamics (MHD). In these models, the variables of interest are the mass density of the plasma ρ, the velocity field $\mathbf{u} = (u_1, u_2, u_3)^T$, the magnetic field $\mathbf{B} = (B_1, B_2, B_3)^T$, the pressure p and the total energy E. The unknowns obey the following conservation (balance) laws (see [66] for details),

(i.) Conservation of mass: Mass of a plasma is conserved, resulting in the standard mass conservation,

$$\rho_t + \operatorname{div}(\rho \mathbf{u}) = 0.$$

(ii.) Faraday's law: The magnetic flux across a surface $\mathbf{S}$ bounded by a curve $\delta\mathbf{S}$ is given by Faraday's law

$$-\frac{d}{dt}\int_S \mathbf{B}\cdot\mathbf{dS} = \int_{\delta S} E\cdot dl.$$

By using Stokes theorem and the fact that the electric field in a co-moving frame is zero at infinite conductivity, Faraday's law leads to

$$\mathbf{B}_t + \mathrm{curl}(\mathbf{B}\times\mathbf{u}) = -\mathbf{u}(\mathrm{div}\mathbf{B}). \tag{4.1.1}$$

The above equation is termed the magnetic induction equation and can also be written in the following divergence form,

$$\mathbf{B}_t + \mathrm{div}(\mathbf{u}\otimes\mathbf{B} - \mathbf{B}\otimes\mathbf{u}) = -\mathbf{u}(\mathrm{div}\mathbf{B}).$$

(iii.) Conservation of Momentum: In differential form, the conservation of momentum is

$$(\rho\mathbf{u})_t + \mathrm{div}(\rho\mathbf{u}\otimes\mathbf{u} + p\mathcal{I}) = \mathbf{J}\times\mathbf{B},$$

where $\mathbf{J}$ denotes the current density and $\mathcal{I}$ the 3×3 identity matrix. The Lorentz force exerted by the magnetic field is given by $\mathbf{J}\times\mathbf{B}$. Under the assumptions of ideal MHD, Ampere's law expresses the current density as

$$\mathbf{J} = \mathrm{curl}(\mathbf{B}).$$

Using standard vector identities results in the following semi-conservative form,

$$(\rho\mathbf{u})_t + \mathrm{div}\left(\rho\mathbf{u}\otimes\mathbf{u} + (p+\frac{1}{2}\mathbf{B}^2)\mathcal{I} - \mathbf{B}\otimes\mathbf{B}\right) = -\mathbf{B}(\mathrm{div}\mathbf{B}).$$

(iv.) Conservation of energy: Defining the hydrodynamic energy of an ideal gas as

$$E^{\mathrm{hd}} = \frac{p}{\gamma-1} + \frac{1}{2}\rho\mathbf{u}^2,$$

and using the conservation of this energy results in

$$E^{\mathrm{hd}}_t + \mathrm{div}((E^{\mathrm{hd}}+p)\mathbf{u}) = \mathbf{J}\cdot(\mathbf{B}\times\mathbf{u}).$$

The right hand side represents the change in energy due to the magnetic field. By using standard vector identities and Ampere's law, we obtain

$$\mathbf{J}\cdot(\mathbf{B}\times\mathbf{u}) = (\mathbf{B}\cdot\frac{\partial\mathbf{B}}{\partial t} - (\mathbf{u}\cdot\mathbf{B})(\mathrm{div}\mathbf{B}) - \mathrm{div}(\mathbf{B}\cdot\mathbf{B})\mathbf{u} - (\mathbf{u}\cdot\mathbf{B})\mathbf{B}).$$

Defining the total energy of the plasma as $E = E^{\mathrm{hd}} + \frac{1}{2}\mathbf{B}^2$, energy conservation takes the form

$$E_t + \mathrm{div}((E+p+\frac{1}{2}\mathbf{B}^2)\mathbf{u} - (\mathbf{u}\cdot\mathbf{B})\mathbf{B}) = -(\mathbf{u}\cdot\mathbf{B})(\mathrm{div}\mathbf{B}).$$

Combining all the above balance laws leads to the following semi-conservative form of the ideal MHD equations,

$$\begin{aligned} \rho_t + \mathrm{div}(\rho\mathbf{u}) &= 0, \\ (\rho\mathbf{u})_t + \mathrm{div}(\rho\mathbf{u}\otimes\mathbf{u} + (p+\frac{1}{2}|\mathbf{B}|^2)I - \mathbf{B}\otimes\mathbf{B}) &= -\mathbf{B}(\mathrm{div}\mathbf{B}), \\ \mathbf{B}_t + \mathrm{div}(\mathbf{u}\otimes\mathbf{B} - \mathbf{B}\otimes\mathbf{u}) &= -\mathbf{u}(\mathrm{div}\mathbf{B}), \\ E_t + \mathrm{div}((E+p+\frac{1}{2}|\mathbf{B}|^2)\mathbf{u} - (\mathbf{u}\cdot\mathbf{B})\mathbf{B}) &= -(\mathbf{u}\cdot\mathbf{B})(\mathrm{div}\mathbf{B}). \end{aligned} \tag{4.1.2}$$

The above semi-conservative form is also called the Godunov-Powell form, and the source on the right-hand side of (4.1.2) is called the Godunov-Powell source term. Magnetic monopoles have not been observed in nature (although their existence has been hypothesized in a number of quantum regimes by both the unified field theory as well as string theory). Hence, it is common to assume that the magnetic field is solenoidal, i.e., it satisfies the divergence constraint,

$$\mathrm{div}(\mathbf{B}) \equiv 0. \tag{4.1.3}$$

Under this constraint, the source terms in (4.1.2) are zero and the constraint is explicitly added to the equations to obtain the following conservative standard form of the ideal MHD equations,

$$\begin{aligned} \rho_t + \mathrm{div}(\rho\mathbf{u}) &= 0, \\ (\rho\mathbf{u})_t + \mathrm{div}(\rho\mathbf{u}\otimes\mathbf{u} + (p+\frac{1}{2}|\mathbf{B}|^2)I - \mathbf{B}\otimes\mathbf{B}) &= 0, \\ \mathbf{B}_t + \mathrm{div}(\mathbf{u}\otimes\mathbf{B} - \mathbf{B}\otimes\mathbf{u}) &= 0, \\ E_t + \mathrm{div}((E+p+\frac{1}{2}|\mathbf{B}|^2)\mathbf{u} - (\mathbf{u}\cdot\mathbf{B})\mathbf{B}) &= 0, \\ \mathrm{div}\mathbf{B} &= 0. \end{aligned} \tag{4.1.4}$$

Taking divergence on both sides of the magnetic induction equation (4.1.1) yields,

$$(\mathrm{div}\mathbf{B})_t + \mathrm{div}(\mathbf{u}(\mathrm{div}\mathbf{B})) = 0. \tag{4.1.5}$$

This means that any solenoidal initial magnetic field remains divergence free. Hence, for smooth solutions, the semi-conservative form (4.1.2) is equivalent to the standard form (4.1.4), if the initial magnetic field is divergence free.

Despite their formal equivalence, the two forms, (4.1.4) and (4.1.2), differ in some respects. We believe that it is more natural to consider and discretize the semi-conservative form (4.1.2), since the derivation from first principles gives (4.1.2). Furthermore, (4.1.2) is Galilean invariant, whereas the standard form (4.1.4) is not. From a mathematical perspective, the semi-conservative form (4.1.2) was shown to be symmetrized by the physical entropy in [35], leading to stability estimates [12]. The standard form (4.1.4) is not symmetrizable.

The standard form (4.1.4) (semi-conservative form (4.1.2)) is a system of conservation (balance) laws. Eigenvalue analysis, see [68, 12], shows that the system is hyperbolic but

not strictly hyperbolic. Solutions are typically complicated and contain interesting discontinuities like shock waves, contact discontinuities, compound and intermediate shocks. Even for "simple" initial value problems, such as the Riemann problem, we do not have existence or well-posedness results. This means that numerical simulations are the main tools to study solutions of these equations.

Finite volume schemes are among the most efficient and widely used numerical methods for the numerical solution of conservation (balance) laws. In these methods (see [50]), the computational domain is divided into cells, and cell-averages of the conserved quantities are evolved by integrating the balance law over the cell. The update requires numerical fluxes, defined in terms of exact or approximate solutions of Riemann problems (along the normal direction) at each cell interface. Higher-order spatial accuracy is recovered by employing non-oscillatory piecewise polynomial reconstructions like second-order TVD ([81]), higher-order ENO ([40]) and WENO ([72]) methods. Higher-order temporal accuracy results from using stability-preserving Runge-Kutta methods ([37]).

Finite volume schemes for the MHD equations have been employed with a fair amount of success. The Riemann problem is too complicated to solve exactly ([79]), and approximate Riemann solvers are employed to define numerical fluxes. Linearized solvers of the Roe-type ([68, 24]) have been devised but often give negative pressures and densities, see [32] for examples. An alternative is to use approximate Riemann-solvers of the HLL-type ([41]). These solvers approximate the wave-structure of the Riemann problem, with up to eight waves, by a smaller number of waves. Three-wave HLL solvers have been designed in [53, 36, 20] and five-wave solvers in [59, 20]. Some of these solvers ([36, 59, 20]) are proved to preserve positive pressures and densities. They also typically ensure that the second law of thermodynamics is not violated, referred to as entropy stability, which is not easily achieved with linearized solvers. Numerical results showing the robustness of these HLL-solvers, particularly in one space dimension, have been presented, see [59, 20].

However, the extension of one-dimensional numerical fluxes to approximate multi-dimensional MHD in standard form (4.1.4) is not straightforward. The divergence constraint (4.1.3) in one-dimension implies that the normal magnetic field must be a constant in space. HLL-type solvers like the ones described in [36, 59] use this information in their definitions of speeds and states. For multi-dimensional MHD, the magnetic field in each normal direction is no longer constant. Consequently, it is not trivial to extend the HLL-solvers in this case. One possible solution consists in using an average of the normal magnetic field across each interface in the expressions. This somewhat arbitrary choice may destroy the stability properties of the solvers.

Another highly non-trivial aspect in several dimensions is the treatment of the divergence constraint $\mathrm{div}\mathbf{B} = 0$. Standard finite volume schemes will generate divergence errors, and these can induce instabilities, see [80]. A popular method to remove divergence is the projection method of [22]. In this method the non-solenoidal approximate magnetic field is corrected at each time step by using an elliptic solver. The method leads to solenoidal fields, but is computationally expensive on account of the elliptic solver. Other stability issues with this method have been discussed in [70, 80].

A popular divergence cleaning method consists in staggering the discretizations of the velocity and magnetic field, this can be used in to design methods leading to a (discrete) divergence free magnetic field. Variants of this method have been proposed in [30, 26,

11, 70, 71] and references therein. Staggering of the variables leads to complications when parallelizing the method, and in designing variable grid methods. Unstaggered variants of this approach have been proposed in [77, 78, 57]. A thorough comparison of divergence cleaning methods was performed in [80]. Another potential problem with both the staggering and projection techniques lies in their numerical stability. In a recent paper [32], we provided examples where the projection method was quite stable on coarse meshes, but exhibited instabilities when the mesh was refined. We have also observed similar behavior for the staggered mesh methods.

A third alternative for divergence cleaning was proposed in [65] and consists of discretizing the semi-conservative Godunov-Powell form (4.1.2). In [65, 66], a linearized solver is used to define numerical fluxes and a simple centered discretization is proposed for the Godunov-Powell source term in (4.1.2). Note that (4.1.5) suggests the initial divergence errors will be transported out of the domain by the flow. In a recent paper [31], examples were constructed showing that a centered discretization of the Godunov-Powell source term can lead to numerical instabilities, even for the simple case of the linear magnetic induction equation (4.1.1). Hence, the Godunov-Powell source term has to be suitably "upwinded" to obtain stable discretizations. Suitable discretizations of a modified form of (4.1.2) based on splitting and on relaxation were proposed in [32] and [21] respectively. The solvers of [21] were proved to be positivity preserving and entropy stable. Second-order extensions of this approach have been presented in a recent paper [83].

Our aim in this paper is to design a stable and high-order accurate finite volume scheme for the semi-conservative form (4.1.2) of ideal MHD in multi-dimensions. We base our approach on the following three ingredients,

- We derive HLL-type three-wave and five-wave approximate Riemann solvers for the semi-conservative form (4.1.2). The fluxes are defined in terms of approximate solutions to Riemann problems (in the normal direction) at each interface. The main difference between existing solvers and our approach lies in the fact that we allow the normal magnetic field to vary across the interface. The resulting solvers extend the three-wave solver of [36] and the highly popular five-wave solver of [59] to non-constant normal magnetic fields and hence trivially to multi-dimensions.

- We discretize the Godunov-Powell source term in (4.1.2) by using the states and speeds of the HLL solvers to calculate the source term in each direction. This is simply and naturally achieved by taking the usual cell averages. Thus, the source term is automatically upwinded.

- Second-order spatial accuracy is obtained by designing suitable ENO and WENO-type reconstructions. Standard ENO-WENO reconstructions are modified to ensure that the resulting schemes preserve positive pressures and densities. We rely on the results of [14, 62] and of a recent paper [83] to design these modifications. Second-order accurate discretizations of the Godunov-Powell source term are also proposed. Second-order temporal accuracy is obtained by using Runge-Kutta methods.

The above ingredients are combined to obtain a second-order finite volume scheme for MHD equations (4.1.2) in multi-dimensions. The resulting schemes are very simple to

implement. Although we are unable to provide rigorous stability proofs, we validate the resulting schemes on a wide variety of benchmark numerical experiments. The numerical results on a sequence of meshes (including uncommonly fine meshes) demonstrate that both the first- and the second-order versions of our schemes are numerically stable.

Stability is the key to numerically resolve details on very fine meshes. We would like to mention that highly resolved solutions are not widely reported in the literature, we suspect that this is due to numerical instabilities.

The rest of this paper is organized as follows: the numerical schemes are presented in Section 4.2 and the numerical experiments are reported in Section 4.3.

4.2 Numerical Schemes

For notational simplicity, we focus on the semi-conservative form of the MHD equations (4.1.2) in two space dimensions,

$$\mathbf{W}_t + \mathbf{f}(\mathbf{W})_x + \mathbf{g}(\mathbf{W})_y = \mathbf{s}^1(\mathbf{W}, \mathbf{W}_x) + \mathbf{s}^2(\mathbf{W}, \mathbf{W}_y), \tag{4.2.1}$$

where

$$\mathbf{W} = (\rho, \rho u_1, \rho u_2, \rho u_3, B_1, B_2, B_3, E)^T,$$

is the vector of conserved variables, and the fluxes are given by

$$\mathbf{f}(\mathbf{W}) = \begin{pmatrix} \rho \\ \rho u_1^2 + \pi_1 - \frac{B_1^2}{2} \\ \rho u_1 u_2 - B_1 B_2 \\ \rho u_1 u_3 - B_1 B_3 \\ 0 \\ u_1 B_2 - u_2 B_1 \\ u_1 B_3 - u_3 B_1 \\ (E + \pi_1) u_1 - u_1 \frac{B_1^2}{2} - B_1 (u_2 B_2 + u_3 B_3) \end{pmatrix},$$

$$\mathbf{g}(\mathbf{W}) = \begin{pmatrix} \rho \\ \rho u_1 u_2 - B_1 B_2 \\ \rho u_2^2 + \pi_2 - \frac{B_2^2}{2} \\ \rho u_1 u_3 - B_1 B_3 \\ u_2 B_1 - u_1 B_2 \\ 0 \\ u_2 B_3 - u_3 B_2 \\ (E + \pi_2) u_2 - u_2 \frac{B_2^2}{2} - B_2 (u_1 B_1 + u_3 B_3) \end{pmatrix},$$

where we have defined

$$\pi_1 = p + \frac{B_2^2 + B_3^2}{2}, \quad \pi_2 = p + \frac{B_1^2 + B_3^2}{2}. \tag{4.2.2}$$

Similarly, the Godunov-Powell source terms in (4.1.2) can be written explicitly as

$$\mathbf{s}^1(\mathbf{W},\mathbf{W}_x) = \begin{pmatrix} 0, \\ -(\frac{B_1^2}{2})_x \\ -B_2(B_1)_x \\ -B_3(B_1)_x \\ -u_1(B_1)_x \\ -u_2(B_1)_x \\ -u_3(B_1)_x \\ -u_1(\frac{B_1^2}{2})_x - (u_2B_2+u_3B_3)(B_1)_x \end{pmatrix},$$

$$\mathbf{s}^2(\mathbf{W},\mathbf{W}_y) = \begin{pmatrix} 0, \\ -B_1(B_2)_y \\ -(\frac{B_2^2}{2})_y \\ -B_3(B_2)_y \\ -u_1(B_2)_y \\ -u_2(B_2)_y \\ -u_3(B_2)_y \\ -u_2(\frac{B_2^2}{2})_y - (u_1B_1+u_3B_3)(B_2)_y \end{pmatrix}.$$

Note that we have used the chain rule $B_1(B_1)_x = (\frac{B_1^2}{2})_x$ and for $B_2(B_2)_y$. While true for smooth solutions, this formula may no longer hold when the magnetic field has discontinuities. However, using this formulation proved to be robust in practice.

We approximate (4.2.1) in a domain $\mathbf{x} = (x,y) \in [X_l, X_r] \times [Y_b, Y_t]$. For simplicity, the domain is discretized by a uniform grid in both directions with the grid spacing Δx and Δy. We set $x_i = X_l + i\Delta x$ and $y_j = Y_b + j\Delta y$, and $I_{i,j} = [x_{i-1/2}, x_{i+1/2}) \times [y_{j-1/2}, y_{j+1/2})$. The cell average of the unknown vector $\mathbf{W}$ at time t^n is denoted $\mathbf{W}_{i,j}^n$.

A standard finite volume scheme (first-order in both space and time) is obtained by integrating the balance law (4.2.1) over the cell $I_{i,j}$ and the time interval $[t^n, t^{n+1}]$ with $t^{n+1} = t^n + \Delta t^n$, where the time-step Δt^n is determined by a suitable CFL condition. The resulting fully-discrete form of the scheme is

$$\mathbf{W}_{i,j}^{n+1} = \mathbf{W}_{i,j}^n - \frac{\Delta t^n}{\Delta x}(\mathbf{F}_{i+1/2,j}^n - \mathbf{F}_{i-1/2,j}^n) - \frac{\Delta t^n}{\Delta y}(\mathbf{G}_{i,j+1/2}^n - \mathbf{G}_{i,j-1/2}^n) + \Delta t^n(\mathbf{S}_{i,j}^1 + \mathbf{S}_{i,j}^2). \quad (4.2.3)$$

The flux $\mathbf{F}_{i+1/2,j}^n = \mathbf{F}(\mathbf{W}_{i,j}^n, \mathbf{W}_{i+1,j}^n)$ and the source $\mathbf{S}_{i,j}^1$ are hence determined from a solution to the following Riemann problem,

$$\mathbf{W}_t + \mathbf{f}(\mathbf{W})_x = \mathbf{s}^1(\mathbf{W},\mathbf{W}_x), \quad \mathbf{W}(x,0) = \begin{cases} \mathbf{W}_L & x < 0, \\ \mathbf{W}_R & x > 0. \end{cases} \quad (4.2.4)$$

Similarly, the flux $\mathbf{G}$ and the approximation of the Godunov-Powell source term $\mathbf{S}^2$ are given in terms of a Riemann problem in the y-direction. The Riemann problem (4.2.4) has an intricate solution involving up to eight waves. Therefore the solution to (4.2.4) is in practice replaced by a so called approximate Riemann solver (see e.g. [50]). The purpose of this section is to derive two such solvers. They will be given as functions of x/t (similarly to the exact solution), and we must ensure local conservation in order to end up with a scheme of the semi-conservative form (4.2.3).

4.2.1 HLL three-wave solver

To derive this solver we follow the approach of [36]. The approximate solution and fluxes for (4.2.4) are given by

$$\mathbf{W}^{\mathrm{HLL3}} = \begin{cases} \mathbf{W}_L & \text{if } \frac{x}{t} \le s_L, \\ \mathbf{W}_L^* & \text{if } s_L < \frac{x}{t} < s_M, \\ \mathbf{W}_R^* & \text{if } s_M < \frac{x}{t} < s_R, \\ \mathbf{W}_R & \text{if } s_R \le \frac{x}{t}, \end{cases} \qquad \mathbf{F}^{\mathrm{HLL3}}(\mathbf{W}_L, \mathbf{W}_R) = \begin{cases} \mathbf{F}_L & \text{if } \frac{x}{t} \le s_L, \\ \mathbf{F}_L^* & \text{if } s_L < \frac{x}{t} < s_M, \\ \mathbf{F}_R^* & \text{if } s_M < \frac{x}{t} < s_R, \\ \mathbf{F}_R & \text{if } s_R \le \frac{x}{t}. \end{cases} \tag{4.2.5}$$

Note that we do not enforce $\mathbf{F} = \mathbf{f}(\mathbf{W})$. The reason is that we allow π_1 of (4.2.2) to be a free variable, hence taking the role of the relaxation pressure in [20]. For consistency we have to set $\pi_1 = p + \frac{B_2^2 + B_3^2}{2}$ in $\mathbf{F}_L$ and $\mathbf{F}_R$. The outer wave speeds s_L and s_R model the fast magneto-sonic waves and are defined as in [36, 28], i.e.,

$$s_L = \min\left\{u_{1L} - c_{fL},\ \bar{u}_1 - \bar{c}_f\right\}, \quad s_R = \max\left\{u_{1R} + c_{fR},\ \bar{u}_1 + \bar{c}_f\right\}, \tag{4.2.6}$$

where $\bar{u}_1$ and $\bar{c}_f$ are the normal velocity and the fast wave speed of the Jacobian matrix $A((\mathbf{W}_L + \mathbf{W}_R)/2)$ respectively. This choice is important for numerical stability and accuracy.

In order to describe the solver, we need to determine the speed of the middle wave s_M and the intermediate states $\mathbf{W}_L^*, \mathbf{W}_R^*$. We follow [36] in letting the middle wave model a material contact discontinuity. Hence, the velocity field and the tangential magnetic fields are assumed to be constant across the middle wave. This allows defining $\mathbf{u}^* = \mathbf{u}_L^* = \mathbf{u}_R^*$, $B_2^* = B_{2L}^* = B_{2R}^*$ and $B_3^* = B_{3L}^* = B_{3R}^*$. Furthermore, the difference in our solver and the three-wave solver of [36] lies in the fact that we consider a non-constant normal magnetic field B_1. The normal magnetic field B_1 only jumps across the middle wave (modeling the linear degenerate "divergence wave" implied by (4.1.5)) and is constant across the outer waves.

We will impose local conservation across each wave to determine the various states. Local conservation across the outermost waves means that

$$s_L\mathbf{W}_L^* - \mathbf{F}_L^* = s_L\mathbf{W}_L - \mathbf{F}_L, \quad s_R\mathbf{W}_R - \mathbf{F}_R = s_R\mathbf{W}_R^* - \mathbf{F}_R^*. \tag{4.2.7}$$

Conservation across the middle wave s_M involves taking the source term $\mathbf{s}^1$ in (4.2.4) into account. The conservation relation is given by,

$$s_M\mathbf{W}_R^* - s_M\mathbf{W}_L^* = \mathbf{F}_R^* - \mathbf{F}_L^* + \mathbf{s}^{1,*} \tag{4.2.8}$$

where

$$\mathbf{s}^{1,*} = \begin{pmatrix} 0 \\ -\frac{(B_{1R})^2 - (B_{1L})^2}{2} \\ -B_2^*(B_{1R} - B_{1L}) \\ -B_3^*(B_{1R} - B_{1L}) \\ -\mathbf{u}^*(B_{1R} - B_{1L}) \\ -u_1^*\frac{(B_{1R})^2 - (B_{1L})^2}{2} - (u_2^*B_2^* + u_3^*B_3^*)(B_{1R} - B_{1L}) \end{pmatrix}, \tag{4.2.9}$$

amounts to integrating the source $\mathbf{s}^1$ in (4.2.4) across the wave fan (as described in the next section). The above expression follows from the assumption that B_1 jumps only across the middle wave while the velocity field and tangential components of the magnetic field remain constant. The use of the source term in the above conservation relations is the key difference in our approach and the one used in [36].

For any middle speed s_M, a straightforward application of the conservation relations (4.2.7) determines unique values of ρ^*_θ given by

$$\rho^*_\theta = \rho_\theta \frac{u_{1\theta} - s_\theta}{s_M - s_\theta}, \quad \theta \in \{L, R\} \tag{4.2.10}$$

Using conservation across all the three waves (adding (4.2.7) and (4.2.8)) results in the global conservation relation,

$$\mathbf{F}_R - \mathbf{F}_L = s_R \mathbf{W}_R - s_L \mathbf{W}_L + (s_M - s_R)\mathbf{W}^*_R + (s_L - s_M)\mathbf{W}^*_L + \mathbf{s}^{1,*}. \tag{4.2.11}$$

We can use the intermediate density states (4.2.10) and global conservation (4.2.11) to obtain

$$s_M = u^*_1 = \frac{\pi_{1R} - \pi_{1L} + \rho_R u_{1R}(u_{1R} - s_R) - \rho_L u_{1L}(u_{1L} - s_L)}{\rho_R(u_{1R} - s_R) - \rho_L(u_{1L} - s_L)}.$$

Similarly, one uses local conservation (4.2.7) across the two outer waves to obtain the intermediate "relaxed" pressures,

$$\pi^*_{1\theta} = \pi_{1\theta} + \rho_\theta(u_{1\theta} - s_\theta)(u_{1\theta} - s_M), \tag{4.2.12}$$

for $\theta \in \{L, R\}$. Note that conservation across the middle wave automatically implies that $\pi^*_{1L} = \pi^*_{1R}$, and that (4.2.12) confirms this assertion. The next step is to determine the tangential velocity and magnetic field. Using global conservation across the wave fan (4.2.11), we obtain that the intermediate values u^*_σ and B^*_σ satisfy the following two linear equations,

$$\alpha u^*_\sigma - \beta B^*_\sigma = c_\sigma, \quad -\beta u^*_\sigma - \zeta B^*_\sigma = d_\sigma, \quad \sigma \in \{2, 3\},$$

where

$$\begin{aligned} c_\sigma &= \rho_R u_{\sigma R}(u_{1R} - s_R) - \rho_L u_{\sigma L}(u_{1L} - s_L) - (B_{1R}B_{\sigma R} - B_{1L}B_{\sigma L}), \\ d_\sigma &= B_{\sigma R}(s_R - u_{1R}) - B_{\sigma L}(s_L - u_{1L}) - (B_{1L}u_{\sigma L} - B_{1R}u_{\sigma R}), \\ \alpha &= \rho_R(u_{1R} - s_R) - \rho_L(u_{1L} - s_L), \quad \zeta = s_R - s_L, \quad \beta = B_{1R} - B_{1L}. \end{aligned} \tag{4.2.13}$$

Solving the linear system (4.2.13), the intermediate tangential components of velocity and magnetic field are obtained as,

$$u^*_\sigma = \frac{\zeta c_\sigma - \beta d_\sigma}{\alpha\zeta + \beta^2}, \quad B^*_\sigma = \frac{-\alpha d_\sigma - \beta c_\sigma}{\alpha\zeta + \beta^2}. \tag{4.2.14}$$

Remark 4.2.1. In general, the denominator; $\alpha\zeta + \gamma^2$, in (4.2.14) can become small, leading to a degeneracy in the states. A simple calculation shows that $\alpha\zeta + \gamma^2 \neq 0$ if $(\rho_R c^R_f + \rho_L c^L_f)(s_R - s_L) > (B_{1R} - B_{1L})^2$. This condition can be ensured by "widening" the

wave fan slightly by modifying the fast wave speeds in (4.2.6). The resulting conditions are

$$s_R \geq u_{1R} + \frac{1}{2}(\max((u_{1L} - u_{1R}), 0)) + \tilde{c}_{fR}, \quad s_L \leq u_{1L} - \frac{1}{2}(\max((u_{1L} - u_{1R}), 0)) - \tilde{c}_{fL}, \tag{4.2.15}$$

where

$$\tilde{c}^2_{f\theta} = \frac{\gamma p_\theta}{\rho_\theta} + \frac{B^2_{1\theta}}{\rho_\theta}(1+\epsilon) + \frac{B^2_{2\theta} + B^2_{3\theta}}{\rho_\theta} + \sqrt{(\frac{\gamma p_\theta + |\mathbf{B}|^2_\theta}{\rho_\theta})^2 - 4\frac{\gamma p_\theta B^2_{1\theta}}{\rho^2_\theta}}, \quad \theta \in \{L, R\},$$

for some small positive ϵ. Using the conditions (4.2.15) to widen the wave fan ensures that the denominator $\alpha\zeta + \beta^2$ is never zero and the states are well defined.

Finally, the intermediate total energy states are determined by local conservation relations (4.2.7) to be

$$\begin{aligned} E^*_\theta = &\frac{E_\theta(u_{1\theta} - s_\theta) + \pi_{1\theta}u_{1\theta} - \pi^*_{1\theta}s_M + \frac{B^2_{1\theta}}{2}(u_{1\theta} - s_M)}{s_M - s_\theta} \\ &+ \frac{B_{1\theta}(B_{2\theta}u_{2\theta} + B_{3\theta}u_{3\theta} - B^*_{2\theta}u^*_{2\theta} - B^*_{3\theta}u^*_{3\theta})}{s_M - s_\theta}, \end{aligned}$$

for $\theta \in \{L, R\}$. Hence, all the intermediate states are determined explicitly. The intermediate fluxes are obtained in terms of the intermediate states by local conservation (4.2.7),

$$\mathbf{F}^*_L = \mathbf{F}_L + s_L(\mathbf{W}^*_L - \mathbf{W}_L), \quad \mathbf{F}^*_R = \mathbf{F}_R + s_R(\mathbf{W}^*_R - \mathbf{W}_R).$$

Combining the above expressions for the states and the fluxes, we write down our explicit flux formula for the three-wave solver as

$$\mathbf{F}^{H_3}_{i+1/2,j} = \begin{cases} \mathbf{F}_{i,j} & , \text{ if } s_{L,i+1/2,j} > 0, \\ \mathbf{F}^*_{i,j} & , \text{ if } s_{L,i+1/2,j} \leq 0 \wedge s_{M,i+1/2,j} \geq 0, \\ \mathbf{F}^*_{i+1,j} & , \text{ if } s_{M,i+1/2,j} < 0 \wedge s_{R,i+1/2,j} \geq 0, \\ \mathbf{F}_{i+1,j} & , \text{ if } s_{R,i+1/2,j} < 0. \end{cases} \tag{4.2.16}$$

Note that this may be discontinuous at $s_{M,i+1/2,j} = 0$ according to (4.2.8). Hence our choice of $\mathbf{F}^{H_3}$ in that case is merely a convention. It is the proper addition of the source term which ensures that the scheme is continuous.

Remark 4.2.2. If we assume that the normal magnetic field B_1 is constant i.e., $B_{1L} = B_{1R}$, then the three-wave solver defined above reduces to the three-wave solver derived in [36]. Hence, our three-wave solver extends the standard three-wave solver of [36] for the case of a non-constant normal magnetic field.

4.2.2 Discretization of the Godunov-Powell source term

In this section we explain (4.2.8), and specify the discrete source $\mathbf{S}^{1,n}_{i,j}$ in (4.2.3). The discrete source must be consistent with the Godunov-Powell source term in x-direction

$\mathbf{s}^1(\mathbf{W}, \mathbf{W}_x)$. It will be determined from our solution of the Riemann problem (4.2.4) along the x-direction at the cell interfaces $(x_{i+1/2}, y_j)$. The HLL three-wave approximate Riemann solver of the previous section provide us with the assumptions we need: The normal magnetic field jumps only across the contact-discontinuity modeled by the middle wave, while the velocity field and the tangential components of the magnetic field are constant across the middle wave.

Let T be a quantity that is constant with value T^* across the middle wave, then

$$(TB_x^1)(x,t) = T^*(B_{1R} - B_{1L})\delta(x + tu_1^*), \tag{4.2.17}$$

where δ denotes the Dirac delta function. If we assume that $|u_1^*|\,\Delta t^n \leq \Delta x$, integrating TB_x^1 over $(0, \Delta t^n) \times (-\Delta x, 0)$ yields

$$\frac{1}{\Delta x}\int_0^{\Delta t^n}\int_{-\Delta x}^{0} TB_x^1 dxdt = \Delta t^n T^* \frac{B_{1R} - B_{1L}}{\Delta x}\mathbf{1}_{\{u_1^*<0\}}, \tag{4.2.18}$$

where $\mathbf{1}_A$ denotes the characteristic function of the set A. Integration over $(0, \Delta t^n) \times (0, \Delta x)$ leads to

$$\frac{1}{\Delta x}\int_0^{\Delta t^n}\int_{0}^{\Delta x} TB_x^1 dxdt = \Delta t^n T^* \frac{B_{1R} - B_{1L}}{\Delta x}\mathbf{1}_{\{u_1^*>0\}},$$

under the same restriction, $|u_1^*|\,\Delta t^n \leq \Delta x$. Similarly, by again using the assumption that B_1 jumps only across the contact and T remains constant across it, we obtain that

$$\frac{1}{\Delta x}\int_0^{\Delta t^n}\int_{-\Delta x}^{0} T(\frac{B_1^2}{2})_x dxdt = \Delta t^n T^* \frac{B_{1R}^2 - B_{1L}^2}{2\Delta x}\mathbf{1}_{\{u_1^*<0\}},$$

and

$$\frac{1}{\Delta x}\int_0^{\Delta t^n}\int_{0}^{\Delta x} T(\frac{B_1^2}{2})_x dxdt = \Delta t^n T^* \frac{B_{1R}^2 - B_{1L}^2}{2\Delta x}\mathbf{1}_{\{u_1^*>0\}}. \tag{4.2.19}$$

Hence, we can derive (4.2.8) from (4.2.18)-(4.2.19) by observing that we must have

$$\mathbf{s}^{1,*} = \int_{t^n}^{t^{n+1}}\int_{-\Delta x}^{\Delta x} \mathbf{s}^1(\mathbf{W}^{H_3}, \mathbf{W}_x^{H_3}) dxdt.$$

The final scheme is defined by evolving the piecewise constant function $\mathbf{W}_{i,j}$ according to the approximate Riemann solver (4.2.5), and then taking the cell average of the conserved quantities. Hence, the scheme is determined by (4.2.7)-(4.2.8), yielding (4.2.16), and

$$\mathbf{S}_{i,j}^{1,n} = \mathbf{s}_{i-1/2,j}^{1,*}\mathbf{1}_{\{(s_{M,i-1/2,j}\geq 0)\}} + \mathbf{s}_{i+1/2,j}^{1,*}\mathbf{1}_{\{(s_{M,i+1/2,j}<0)\}}, \tag{4.2.20}$$

where $\mathbf{s}_{i\pm1/2,j}^{1,*}$ is defined in (4.2.9). For the case that $s_{M,i+1/2,j} = 0$ our choice here was dictated by our choice in (4.2.16). Integration along the y-direction is taken care of by the midpoint rule.

We emphasize that the discrete Godunov-Powell source term in each cell consists of contributions from Riemann solutions at the bordering interfaces and depends on the sign of the middle wave at each interface. Thus, the Godunov-Powell source term is suitably upwinded. Note that assuming the normal magnetic field B_1 to be constant for the whole domain leads to the source term being zero. This approach is novel (but see [20]), and is very different from the usual centered discretization of the Godunov-Powell source term ([66] and other references therein).

4.2.3 HLL five-wave solver

The three-wave solver of the previous section does not model Alfvén waves precisely, and instead diffuse these waves more than necessary. Alfvén waves can be approximated better by extending the three-wave solver to an HLL type five-wave solver. In addition to the three waves with wave speeds s_L, s_R and s_M, we add two new waves with speeds s_L^* and s_R^* respectively with the requirement that $s_L \leq s_L^* \leq s_M \leq s_R^* \leq s_R$. Hence, solution of the Riemann problem at each interface is approximated by four intermediate states $\mathbf{W}_L^*$, $\mathbf{W}_L^{**}$, $\mathbf{W}_R^{**}$ and $\mathbf{W}_R^*$. A five-wave solver for ideal MHD equations with constant normal magnetic fields was developed in [59] and we will extend this solver to the case of non-constant normal magnetic fields below.

The outer-wave speeds s_L and s_R are determined by (4.2.6) (using the correction (4.2.15)) as in the three-wave solver. We assume that the normal velocity is constant across the three inner waves i.e.,

$$s_M = u_{1L}^* = u_{1L}^{**} = u_{1R}^{**} = u_{1R}^*, \tag{4.2.21}$$

as the inner waves model a contact discontinuity and Alfvén waves, and the normal velocity remains constant across all three of them. Similarly, the waves with speeds s_L^* and s_R^* model Alfvén waves. Hence, as in [59], the density and the "relaxed" pressures are constant across them leading to

$$\rho_\theta^{**} = \rho_\theta^*, \quad \pi_{1\theta}^{**} = \pi_{1\theta}^*, \quad \theta \in \{L, R\}.$$

Furthermore, the wave with speed s_M models a contact discontinuity and the tangential components of the velocity and the magnetic field remain constant across it leading to

$$u_{\sigma L}^{**} = u_{\sigma R}^{**} = u_\sigma^{**}, \quad B_{\sigma L}^{**} = B_{\sigma R}^{**} = B_\sigma^{**}, \tag{4.2.22}$$

for $\sigma \in \{2, 3\}$. The normal magnetic field should only jump across the middle wave,i.e,

$$B_{1\theta}^* = B_{1\theta}^{**} = B_{1\theta}, \quad \theta \in \{L, R\}. \tag{4.2.23}$$

As a result of (4.2.22) and (4.2.23), the Godunov-Powell source term takes the same form as in (4.2.9) with u_σ^*, B_σ^* being replaced by u_σ^{**} and B_σ^{**} for $\sigma \in \{2, 3\}$. We denote this source term by $\mathbf{s}^{**,1}$.

Using local conservation (4.2.7) across the outermost waves and (4.2.21), we obtain unique values of ρ_θ^* of the form,

$$\rho_\theta^* = \rho_\theta \frac{u_{1\theta} - s_\theta}{s_M - s_\theta}, \quad \theta \in \{L, R\}. \tag{4.2.24}$$

Conservation across the entire wave fan leads to the following relation,

$$\mathbf{F}_R - \mathbf{F}_L = s_R\mathbf{W}_R - s_L\mathbf{W}_L + (s_R^* - s_R)\mathbf{W}_R^* + (s_M - s_R^*)\mathbf{W}^{**} + (s_L^* - s_M)\mathbf{W}_L^{**} + (s_L - s_L^*)\mathbf{W}_L^* + \mathbf{s}^{1,**}. \tag{4.2.25}$$

We can use the intermediate density states (4.2.24) and global conservation (4.2.25) to obtain the following expression for the middle speed,

$$u_{1,L}^* = u_{1,R}^* = s_M = \frac{\pi_{1R} - \pi_{1L} + \rho_R u_{1R}(u_{1R} - s_R) - \rho_L u_{1L}(u_{1L} - s_L)}{\rho_R(u_{1R} - s_R) - \rho_L(u_{1L} - s_L)}.$$

Note that this is the same expression as the middle speed in the three-wave solver. Similarly, one uses local conservation (4.2.7) across the two outer waves to obtain the intermediate "relaxed" pressures,

$$\pi^*_{1\theta} = \pi_{1\theta} + \rho_\theta(u_{1\theta} - s_\theta)(u_{1\theta} - s_M),$$

for $\theta \in \{L, R\}$. Note that $\pi^*_{1L} = \pi^*_{1R}$. Following [59], we can use conservation across the outer-most waves (4.2.7) and obtain a system of two linear equations for $u^*_{\sigma\theta}$ and $B^*_{\sigma\theta}$ for $\sigma = \{2, 3\}$. These equations can be explicitly solved to obtain,

$$u^*_{\sigma\theta} = u_{\sigma\theta} + \frac{B_{1\theta}B_{\sigma\theta}(u_{1\theta} - s_M)}{\rho_\theta(u_{1\theta} - s_\theta)(s_M - s_\theta) - (B_{1\theta})^2}, \quad B^*_{\sigma\theta} = B_{\sigma\theta}\frac{\rho_\theta(u_{1\theta} - s_\theta)^2 - (B_{1\theta})^2}{\rho_\theta(u_{1\theta} - s_\theta)(s_M - s_\theta) - (B_{1\theta})^2}. \tag{4.2.26}$$

Remark 4.2.3. The denominator in the above states (4.2.26) can become zero. This will typically occur in the degenerate case that the Alfvén speed $|B_1|/\sqrt{\rho}$ approaches the fast speed c_f. Therefore, it is natural to switch to the three-wave solver of the previous section when

$$\left|\rho_\theta(u_{1\theta} - s_\theta)(s_M - s_L) - (B_{1\theta})^2\right| < \epsilon\rho_\theta c^2_{f\theta}$$

for some small $\epsilon > 0$.

The intermediate energy states can be determined by local conservation (4.2.7) as

$$\begin{aligned} E^*_\theta = &\frac{E_\theta(u_{1\theta} - s_\theta) + \pi_{1\theta}u_{1\theta} - \pi^*_{1\theta}s_M + \frac{B^2_{1\theta}}{2}(u_{1\theta} - s_M)}{s_M - s_\theta} \\ &+ \frac{B_{1\theta}(B_{2\theta}u_{2\theta} + B_{3\theta}u_{3\theta} - B^*_{2\theta}u^*_{2\theta} - B^*_{3\theta}u^*_{3\theta})}{s_M - s_\theta}, \end{aligned}$$

for $\theta \in \{L, R\}$. The local conservation relations across the new waves imply that

$$s^*_L = s_M - \frac{|B_{1L}|}{\sqrt{\rho^*_L}}, \qquad s^*_R = s_M + \frac{B_{1R}}{\sqrt{\rho^*_R}}.$$

Hence the Alfvén wave speeds are accurately represented. Note that we use essentially the same Alfvén speeds as in [59], but account for the variation of the normal magnetic field across the contact discontinuity. Furthermore, conservation across the new waves reduces to

$$B^{**}_\sigma - B^*_{\sigma L} = \text{sign}\,(B_{1L})\sqrt{\rho^*_L}(u^{**}_\sigma - u^*_{\sigma L}), \quad B^{**}_\sigma - B^*_{\sigma R} = -\text{sign}\,(B_{1L})\sqrt{\rho^*_R}(u^{**}_\sigma - u^*_{\sigma R}). \tag{4.2.27}$$

These relations are identical to the exact Alfvén wave jump conditions. They imply that

$$\begin{aligned} u^{**}_\sigma &= \frac{\text{sign}\,(B_{1L})\sqrt{\rho^*_L}u^*_{\sigma L} + \text{sign}\,(B_{1R})\sqrt{\rho^*_R}u^*_{\sigma R} + B^*_{\sigma R} - B^*_{\sigma L}}{\text{sign}\,(B_{1L})\sqrt{\rho^*_L} + \text{sign}\,(B_{1R})\sqrt{\rho^*_R}} \\ B^{**}_\sigma &= \frac{\text{sign}\,(B_{1L})\sqrt{\rho^*_R}B^*_{\sigma L} + \text{sign}\,(B_{1R})\sqrt{\rho^*_L}B^*_{\sigma R} + \sqrt{\rho^*_L\rho^*_R}(u^*_{\sigma R} - u^*_{\sigma L})}{\text{sign}\,(B_{1L})\sqrt{\rho^*_R} + \text{sign}\,(B_{1R})\sqrt{\rho^*_L}} \end{aligned} \tag{4.2.28}$$

Remark 4.2.4. Observe that if

$$\operatorname{sign}(B_{1R}) \neq \operatorname{sign}(B_{1L}) \quad \text{and} \quad \rho_R^* = \rho_L^*, \tag{4.2.29}$$

the relations (4.2.27) can not be solved, and the formulas (4.2.28) break down. In this case we relax to the HLL three-wave solver of the previous section. This should be seen in light of the discontinuity in the jump conditions (4.2.27) in the nonstrictly hyperbolic case $B_1 = 0$. Furthermore, if $B_{1L} = 0$ and $B_{1R} \neq 0$ or vice versa, we get meaningful formulas, but we need to check that the jump conditions across the middle wave hold. They become

$$S_M \mathbf{W}_L^* - \mathbf{F}_L^* = S_M \mathbf{W}_R^{**} - \mathbf{F}_R^{**} + \mathbf{s}^{1,**},$$

which is easily verified. When $B_{1L} = B_{1R} = 0$, it simply means that $s_L^* = s_M = s_R^*$, hence we do not need to calculate the $**$-states. The jump conditions are again easily verified, if we assume that the source $\mathbf{s}^{1,**}$ is zero (which is the limiting value away from (4.2.29)). Hence, the numerical fluxes and sources can be calculated in the same manner as for non-zero B_1.

Finally, the remaining energy states are given by conservation across the Alfvén waves resulting in,

$$E_\theta^{**} = E_\theta^* + \frac{B_{1\theta}(B_{2\theta}^* u_{2\theta}^* + B_{3\theta}^* u_{3\theta}^* - B_2^{**} u_2^{**} - B_3^{**} u_3^{**})}{s_\theta^* - s_M}$$

for $\theta \in \{L, R\}$. This completes a description of the states of the five-wave solver. The corresponding fluxes can be determined by local conservation and the numerical flux is obtained similar to the formula (4.2.16). We remark that whenever $B_{1L} = B_{1R}$, the above solver reduces to the five-wave solver derived in [59].

For the discretization of the corresponding Godunov-Powell source term in this case, we use exactly the same arguments as in the case of the three-wave solver (as B_1 jumps only across the middle wave where the velocity and the tangential magnetic fields are constant) to obtain that

$$\mathbf{S}_{i,j}^{1,n} = \mathbf{s}_{i-1/2,j}^{1,**} \mathbf{1}_{\left\{s_{M,i-1/2,j} \geq 0\right\}} + \mathbf{s}_{i+1/2,j}^{1,**} \mathbf{1}_{\left\{s_{M,i+1/2,j} < 0\right\}},$$

where $\mathbf{s}_{i\pm1/2,j}^{1,**}$ is defined as in (4.2.9) with the $**$ replacing the $*$ states.

4.2.4 Fluxes and sources in the y-direction

We have completed a description of the numerical flux $\mathbf{F}$ and discretized source $\mathbf{S}^1$ in the x-direction. In-order to complete the scheme (4.2.3), we need to specify the numerical flux in the y-direction $\mathbf{G}$ and the corresponding Godunov-Powell source term $\mathbf{S}^2$. This is straightforward as the form of equations in each direction is similar.

The numerical flux $\mathbf{G}$ is defined in terms of both a three-wave solver and a five-wave solver. The three-wave solver is analogous to the states and fluxes obtained in (4.2.5) with normal velocity u_2 and normal magnetic field B_2. Similarly, the discretized source term $\mathbf{S}^2$ is similar to $\mathbf{S}^1$ defined in (4.2.20). The only change is to replace the normal velocity and magnetic fields to u_2 and B_2 respectively. The five-wave solver is analogously defined. The specification of $\mathbf{G}, \mathbf{S}^2$ completes the description of the scheme (4.2.3).

4.2.5 Second-order accurate schemes

The finite volume scheme (4.2.3) is first-order accurate in both space and time. For practical applications, we need higher order of accuracy. We will design a finite volume scheme based on (4.2.3) that is second-order accurate in both space and time. The semi-discrete form of this scheme is given by,

$$\frac{d}{dt}\mathbf{W}_{i,j} = \boldsymbol{\mathcal{F}}_{i,j} = -\frac{1}{\Delta x}(\mathbf{F}_{i+1/2,j} - \mathbf{F}_{i-1/2,j}) - \frac{1}{\Delta y}(\mathbf{G}_{i,j+1/2} - \mathbf{G}_{i,j-1/2}) + \tilde{\mathbf{S}}^1_{i,j} + \tilde{\mathbf{S}}^2_{i,j}, \quad (4.2.30)$$

where $\mathbf{W}_{i,j}(t)$ is the cell-average of the unknown at time t. We will define the numerical fluxes $\mathbf{F}, \mathbf{G}$ and the sources $\tilde{\mathbf{S}}^1, \tilde{\mathbf{S}}^2$ below.

It is standard ([50]) to replace the piecewise constant approximation $\mathbf{W}_{i,j}$ with non-oscillatory piecewise linear reconstructions in-order to obtain second-order spatial accuracy. There are a variety of reconstructions including the popular TVD-MUSCL limiters ([81]). We will use second-order ENO reconstruction ([40]) and WENO reconstruction ([72]) as these procedures can be easily extended to obtain even higher-order schemes.

ENO Reconstruction:

Given the cell averages $\mathbf{W}_{i,j}$, we reconstruct in the primitive variables $\mathbf{V}_{i,j} = \{\rho_{i,j}, \mathbf{u}_{i,j}, \mathbf{B}_{i,j}, p_{i,j}\}$. Define the ENO-differences in each direction as

$$D^x\mathbf{V}_{i,j} = \begin{cases} \mathbf{V}_{i+1,j} - \mathbf{V}_{i,j} & \text{if } \Gamma^x_{i,j} \le 1, \\ \mathbf{V}_{i,j} - \mathbf{V}_{i-1,j} & \text{otherwise.} \end{cases} \quad D^y\mathbf{V}_{i,j} = \begin{cases} \mathbf{V}_{i,j+1} - \mathbf{V}_{i,j} & \text{if } \Gamma^y_{i,j} \le 1, \\ \mathbf{V}_{i,j} - \mathbf{V}_{i,j-1} & \text{otherwise.} \end{cases}$$

where

$$\Gamma^x_{i,j} = \frac{|\psi(\mathbf{V}_{i+1,j}) - \psi(\mathbf{V}_{i,j})|}{|\psi(\mathbf{V}_{i,j}) - \psi(\mathbf{V}_{i-1,j})|}, \qquad \Gamma^y_{i,j} = \frac{|\psi(\mathbf{V}_{i,j+1}) - \psi(\mathbf{V}_{i,j})|}{|\psi(\mathbf{V}_{i,j}) - \psi(\mathbf{V}_{i,j-1})|},$$

and ψ for some function ψ called the global smoothness indicator. We use $\psi(\mathbf{V}) = \rho + \mathbf{B}^2$.

Note that for piecewise linear reconstruction, the ENO procedure reduces to providing a limiter for the slopes in each direction. The reconstructed piecewise linear function is each cell $I_{i,j}$ is denoted by

$$\overline{\mathbf{V}}_{i,j}(x,y) = \mathbf{V}_{i,j} + \frac{1}{\Delta x} D^x\mathbf{V}_{i,j}(x - x_i) + \frac{1}{\Delta y} D^y\mathbf{V}_{i,j}(y - y_j).$$

The reconstructed conservative variables can be easily obtained by transforming the reconstructed primitive variables.

WENO procedure:

As an alternative to the above reconstruction, consider the following cell-gradients

$$\bar{D}^x\mathbf{V}_{i,j} = \Big(\omega^x_{i,j}\left(\mathbf{V}_{i+1,j} - \mathbf{V}_{i,j}\right) + \left(1 - \omega^x_{i,j}\right)\left(\mathbf{V}_{i,j} - \mathbf{V}_{i-1,j}\right)\Big),$$
$$\bar{D}^y\mathbf{V}_{i,j} = \Big(\omega^y_{i,j}\left(\mathbf{V}_{i,j+1} - \mathbf{V}_{i,j}\right) + \left(1 - \omega^y_{i,j}\right)\left(\mathbf{V}_{i,j} - \mathbf{V}_{i,j-1}\right)\Big),$$

where the weights are given by,

$$\omega^x_{i,j} = \frac{a^0_{i,j}}{a^0_{i,j} + a^1_{i,j}}, \quad a^0_{i,j} = \frac{1}{3(\epsilon + \beta^{x,0}_{i,j})}, \quad a^1_{i,j} = \frac{2}{3(\epsilon + \beta^{x,1}_{i,j})},$$
$$\omega^y_{i,j} = \frac{b^0_{i,j}}{b^0_{i,j} + b^1_{i,j}}, \quad b^0_{i,j} = \frac{1}{3(\epsilon + \beta^{y,0}_{i,j})}, \quad b^1_{i,j} = \frac{2}{3(\epsilon + \beta^{y,1}_{i,j})},$$

where ϵ is a small positive number, and the parameters are given by

$$\beta^{x,0}_{i,j} = (\psi(\mathbf{V}_{i+1,j}) - \psi(\mathbf{V}_{i,j}))^2, \quad \beta^{x,1} = (\psi(\mathbf{V}_{i,j}) - \psi(\mathbf{V}_{i-1,j}))^2,$$
$$\beta^{y,0}_{i,j} = (\psi(\mathbf{V}_{i,j+1}) - \psi(\mathbf{V}_{i,j}))^2, \quad \beta^{y,1} = (\psi(\mathbf{V}_{i,j}) - \psi(\mathbf{V}_{i,j-1}))^2,$$

and the indicator function ψ is defined above. The corresponding linear reconstruction is given by,

$$\underline{\mathbf{V}}_{i,j}(x,y) = \mathbf{V}_{i,j} + \frac{1}{\Delta x}\overline{D}^x\mathbf{V}_{i,j}(x - x_i) + \frac{1}{\Delta y}\overline{D}^y\mathbf{V}_{i,j}(y - y_j). \tag{4.2.31}$$

Note that the choice of weights implies that the WENO approximation (4.2.31) is third-order accurate for smooth solutions (at least in one-space dimension).

Both the ENO and WENO reconstructions suffer from a common problem: the reconstructed densities and pressures may not be positive. Since the positivity of density and pressure is absolutely essential for obtaining any physically meaningful results, the reconstructions have to be modified further. A simple modification consists of further limiting the slope in either direction. Let $D^x\rho$ and D^xp be the ENO-gradients of density and pressure in the x-direction, we follow [62] and introduce the following clipping,

$$D^{x,c}\rho_{i,j} = \max\left\{-\overline{\omega}\rho_{i,j}, \min\left\{\overline{\omega}, D^x\rho_{i,j}\right\}\right\}, \qquad D^{x,c}p_{i,j} = \max\left\{-\overline{\omega}p_{i,j}, \min\left\{\overline{\omega}, D^xp_{i,j}\right\}\right\},$$

where $\overline{\omega} < 2$ is a positive parameter. Simple calculations show that the above modification ensures that the reconstructed pressure and density remain positive. We choose $\overline{\omega} = 1.9$ in our simulations. Similarly in the y-direction, we have

$$D^{y,c}\rho_{i,j} = \max\left\{-\overline{\omega}\rho_{i,j}, \min\left\{\overline{\omega}, D^y\rho_{i,j}\right\}\right\}, \qquad D^{y,c}p_{i,j} = \max\left\{-\overline{\omega}p_{i,j}, \min\left\{\overline{\omega}, D^yp_{i,j}\right\}\right\}.$$

However, this only guarantees positivity of the reconstructed variables, not for the updated ones. A further modification of the gradients was suggested in a recent paper [83]. Denote

$$D^{x,c}\mathbf{V}_{i,j} = \left\{D^{x,c}\rho_{i,j}, D^x\mathbf{u}_{i,j}, D^x\mathbf{B}_{i,j}, D^{x,c}p_{i,j}\right\},$$
$$D^{y,c}\mathbf{V}_{i,j} = \left\{D^{y,c}\rho_{i,j}, D^y\mathbf{u}_{i,j}, D^y\mathbf{B}_{i,j}, D^{y,c}p_{i,j}\right\},$$

and

$$L^x_{i,j} = \frac{1}{8}\left(\rho_{i,j}\left(\left|D^x\mathbf{u}_{i,j}\right|^2 + \left|D^x\mathbf{B}_{i,j}\right|^2 + \frac{1}{2}\left(\min\left\{0, \rho_{i,j}\left(\mathbf{u}_{i,j}\cdot D^x\mathbf{u}_{i,j}\right)\right\}\right)\right)\right.$$
$$\left. + \frac{1}{2\rho_{i,j}}\left(D^{x,c}\rho_{i,j}\right)^2\left|D^x\mathbf{u}_{i,j}\right|^2,\right.$$

$$L^y_{i,j} = \frac{1}{8}\left(\rho_{i,j}\left(|D^y\mathbf{u}_{i,j}|^2 + |D^y\mathbf{B}_{i,j}|^2 + \frac{1}{2}\left(\min\left\{0, \rho_{i,j}\left(\mathbf{u}_{i,j}\cdot D^y\mathbf{u}_{i,j}\right)\right\}\right)\right)\right)$$
$$+ \frac{1}{2\rho_{i,j}}\left(D^{y,c}\rho_{i,j}\right)^2|D^y\mathbf{u}_{i,j}|^2,$$
$$R_{i,j} = \frac{p_{i,j}}{\gamma-1}.$$

Then, we further modify the gradients by

$$\hat{D}^x\mathbf{V}_{i,j} = D^{x,c}\mathbf{V}_{i,j}\sqrt{\frac{R_{i,j}}{\max\{L^x_{i,j}, R_{i,j}\}}}, \qquad \hat{D}^y\mathbf{V}_{i,j} = D^{y,c}\mathbf{V}_{i,j}\sqrt{\frac{R_{i,j}}{\max\{L^y_{i,j}, R_{i,j}\}}}.$$

Thus $\hat{D}^x, \hat{D}^y$ are the gradients that we use for the final reconstruction. The choice of this modified gradient has been motivated in recent papers [83]. With an underlying positivity preserving first order scheme and an appropriate treatment of the Godunov-Powell source term, this modification ensures positivity of the updated pressure and density. The reconstructed states are now given by

$$\hat{\mathbf{V}}_{i,j}(x,y) = \mathbf{V}_{i,j} + \frac{1}{\Delta x}\hat{D}^x\mathbf{V}_{i,j}(x-x_i) + \frac{1}{\Delta y}\hat{D}^y\mathbf{V}_{i,j}(y-y_j). \tag{4.2.32}$$

A similar procedure can be used for the WENO-gradients to obtain a modified WENO reconstruction.

The reconstructed primitive variables correspond to the reconstructed conservative function $\hat{\mathbf{W}}_{i,j}(x,y)$. Define the point-values,

$$\mathbf{W}^E_{i,j} = \hat{\mathbf{W}}_{i,j}(x_{i+1/2}, y_j), \qquad \mathbf{W}^W_{i,j} = \hat{\mathbf{W}}_{i,j}(x_{i-1/2}, y_j),$$
$$\mathbf{W}^N_{i,j} = \hat{\mathbf{W}}_{i,j}(x_i, y_{j+1/2}), \qquad \mathbf{W}^S_{i,j} = \hat{\mathbf{W}}_{i,j}(x_i, y_{j+1/2}).$$

We can use the above defined values to define the second-order numerical fluxes as

$$\mathbf{F}_{i+1/2,j} = \mathbf{F}\left(\mathbf{W}^E_{i,j}, \mathbf{W}^W_{i+1,j}\right), \qquad \mathbf{G}_{i,j+1/2} = \mathbf{G}\left(\mathbf{W}^N_{i,j}, \mathbf{W}^S_{i,j+1}\right),$$

where $\mathbf{F}$,and $\mathbf{G}$ are given by either the three-wave solver or the five-wave solver of the previous section. Similarly, the second-order source terms can be calculated as

$$\mathbf{S}^1_{i,j} = \mathbf{s}^{1,*}_{i-1/2,j}\mathbf{1}_{\left\{s_{M,i-1/2,j}\geq 0\right\}} + \mathbf{s}^{1,*}_{i+1/2,j}\mathbf{1}_{\left\{s_{M,i+1/2,j}<0\right\}},$$

where $\mathbf{s}^{1,*}_{i+1/2,j}$ is defined as in (4.2.9), but with the values $\mathbf{W}_{i,j}$, $\mathbf{W}_{i+1,j}$ replaced by $\mathbf{W}_{i+1/2,j}$, $\mathbf{W}^W_{i+1,j}$. The source $\mathbf{S}^2_{i,j}$ in the y-direction is defined analogously. Observe that for smooth solutions, the discretized source $\mathbf{S}^1_{i,j}$ vanishes to truncation order with $(B^E_1)_{i,j} - (B^W_1)_{i+1,j}$. Hence, we need to add an extra term for second-order consistency. However, this term should vanish when $\mathbf{S}^1_{i,j}$ becomes significant at jumps (see e.g., [7] for an analogous situation). We suggest the following simple modification,

$$\tilde{\mathbf{S}}^1_{i,j} = \mathbf{S}^1_{i,j} + \begin{pmatrix} 0 \\ \mathbf{B}_{i,j} \\ \mathbf{u}_{i,j}\cdot\mathbf{B}_{i,j} \\ \mathbf{u}_{i,j} \end{pmatrix}\frac{1}{\Delta x}\hat{D}^x B^1_{i,j}.$$

The term $\tilde{\mathbf{S}}^2_{i,j}$ in the y-direction is analogously defined. A similar form of the discrete source was found to be very stable in [83]. Note that $\tilde{\mathbf{S}}^{1,2}_{i,j}$, are consistent second-order discretizations of the Godunov-Powell source terms $\mathbf{s}^{1,2}$. Hence, we have completed a description of the (formally) second-order accurate in space semi-discrete scheme (4.2.30).

4.2.6 Time Stepping:

The standard scheme for a first order approximation in time is the forward-Euler time stepping, formally written

$$\mathbf{W}^{n+1}_{i,j} = \mathbf{W}^n_{i,j} + \Delta t^n \boldsymbol{\mathcal{F}}^n_{i,j}$$

where $\boldsymbol{\mathcal{F}}^n_i$ is defined in (4.2.30). For overall second-order schemes, we use the second-order strong-stability preserving Runge-Kutta (SSP) time stepping ([37]),

$$\begin{aligned}
\mathbf{W}^*_{i,j} &= \mathbf{W}^n_{i,j} + \Delta t^n \boldsymbol{\mathcal{F}}^n_{i,j}, \\
\mathbf{W}^{**}_{i,j} &= \mathbf{W}^*_{i,j} + \Delta t^n \boldsymbol{\mathcal{F}}^*_{i,j}, \\
\mathbf{W}^{n+1}_{i,j} &= \frac{1}{2}(\mathbf{W}^n_{i,j} + \mathbf{W}^{**}_{i,j}).
\end{aligned}$$

The time step is determined by a standard CFL condition. This completes our description of the finite volume schemes for (4.2.1).

4.3 Numerical Experiments

We will validate the first- and second-order finite volume schemes on a series of numerical experiments in both one- and two-space dimensions. We test a total of six schemes:

H_3	First order with the HLL three-wave solver,
H_5	first order with the HLL five-wave solver,
H_3E	second order with HLL three-wave solver and ENO reconstruction,
H_3W	second order with HLL three-wave solver and WENO reconstruction,
H_5E	second order with HLL five-wave solver and ENO reconstruction,
H_5W	second order with HLL five-wave solver and WENO reconstruction.

All the second order schemes use the positivity preserving modifications (4.2.32). The first order schemes are evolved with a CFL number of 0.45 (which is theoretically sound due to excluding wave interactions in the cells), and the second order schemes use a CFL number of 0.9. In all our computations we use $\gamma = 5/3$.

Regarding the measurement of errors, if we have a reference solution available, then we define the relative error as

$$100 \times \frac{\|\alpha - \alpha_{\text{ref}}\|}{\|\alpha_{\text{ref}}\|},$$

where α is (a component of) the numerical approximation and α_{ref} is (the same component of) the reference solution, and $\|\cdot\|$ is some (usually L^1) norm.

Brio-Wu shock tube

This is a standard one-dimensional numerical test case for ideal MHD ([23]). The initial conditions are given by

$$(\rho, \rho\mathbf{u}, p, \mathbf{B}) = \begin{cases} (1.0, +1.0, 0, 0, 0, 0.7, 0, 1.0), & \text{if } x < 0.5, \\ (0.3, -0.3, 0, 0, 0, 0.7, 0, 0.2), & \text{otherwise.} \end{cases}$$

The computational domain is $(x, t) \in [0, 1.5] \times [0, 0.5]$ with Neumann boundary conditions. Note that the normal magnetic field is constant. Therefore, the H_3 scheme and H_5 scheme reduce to the solvers presented in [36] and [59] respectively. However, the four higher-order schemes are different from those presented in the literature. We present the computed total energy and the magnetic field B_2 with the schemes at time $t = 0.5$ in figure 4.3.1. The reference solution in this case is calculated with the H_5W second-order scheme on a

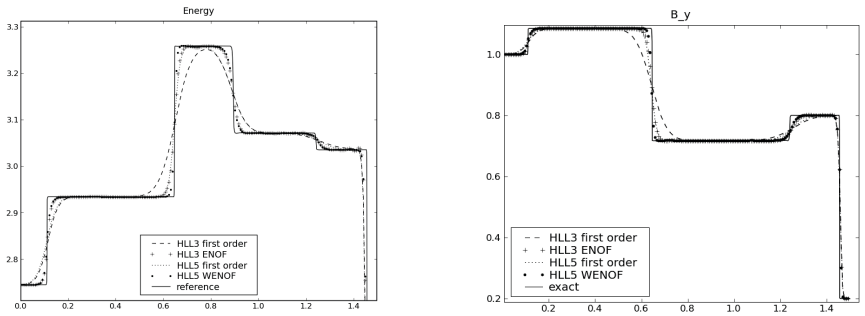

Figure 4.3.1: Results for the Brio-Wu shock tube with 200 grid points at $t = 0.5$. Reference solution is the H_5W scheme with 3200 grid points. Left: Energy Right: Magnetic field component B_2

mesh with 3200 points. The solution is quite complicated containing shock waves, contact discontinuities and rarefaction waves. As expected, the H_5 scheme is more accurate than the H_3 scheme, particularly near Alfvén waves. The second-order schemes are clearly more accurate than the first-order schemes. The differences are also illustrated in Table 4.3.1, showing the relative percentage errors in the L^1 norm of the total energy on a sequence of meshes. The table confirms the observations obtained from the figure. The H_5 scheme is more accurate than the H_3 scheme. Both the formal first-order accurate schemes have an average convergence rate close to 0.7 . The second-order schemes are more accurate than the first-order schemes with considerably smaller errors. The H_5E and H_5W are slightly more accurate than the corresponding H_3E and H_3W scheme. Similarly, H_3E and H_3E schemes are slightly more dissipative than the H_3W and H_5W schemes respectively. The second-order schemes have an average rate of convergence around 1. This is to be expected as the solution contains discontinuities, and the order of accuracy deteriorates near these.

M	H_3	rate	H_3E	rate	H_3W	rate
50	2.2e-00		1.3e-00		1.3e-00	
100	1.5e-00	0.6	7.9e-01	0.7	7.2e-01	0.9
200	9.8e-01	0.6	5.0e-01	0.7	4.6e-01	0.6
400	5.3e-01	0.9	1.9e-01	1.4	1.7e-01	1.4
800	3.4e-01	0.6	1.1e-01	0.8	9.7e-02	0.8
1600	1.9e-01	0.8	5.4e-02	1.0	4.4e-02	1.1

M	H_5	rate	H_5E	rate	H_5W	rate
50	1.7e-00		1.2e-00		1.2e-00	
100	1.2e-00	0.5	7.1e-01	0.8	6.5e-01	0.9
200	7.4e-01	0.7	4.4e-01	0.7	4.1e-01	0.7
400	3.7e-01	1.0	1.6e-01	1.5	1.4e-01	1.6
800	2.2e-01	0.8	9.6e-02	0.7	8.3e-02	0.8
1600	1.2e-01	0.9	4.8e-02	1.0	3.9e-02	1.1

Table 4.3.1: Relative percentage errors for the total energy in L^1 at time $t = 0.5$ and the order of convergence for the Brio-Wu shock tube for various mesh sizes M using the H_5W scheme with 3200 grid points as a reference solution.

Godunov-Powell Magnetic Advection

This test case is constructed to demonstrate the performance of the schemes in one-dimension with a non-constant normal magnetic field. Consider the one-dimensional semi-conservative form of the MHD equations (4.1.2) with the following initial data,

$$(\rho, u_1, u_2, u_3, B_1, B_2, B_3, p) = (1, 1, 0, 0, 1 - c\sin(2\pi x), 0.5, 0, 0, 0.5),$$

where c is a constant. A straightforward calculation shows that the exact solution is given by,

$$(\rho, u_1, u_2, u_3, B_1, B_2, B_3, p) = (1, 1, 0, 0, 1 - c\sin(2\pi(x - t)), 0.5, 0, 0, 0.5),$$

Thus, the solution consists of advection of the normal magnetic field due to the presence of the Godunov-Powell source term. Note that putting $c = 0$ gives a constant solution. The aim is to take non-zero values of c and test the schemes. It turns out that any standard scheme like the three-wave solver of [36] or the five-wave solver of [59] crashes almost immediately if $c > 0.01$ due to unphysical state values. This is not unexpected since these schemes are based on the form (4.1.4) which needs the normal magnetic field to be a constant in space. Hence, this test case is vital in showing the effectiveness of our new schemes based on the semi-conservative form.

We consider this problem on a domain $[0, 1]$ and $c = 1$ with periodic boundary conditions. Figure 4.3.2 shows the approximate normal magnetic field B_1 at time $t = 1$. The H_3 and H_5 schemes approximate the solution like any standard first-order scheme for linear advection. The second-order schemes resolve the solution much better, and there is very little visual difference between the exact solution and the second-order schemes at this mesh resolution. Further study of the approximation is reported in the Table 4.3.2, which shows the relative percentage errors in L^1 for the magnetic field B_1 on a sequence of meshes. There is no difference between the H_3 and H_5 solvers. Both the first-order

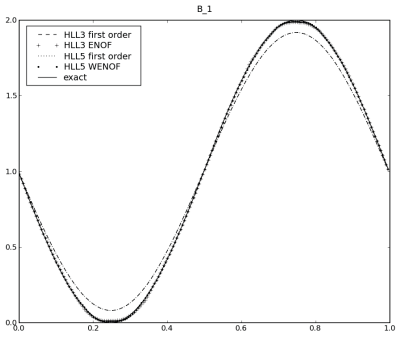

Figure 4.3.2: B_1 distribution for Powell magnetic advection test with 200 grid points.

schemes have the expected rate of convergence 1. Among the second-order schemes, the WENO based H_3W and H_5W are more accurate than their ENO based counterparts. In fact, the observed order of convergence for the ENO schemes is 2, but the WENO schemes approach an order of convergence close to 3. This is on account of the design of a WENO scheme where third-order is achieved for piecewise linear reconstruction. Note that the positivity-preserving modifications have not reduced the orders of accuracy of either the ENO or the WENO schemes. Thus, this experiment demonstrates that our schemes approximate the semi-conservative form (4.1.4) in one-dimension quite well, particularly for problems with perturbations from constant normal magnetic fields (standard schemes fail in these cases).

M	H_3	rate	H_3E	rate	H_3W	rate
50	9.4e-00		3.2e-00		2.2e-00	
100	5.1e-00	0.9	9.9e-01	1.7	6.0e-01	1.9
200	2.8e-00	0.9	2.9e-01	1.8	1.5e-01	2.0
400	1.5e-00	0.9	8.7e-02	1.7	3.5e-02	2.1
800	8.1e-01	0.9	2.4e-02	1.9	7.3e-03	2.3
1600	4.1e-01	1.0	6.4e-03	1.9	1.2e-03	2.6
3200	2.1e-01	1.0	1.7e-03	1.9	1.5e-04	3.0

M	H_5	rate	H_5E	rate	H_5W	rate
50	9.4e-00		3.2e-00		2.2e-00	
100	5.2e-00	0.9	9.9e-01	1.7	6.0e-01	1.9
200	2.8e-00	0.9	2.9e-01	1.8	1.5e-01	2.0
400	1.5e-00	0.9	8.7e-02	1.7	3.5e-02	2.1
800	8.1e-01	0.9	2.4e-02	1.9	7.3e-03	2.3
1600	4.1e-01	1.0	6.4e-03	1.9	1.2e-03	2.6
3200	2.1e-01	1.0	1.7e-03	1.9	1.5e-04	3.0

Table 4.3.2: Relative percentage errors for B_1 at time $t = 1$ and the order for the Powell magnetic advection test for various mesh sizes M.

Rotor Problem:

We start considering two-dimensional numerical experiments with this standard example (introduced in [11], considered in [80] among others). The computational domain is $(\mathbf{x}, t) \in [0,1]^2 \times [0, 0.295]$ with Neumann boundary conditions. The initial data are given by

$$\rho = \begin{cases} 10.0 & \text{if } r < 0.1, \\ 1 + 9f(r) & \text{if } 0.1 \leq r < 0.115, \\ 1.0 & \text{otherwise,} \end{cases}$$

with $r(\mathbf{x}) = |\mathbf{x} - (0.5, 0.5)|$ and

$$f(r) = \frac{23 - 200r}{3}.$$

The other variables are initially

$$\left(\rho u^1, \rho u^2\right) = \begin{cases} (-(10y-5)\rho, (10x-5)\rho) & \text{if } r < 0.1, \\ (-(10y-5)f(r)\rho, (10x-5)f(r)\rho) & \text{if } 0.1 \leq r < 0.115, \\ (0.0, 0.0) & \text{otherwise,} \end{cases}$$

$$\left(\rho u^3, B^1, B^2, B^3, p\right) = \left(0.0, 2.5/\sqrt{\pi}, 0.0, 0.0, 0.5\right).$$

This describes a dense rotating region surrounded by static plasma with a uniform magnetic field. The pressure drops to very low values in the center. The main difficulty in the numerical solution of this problem is the low pressure, particularly on fine meshes. As stated in the introduction, most results presented in the literature show the approximation obtained on relatively coarse meshes. On coarse meshes, the numerical dissipation is large and provides some stability. However, computations on fine meshes lead to crashes due to negative pressures (see [32] for illustrations of this). We compute with all the six schemes and show the computed pressures at time $t = 0.295$ and on a mesh with 200×200 mesh points in Figure 4.3.3. The figure shows that both the first-order schemes provide a stable but diffusive approximation and the H_5 scheme is more accurate than the H_3 scheme. The second-order schemes are much more accurate and capture the shocks and smooth regions sharply at this resolution. For a more elaborate quantitative study of this problem, we compute solutions on a very fine 1600×1600 mesh and find that all the six schemes are stable and approximate the solution very well. We show the computed pressure with the H_5 scheme on a 1600×1600 mesh in Figure 4.3.4.

We tabulate the relative percentage errors in L^1 for the pressure with respect to this reference solution and present them in table 4.3.3. The table shows that the first-order H_5 scheme is (about thirty percent) more accurate than the first-order H_3 scheme. However, the second-order schemes are much more accurate than the first-order schemes. Sometimes, the gain in accuracy is an order of magnitude by using a second-order scheme. There is a gain in accuracy using the H_5 solver together with a second-order scheme. Similarly, the WENO-based schemes H_3W and H_5W are more accurate than their ENO-based counterparts. The observed rate of convergence for the first-order schemes is around 0.5 and that of the second-order schemes is better than 1 (except at the lowest resolutions).

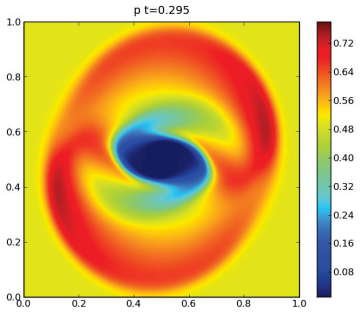

(a) H_3

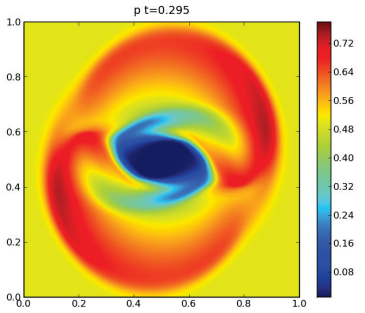

(b) H_5

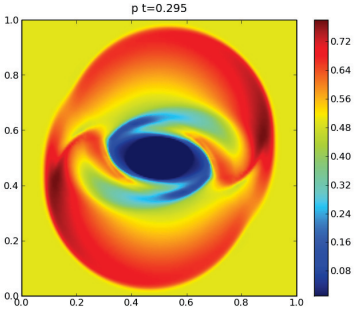

(c) H_3E

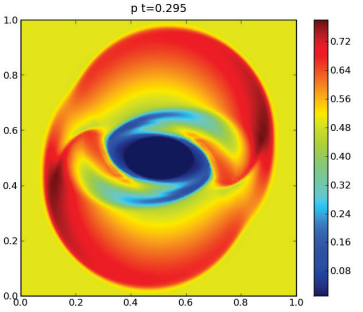

(d) H_5E

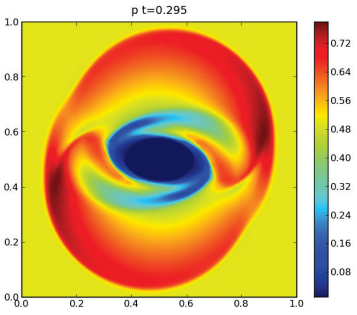

(e) H_3W

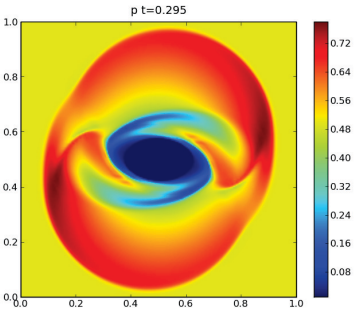

(f) H_5W

Figure 4.3.3: Pressure for the rotor problem on a 200×200 mesh at time $t = 0.295$ all scaled to the extrema of the pressure obtained for a 200×200 mesh.

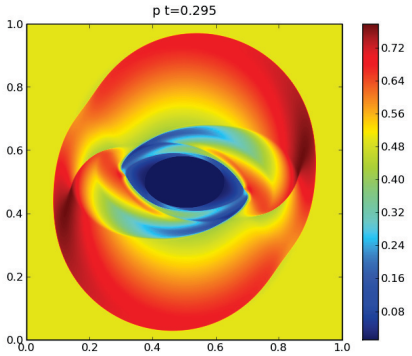

Figure 4.3.4: This figure shows the pressure for the rotor problem on a 1600×1600 mesh at time $t = 0.295$ using the H_5W scheme.

M	H_3	rate	H_3E	rate	H_3W	rate
50	10.0e-00		5.3e-00		5.1e-00	
100	7.7e-00	0.4	3.1e-00	0.8	2.9e-00	0.8
200	5.3e-00	0.5	1.6e-00	1.0	1.4e-00	1.1
400	3.5e-00	0.6	7.6e-01	1.1	6.3e-01	1.2
800	2.2e-00	0.7	3.5e-01	1.1	2.8e-01	1.2

M	H_5	rate	H_5E	rate	H_5W	rate
50	9.2e-00		4.6e-00		4.4e-00	
100	6.6e-00	0.5	2.5e-00	0.9	2.3e-00	0.9
200	4.5e-00	0.6	1.3e-00	0.9	1.1e-00	1.1
400	2.8e-00	0.7	6.0e-01	1.1	5.1e-01	1.1
800	1.7e-00	0.7	2.7e-01	1.2	2.0e-01	1.4

Table 4.3.3: Relative percentage errors in L^1 for the pressure at time $t = 0.295$ for the rotor problem for various mesh sizes M using the H_5W scheme on a 1600×1600 mesh as a reference solution.

Another key issue in numerical simulations of multi-dimensional MHD is the behaviour of div$B$. Note that the initial magnetic field is divergence free, hence the solutions of (4.2.1) are expected remain divergence free. However, the schemes we use do not preserve any discrete divergence. We consider the standard second order discrete divergence,

$$\mathrm{div}(B)_{i,j} = \frac{(B_1)_{i+1,j} - (B_1)_{i-1,j}}{2\Delta x} + \frac{(B_2)_{i,j+1} - (B_2)_{i,j-1}}{2\Delta y} \tag{4.3.1}$$

and present the L^1 norm of the above discrete divergence in Table 4.3.4. As expected, all the six schemes produce a nonzero discrete divergence. However, the values are quite small, and seem to be decreasing with increasing mesh size. Note that the divergence values are higher with the second-order schemes than with the first-order schemes. This is not unexpected as the second-order schemes resolve the shocks within fewer mesh points and hence generate a larger discrete divergence. Perhaps data such as these, although commonly reported, primarily point towards the difficulty of numerically evaluating derivatives at underresolved flow features. The key point is that divergence errors are not effecting the stability of the schemes as all the schemes are stable even at the finest mesh resolution of 1600×1600 mesh. This is unusual, and we have not come across other papers presenting solutions on comparable mesh sizes. As an example, the reference solutions in [80] were computed on a 400×400 mesh.

M	H_3	H_3E	H_3W	H_5	H_5E	H_5W
50	2.2e-01	2.5e-01	2.1e-01	2.2e-01	2.4e-01	2.2e-01
100	1.7e-01	1.9e-01	1.8e-01	1.7e-01	2.0e-01	1.9e-01
200	1.4e-01	1.8e-01	1.6e-01	1.5e-01	1.9e-01	1.6e-01
400	1.3e-01	1.8e-01	1.5e-01	1.2e-01	1.6e-01	1.4e-01
800	1.1e-01	1.7e-01	1.5e-01	9.6e-02	1.5e-01	1.2e-01
1600	1.0e-01	1.6e-01	1.4e-01	8.2e-02	1.4e-01	1.2e-01

Table 4.3.4: The L^1-norm of the discrete divergence at time $t = 0.295$ for the rotor problem for various mesh sizes M.

Orszag-Tang vortex

This commonly used benchmark test ([80]) has initial conditions given by

$$(\rho, \rho\mathbf{u}, \mathbf{B}, p) = \left(\gamma^2, -\gamma^2 \sin(\pi y), \gamma^2 \sin(\pi x), 0, -\sin(\pi y), \sin(2\pi x), 0, \gamma\right). \tag{4.3.2}$$

The computational domain is $(\mathbf{x}, t) \in [0, 2]^2 \times [0, 1]$ with periodic boundary conditions.

Even though the initial data are smooth, the solution develops shocks near the diagonals and a current sheet in the center of the domain. The solution also has interesting smooth features. We compute with all the six schemes and present the computed pressure at the final time on a 200×200 mesh in Figure 4.3.5. Both the first-order H_3 and H_5 schemes are stable but dissipative. The shocks are smeared and the central vortex is not resolved. The H_5 scheme is better at approximating the solution than the H_3 scheme. The second-order schemes resolve the solution far better. The resolution of the shocks with

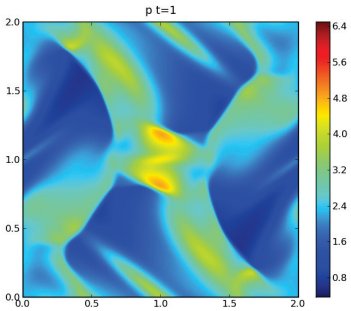

(a) H_3

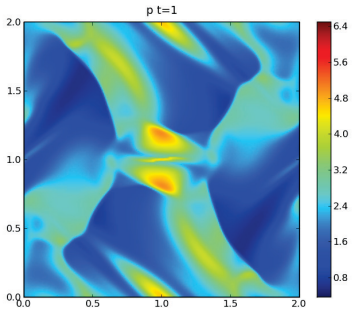

(b) H_5

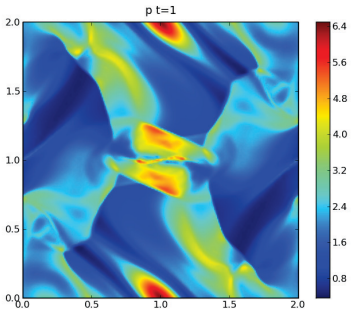

(c) H_3E

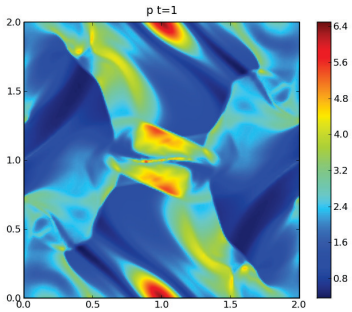

(d) H_5E

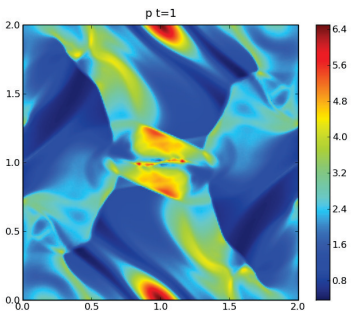

(e) H_3W

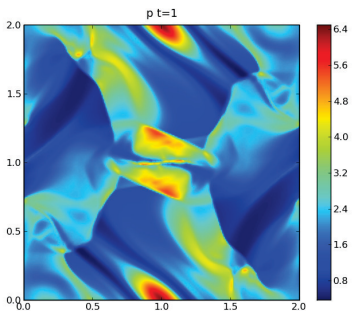

(f) H_5W

Figure 4.3.5: Pressure for the Orszag-Tang vortex on a 200×200 mesh at time $t = 1$ scaled to the extrema of the pressure in the reference solution.

the second-order schemes is very impressive. The smooth regions are also resolved quite accurately. We compute the a reference solution using the H_5W scheme on a 1600×1600 mesh. Figure 4.3.6 shows the pressure of the reference solution. We observe that the H_5W scheme at this very fine mesh is stable and resolves the shocks as well as the central current sheet very well. Table 4.3.5 shows relative percentage L^1 errors in pressure on a sequence of meshes. As shown in the table, the first-order H_5 scheme has lower errors than the

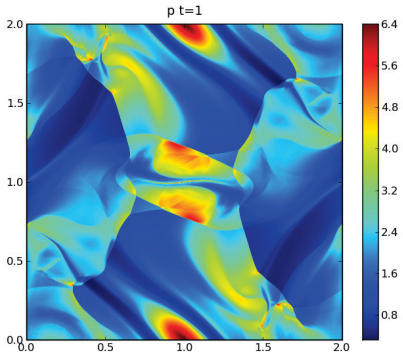

Figure 4.3.6: This figure shows the computed pressure for the Orszag-Tang vortex using the H_5W scheme on a 1600×1600 mesh at time $t = \pi$.

first-order H_3 scheme. Similarly, the second-order schemes significantly outperform (by an order of magnitude) the first-order schemes. In particular, the WENO-based schemes have lower errors than the ENO-based ones. Note that the second-order H_5W scheme is the most accurate with respect to the errors and has the best rate of convergence of about 1.3. The results are consistent with those obtained for the rotor problem.

We also calculated the discrete divergence for this test case. The results of this was very similar to the divergence measured for the rotor problem.

Cloud-Shock Interaction

This is a benchmark test describing the interaction of a dense region (cloud) at rest with a moving shock. The computational domain is $(\mathbf{x}, t) \in [0,1]^2 \times [0, 0.06]$ with artificial Neumann type boundary conditions. The initial conditions consist of a shock moving to the right initially located at $x = 0.05$, and a circular cloud of density $\rho = 10$ and radius $r = 0.15$ centered at $\mathbf{x} = (0.25, 0.5)$.

$$\rho = \begin{cases} 3.86859 & \text{if } x < 0.05, \\ 10.0 & \text{if } |\mathbf{x} - (0.25, 0.5)| < 0.15, \\ 1.0 & \text{otherwise,} \end{cases}$$

$$\mathbf{u} = \begin{cases} (11.2536, 0, 0) & \text{if } x < 0.05, \\ (1.0, 0, 0) & \text{otherwise,} \end{cases}$$

M	H_3	rate	H_3E	rate	H_3WE	rate
50	3.6e+01		1.5e+01		1.4e+01	
100	2.9e+01	0.3	8.8e-00	0.8	8.0e-00	0.8
200	2.2e+01	0.4	5.0e-00	0.8	4.4e-00	0.9
400	1.5e+01	0.6	2.6e-00	0.9	2.4e-00	0.9
800	1.0e+01	0.6	1.5e-00	0.8	1.3e-00	0.9

M	H_5	rate	H_5E	rate	H_5W	rate
50	2.9e+01		1.2e+01		1.1e+01	
100	2.3e+01	0.3	7.1e-00	0.8	6.2e-00	0.8
200	1.6e+01	0.5	4.0e-00	0.8	3.4e-00	0.9
400	1.1e+01	0.5	2.0e-00	1.0	1.6e-00	1.1
800	7.2e-00	0.6	8.3e-01	1.3	5.9e-01	1.4

Table 4.3.5: Percentage relative errors in L^1 for pressure at time $t = \pi$ for the Orszag-Tang vortex for various mesh sizes M using the H_5W scheme on a 1600×1600 mesh as a reference solution.

$$p = \begin{cases} 167.345 & \text{if } x < 0.05, \\ 1.0 & \text{otherwise,} \end{cases}$$

$$\mathbf{B} = \begin{cases} (0, 2.18261820, -2.18261820) & \text{if } x < 0.05, \\ (0, 0.56418958, 0.56418958) & \text{otherwise.} \end{cases}$$

The cloud is initially in hydrostatic equilibrium with the surrounding fluid. The bubble should stay stationary whereas the shock travels towards it, hits it and starts interacting with it. This interaction generates a bow shock in the front, tail shocks in the rear and we expect the creation of interesting turbulent-like structures where the cloud interacts with the shock. A graphical description of this complex evolution is provided in figure 4.3.7 where the total energy at four different times is plotted on a 200×200 mesh with the H_3W scheme. Again, we compute the solutions with all the six schemes and present numerical results of the total energy on a very fine mesh 1600×1600 mesh with all the six schemes in Figure 4.3.8. The figure illustrates the stability of all the six schemes at this fine mesh resolution. The first-order schemes are a bit dissipative and do not approximate the turbulent like structures that are visible in the second order computations. The second order schemes are much more accurate with good resolution of the shocks as well as the turbulent-like structures in the bubble. The differences between the first-order and the second-order schemes are considerable while there are some minor differences between the ENO and WENO approximations.

In this test case we found the discrete divergence to be larger than in the other test cases, with L^1 norms in the range 0.1–4.0. Furthermore we did not observe a strong convergence to zero as the mesh was refined. This might be due to the strong shocks present in this test case. However, there is no sign that these divergence errors affect either the stability or the resolution of the schemes.

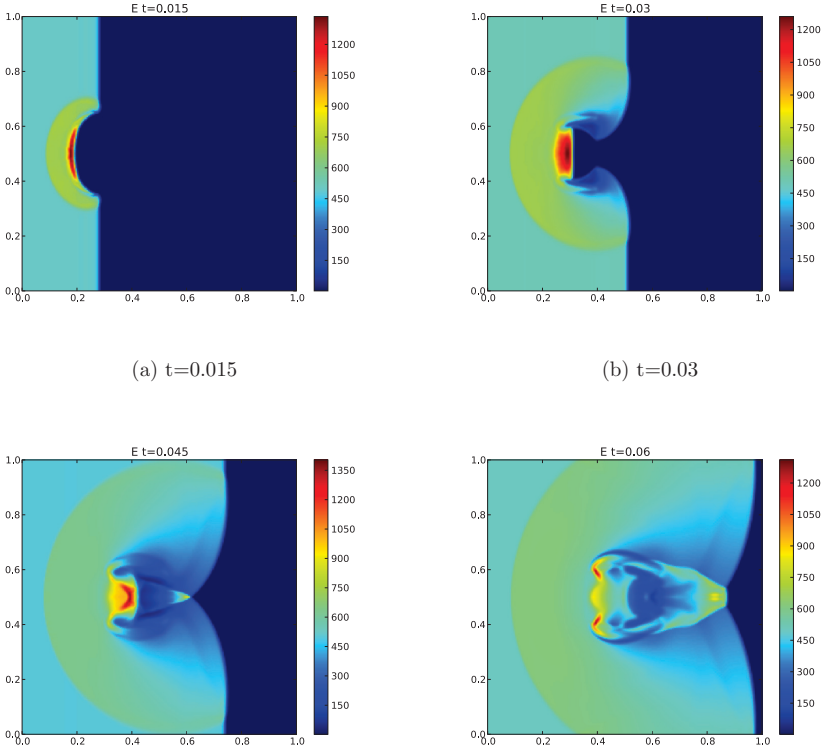

(a) t=0.015

(b) t=0.03

(c) t=0.045

(d) t=0.06

Figure 4.3.7: Energy distribution for the cloud-shock interaction at four different times on a 200×200 mesh with the H_3W scheme.

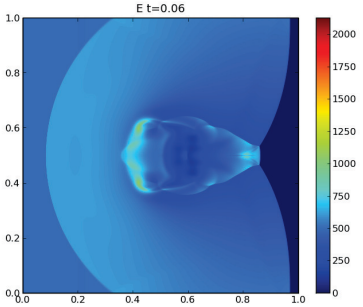

(a) H_3

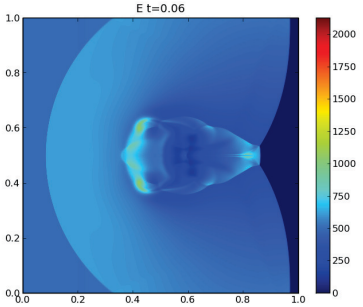

(b) H_5

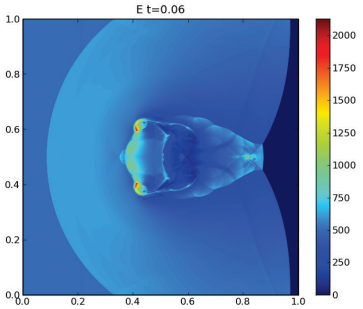

(c) H_3E

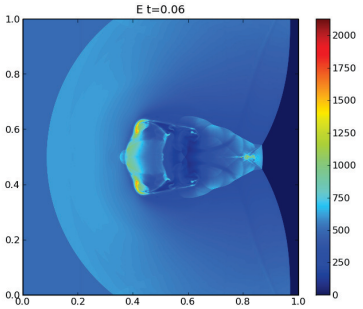

(d) H_5E

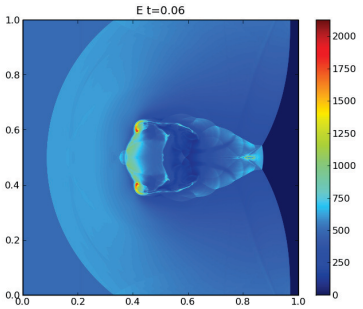

(e) H_3W

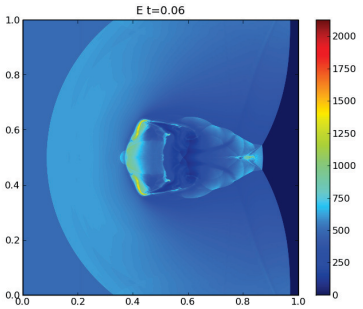

(f) H_5W

Figure 4.3.8: Energy distribution for the cloud-shock interaction on a 1600×1600 mesh at time $t = 0.06$.

4.4 Conclusion

We describe finite volume schemes for the MHD equations in the semi-conservative form (4.1.2). This form is symmetrizable as well as Galilean-invariant. Furthermore, the form of the semi-conservative version of the equations in several dimensions is similar to that in one-space dimension, enabling us to design one-dimensional schemes that are easily generalized to multidimensional data. We design suitable three-wave and five-wave approximate Riemann solvers. Both solvers can handle the presence of non-constant normal magnetic fields and can be thought of as extensions of the highly popular three-wave and five-wave solvers of [36] and [59] respectively. The Godunov-Powell source term is discretized in a novel manner by using the waves and states of the approximate Riemann solver. The resulting first-order schemes can be extended to second-order spatial accuracy by using ENO and WENO-type reconstructions. The reconstructions need to be modified to preserve positive pressures and densities.

We test the schemes on a variety of numerical experiments in both one- and two-space dimensions. The results obtained by the schemes (particularly the second-order versions) were impressive, both with respect to stability and accuracy. In particular, the schemes were able to compute the solutions for the advection of varying normal magnetic field in one-dimension and the expected orders of convergence were obtained. The benchmark two-dimensional numerical experiments showed that the schemes were very stable, even on fine meshes. It is well known that computing two-dimensional MHD on very fine meshes leads to stability problems and the schemes of this paper were able to handle these fine mesh resolutions. Similarly, the accuracy of the schemes was impressive. Among the schemes, the HLL five-wave solver was better in terms of resolution (even at second-order) than the HLL three-wave solver. Similarly the WENO-based schemes were more accurate than the ENO-based schemes. The highly resolved solutions (obtained on very fine meshes) can serve as benchmark reference solutions for future computations. Discrete values of div$\mathbf{B}$ were low in general and reduced as the mesh was refined. Divergence errors did not affect either the stability or the accuracy of the resulting solutions.

Based on the numerical evidence, we conclude that using the semi-conservative form of the MHD equations, with very careful discretizations of the fluxes and the Godunov-Powell source term together with proper high-order reconstructions is a very appealing strategy for designing robust schemes for MHD equations. These robust schemes are trivial to extend to three dimensions and we aim to employ them for more realistic astrophysical simulations in a forthcoming paper. Similarly, designing higher than second-order schemes is a work in progress.

5

Finite volume methods for wave propagation in stratified magneto-atmospheres

F. G. Fuchs, A. D. McMurry, S. Mishra, N.H. Risebro, K. Waagan
Communications in Computational Physics, to appear

Abstract

We present a model for simulating wave propagation in stratified magneto-atmospheres. The model is based on equations of ideal MHD together with gravitational source terms. In addition, we present suitable boundary data and steady states to model wave propagation. A finite volume framework is developed to simulate the waves. The framework is based on HLL and Roe type approximate Riemann solvers for numerical fluxes, a positivity preserving fractional steps method for discretizing the source and modified characteristic and Neumann type numerical boundary conditions. Second-order spatial and temporal accuracy is obtained by using a ENO piecewise linear reconstruction and a stability preserving Runge-Kutta method respectively. The boundary closures are suitably modified to ensure mass balance. The numerical framework is tested on a variety of test problems both for hydrodynamic as well as magnetohydrodynamic configurations. It is observed that only suitable choices of HLL solvers for the numerical fluxes and novel Neumann type boundary closures yield stable results for numerical wave propagation in the presence of complex magnetic fields.

5.1 Introduction

There is considerable interest in the astrophysics community regarding the problem of wave propagation in magnetized stellar atmospheres. The main theme of this research is to determine how convection generated waves transport and deposit energy in the overlying chromospheric and coronal plasmas. Models aim to explain the observed energy distribution in interesting astrophysical objects like the sun. The mathematical description of the underlying physical processes in realistic magneto-atmospheres is extremely complicated. The models for this wave heating problem include the equations of ideal magneto-hydrodynamics (MHD) together with complicated source and diffusion terms.

In addition, radiative transfer and non-equilibrium thermodynamics also play leading roles. These models are described by systems of nonlinear partial differential and integral equations in three dimensions, coupled with realistic initial and boundary data. The issue of determining model parameters along with proper initial and boundary data requires considerable observational work.

It is not possible to obtain analytical solutions for the full model or even extremely simplified versions of it. Also for these equations, theoretical results concerning existence, uniqueness and qualitative behavior are currently unavailable. Therefore, in order to investigate these models, one must resort to numerical methods. Even this task faces formidable difficulties due to nonlinearity and sheer computational complexity. A detailed account of the physical processes involved in wave propagation along with extensive references to the corresponding astrophysics literature can be found in in [69, 18].

In [69, 18], the authors consider a relatively simple model for wave propagation in the solar atmosphere. This model takes into account the equations of compressible ideal MHD along with gravitational source terms, supplemented by a description of the underlying steady states. Waves in the "solar" atmosphere are modeled by inducing perturbations of these steady states. We adopt the modeling framework of the above papers as a starting point of this work and develop a class of schemes of the finite volume type to simulate this model. A complete description of these schemes involves suitable approximate Riemann solvers for the ideal MHD equations, proper treatment of the gravitational source term and an appropriate implementation of boundary conditions.

The core of the model we consider consists of the equations of ideal MHD. Consequently, most of the computational effort is directed at MHD solvers. The MHD equations are an example of a system of non-linear hyperbolic conservation laws. Solutions of these equations develop discontinuities such as shock waves and contact discontinuities even for smooth initial data. Furthermore, the MHD equations are not strictly hyperbolic and contain a large number of waves. Some of the characteristic fields are not convex (i.e. genuinely nonlinear except in some subset of state space), and the resulting solutions can have intermediate and compound shocks. All these issues have to be addressed in order to design efficient numerical methods for ideal MHD.

Finite volume methods are a popular type of numerical framework for approximating solutions to conservation laws. These methods are based on approximating the integral form of the conservation law on each cell or control volume. Numerical fluxes at each cell interface are based on either exact or approximate solutions of Riemann problems at the interface. Higher order of accuracy in space can be obtained by using non-oscillatory ENO/WENO type piecewise polynomial functions in each cell. Higher order accuracy in time is obtained by using suitable Runge-Kutta solvers. A detailed account of these methods is presented in [50].

In this paper, we will consider approximate Riemann solvers of the HLL type (see [50]) when constructing numerical fluxes. These solvers are based on approximating the solution of Riemann problems by a piecewise constant function containing fewer discontinuities than there are waves in the exact solution. A complete description of the solver is provided by specifying the wave speeds and intermediate states. The ideal MHD equations have seven waves (in one space dimension). Typical HLL solvers for the MHD equations involving 2, 3, 5 and 7 waves have been developed. Among these are the 3 wave solvers

of [53] and[36], the 5 wave solver of [59] and the 3, 5 and 7 wave solvers of [20, 21]. The latter ones are based on an extended Suliciu type relaxation system.

Another alternative is to use linearized approximate Riemann solvers. In this case, the exact solution of Riemann problems at each cell interface is replaced by an exact solution of a suitable linearization of the non-linear flux function across the interface. The resulting solvers are denoted as Roe type approximate Riemann solvers for systems of conservation laws (see [50]) for details). These solvers are known to have high accuracy, in particular they resolve isolated discontinuities exactly. Roe type solvers for ideal MHD have been developed in [23], [24],[8] and other references therein.

When choosing an approximate Riemann solver, the key issues are computational cost, accuracy and stability. One essential stability criteria for ideal MHD is maintaining positive density and pressure. Another desirable property for a solver is that a discrete entropy condition should hold, in which case the solver is said to be entropy stable. In one space dimension, the standard HLL two wave solver, three wave solver of [36], five wave solver of [59] and the relaxation based solvers of [20, 21] are provably positivity preserving [1]. The three wave solver of [53] has not been proven to be positivity preserving. It is well known that Roe type solvers are not positivity preserving. The solvers of [20, 21] are also entropy stable. However, for MHD all these results are valid in only one space dimension.

The above schemes are restricted to first-order accuracy in both space and time. We use standard piecewise linear ENO ([40]) reconstruction to obtain second-order spatial accuracy. Second-order accuracy in time is obtained by using the strong stability preserving (SSP) Runge-Kutta method ([37]).

When simulating stratified atmospheres, the numerical treatment of the gravitational source term has to be taken into account. The presence of this source term leads to interesting steady states that need to be preserved. Furthermore, waves are modeled as perturbations of these steady states. The pressure and density at a steady state decay exponentially in the vertical direction due to the presence of gravity, which leads to very low densities and pressures at the top of the computational domain. Since preserving positivity is a challenge for any solver, this problem is particularly acute in stratified atmospheres. We treat the source term by using the method of fractional steps and identify suitable stability conditions and discretizations which still keep the HLL solvers positivity preserving. Second-order accurate fractional steps is obtained by using Strang splitting ([50]).

The next issue that needs to be addressed for the simulation of waves is that of boundary conditions. For simplicity, consider a two-dimensional model with x- and z-directions being associated with the horizontal and vertical directions respectively. Since we are interested in simulating a small part of the solar atmosphere, we use periodic boundary conditions at the x-boundary. At the bottom z-boundary, we have to prescribe boundary conditions in order to model incoming waves. At the top z-boundary, we need to implement numerical boundary conditions that minimize reflections when waves (from the bottom of the domain) reach this boundary. Furthermore, this boundary should not generate any waves or numerical artifacts that affect the quality of the solution in the interior of the domain. The vertical boundary conditions have to retain the mass

[1] We define a positivity preserving scheme as a scheme that ensures that density and pressure remains positive under a suitable CFL-condition.

balance and not lead to conservation errors. Conservation errors will force solutions away from the steady state. Since the solutions have very low pressures at the top boundary, conservation errors can easily lead to negative pressures and densities.

We adapt the non-reflecting characteristic boundaries developed in [78, 79, 63] to this problem. The adaptation is complicated on account of the complex eigenstructure and the non-strict hyperbolicity of the equations. We also introduce an alternative implementation of the non-reflecting boundary conditions of [78, 79]. Additionally, we have to adapt the boundary conditions in order to ensure mass balance. Another alternative implementation of boundary conditions is to modify simple Neumann type numerical boundary conditions to enforce mass balance. This choice might lead to greater amount of reflections. Furthermore, we propose a novel set of boundary conditions based on extrapolating (by an exponential profile) the pressure and the density from the interior of the domain into the ghost cells together with Neumann type conditions for the velocity and magnetic fields. We compare all the boundary conditions in numerical experiments.

The aim of the paper is to develop a finite volume based numerical framework that simulates wave propagation in an idealized magneto-atmosphere. We implement different first- and second-order accurate HLL type solvers as well as Roe solvers for the finite volume fluxes and compare them in a series of experiments. The sources are discretized by using a method of fractional steps that keeps pressures and densities positive. The model is completed by boundary conditions of the characteristic type as well as Neumann type that are modified to ensure mass balance in the domain. All the above ingredients are combined together to obtain a finite volume framework that can simulate waves in stratified magneto atmospheres. We emphasize that a successful simulation of wave propagation requires proper choices of all the above ingredients and we present them in this paper.

The rest of the paper is organized as follows: in Section 5.2, we present the model of the idealized solar atmosphere and specify the detailed eigenstructure of ideal MHD equations. The approximate Riemann solvers are described and compared in a series of numerical experiments in Section 5.3. In section 5.4, we explain the numerical approximation of the gravity source term and provide a complete description of the boundary conditions in Section 5.5. Numerical experiments for wave propagation in the idealized solar atmosphere are provided in Section 5.6.

5.2 The model

In this section, we present the equations and initial and boundary conditions modeling an idealized solar atmosphere. The basic equations of the model are the equations of ideal MHD along with source terms due to gravity given by

$$\begin{aligned}
\rho_t + \operatorname{div}(\rho\mathbf{u}) &= 0,\\
(\rho\mathbf{u})_t + \operatorname{div}(\rho\mathbf{u}\otimes\mathbf{u} + (p+\frac{1}{2}|\mathbf{B}|^2)I - \mathbf{B}\otimes\mathbf{B}) &= -\rho g\mathbf{e}_3,\\
\mathbf{B}_t + \operatorname{div}(\mathbf{u}\otimes\mathbf{B} - \mathbf{B}\otimes\mathbf{u}) &= 0,\\
E_t + \operatorname{div}((E+p+\frac{1}{2}|\mathbf{B}|^2)\mathbf{u} - (\mathbf{u}\cdot\mathbf{B})\mathbf{B}) &= -\rho g(\mathbf{u}\cdot\mathbf{e}_3),\\
\operatorname{div}(\mathbf{B}) &= 0.
\end{aligned} \tag{5.2.1}$$

where ρ is the density, $\mathbf{u} = \{u^1, u^2, u^3\}$ and $\mathbf{B} = \{B^1, B^2, B^3\}$ are the velocity and magnetic fields respectively, p is the thermal pressure, g is constant acceleration due to gravity , $\mathbf{e}_3 = \{0, 0, 1\}$, E is the total energy determined by an ideal gas equation of state of the form,

$$E = \frac{p}{\gamma - 1} + \frac{1}{2}\rho|\mathbf{u}|^2 + \frac{1}{2}|\mathbf{B}|^2. \tag{5.2.2}$$

where γ is the adiabatic gas constant. The above equations describe the conservation of mass, momentum and energy and the evolution of the magnetic field due to the velocity. In addition, magnetic monopoles have not been observed in nature and this fact is modeled by the constraint that the divergence of the magnetic field remains zero during the evolution.

In condensed form, the above equations (5.2.1) can be written as a system of balance laws of the form,

$$U_t + (f(U))_x + (g(U))_y + (h(U))_z = S(U), \tag{5.2.3}$$

where U is the vector of conserved variables, f, g and h are the directional fluxes and S is the source.

For simplicity, we consider the equations in two dimensions. The x coordinate represents the horizontal direction and the z coordinate the vertical direction. In particular this means that no variable depends on y, i.e., $\partial_y \equiv 0$ in (5.2.1). We consider (5.2.1) in the domain $[0, X] \times [0, Z]$ where X and Z are positive numbers. Next, we specify steady states (stationary solutions) that are of interest as they will serve as a background for the propagation of waves.

5.2.1 Hydrodynamic steady state.

To begin with, we assume that the magnetic field $\mathbf{B}$ is set to zero implying that the model is driven by ideal compressible hydrodynamics. In addition, the atmosphere is assumed to be steady by setting the velocity field $\mathbf{u}$ to zero. With this ansatz the pressure and the density have to satisfy the following ordinary differential equation

$$\frac{\partial p}{\partial z} = -\rho g. \tag{5.2.4}$$

We look for solutions of (5.2.4) satisfying $p(x, z) = c\rho(x, z)$ for some constant c and for all x and z, which amounts to assuming an isothermal atmosphere. This is a reasonable approximation since we are interested in simulating the region around the lower chromosphere of the sun where the temperature remains approximately constant. Substituting this into (5.2.4) leads to the following hydrodynamic steady state,

$$\mathbf{u} = 0, \quad \mathbf{B} = 0, \quad \rho(x, z) = \rho_0 e^{-\frac{z}{H}}, \quad p(x, z) = p_0 e^{-\frac{z}{H}}. \tag{5.2.5}$$

where the scale height H is given by $H = \frac{p_0}{g\rho_0}$ and p_0 and ρ_0 are the values of the pressure and density at the bottom boundary of the domain. Observe that the pressure and density decay exponentially with height, giving very low values near the top of the computational domain. As a consequence, when we are performing numerical calculations of small perturbations of this state, retaining positivity of pressure and density (particularly at the top of the computational domain) is going to be a key difficulty.

5.2.2 Magnetic steady states

Any realistic description of the solar atmosphere has to include magnetic fields. Hence, we need to calculate steady states of (5.2.1) with non-trivial magnetic fields. Momentum balance in (5.2.1) can also be written as

$$(\rho \mathbf{u})_t + \mathrm{div}(\rho \mathbf{u} \otimes \mathbf{u} + pI) = \mathrm{curl}(\mathbf{B}) \times \mathbf{B} - \rho g \mathbf{e}_3$$

This form makes the role of gravity and the Lorentz force explicit. The magnetic steady state is a stationary solution of (5.2.1) with the additional ansatz that $p = c\rho$, $\mathrm{curl}(\mathbf{B}) = 0$ and $\mathbf{u} = 0$. This corresponds to stationary and Lorentz-force free fields. Substituting the above ansatz into (5.2.1), we obtain that the density and the pressure is given by (5.2.5). Furthermore, since the magnetic field $\mathbf{B}$ is assumed to be such that $\mathrm{curl}(\mathbf{B}) \equiv 0$ and $\mathrm{div}(\mathbf{B}) \equiv 0$, it can be expressed in terms of vector harmonic functions. As we consider a small part of the solar atmosphere and assume periodic boundary conditions in the horizontal direction, we choose to express the magnetic field in terms of a finite number of modes in a Fourier expansion. A resulting steady state is given by

$$\begin{aligned} \mathbf{u} = 0, \quad B_2 = 0, \quad p(x,z) = p_0 e^{-\frac{z}{H}}, \quad \rho(x,z) = \rho_0 e^{-\frac{z}{H}}, \\ B^1(x,z) = \sum_{k=0}^{M} f_k \sin\left(\frac{2k\pi x}{X}\right) e^{-\frac{2\pi k z}{X}}, \\ B^3(x,z) = \sum_{k=0}^{M} f_k \cos\left(\frac{2k\pi x}{X}\right) e^{-\frac{2\pi k z}{X}}, \end{aligned} \tag{5.2.6}$$

where f_k's are the Fourier coefficients corresponding to the data $B^1(x,0)$ and $B^3(x,0)$ at the bottom boundary and M is the total number of Fourier modes for the boundary data. We choose $B_2 \equiv 0$ as the resulting magnetic field is planar. This is done for simplicity.

A simple calculation shows that (5.2.6) is indeed a steady state of (5.2.1). Furthermore, the pressure and density have an exponential decay along the vertical direction. The magnetic field is quite complicated and leads to a genuinely multi-dimensional description of the model. These factors complicate design of numerical schemes.

5.2.3 The characteristic structure of ideal MHD

For the sake of completeness we give some details regarding the eigensystem of the MHD equations. Consider the equation (5.2.1) in the x-direction without gravity i.e., $g = 0$. The divergence constraint in one space dimension forces the magnetic field in x direction, B^1, to be constant in space and time, and thus act only as a parameter in the equations. Defining the vector of primitive variables,

$$V = \{\rho, u^1, u^2, u^3, B^2, B^3, p\}$$

the system (5.2.1) reduces to the following quasilinear form in one dimension,

$$V_t + A_1(V) V_x = 0. \tag{5.2.7}$$

For the precise expression for the Jacobian matrix A_1, see [68]. Defining the speeds

$$a^2 = \frac{\gamma p}{\rho} \quad \text{and} \quad b_{1,2,3} = \frac{B^{1,2,3}}{\sqrt{\rho}},$$
$$b^2 = b_1^2 + b_2^2 + b_3^2, \quad b_\perp^2 = b_2^2 + b_3^2,$$

the eigenvalues of A_1 read

$$\lambda_1 = u_1 - c_f, \quad \lambda_2 = u_1 - b_1, \quad \lambda_3 = u_1 - c_s, \quad \lambda_4 = u_1,$$
$$\lambda_5 = u_1 + c_s, \quad \lambda_6 = u_1 + b_1, \quad \lambda_7 = u_1 + c_f,$$

where c_f and c_s are given by

$$\begin{aligned} c_f^2 &= \frac{1}{2}\left(a^2 + b^2 + \sqrt{\left(a^2+b^2\right)^2 - 4a^2 b_1^2}\right), \\ c_s^2 &= \frac{1}{2}\left(a^2 + b^2 - \sqrt{\left(a^2+b^2\right)^2 - 4a^2 b_1^2}\right). \end{aligned} \tag{5.2.8}$$

The waves corresponding to λ_1 and λ_7 are called fast waves, the ones corresponding to λ_3 and λ_5 slow waves, those corresponding to λ_2 and λ_6 Alfvén waves and the wave associated with λ_4 is called a contact wave. As the above eigenvalues are real, the system is hyperbolic. But the eigenvalues are not always distinct, and the system is not strictly hyperbolic. This non-strict hyperbolicity is a formidable obstacle to the development of mathematical theory and numerical methods for MHD.

It is well known that the eigenvectors of (5.2.7) have to be scaled properly in order to be well-defined. We now present the orthonormal set of eigenvectors first described in [68]. The right and left eigenvectors corresponding to the contact wave λ_4 are given by,

$$r_e = (1,0,0,0,0,0,0)^T, \quad l_e = \frac{1}{a^2}\left(a^2,0,0,0,0,0,-1\right).$$

Define $\beta_{2,3} = \frac{b_{2,3}}{b_\perp}$. Then, the eigenvectors corresponding to the Alfvén waves λ_2 and λ_6 are given by

$$\begin{aligned} r_A^\pm &= \left(0,0,\pm\beta_3,\mp\beta_2,-\sqrt{\rho}\beta_3 \text{sign}\left(b_1\right),\sqrt{\rho}\beta_2 \text{sign}\left(b_1\right),0\right)^T, \\ l_A^\pm &= \frac{1}{2}\left(0,0,\pm\beta_3,\mp\beta_2,-\beta_3 \text{sign}\left(b_1\right)/\sqrt{\rho},\beta_2 \text{sign}\left(b_1\right)/\sqrt{\rho},0\right), \end{aligned}$$

where r_A^+ and l_A^+ correspond to λ_2.

As in [68], we introduce the following normalizing factors,

$$\alpha_f^2 = \frac{a^2 - c_s^2}{c_f^2 - c_s^2}, \quad \alpha_s^2 = \frac{c_f^2 - a^2}{c_f^2 - c_s^2}.$$

Note that $\alpha_f^2 + \alpha_s^2 = 1$. The eigenvectors corresponding to the fast and slow waves read,

$$r_f^\pm = \begin{pmatrix} \alpha_f \rho \\ \pm\alpha_f c_f \\ \mp\alpha_s c_s \beta_2 \text{sign}\left(b_1\right) \\ \mp\alpha_s c_s \beta_3 \text{sign}\left(b_1\right) \\ \alpha_s \sqrt{\rho} a \beta_2 \\ \alpha_s \sqrt{\rho} a \beta_3 \\ \alpha_f \rho a^2 \end{pmatrix}, \quad r_s^\pm = \begin{pmatrix} \alpha_s \rho \\ \pm\alpha_s c_s \\ \mp\alpha_f c_f \beta_2 \text{sign}\left(b_1\right) \\ \mp\alpha_f c_f \beta_3 \text{sign}\left(b_1\right) \\ \alpha_f \sqrt{\rho} a \beta_2 \\ \alpha_f \sqrt{\rho} a \beta_3 \\ \alpha_s \rho a^2 \end{pmatrix},$$

$$l_f^{\pm} = \frac{1}{2a^2}\left(0, \pm\alpha_f c_f, \mp\alpha_s c_s \beta_2 \text{sign}\,(b_1), \mp\alpha_s c_s \beta_3 \text{sign}\,(b_1), \alpha_s a\frac{\beta_2}{\sqrt{\rho}}, \alpha_s a\frac{\beta_3}{\sqrt{\rho}}, \frac{\alpha_f}{\rho}\right),$$
$$l_s^{\pm} = \frac{1}{2a^2}\left(0, \pm\alpha_s c_s, \mp\alpha_f c_f \beta_2 \text{sign}\,(b_1), \mp\alpha_f c_f \beta_3 \text{sign}\,(b_1), \alpha_f a\frac{\beta_2}{\sqrt{\rho}}, \alpha_f a\frac{\beta_3}{\sqrt{\rho}}, \frac{\alpha_s}{\rho}\right).$$

The normalization factors α_f and α_s are not well-defined at the triple point where $b_1 = a$ and $b_\perp = 0$. In this case, we use the fact that $\alpha_f^2 + \alpha_s^2 = 1, \beta_2^2 + \beta_3^2 = 1$ and define $\alpha_f = \alpha_s = \beta_2 = \beta_3 = 1/\sqrt{2}$.

5.3 Approximate Riemann solvers

In this section we review the different approximate Riemann solvers that we want to test. Consider the ideal MHD equations (5.2.1) with $g = 0$ in the domain $[0, X] \times [0, Z]$. We divide this into $I \times K$ cells (or control volumes), and define $x_i = -\Delta x/2 + i\Delta x$, $i = 0, \ldots, I+1$, and $z_k = -\Delta z/2 + k\Delta z$, $k = 0, \ldots, K+1$, so that $z_{k+1/2} = k\Delta z$. Let $I_{i,k}$ denote the control volume $[x_{i-1/2}, x_{i+1/2}) \times [z_{k-1/2}, z_{k+1/2})$. The cell average of the vector of conserved variables at time t^n over the cell $I_{i,k}$ is given by $U_{i,k}^n$. Let $\Delta = \min\{\Delta x, \Delta z\}$, then the time step Δt^n is chosen by the CFL condition,

$$\max_{i,k}\left\{\left|u_{i,k}^{1,n}\right| + c_{i,k}^{f1,n},\ \left|u_{i,k}^{3,n}\right| + c_{i,k}^{f3,n}\right\}\frac{\Delta t^n}{\Delta} \le 1 \tag{5.3.1}$$

where $c_{i,k}^{fj,n}$ is the fast speed in the j-th direction in the cell $I_{i,k}$. Then, a general finite volume scheme is written,

$$\begin{aligned} U_{i,k}^{n+1} &= \mathcal{F}\left(U_{i-1,k}^n, U_{i,k-1}^n, U_{i,k}^n, U_{i+1,k}^n, U_{i,k+1}^n\right), \\ &= U_{i,k}^n - \frac{\Delta t^n}{\Delta x}\left(F_{i+1/2,k}^n - F_{i-1/2,k}^n\right) - \frac{\Delta t^n}{\Delta z}\left(H_{i,k+1/2}^n - H_{i,k-1/2}^n\right), \end{aligned} \tag{5.3.2}$$

where the numerical fluxes are functions of the neighboring cell averages, i.e.,

$$F_{i+1/2,k}^n = F\left(U_{i,k}^n, U_{i+1,k}^n\right), \quad H_{i,k+1/2}^n = H\left(U_{i,k}^n, U_{i,k+1}^n\right).$$

These numerical fluxes should be such that $F(A, B)$ is an approximation to the solution at $x = 0$ of the Riemann problem in the x direction for (5.2.1). To be concrete, if U satisfies

$$U_t + f(U)_x = 0, \quad U(x,0) = \begin{cases} U_L & x < 0, \\ U_R & x > 0, \end{cases}$$

then $F(U_L, U_R) \approx f(U(0,t))$. The numerical flux $H(U_L, U_R)$ is defined analogously.

We will use approximate Riemann solvers of the HLL type, see [50], in order to define the numerical fluxes.

5.3.1 HLL2 solver

The number "2" denoting this approximate Riemann solver means that we approximate the full Riemann solution using two moving discontinuities (waves). Let $U_{L,R}$ and $f_{L,R}$

denote the left and right state and flux respectively. If the speed of the two waves are s_L and s_R then the constant state in between these waves, U_* will be determined from conservation by

$$f_R - f_* = s_R (U_R - U_*), \quad f_* - f_L = s_L (U_* - U_L),$$

where f_* denotes the numerical flux between these two waves. Solving the above equations yields

$$U_* = \frac{f_R - f_L - s_R U_R + s_L U_L}{s_L - s_R}, \quad f_* = \frac{s_R f_L - s_L f_R + s_L s_R (U_R - U_L)}{s_R - s_L}. \tag{5.3.3}$$

Then, the numerical flux can be written as

$$F^{\text{hll2}}(U_L, U_R) = \begin{cases} f_L & \text{if } s_L \geq 0, \\ f_* & \text{if } s_L < 0 < s_R, \\ f_R & \text{if } s_R \leq 0. \end{cases} \tag{5.3.4}$$

It remains to define the waves speeds s_L and s_R, and we do this as in [28]. Let $\bar{U} = (U_L + U_R)/2$, then the wave speeds are given by

$$s_L = \min\left\{u_L^1 - c_{fL},\ \bar{u}_1 - \bar{c}_f\right\}, \quad s_R = \max\left\{u_R^1 + c_{fR},\ \bar{u}_1 + \bar{c}_f\right\}, \tag{5.3.5}$$

where $\bar{u}_1$ and $\bar{c}_f$ are the normal velocity and the fast wave speed of $A(\bar{U})$ respectively. This solver only approximates the outermost (fast) waves of the Riemann solution and can be very dissipative, particularly at contact discontinuities.

5.3.2 HLL3 solvers

This type of solver uses three moving discontinuities to approximate the solution of the Riemann problem. Let the $U_{L,R}$ and $f_{L,R}$ be as before. With this notation a HLL3 solver gives the approximate solution

$$U^{\text{hll3}} = \begin{cases} U_L & \text{if } s_L \geq 0, \\ U_L^* & \text{if } s_L < 0 < s_M, \\ U_R^* & \text{if } s_M < 0 < s_R, \\ U_R & \text{if } s_R \leq 0, \end{cases} \quad F^{\text{hll3}}(U_L, U_R) = \begin{cases} f_L & \text{if } s_L \geq 0, \\ f_L^* & \text{if } s_L < 0 < s_M, \\ f_R^* & \text{if } s_M < 0 < s_R, \\ f_R & \text{if } s_R \leq 0, \end{cases} \tag{5.3.6}$$

where the outer wave speeds s_L and s_R are given by (5.3.5) and the middle wave speed is given by s_M. Local conservation implies,

$$s_L U_L^* - f_L^* = s_L U_L - f_L, \quad s_M U_R^* - f_R^* = s_M U_L^* - f_L^*, \quad s_R U_R - f_R = s_R U_R^* - f_R^*. \tag{5.3.7}$$

From this we obtain the following expressions for f_L^* and f_R^*

$$f_L^* = f_* - \frac{s_L(s_R - s_M)}{s_R - s_L} \Delta U^*, \quad f_R^* = f_* + \frac{s_R(s_M - s_L)}{s_R - s_L} \Delta U^*, \tag{5.3.8}$$

where $\Delta U^* = U_R^* - U_L^*$ and f_* is given by (5.3.3).

HLL3L solver:

In [53], the author determines the two middle states by making the following *ansatz*,

$$\Delta U^* = \alpha(U_R - U_L),$$

where α is a parameter to be determined. If we set $\alpha = 0$ the middle wave disappears and we get the $HLL2$ solver. When $\alpha = 1$, an HLL3 solver will give a single discontinuity approximating the contact wave.

Since the middle wave is supposed to model the contact discontinuity, we can choose the middle wave speed as the corresponding velocity of the Jacobian $A(\bar{U})$, i.e., $s_M = \bar{u}^1$. Set $c_* = |\bar{c}_f - s_M|$ and

$$s = \frac{|\Delta f - s_M \Delta U|}{|\Delta U|},$$

where $\Delta U = U_R - U_L$ and $\Delta f = f_R - f_L$, the interpolation factor α is then defined as

$$\alpha = \max\left\{0, 1 - \frac{s}{c_*}\right\}$$

This heuristic choice of α, which was suggested in [53], is motivated by the following argument. If the true solution of

$$V_t + A(\bar{U})V_x = 0, \quad V(x,0) = \begin{cases} U_L & x < 0, \\ U_R & x > 0, \end{cases}$$

consisted of a single contact discontinuity, then $\Delta f = s_M \Delta U$, which gives $s = 0$ and $\alpha = 1$. Similarly, if the solution consisted of a single fast shock with speed $s_M + \bar{c}_f$ (a particular form of the HLL2 solution) $s = c_*$, which gives $\alpha = 0$.

Although the pressure and density computed by this solver are not provably positive, the HLL3L solver gives satisfactory numerical results on many test problems (see Section 5.6).

HLL3G solver

A positivity preserving HLL three wave solver was proposed by Gurski in [36]. We use the notation of the previous section and the fluxes are defined in (5.3.6). We choose s_L and s_R as the Einfeldt speeds of (5.3.5) and the middle speed s_M as the normal Roe velocity as in the HLL3L solver. Then from the conservation equations (5.3.7), we can express the middle states in terms of s_M,

$$\begin{aligned} \rho_L^* &= \rho_L \frac{(s_L - u_L^1)}{(s_L - s_M)}, \quad \rho_R^* = \rho_R \frac{(s_R - u_R^1)}{(s_R - s_M)} \\ p^* &= p_L + \rho_L(u_L^1 - s_L)(u_L^1 - s_M) + \frac{|\mathbf{B}_L|^2}{2}. \end{aligned} \tag{5.3.9}$$

Note that the pressure does not jump across the contact discontinuity modeled by the middle wave. Since we are considering (5.2.1) in one dimension, B^1 is taken to be a

constant. The tangential components of the velocity and the magnetic field do not jump across the contact discontinuity and hence

$$u_L^{2,*} = u_R^{2,*} = u^{2,*}, \quad B_L^{2,*} = B_R^{2,*} = B^{2,*}.$$

Identical expressions hold for u^3 and B^3, and we substitute them into the conservation equations in order to get (in the case when $B^1 \neq 0$),

$$\begin{aligned}
u^{2,*} &= \frac{\rho_L u_L^2(u_L^1 - s_L) - \rho_R u_R^2(u_R^1 - s_R) + 0.5(B^1(B_R^2 - B_L^2)}{\rho_L(u_L^1 - s_L) - \rho_R(u_R^1 - s_R)} \\
u^{3,*} &= \frac{\rho_L u_L^3(u_L^1 - s_L) - \rho_R u_R^3(u_R^1 - s_R) + 0.5(B^1(B_R^3 - B_L^3)}{\rho_L(u_L^1 - s_L) - \rho_R(u_R^1 - s_R)} \\
B^{2,*} &= \frac{B_L^2(u_L^1 - s_L) - B_R^2(u_R^1 - s_R) + B^1(u_R^2 - u_L^2)}{s_R - s_L} \\
B^{3,*} &= \frac{B_L^3(u_L^1 - s_L) - B_R^3(u_R^1 - s_R) + B^1(u_R^3 - u_L^3)}{s_R - s_L} \\
E_L^* &= \frac{0.5(|\mathbf{B}_L|^2 u_L^1) + (p_L u_L^1 + E_L(u_L^1 - s_L) - s_M p^*) + B^1(\mathbf{B}_L^* \cdot \mathbf{u}_L^* - \mathbf{B}_L \cdot \mathbf{u}_L)}{s_M - s_L} \\
E_R^* &= \frac{0.5(|\mathbf{B}_R|^2 u_R^1) + (p_R u_R^1 + E_R(u_R^1 - s_R) - s_M p^*) + B^1(\mathbf{B}_R^* \cdot \mathbf{u}_R^* - \mathbf{B}_R \cdot \mathbf{u}_R)}{s_M - s_R}
\end{aligned}$$

If $B = 0$ we can find the relevant formulas in [36]. The pressure and density computed using this solver are always positive. In [36], the author noted that a modified version of this solver resolves Alfvén and slow waves better, but we found that this modification might lead to negative pressures in some of our simulations, and hence we use the original version of this solver.

HLL3R solver:

In [20] and [21], an MHD 3-wave solver is derived from a relaxation system as an extension of the work for hydrodynamics in [19]. This solver is positivity preserving, and it also satisfies a discrete entropy inequality. We refer to [20] and [21] for justification, and only describe the solver here. First assume that the outer wave speeds $s_L = u_L - c_L/\rho_L$ and $s_R = u_R + c_R/\rho_R$ are given for some positive c_L, c_R. Define the relaxation pressure

$$\pi_{L,R} = \left(p + \frac{1}{2}\mathbf{B}^2 - (B^1)^2, -B^1B^2, -B^1B^3\right)_{L,R}.$$

Then define the intermediate states

$$\begin{aligned}
\mathbf{u}_* = \mathbf{u}_*^L = \mathbf{u}_*^R &= \frac{c_L\mathbf{u}_L + c_R\mathbf{u}_R + \pi_L - \pi_R}{c_L + c_R}, \\
\pi_* = \pi_*^L = \pi_*^R &= \frac{c_R\pi_L + c_L\pi_R + c_Lc_R(\mathbf{u}_L - \mathbf{u}_R)}{c_L + c_R}.
\end{aligned}$$

These are constant across the middle wave, so we can define the middle wave speed $s_M = u_*^1$. The intermediate state values for ρ, $B^{2,3}$ and E are given by B^1 being constant,

and

$$\frac{\mathbf{B}_{L,R}}{\rho_{L,R}} - B^1\frac{\pi_{L,R}}{c^2_{L,R}} = \frac{\mathbf{B}^*_{L,R}}{\rho^*_{L,R}} - B^1\frac{\pi_*}{c^2_{L,R}},$$

$$e_{L,R} + \frac{(\mathbf{B}_{L,R})^2}{2\rho_{L,R}} - \frac{\pi^2_{L,R}}{2c^2_{L,R}} = e^*_{L,R} + \frac{\left(\mathbf{B}^*_{L,R}\right)^2}{2\rho^*_{L,R}} - \frac{\pi^2_*}{2c^2_{L,R}}.$$

Finally, adopting the notation of (5.3.6), the numerical flux is given by

$$f^*_{L,R} = \left(\rho u^1, \rho u^1\mathbf{u} + \pi, u^1\mathbf{B} - B^1\mathbf{u}, Eu^1 + \pi\cdot\mathbf{u}\right)^*_{L,R}.$$

The coefficients c_L and c_R are given by

$$c_L = \rho_L\left(a^0_L + \frac{1}{2}(\gamma+1)X_L\right), \quad c_R = \rho_R\left(a^0_R + \frac{1}{2}(\gamma+1)X_R\right)$$

with γ as in the equation of state (5.2.2),

$$X_L = (u^1_L - u^1_R)^+ + \frac{(\pi^1_R - \pi^1_L)^+}{\sqrt{\gamma\rho_L p_L} + \rho_R c^R_f}, \quad X_R = (u^1_L - u^1_R)^+ + \frac{(\pi^1_L - \pi^1_R)^+}{\sqrt{\gamma\rho_R p_R} + \rho_L c^L_f},$$

and $a^0_{L,R}$ given by (using the notation of (5.2.8))

$$(a^0_{L,R})^2 = \frac{1}{2}\left(a^2 + \frac{b^2}{\xi} + \sqrt{\left(a^2 + \frac{b^2}{\xi}\right)^2 - 4a^2\frac{b^2_1}{\xi}}\right)_{L,R},$$

$$\text{with} \quad \xi_{L,R} = \left(\frac{c_f + \frac{1}{2}(\gamma-1)X}{c_f + \frac{1}{2}(\gamma+1)X}\right)_{L,R}.$$

5.3.3 Roe Solver

Although our focus in this paper is on the approximate Riemann solvers of the HLL type, we briefly describe the Roe solver in order to compare it with the HLL solvers as well as to use it in our implementation of non-reflecting characteristic boundary conditions.

Given two states U_L, U_R across an interface, let $\hat{A}$ (see [24]) be the Roe matrix associated with U_L, U_R (the simple average $A(\frac{U_L+U_R}{2})$ also suffices for most practical purposes). Let $\hat{R}, \hat{L}$ be the right and left eigenvector matrices associated with $\hat{A}$. We can use the Roe-Balsara eigensystem used in section 2 for the eigen-system decomposition, then the Roe solver ([67]) is given by,

$$F^{\text{Roe}}(U_L, U_R) = \frac{1}{2}(f_L + f_R - \hat{R}|\hat{\Lambda}|\hat{L}(U_R - U_L)) \tag{5.3.10}$$

where $|\hat{\Lambda}| = \text{diag}\{|\hat{\lambda}_1|, \ldots, |\hat{\lambda}_7|\}$ with $\hat{\lambda}$'s being the eigenvalues of the Roe-matrix. This flux needs to be augmented with some standard entropy fix like the Harten ([38]) or Harten-Hyman ([39]) entropy fix in order to comply with the entropy condition. We use the Harten fix ([38]) in the numerical experiments presented later. It is well known that the Roe solver is a linearized, low dissipative solver that resolves isolated shocks exactly. Furthermore, it doesn't necessarily preserve positivity leading to problems when it is implemented in our solar atmosphere model.

Remark 5.3.1. The above HLL and Roe solvers are based on the one-dimensional form of the equations and require that the normal magnetic field B^i for $i = 1, 3$ is constant in each direction. However, in multi dimensional computations, the normal magnetic field is no longer constant. Hence, we need to suitably modify the solvers for multidimensional problems.

We use a simple modification, in the i-th direction, we use $B^i = \frac{B^i_L + B^i_R}{2}$ in our formulas to define the numerical fluxes in each direction. This simple modification does not guarantee that the solver remains positive but works reasonably well in all the numerical experiments that we performed. A careful modification of the solvers to make them handle genuinely multidimensional data requires a suitable discretization of the Powell source term, see [65] and, for HLL3R, [21].

5.3.4 Numerical Experiments

We will compare all the above solvers in a series of numerical experiments. Furthermore, for all numerical examples in this paper we use $\gamma = 5/3$.

Regarding the measurement of errors, if we have a reference solution available, then we define the relative error as

$$100 \times \frac{\|\alpha - \alpha_{\text{ref}}\|}{\|\alpha_{\text{ref}}\|},$$

where α is (a component of) the numerical approximation and α_{ref} is (the same component of) the reference solution, and $\|\cdot\|$ is some norm.

The Brio-Wu shock tube

We start with a one-dimensional test case proposed in [23]. The initial data are given by

$$\rho_0 = \begin{cases} 1.0 & \text{if } x < 1.0, \\ 0.3 & \text{if } x \geq 1.0, \end{cases} \quad u^1_0 = 0, \quad u^2_0 = 0, \quad u^3_0 = 0,$$

$$B^1_0 = 0.7, \quad B^2_0 = \begin{cases} 0.0 & \text{if } x < 1.0, \\ 1.0 & \text{if } x \geq 1.0, \end{cases} \quad B^3_0 = 0, \quad p_0 = \begin{cases} 1.0 & \text{if } x < 1.0, \\ 0.1 & \text{if } x \geq 1.0. \end{cases}$$

The computational domain is $(x, t) \in [0, 1.5] \times [0, 0.35]$, and we use Neumann type artificial boundary conditions for $x = 0$ and $x = 1.5$. The numerical results for 200 mesh points at time $t = 0.35$ are shown in figure 5.3.1 and are compared in table 5.3.1. We calculate the reference solution using the HLL3L solver and 8000 mesh points. As seen from the error table as well as from Figure 5.3.1, the different solvers do quite well at resolving the complicated solution which has a large number of waves. The error table shows that the Roe-scheme has the best resolution, and the other schemes give very similar results. As expected, all the schemes exhibit a convergence order roughly between $\frac{1}{2}$ and 1 as the number of mesh points increases. Among the HLL solvers, the HLL2 solver seems to be the most dissipative and least accurate.

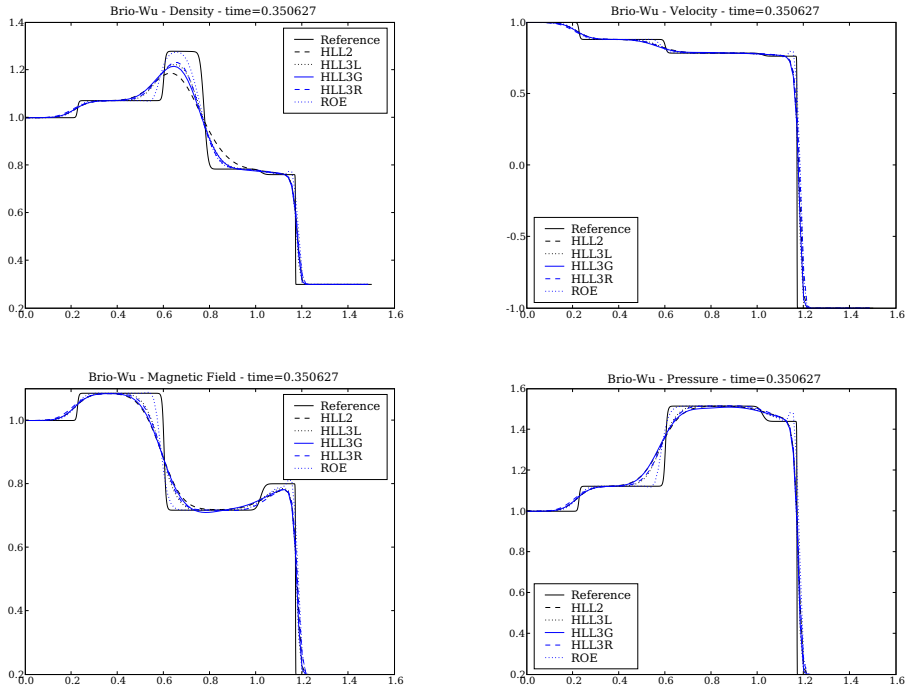

Figure 5.3.1: Results for the Brio-Wu shock tube for 200 mesh points at time $t = 0.35$. Top left: ρ, top right: u^1, bottom left: B^2 and bottom right: P

Relative errors in ρ.

M	HLL	HLL3L	HLL3G	HLL3R	Roe
100	4.42	3.35	3.71	3.49	2.64
200	3.21	2.31	2.61	2.33	1.60
400	1.92	1.25	1.50	1.30	0.72
800	1.19	0.73	0.91	0.77	0.37
1600	0.64	0.31	0.43	0.34	0.10

Relative errors in B^2.

M	HLL	HLL3L	HLL3G	HLL3R	Roe
100	3.64	2.91	3.45	3.38	2.36
200	2.68	2.16	2.59	2.34	1.43
400	1.43	1.07	1.39	1.21	0.50
800	0.88	0.67	0.88	0.76	0.29
1600	0.43	0.28	0.43	0.34	0.11

Table 5.3.1: Relative errors in L^1 for the density and B^2 for the Brio-Wu shock tube using M mesh points.

An expansion problem

From the previous experiment, the Roe solver was found to be most accurate. However, it is well known that the Roe solver fails to be positivity preserving. We present a test case illustrating this phenomenon. Consider the initial data,

$$\rho_0 = p_0 \equiv 1, \quad u_0^2 = u_0^3 = B_0^1 = B_0^3 \equiv 0,$$
$$u_0^1 = \begin{cases} -4.0 & \text{if } x < 0.7, \\ 4.0 & \text{if } x \geq 0.7, \end{cases} \quad B_0^2 = \begin{cases} 1.0 & \text{if } x < 0.7, \\ -1.0 & \text{if } x \geq 0.7. \end{cases}$$

and the computational domain $[0, 0.14] \times [0, 0.12]$ and test all the solvers on this test case. The data is set up in a manner such that the exact solution loses mass in the center of the domain and the resulting pressure and density are quite close to zero. The numerical results for the pressure at 400 mesh points near the final time is shown in figure 5.3.2. From figure 5.3.2, the HLL solvers do well in this case in resolving very low pressures

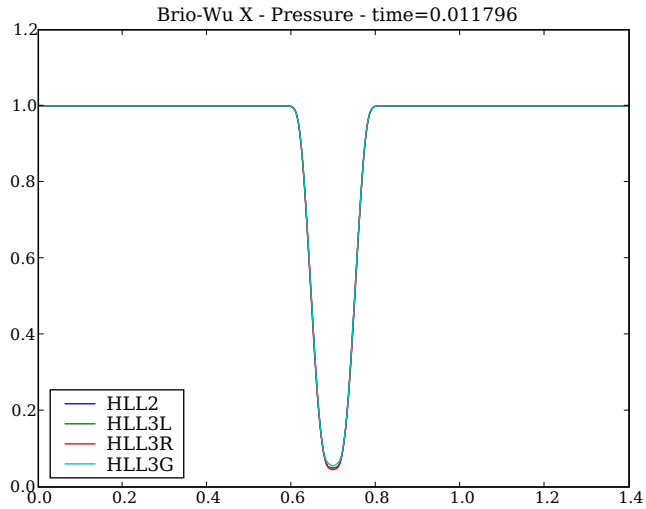

Figure 5.3.2: Results for the pressure in the expansion problem for 400 mesh points at time $t = 0.12$ with all the HLL solvers

near the center of the domain. There are minor differences in the resolution between different HLL solvers. On the other hand, the Roe solver crashed on this test problem at time $t = 0.004$ i.e about 4 percent of the final time, showing that its high accuracy and resolution comes at a price i.e low stability particularly with respect to negative pressures. This example serves as a caution in using the Roe solver on problems involving stratified atmosphere, as low pressures are expected at the top boundary.

The Orszag-Tang vortex

This is a commonly used two dimensional test problem, see e.g. [80], with initial data given by

$$\left\{\rho_0, u_0^1, u_0^2, u_0^3, B_0^1, B_0^2, B_0^3, p_0\right\} = \left\{\gamma^2, -\sin(y), \sin(x), 0, -\sin(y), \sin(2x), \gamma\right\}.$$

The computational domain is $(x, y, t) \in [0, 2\pi]^2 \times [0, 2.85]$ with periodic boundary conditions in space. The initial data are smooth but shocks form even for small times. The solution also contains a vortex structure in the center of the domain, and it is a computational challenge to resolve the shock-vortex interaction. Note that $\mathrm{div}\mathbf{B}_0 = 0$. In Figure 5.3.3, we show the pressure at time $t = 2.85$ and compare the HLL3L, HLL3R, HLL3G and Roe solvers on a uniform 200×200 mesh. From the figure, it is clear that the

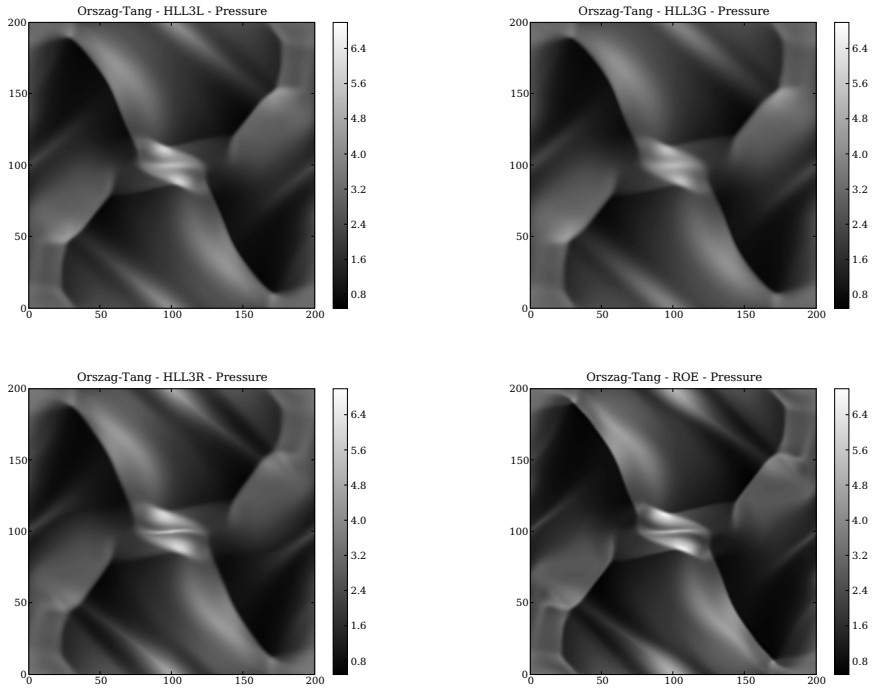

Figure 5.3.3: The pressure in the Orszag-Tang vortex at time $t = 2.85$ on a 200×200 mesh. Top left: HLL3L, top right: HLL3G, bottom left: HLL3R and bottom right: Roe

Roe scheme is the least dissipative and that the HLL3G scheme is the most dissipative. The HLL3R has better resolution than the HLL3L solver for this particular problem, although the differences are minor.

For this problem a reference solution is not available, and it is common to use the pressure at the center of the domain as a measure of the accuracy of approximate solutions.

In Table 5.3.2 we show the maximum pressure for the various solvers on a sequence of meshes. It is generally assumed that the maximum pressure correlates with the quality of the approximation. From table 5.3.2, it is clear that the Roe solver is the most accurate.

M	HLL	HLL3L	HLL3G	HLL3R	Roe
100	4.00	4.41	4.01	4.90	5.27
200	4.74	4.94	4.73	5.38	5.39
400	5.11	5.21	5.09	5.59	5.88
800	-	-	-	5.97	-

Table 5.3.2: Maximum pressure for the Orszag-Tang vertex on an $M \times M$ grid for $t = 2.85$. A "-" indicates that the computation was stopped due to negative pressure or density.

Among the HLL solvers, the HLL3R solver seems to have the best resolution. However, when we refine the mesh up to 800 mesh points in either direction, all the solvers except the HLL3R solver crash on account of negative pressures with the symbol $-$ denoting a crash of the solver. Even the HLL3R solver crashed on a 1600×1600 mesh.

One possible reason might be the discretization of the divergence constraint ([9]). Since none of our solvers are divergence preserving, and although the divergence of $\mathbf{B}_0$ is zero, for $t > 0$ discretizations of the divergence may not necessarily remain small. It has been speculated that these divergence errors are the source of the instabilities and negative pressures and densities experienced with many solvers. Therefore we exhibit the L^1 norm of the central difference approximation to the divergence in Table 5.3.3. The divergence errors are quite large. Nevertheless, they do not seem to influence the quality of the solution (as measured by the maximum pressure). Furthermore, the HLL3R solver had the largest divergence errors, yet this was the only solver which managed to compute a solution on the 800×800 mesh. From the available data, it also seems that the divergence errors decrease with increasing mesh size. These preliminary observations indicate that

M	HLL	HLL3L	HLL3G	HLL3R	Roe
100	1.92	2.81	1.86	9.66	7.77
200	1.77	2.93	1.71	8.28	6.94
400	1.47	2.60	1.44	6.95	5.64
800	-	-	-	6.03	-

Table 5.3.3: The L^1 norm of the central discrete divergence for the Orszag-Tang vertex, calculated on a sequence of meshes.

the relationship between accuracy, positivity and divergence preservation is likely to be a complicated one. Similar features were observed in other two-dimensional numerical experiments like the Rotor problem ([80]).

Remark 5.3.2. *We would like to mention that divergence cleaning for MHD is a very active research area and many methods to preserve discrete versions of the divergence constraint have been proposed. See [80] for a comparison of different divergence cleaning methods. We don't consider such methods here as it is difficult to design stable boundary*

closures for these methods and boundary conditions are key ingredient in our numerical recipe.

Another approach would be to add the Godunov-Powell source term (see [65]) that transports divergence errors out of the domain. However, this method requires a very careful "upwind" discretization of the source term. Furthermore, all divergence cleaning procedures suffer from stability problems, particularly for string test cases ([10]). Hence, we restrict ourselves to schemes without any special divergence cleaning in this paper.

5.3.5 Second-order accurate scheme

The above finite volume (5.3.2) is first-order accurate in both space and time. Hence, the schemes were quite dissipative atleast on coarse meshes in the numerical experiments presented above. Most realistic applications require the design of a scheme with higher-order spatial and temporal accuracy. The semi-discrete form of this scheme is given by

$$\frac{d}{dt}U_{i,k} = \boldsymbol{\mathcal{F}}_{i,k} = -\frac{1}{\Delta x}(F_{i+1/2,k} - F_{i-1/2,k}) - \frac{1}{\Delta z}(H_{i,k+1/2} - H_{i,k-1/2}), \tag{5.3.11}$$

where $U_{i,k}(t)$ is the cell-average of the unknown at time t. Note that we have dropped time dependence in (5.3.11) for notational convenience. We will define the numerical fluxes F, H below.

It is standard ([50]) to replace the cell averages $U_{i,k}$ by non-oscillatory piecewise linear reconstructions in-order to obtain second-order spatial accuracy. There are a variety of reconstructions including the popular TVD MUSCL limiters ([50]). However, we will use second-order ENO reconstruction ([40]) as this procedure can be easily extended to obtain even higher-order schemes.

ENO Reconstruction:

Given the cell averages $U_{i,k}$, define the ENO-gradients in each direction as

$$D^x U_{i,k} = \frac{1}{\Delta x}\begin{cases} U_{i+1,k} - U_{i,k} & , \text{ if } \Gamma^x_{i,k} \le 1 \\ U_{i,k} - U_{i-1,k} & , \text{ otherwise.} \end{cases}, \quad D^z U_{i,j} = \frac{1}{\Delta z}\begin{cases} U_{i,k+1} - U_{i,k} & , \text{ if } \Gamma^z_{i,k} \le 1 \\ U_{i,k} - U_{i,k-1} & , \text{ otherwise.} \end{cases} \tag{5.3.12}$$

where

$$\Gamma^x_{i,k} = \frac{|\Psi(U_{i+1,k}) - \Psi(U_{i,k})|}{|\Psi(U_{i,k}) - \Psi(U_{i-1,k})|}, \quad \Gamma^z_{i,k} = \frac{|\Psi(U_{i,k+1}) - \Psi(U_{i,k})|}{|\Psi(U_{i,k}) - \Psi(U_{i,k-1})|},$$

and Ψ is a global smoothness indicator. We use $\Psi(U) = \rho + |\mathbf{B}|^2$ as the smoothness indicator as it provides adequate representation of all the discontinuities in the solution of the Riemann problem for the MHD equations. Other global smoothness indicators can also be used. Note that for piecewise linear reconstruction, the ENO procedure reduces to providing a limiter for the slopes in each direction. The reconstructed piecewise linear function is each cell is denoted by,

$$\overline{U}_{i,k}(x,z) = U_{i,k} + D^x U_{i,k}(x - x_i) + D^z U_{i,k}(y - y_k). \tag{5.3.13}$$

We define the following point values,

$$UE_{i,k} = \overline{U}_{i,k}(x_{i+1/2}, z_k), \quad UW_{i,k} = \overline{U}_{i,k}(x_{i-1/2}, z_k),$$
$$UN_{i,k} = \overline{U}_{i,k}(x_i, z_{k+1/2}), \quad US_{i,k} = \overline{U}_{i,k}(x_i, y_{k+1/2}).$$

We use the above defined values to define the second-order numerical fluxes as

$$F_{i+1/2,k} = F(UE_{i,k}, UW_{i+1,k}), \quad H_{i,k+1/2} = H(UN_{i,k}, US_{i,k+1}),$$

where F, H are given by any of the HLL2, HLL3L, HLL3G, HLL3R and Roe solvers of the previous section. This completes the description of the second-order spatial accurate semi-discrete scheme (5.3.11).

Second-order time stepping:

We augment the second-order spatially accurate scheme (5.3.11) with the following strong-stability preserving TVD second-order accurate Runge-Kutta time stepping ([37]),

$$\begin{aligned} U^*_{i,k} &= U^n_{i,k} + \Delta t^n \mathcal{F}^n_{i,k}, \\ U^{**}_{i,k} &= U^*_{i,k} + \Delta t^n \mathcal{F}^*_{i,k}, \\ U^{n+1}_{i,k} &= \frac{1}{2}(U^n_{i,k} + U^{**}_{i,k}), \end{aligned} \tag{5.3.14}$$

where $\mathcal{F}$ is the residual in the semi-discrete scheme (5.3.11). The time step Δt^n is determined by a standard CFL condition.

5.3.6 Numerical Experiments with second-order schemes:

We present a one-dimensional numerical experiment to demonstrate the gain in accuracy for a second-order scheme. We choose the Brio-Wu shock tube of the previous subsection and show the results obtained with second-order schemes in figure 5.3.4. We show the density and B_2 computed on a mesh with 200 points. In-order to prevent cluttering in the figure, we present the results with just three schemes: HLL2, HLL3L and HLL3R in both the first-order (spatial and temporal) and second-order (spatial and temporal) versions. The results show that there is a large gain in accuracy and resolution by going to second-order. In particular, notice the sharp resolution of the contact discontinuity (even for the HLL2 solver). Furthermore, the differences between the solvers are far less pronounced in the second-order versions than in the first-order ones. A quantitative confirmation of the above observations is provided in the error table 5.3.4 where we present the relative errors in pressure on a sequence of meshes for both the first- and second-order versions of the HLL-solvers. The results show that the second-order errors schemes have lower errors than the first-order schemes. The different second-order schemes with HLL2, HLL3L and HLL3R solvers are very similar in their numerical performance. Furthermore, the observed rate of convergence for the first-order schemes is around 0.7 and for the second-order schemes is around 1.05. This is expected as the presence of discontinuities in the solution erodes the expected convergence rates. The above test case serves to demonstrate the improvement obtained by using second-order accurate schemes. We will present two-dimensional second-order numerical results in the section on wave propagation.

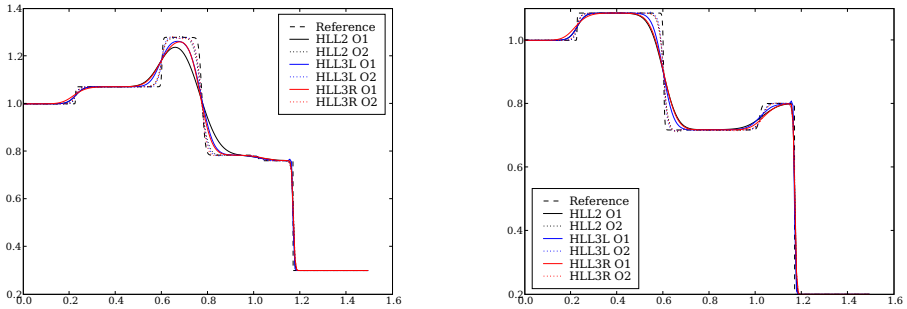

Figure 5.3.4: The density and the magnetic field B_2 in the Brio-Wu shock tube at time $t = 0.35$ on a 200 mesh comparing first and second-order schemes.

M	HLL2		HLL2(2nd)		HLL3L		HLL3L(2nd)		HLL3R		HLL3R(2nd)	
50	4.2		3.2		3.4		3.0		4.2		3.2	
100	2.5	0.79	1.4	1.19	2.0	0.76	1.3	1.20	2.5	0.69	1.5	1.1
200	1.6	0.64	0.82	0.77	1.3	0.62	0.75	0.8	1.6	0.8	0.82	0.87
400	0.90	0.83	0.31	1.40	0.67	0.95	0.28	1.42	0.92	0.75	0.32	1.35
800	0.58	0.63	0.17	0.86	0.48	0.79	1.16	0.84	0.57	0.64	0.17	0.91

Table 5.3.4: Relative percentage errors for the pressure in L^1 at time $t = 0.35$ and the order of convergence for the Brio-Wu shock tube for various mesh sizes M taking the HLL3L scheme with 6400 grid points as a reference solution.

5.4 Discretization of the source term

In order to complete the description of a finite volume scheme of the last section, it remains to include the gravity source term in (5.2.1). As stated before, a key issue that has to be considered is to discretize the source term in an appropriate manner so that the updated pressures and densities remain positive and the interesting steady states (5.2.5) and (5.2.6) are preserved to a sufficient degree of accuracy. The source term is included by the method of fractional steps or operator splitting. In the first step, we need to update the fluxes in the finite volume scheme.

In this step, we advance the approximate solution $U^n_{i,k}$ by a finite volume method using the approximate Riemann solvers of the previous section. This results in the following scheme,

$$U^{n+1/2}_{i,k} = \mathcal{F}\left(U^n_{i-1,k}, U^n_{i,k-1}, U^n_{i,k}, U^n_{i+1,k}, , U^n_{i,k+1}\right), \tag{5.4.1}$$

where $\mathcal{F}$ is the update function given in (5.3.2).

In the next step, we update U by solving the following ordinary differential equation,

$$U_t = S(U), \tag{5.4.2}$$

where S represents the right hand side of (5.2.1). This means that the cell average $U^{n+1}_{i,j} = U(\Delta t)$ where U is the solution of the differential equation

$$\frac{d}{dt}U(t) = S(U(t)), \quad U(0) = U^{n+1/2}_{i,k}.$$

We can solve this ODE by any suitable numerical method. However, due to the simple form of S, we are able to calculate the exact solution as

$$\begin{aligned} U^{n+1}_{i,k} &= U^{n+1/2}_{i,k} \\ &\quad + \Delta t \left(0, 0, 0, -g\rho^{n+1/2}_{i,k}, 0, 0, 0, -\rho^{n+1/2}_{i,k} u^{3,n+1/2}_{i,k} g + \frac{\rho^{n+1/2}_{i,k} g^2 \Delta t^n}{2}\right). \end{aligned} \tag{5.4.3}$$

Remark 5.4.1. If the update function $\mathcal{F}$ in (5.4.1) is positivity preserving, it is desirable that the scheme retains this positivity. If we use the exact update, (5.4.3), a straightforward calculation shows that the positivity still holds. If we use an implicit Euler method the resulting scheme is positive, while if we use an explicit Euler method, positivity holds for sufficiently small Δt.

If $\mathcal{W}$ denotes the solution operator of (5.4.2), then the resulting scheme reads

$$\begin{aligned} U^{n+1/2}_{i,k} &= \mathcal{F}\left(U^n_{i-1,k}, U^n_{i,k-1}, U^n_{i,k}, U^n_{i+1,k}, , U^n_{i,k+1}\right), \\ U^{n+1}_{i,k} &= \mathcal{W}\left(U^{n+1/2}_{i,k}\right). \end{aligned} \tag{5.4.4}$$

Remark 5.4.2. *The above splitting is first-order accurate in time. It is straightforward to extend it to second-order accuracy by using the fairly standard Strang splitting procedure ([50]). However, numerical experiments didn't show a big improvement using this procedure and we will show results only the above splitting, even when second-order accurate spatial and temporal discretizations are employed for evolving the homogeneous part.*

5.5 Non-reflecting characteristic boundary conditions

To complete the description of the numerical scheme (5.4.4) we now specify boundary values. As is standard for finite volume methods, this will be done by specifying values in ghost cells outside the computational domain.

Since we are aiming at modeling a small part of a stratified atmosphere we use periodic boundary values in the x direction. This amounts to setting $U^n_{0,k} = U^n_{I,k}$ and $U^n_{I+1,k} = U^n_{1,k}$ for $k = 1, \ldots, K$.

At the bottom boundary we specify the values in the ghost cells, i.e., we set $U^n_{i,0}$, $i = 1, \ldots, I$. This is supposed to model an inflow situation.

The top boundary has no physical significance, and its placement is a function of computational resources, most notably available storage and computing speed. The values in the ghost cells at the top of the computational domain are supposed to model the "rest of space". Therefore, waves should not be reflected from this numerical boundary, and we do not wish this boundary to generate any other numerical artifacts. Furthermore, we have to ensure that no mass leaks out via the top boundary. We also want these boundary conditions to result in a stable discretization which keeps density and pressure positive.

There is considerable amount of research on numerical boundary conditions. A very incomplete list includes [29, 47] and references therein. In [78], the author designed boundary conditions based on the characteristic decomposition for the Euler equations of gas dynamics. The "no-reflection" property is ensured by discretizing derivatives suitably. This scheme was extended to multiple space dimensions by a locally one-dimensional projection. Some further modifications were proposed by [63]. This characteristic based approach is very popular in the computational fluid dynamics community. They have been advocated as suitable boundary conditions for MHD equations and we present a version of this approach to the ideal MHD equations in this paper. Furthermore, we provide an alternative formulation of the characteristic boundary conditions of [78, 79] in terms of linearized solvers. This alternative formulation is easier to implement with the finite volume procedure used in the interior of the computational domain. They also reveal that the resulting schemes may lead to negative pressures and densities. The resulting boundary conditions are designed to minimize reflections but are not well-balanced; i.e, don't ensure mass balance in the domain and lead to leakage of mass. We introduce a novel modification of the boundary conditions in order to ensure mass balance in the domain. This modification implies that there are some reflections from the boundary as information has to be propagated to the interior in order to preserve mass balance. Therefore this modification must be made in a such a way that the magnitude of reflections remains small. We begin with a description of the characteristic boundary conditions below,

5.5.1 Characteristic boundary conditions

Consider the partially linearized equations (5.2.1) in the primitive form,

$$U_t + AU_z = \bar{S}(U), \tag{5.5.1}$$

where $\bar{S}(U) = S(U) - f(U)_x$, and A is the Jacobian $dh(U_0)$ evaluated at some constant U_0. We consider this equation for $z = Z$, i.e., at the top boundary. Let R and R^{-1}

be an orthonormal eigensystem corresponding to A. Then we can diagonalize (5.5.1) by introducing the vector of characteristic variables $W = R^{-1}U$. The equations decouple to yield,

$$W_t + \Lambda W_z = R^{-1}\bar{S} \tag{5.5.2}$$

where $\Lambda = \text{diag}\{\lambda^1, \lambda^2, \ldots, \lambda^7\}$. We can use the Roe-Balsara eigensystem of Section 5.2.3 as the orthogonal eigensystem of A. Let $\hat{j}$ be such that $\lambda_j \leq 0$ for $j \leq \hat{j}$ and $\lambda_j > 0$ for $j > \hat{j}$. If $j \leq \hat{j}$ the characteristics of the jth equation of (5.5.2) are moving in the negative z-direction, i.e., they are *incoming*. Similarly, for $j > \hat{j}$ the characteristics associated with the jth equation in (5.5.2) are *outgoing*. The basis of the characteristic boundary conditions of [78, 79] is to discretize the z-derivative based on the direction of the characteristics. If the characteristic is outgoing, then we use an upwind derivative. This is possible as all the information is taken out of the domain. While if the characteristic is incoming, information is supposed to flow into the domain. However, we don't want any information to go into the domain, and we will set the derivative in the incoming characteristics to zero. This is the basis of the "no incoming wave" philosophy of the characteristic type boundary conditions. When implementing this in practice, we use a single row of ghost cells, located at $k = K + 1$. This row is updated using a discretized version of (5.5.2) or (5.5.1), where we specify values for the characteristic variables in the ghost cells depending on the direction of the corresponding characteristics.

This update of the ghost cells is consistent with the direction of the flow and implies that there are no "incoming" waves into the domain and reflections are small. The algorithm for the update of the ghost cells reads

Algorithm 5.5.1.

Step 1 *Given $U^n_{i,K}$ and $U^n_{i,K+1}$, choose a suitable Jacobian matrix $A^n_{i,K+1/2}$ determined by these two values. Two examples are the Jacobian evaluated at the average of $U^n_{i,K}$ and $U^n_{i,K+1}$ and the Roe matrix given in [24].*

Step 2 *Compute the Roe-Balsara eigensystem*

$$R^n_{i,K+1/2} \text{ and } \left\{\lambda^{1,n}_{i,K+1/2} \ldots, \lambda^{7,n}_{i,K+1/2}\right\}$$

from $A^n_{i,K+1/2}$. Using this eigensystem, compute the characteristic variables

$$W^n_{i,K} = R^{-1,n}_{i,K+1/2} U^n_{i,K} \text{ and } W^n_{i,K+1} = R^{-1,n}_{i,K+1/2} U^n_{i,K+1}.$$

Step 3 *Compute the vector $\mathbf{d}^n_{i,K+1/2} = \left\{d^{1,n}_{i,K+1/2}, \ldots, d^{7,n}_{i,K+1/2}\right\}$ by*

$$d^{j,n}_{i,K+1/2} = \begin{cases} \lambda^{j,n}_{i,K+1/2} \frac{W^{j,n}_{i,K+1} - W^{j,n}_{i,K}}{\Delta z} & \text{if } \lambda^{j,n}_{i,K+1/2} > 0, \\ 0 & \text{otherwise,} \end{cases}$$

where $W^{j,n}_{i,k}$ is the characteristic weight in the (i, K) cell for the j-th characteristic field at the n-th timestep.

Step 4 *The update of the ghost cells then reads*

$$\begin{aligned} U^{n+1}_{i,K+1} = U^n_{i,K+1} - \frac{\Delta t^n}{\Delta x}\left(F^n_{i+1/2,K+1} - F^n_{i-1/2,K+1}\right) \\ - \Delta t^n R^n_{i,K+1/2}\mathbf{d}^n_{i,K+1/2} + \Delta t^n S\left(U^n_{i,K+1}\right) \end{aligned} \tag{5.5.3}$$

The above algorithm describes the implementation of the characteristic boundary conditions for the ideal MHD equations with the gravitational source term. The key step is step 3 above where the spatial derivative at the boundary is computed. Note that this is based on the "no incoming wave" philosophy of [78, 79]. It turns out that this boundary condition can be formulated in an alternative manner. This alternative formulation is easier to use and more revealing about what happens when we use non-reflecting characteristic boundary conditions. We give the alternative formulation below.

Algorithm 5.5.2.

Step 1 *Compute* $\Lambda^n_{i,K+1/2}$ *and* $R^n_{i,K+1/2}$ *as in Algorithm 5.5.1.*

Step 2 *Set*

$$W^{j,n}_{i,K+1/2} = \begin{cases} W^{j,n}_{i,K} & \text{if } \lambda^{j,n}_{i,K+1/2} > 0, \\ W^{j,n}_{i,K+1} & \text{otherwise,} \end{cases}$$

and set $U^n_{i,K+1/2} = R^n_{i,K+1/2} W^n_{i,K+1/2}$.

Step 3 *The update of the ghost cells then reads*

$$\begin{aligned} U^{n+1}_{i,K+1} = U^n_{i,K+1} - \frac{\Delta t^n}{\Delta x}\left(F^n_{i+1/2,K+1} - F^n_{i-1/2,K+1}\right) \\ - \frac{\Delta t^n}{\Delta z} A^n_{i,K+1/2}\left(U^n_{i,K+1} - U^n_{i,K+1/2}\right) + \Delta t^n S\left(U^n_{i,K+1}\right) \end{aligned} \tag{5.5.4}$$

In this formulation we see that what we are doing is adding (yet) another ghost cell at $(i, K+2)$, setting the value at this ghost cell to $U^n_{i,K+1}$ and then updating $U^n_{i,K+1}$ via a Roe type solver.

Thus, the "non-reflecting" characteristic boundary conditions in this formulation are based on linearizing the equations at the boundary and using a Neumann-type boundary condition as the normal derivative is taken to be zero by putting the same value on the second ghost cell. In the lemma below we show that Algorithms 5.5.1 and 5.5.2 give the same result.

Lemma 5.5.1. *Let* $U^n_{i,K}$ *and* $U^n_{i,K+1}$ *be given and* $A^n_{i,K+1/2}$ *be the linearization defined above. Let* $\mathbf{d}^n_{i,K+1}$ *be calculated as in* ***Step 3*** *of Algorithm 5.5.1 and* $U^n_{i,K+1/2}$ *be defined as in* ***Step 2*** *of Algorithm 5.5.2. Then*

$$A^n_{i,K+1/2}(U^n_{i,K+1} - U^n_{i,K+1/2}) = \Delta z R^n_{i,K+1/2}\mathbf{d}^n_{i,K+1/2}, \tag{5.5.5}$$

and thus the two algorithms give the same result.

Proof. For clarity, we momentarily suppress "i" and "n" in our notation. Set

$$\hat{j} = \operatorname*{argmax}_j \left\{ \lambda^j_{K+1/2} \leq 0 \right\},$$

and set $\hat{j} = 0$ if $\lambda^j_{K+1/2} > 0$ for all j. Then

$$W_{K+1} - W_{K+1/2} = \left\{ 0, \ldots, 0, W^{\hat{j}+1}_{K+1} - W^{\hat{j}+1}_K, \ldots, W^7_{K+1} - W^7_K \right\}.$$

From **Step 3** of Algorithm 5.5.1 we get

$$\Delta z \mathbf{d}_{K+1} = \left\{ 0, \ldots, 0, \lambda^{\hat{j}+1}_{K+1/2} \left(W^{\hat{j}+1}_{K+1} - W^{\hat{j}+1}_K \right), \ldots, \lambda^7_{K+1/2} \left(W^7_{K+1} - W^7_K \right) \right\}.$$

Therefore

$$\begin{aligned} A_{K+1/2} \left(U_{K+1} - U_{K+1/2} \right) &= R_{K+1/2} \Lambda_{K+1/2} R^{-1}_{K+1/2} \left(U_{K+1} - U_{K+1/2} \right) \\ &= R_{K+1/2} \Lambda_{K+1/2} \left(W_{K+1} - W_{K+1/2} \right) \\ &= R_{K+1/2} \mathbf{d}_{K+1}. \end{aligned}$$

□

Hence, both the above formulations are equivalent. The second formulation based on linearization and zero Neumann boundary conditions is very easy to use with the finite volume framework of this paper. Numerical non-reflecting boundary conditions for finite volume methods often use zero Neumann boundary conditions in ghost cells (see [50]). The above lemma establishes that the characteristic boundary conditions of [78, 79, 63] are of the same spirit and one has to replace the finite volume solver at the boundary with a Roe solver to obtain the characteristic boundary conditions. This also paves the way for further analysis of these boundary conditions in the finite volume framework. Furthermore, it exposes a potential problem. As we discovered the Roe solver is not positivity preserving, so using it at the top boundary where the pressures are expected to be very low might lead to instabilities. Hence, characteristic boundary conditions might run into problems near low pressures. We will investigate this issue further in numerical experiments.

5.5.2 "Balanced" Boundary conditions.

When simulating stratified atmospheres we expect the density and pressure to be very low near the top boundary of the computational domain. Furthermore, we desire to preserve the steady states (5.2.5) and (5.2.6) at least approximately also in our numerical approximations. This means that mass should not "leak" from the top boundary, since such leakage is likely to lead to negative pressure or density. Hence, we have to balance the boundary conditions suitably.

The strategy to "balance" the boundary conditions at the top boundary is based on the following argument. The crucial step in Algorithm 5.5.1 is **Step 3** where the vector $\mathbf{d}^n_{i,K+1}$

is computed. If the j-th characteristic is outgoing, then using a upwind discretization is consistent with the direction of propagation.

If the j-th characteristic is incoming, we set $d^{n,j}_{i,k+1} = 0$. The reasoning behind this is based on the "no incoming wave" philosophy. However, in order to balance the boundary conditions, we need to introduce some information from outside the domain. One reasonable way of doing so is to put conditions on the incoming characteristics. A (semi) discrete discretization of the jth equation of (5.5.2) reads

$$\frac{dW^{n,j}_{i,K+1}}{dt} + d^{n,j}_{i,K+1} = \left(R^{n,-1}_{i,K+1/2}\bar{S}\right)^j.$$

Since, we aim to preserve the steady states (5.2.5), (5.2.6), and calculate perturbations of them, it is reasonable to enforce the following steady state condition for the incoming characteristics,

$$\frac{dW^{n,j}_{i,K+1}}{dt} = 0,$$

which is obtained by setting,

$$d^{n,j}_{i,K+1} = \left(R^{n,-1}_{i,K+1/2}\bar{S}\right)^j.$$

This modification ensures some form of mass balance across the boundary as the incoming characteristic variables are kept steady, and will only affect Algorithm 5.5.1 in **Step 3**, whose modified version now reads.

Step 3, balanced Set

$$\bar{S}^n_{i,K+1} = R^{n,-1}_{i,K+1/2}\left(S\left(U^n_{i,K+1}\right) - \frac{F^n_{i+1/2,K+1} - F^n_{i-1/2,K+1}}{\Delta z}\right).$$

Then

$$d^{j,n}_{i,K+1/2} = \begin{cases} \lambda^{j,n}_{i,K+1/2}\frac{W^{j,n}_{i,K+1} - W^{j,n}_{i,K}}{\Delta z} & \text{if } \lambda^{j,n}_{i,K+1/2} > 0, \\ \bar{S}^{j,n}_{i,K+1} & \text{otherwise.} \end{cases}$$

Note that we enforce the steady state condition only on the incoming characteristic variables. No conditions are imposed on the outgoing characteristic variables. The non-zero values for the incoming characteristic variables ensure the mass-balance, and (unfortunately) this means that the "no-reflection" condition is violated and there will be some reflections from the top boundary.

Remark 5.5.1. *The second-order version of the characteristic-boundary conditions is much more involved ([63]) and requires using second-order differences in Step* 3 *of Algorithm 5.5.1. We will not consider the second-version in the remaining part of the paper as it led to numerical instabilities.*

5.5.3 Simple Boundary conditions

Lemma 5.5.1 provided a connection between characteristic boundary conditions and zero Neumann boundary conditions. Characteristic boundary conditions are equivalent to zero Neumann boundary conditions if the given finite volume solver is replaced at the boundary by a Roe solver. We can also use the zero Neumann boundary conditions by specifying the ghost cell value to be the same as the value in the last physical cell of the domain. However, this boundary implementation is not balanced. We can balance it by the following simple modification. We compute the ghost cell values as follows,

$$\begin{aligned} \rho^{n+1}_{i,K+1} &= \rho^{0}_{i,K+1}, \quad P^{n+1}_{i,K+1} = P^{0}_{i,K+1}, \\ \mathbf{B}^{n+1}_{i,K+1} &= \mathbf{B}^{0}_{i,K+1}, \quad \mathbf{u}^{n+1}_{i,K+1} = \mathbf{u}^{n+1}_{i,K}, \end{aligned} \tag{5.5.6}$$

where $U^{0}_{i,K+1}$ are the values of the variables initially in the ghost cell. These conditions imply that ρ, P and $\mathbf{B}$ in the ghost cells are set to their initial values. This step ensures mass and magnetic field balance across the boundary. Furthermore, we put Neumann boundary conditions for the velocity $\mathbf{u}$ which should minimize reflections when waves from the interior reach the top boundary. It is quite straight-forward to extend (5.5.6) to second-order accurate schemes. For second-order schemes, we need to specify values in two layers of ghost cells in each boundary. Periodic boundary conditions along the x-boundary are trivial to implement in the second-order version. The above simple boundary conditions lead to the following values in the outermost ghost layer at the top boundary,

$$\begin{aligned} \rho^{n+1}_{i,K+2} &= \rho^{0}_{i,K+2}, \quad P^{n+1}_{i,K+2} = P^{0}_{i,K+2}, \\ \mathbf{B}^{n+1}_{i,K+2} &= \mathbf{B}^{0}_{i,K+2}, \quad \mathbf{u}^{n+1}_{i,K+2} = \mathbf{u}^{n+1}_{i,K-1}. \end{aligned} \tag{5.5.7}$$

5.5.4 Extrapolated Neumann Boundary conditions:

Numerical experiments will show that the simple Neumann boundary conditions (5.5.6) presented above lead to large reflections and the characteristic type boundary conditions are potentially unstable (due to the lack of positivity), particularly for magnetic fields. Hence, we design a different set of boundary conditions that are stable, preserve the mass balance and keep reflections at the top boundary low. These boundary conditions are inspired by the specific structure of the exponentially decaying steady state pressure and density profiles in (5.2.5) and (5.2.6). The first-order version of these extrapolated boundary conditions are the of the form,

$$\begin{aligned} \rho^{n+1}_{i,K+1} &= \rho^{n+1}_{i,K} e^{-\frac{\Delta z}{H}}, \quad P^{n+1}_{i,K+1} = P^{n+1}_{i,K} e^{-\frac{\Delta z}{H}}, \quad \forall i, \\ \mathbf{u}^{n+1}_{i,K+1} &= \mathbf{u}^{n+1}_{i,K}, \quad \mathbf{B}^{n+1}_{i,K+1} = \mathbf{B}^{n+1}_{i,K}. \end{aligned} \tag{5.5.8}$$

The above boundary conditions extrapolate the pressure and density in the ghost cells based on the exponential decay profile in (5.2.5),(5.2.6). The velocity and magnetic fields are simply mirrored in the ghost cells. The differences between the extrapolated boundary conditions in (5.5.8) and the simple boundary conditions in (5.5.6) lies in the way the pressure and the density are extrapolated from the interior by using a exponential decay rather than keeping the pressure and density fixed to their initial values. Furthermore, a

Neumann condition is used for the magnetic field rather than keeping it fixed to the initial value. The second-order version of these boundary conditions are based on specifying the following values at the outermost ghost layer of the top boundary,

$$\begin{aligned} &\rho^{n+1}_{i,K+2} = \rho^{n+1}_{i,K} e^{-\frac{2\Delta z}{H}}, \quad P^{n+1}_{i,K+2} = P^{n+1}_{i,K} e^{-\frac{2\Delta z}{H}}, \quad \forall i, \\ &\mathbf{u}^{n+1}_{i,K+2} = \mathbf{u}^{n+1}_{i,K-1}, \quad \mathbf{B}^{n+1}_{i,K+2} = \mathbf{B}^{n+1}_{i,K-1}. \end{aligned} \tag{5.5.9}$$

Note that the above boundary condition is very simple to implement.

5.6 Wave propagation: Numerical experiments

In this section, we use the complete scheme including approximate Riemann solvers for the numerical fluxes, proper discretization of source terms and boundary conditions to simulate wave propagation in an idealized solar atmosphere. We present four different sets of experiments, two without the magnetic field and two including the magnetic field.

5.6.1 Hydrodynamics: Steady state

We begin with simulations of the hydrodynamic steady state (5.2.5). The computational domain is $[0.4]\times[0,1]$. The initial conditions are given by the steady state (5.2.5) with scale height $H = 0.158$, initial pressure $p_0 = 1.13$ and gravitational constant $g = 2.74$. Periodic boundary conditions are used for the x-boundary. We test with the first- and second-order versions of all the schemes proposed in this paper and with all three boundary conditions at the top and bottom boundaries i.e, the characteristic type boundary conditions, the Neumann-type simple boundary conditions (5.5.6),(5.5.7) and the extrapolated Neumann boundary conditions (5.5.8),(5.5.9). The aim of this experiment is to see if the steady state is preserved to a reasonable degree of accuracy.

The exact form of boundary conditions didn't matter in this steady state experiment and different boundary conditions led to similar qualitative results. Hence, we present results only with the extrapolated boundary conditions in Table 5.6.1. In this table, we present absolute errors in L^1 for the pressure at the final time with the first- and second-order versions of the HLL3G and HLL3R solvers. The results show that the steady state is not preserved exactly. For the first-order schemes, the errors are quite large (of order one). The $HLL3R$ solver is slightly more accurate than the $HLL3G$ solver. However, the gain in accuracy obtained by using a second-order scheme is considerable. The errors are reduced by two or three orders of magnitude and are quite low when one uses the second-order schemes in this case. Also, the table demonstrates that the second-order schemes result in the expected rates of convergence 2 in this case. The rates of convergence with the first-order schemes show large variability (mostly due to the large errors) and the trend suggests that we get a rate of close to one by refining the mesh further. We are not presenting the corresponding results with the HLL2, HLL3L and Roe solvers as these solvers gave very similar results. The HLL2 solver was slightly less accurate than the HLL3G or HLL3R solvers and the HLL3L and Roe solvers were slightly more accurate. The differences were much less pronounced when using the second-order versions of these solvers. Similarly, the mass balance in the boundary conditions was absolutely essential.

M	HLL3G		HLL3G (2nd)		HLL3R		HLL3R (2nd)	
50	$4.7e+1$		$2.1e-1$		$2.4e+1$		$1.6e-1$	
100	$6.2e-0$	2.9	$4.9e-2$	2.09	$4.0e-0$	2.58	$3.8e-2$	2.07
200	$1.6e-0$	1.9	$1.2e-2$	2.09	$1.2e-0$	1.73	$9.5e-3$	2.0
400	$6.2e-1$	1.36	$3.1e-3$	1.95	$4.9e-1$	1.29	$2.4e-3$	1.98

Table 5.6.1: Absolute errors in p and the rate of convergence for first- and second-order versions of the HLL3G and HLL3R schemes for the hydrodynamic steady state at $t = 1.8$ on a $4M \times M$ mesh.

Using any of the boundary conditions without the balance led to errors, several orders of magnitude more than the errors with the balanced versions of the boundary conditions.

5.6.2 Hydrodynamics: Wave propagation

The next step is to numerically simulate a hydrodynamic wave propagation model. The computational domain is the same as in the previous experiment and we use a balanced form of the boundary conditions at the top boundary. The propagation of waves is initiated by sending in a sinusoidal (in time) sequence of waves from the bottom boundary and letting them propagate across the domain and (hopefully) exit at the top. The hydrodynamic steady state (5.2.5) serves as the background for the propagation of waves. At the bottom boundary, the pressure, density and tangential velocities are specified by a simple boundary condition analogous to (5.5.6). The waves are modeled by the following boundary conditions for the normal velocity at the bottom,

$$u_{i,-1}^{3,n+1} = c \sin\left(6\pi t^{n+1}\right) \chi_{[1.85,1.95]} \tag{5.6.1}$$

Hence, we model the bottom boundary as a localized piston in the interval $[1.85, 1.95]$ sending in sinusoidal waves. These waves move up the domain and are modified by the flow equations. In Figure 5.6.1 we show u_3 at $t = 1.8$ computed using different solvers and boundary conditions. The results presented in figure 5.6.1 show that there is very little difference between the HLL3G and HLL3R solvers when the boundary condition is fixed. In fact all the five solvers showed very similar results for a given boundary condition and we choose to present the results with the HLL3G and HLL3R solvers. However, the differences in boundary conditions at the top boundary are much more pronounced. The simple boundary conditions (5.5.6) reflect the waves considerably and are quite unsuitable for simulating wave propagation. The reflection is reduced quite a bit by employing either the characteristic boundary conditions or the extrapolated boundary conditions (5.5.8). The results with the characteristic and extrapolated boundary conditions are a bit different, on account of differences in the bottom boundary conditions. It is difficult to decide which one is better in the current example although the extrapolated boundary conditions seem to be slightly better at reducing reflections.

The effect of using second-order schemes is shown in figure 5.6.2 in which we present u_3 at time $t = 1.8$ with the first- and second-versions of the HLL3G and HLL3R solvers and the extrapolated Neumann type boundary conditions (5.5.8),(5.5.9) This figure shows that the second-order results are much less dissipative and the wave fronts are resolved

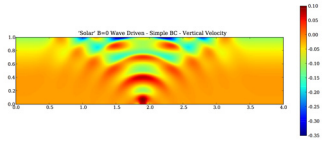

(a) HLL3G,Simple

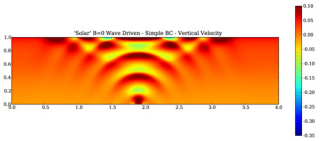

(b) HLL3R,Simple

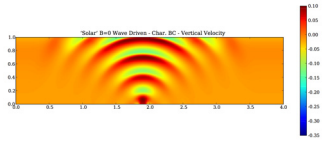

(c) HLL3G,Characteristic

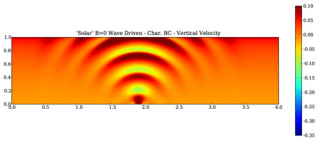

(d) HLL3R,Characteristic

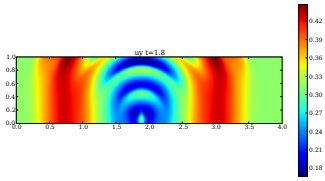

(e) HLL3G,Extrapolated

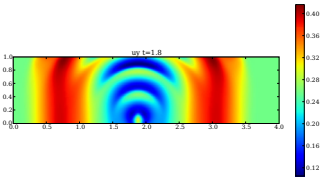

(f) HLL3R,Extrapolated

Figure 5.6.1: $u^3(x, z, 1.8)$ for the hydrodynamic wave propagation with the HLL3G and HLL3R schemes with different boundary conditions at the top boundary on a 400×100 mesh.

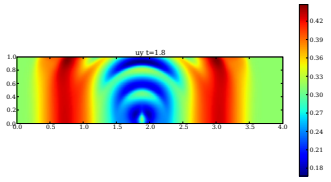

(a) HLL3G,first-order, Extrapolated

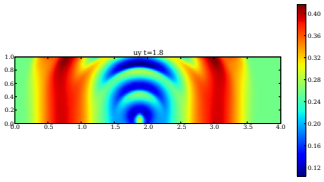

(b) HLL3R,first- order, Extrapolated

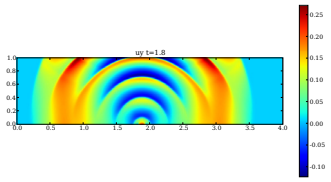

(c) HLL3G,second-order, Extrapolated

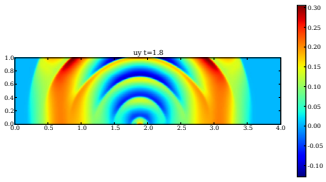

(d) HLL3R,second- order, Extrapolated

Figure 5.6.2: Results for u_3 at time $t = 1.8$ for the hydrodynamic wave propagation on a 400×100 mesh with the first- and second-order versions of the HLL3G and HLL3R solvers with the extrapolated Neumann type boundary conditions.

quite sharply at this resolution. The reflections are also quite low indicating the robustness of the extrapolated boundary conditions. Summarizing, the hydrodynamic simulations suggest that the HLL solvers are quite robust and the steady state is preserved reasonably well, atleast with the second-order accurate schemes. However, the boundary conditions at the top boundary have to chosen carefully. The simple Neumann type boundary conditions (5.5.6) preserve mass balance but lead to high reflections. The reflections are reduced somewhat for the characteristic-type boundary conditions but these are complicated to implement and expensive (atleast for the second-order versions). The extrapolated boundary conditions (5.5.8), (5.5.9) are very simple to implement and have atleast as low reflections as the characteristic boundary conditions. Furthermore, they allow robust and accurate simulations of waves when combined with second-order spatially and temporally accurate schemes.

5.6.3 Magneto-hydrodynamics: Steady states

A realistic model of the solar atmosphere must account for the magnetic field. To test the boundary conditions of the last section on this more complicated problem, we first examined how the various methods manage to preserve the magnetohydrodynamic steady state (5.2.6). The hydrodynamic variables and the computational domain were the same as in the previous section, while the magnetic field was given in terms of its Fourier components, see (5.2.6). These are listed in (5.6.2). (The X in (5.2.6) is in this case equal to 4.)

$$\begin{aligned}\{f_0, f_1, \ldots, f_{14}\} = 10^{-1}\big\{&0.21,\ -0.10,\ 0.11,\\ &-0.11,\ 0.10,\ -0.08,\ 0.07,\ -0.05,\ 0.03,\ -0.02,\ 0.01,\\ &-0.008,\ 0.005,\ -0.002,\ 0.001\big\}.\end{aligned} \tag{5.6.2}$$

The above magnetic field is both divergence and curl free and is complicated on account of the Fourier modes. However, the coefficients of the larger modes are very small and the initial modes dominate. We choose such a magnetic field to test whether the schemes can handle a realistic configuration. Our aim is to test the solvers (in both first- and second-order versions) and the boundary conditions. The results were very different from the hydrodynamic case, particularly with regards to stability.

First, the characteristic type boundary conditions were quite unstable and led to crashes due to oscillations and negative pressures. This is not entirely unexpected as the alternative characterization of the characteristic boundary conditions in Lemma 5.5.1 shows that these boundary conditions use the Roe solver at the boundary. The Roe solver is known to have problems with low pressures and densities, as is the case at the top boundary. Hence, the characteristic boundary condition (used with any of the solvers) is quite unstable with magnetic fields. The simple boundary conditions (5.5.6) are more stable but lead to large errors. The extrapolated Neumann boundary conditions (5.5.8) were found to the most stable among the three alternatives as well as the most accurate.

Furthermore, the HLL3L and Roe solvers fail to be stable with this magnetic field (even on the coarsest mesh) resulting in crashes due to negative pressures. This was independent of the boundary condition used. The HLL2 solver is stable but inaccurate.

The best results were obtained with the HLL3G and HLL3R solvers, together with the extrapolated boundary conditions (5.5.8),(5.5.9) and we show results obtained with them in tables 5.6.2. The pressure errors shown in table 5.6.2 establish that the differences

Mesh	HLL3G		HLL3G (2nd)		HLL3R		HLL3R (2nd)	
200×50	$2.3e+1$		$1.5e-1$		$2.5e+1$		$1.6e-1$	
400×100	$4.2e+0$	2.45	$3.6e-2$	2.05	$4.0e+0$	2.64	$3.8e-2$	2.07
800×200	$1.5e+0$	1.48	$9.0e-3$	2.0	$1.3e+0$	1.62	$9.2e-3$	2.04

Table 5.6.2: Absolute errors in p and the rate of convergence for first- and second-order versions of the HLL3G and HLL3R schemes for the magneto-hydrodynamic steady state at $t = 1.8$ on a sequence of meshes with the extrapolated Neumann boundary conditions.

between the HLL3G and HLL3R solvers are minor in this case. The HLL3L and Roe solvers crashed even on the coarsest mesh. However, the errors are large and of the order one for the first-order schemes. The convergence rates for first-order schemes are better than expected, probably on account of the large errors on these meshes. The second-order schemes are much more (two to three orders of magnitude) accurate in this case and the expected rates of convergence are obtained. Observe that the errors are very similar to those obtained for the hydrodynamic steady case (table 5.6.1).

5.6.4 Magneto-hydrodynamics:Wave propagation

We use the same initial condition as the steady state computation (5.2.6) and introduce waves by sinusoidally perturbing the bottom boundary like in (5.6.1). The wave propagation results are presented by showing u_3 at time $t = 1.8$ with the HLL3G solver (in both first- and second-order versions) and the extrapolated Neumann type boundary conditions (5.5.8),(5.5.9) in figure 5.6.3. The norm of the magnetic field $|\mathbf{B}|^2$ is also shown in the figure 5.6.3. We present the results only with the HLL3G solver as the second-order version of HLL3R solver crashed on some meshes in this case. From 5.6.3, the HLL3G solver and the extrapolated boundary conditions seem to be robust in simulating the waves. Observe that the magnetic field is perturbed on account of the waves. The second-order scheme is more accurate and resolves the wave-fronts sharply.

5.7 Conclusion

Summing up, we proposed a model for wave propagation in stratified magneto-atmospheres. The model was based on the ideal MHD equations with gravitational source term. The object of interest was to simulate waves by perturbing steady states. Both hydrodynamic and magneto-hydro dynamic steady states were considered and waves introduced by perturbing the bottom boundary. Numerical difficulties included employing appropriate approximate Riemann solvers, suitable discretizations of the gravity source term and design of numerical boundary conditions to maintain stability, mass balance and reduce reflections at the top boundary.

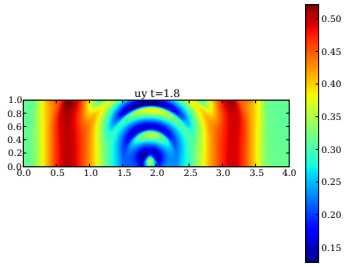

(a) u_3,first-order

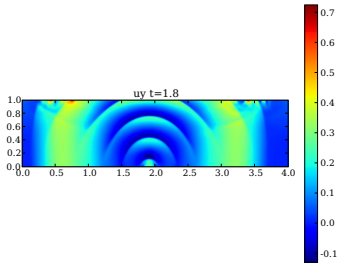

(b) u_3,second- order

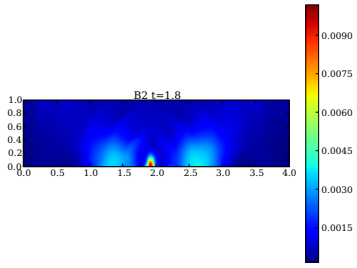

(c) $|\mathbf{B}|^2$,first-order

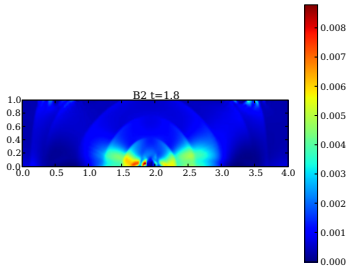

(d) $|\mathbf{B}|^2$,second- order

Figure 5.6.3: Results for u_3 and $|\mathbf{B}|^2$ at time $t = 1.8$ for the magneto-hydrodynamic wave propagation on a 400×100 mesh with the first- and second-order versions of the HLL3G solver with the extrapolated Neumann type boundary conditions.

We implemented various approximate Riemann solvers of both the HLL-type and Roe-type. Second-order accuracy in space was obtained by using a ENO-type limiter. Temporal accuracy was increased to second-order by employing Runge-Kutta discretizations. No special form of divergence cleaning was used in this paper. The solvers were compared on some benchmark one-dimensional and two-dimensional test cases.

The gravity source term was discretized by using a fractional steps method that preserved positivity. The choice of source discretization didn't influence the results to a great extent. A critical issue was the use of numerical boundary conditions at the top boundary. A characteristic type boundary condition was used (together with modifications to ensure mass balance). This boundary condition was characterized in terms of a Roe solver, thus revealing a potential problem with preservation of positive densities and pressures. A simple Neumann type boundary condition (fixing density and magnetic fields at the boundary to their initial value) was also used. A novel extrapolated Neumann type boundary condition was proposed. This boundary condition extrapolated (by a exponential profile) the values of the density and pressure along with Neumann type conditions for the velocity and magnetic fields.

Computations with the hydrodynamic steady state showed a considerable improvement in accuracy by using second-order schemes. Hydrodynamic wave propagation revealed that the extrapolated boundary condition was as good ad the characteristic boundary condition with the added advantages of being cheaper to implement and faster to runs. The differences between the solvers for hydrodynamics were minor.

The magneto-hydrodynamic computations (for steady states as well as waves) were much more difficult on account of numerical instabilities. The HLL3L and Roe solvers crashed in most cases. Similarly, the characteristic boundary conditions were quite unstable. On the other hand, the HLL3G and HLL3R solvers, together with the extrapolated Neumann boundary conditions were quite robust, particularly at second-order. The errors were however larger than in the hydrodynamics cases. Another problem was instabilities when strong magnetic fields were used. All the solvers and boundary conditions led to instabilities in this case. These could be on account of divergence errors or the fact that the schemes didn't preserve a discrete version of the steady state exactly. These questions are going to be addressed in a forthcoming paper.

Acknowledgments. The National Center for Atmospheric Research is sponsored by the National Science Foundation.

6

High order finite volume schemes for wave propagation in stratified atmospheres

F. G. Fuchs, A. D. McMurry, S. Mishra
HYP 2008 preceedings, to appear

Keywords: Stratified atmospheres, hydro-dynamics, Finite volumes, approximate Riemann solvers, balanced boundary conditions

Abstract

We model wave propagation in stellar atmospheres by compressible gas dynamics, together with gravitational source terms. Finite volume schemes based on approximate Riemann solvers , non-oscillatory reconstructions and novel non-reflecting boundary conditions are designed and shown to be efficient in preserving steady states and simulating propagating waves.

6.1 Introduction

The problem of wave propagation in stellar atmospheres has generated considerable attention in the astro-physics community. The main theme of this research is to study the effect of waves generated in the stellar atmosphere and their impact on the energy balance. Although, most realistic models include magnetic fields (see [18] and references therein for a detailed physical description), a lot of qualitative and quantitative information can be obtained by studying simpler models that ignore magnetic fields.

We consider the hydrodynamic version of the model proposed in [18]. The resulting model consists of the Euler equations of compressible gas dynamics together with source terms modeling the action of gravity. The gravitational source terms serve to model the stratification of the stellar atmosphere. In addition, one needs to consider realistic steady states that reflect hydrostatic balance. These steady states serve as the background for the wave propagation. The waves are modeled by inducing sinusoidal perturbations of the steady state.

Even at the level of this very simple model of wave propagation, it is impossible to obtain any realistic analytical (or semi-analytical) solutions. The Euler equations are

a system of non-linear conservation laws and the solutions of these equations (even for smooth initial data) consist of discontinuities like shock waves and contact discontinuities. Furthermore, we have to consider the model in multi-space dimensions and no global existence and uniqueness results for the Euler equations are available in this case. Hence, numerical simulations are the main tools for obtaining detailed information about the wave propagation.

Finite volume methods are the most popular methods (see [50]) for simulating conservation laws. These methods are based on dividing the computational domain into cells or control volumes. The method consists of updating cell-averages of the unknown in terms of interface fluxes. The numerical fluxes are obtained by solving Riemann problems either exactly or approximately in the direction, normal to the interface. The finite volume scheme based on piecewise constant approximations in each cell is restricted to first-order accuracy in both space and time. Higher-order accuracy in space is obtained by using non-oscillatory piecewise polynomial reconstructions. High-order time integration is performed by suitable Runge-Kutta solvers.

Finite volume schemes for gas dynamics have undergone extensive development in the last few decades. In particular, it is well known that the Riemann problems are very expensive to solve exactly at each interface. Consequently, suitable approximate Riemann solvers have been developed. In this paper, we will focus on the non-linear approximate Riemann solvers of the HLL type ([50]). These solvers are very simple to implement and are proved to preserve positive densities and pressures ([28]). This stability requirement is essential in problems involving stratification as the pressure and density decrease exponentially with height. Hence, the pressure and density at the top of the model is very low leading to stability issues with linearized approximate Riemann solvers of the Roe-type ([50]). Furthermore, the first-order versions of finite volume schemes smear shocks and contact discontinuities and approximate the smooth parts of the waves with a large error (due to the order of accuracy). Hence, it is essential to use high-order schemes to resolve wave propagation to a reasonable extent. Another issue that needs to be addressed is the discretization of the gravitational source term. In particular, the interesting hydrostatic states need to be preserved to a high-degree of accuracy.

The key issue in simulating wave propagation in stellar atmospheres is the treatment of boundary conditions. Since, we are interested in modeling only a small part of the atmosphere, one can use periodic boundary conditions in the horizontal directions. At the bottom vertical boundary, we need to impose suitable inflow boundary conditions in-order to start the wave motion. However, the top vertical boundary is an artificial one due to the truncation of the computational domain. We have to design suitable non-reflecting boundary conditions so that waves reaching the top boundary can exit the domain without large amounts of reflection. Furthermore, the top boundary shouldn't generate numerical waves that spread inside the domain. In addition, the boundary conditions should maintain mass balance in the domain. These considerations imply that the design of numerical boundary conditions at the top boundary is very involved.

Our aim in this paper is to simulate wave propagation in a model stellar atmosphere. We need the following ingredients : a robust modeling framework with steady states of interest, a suitable numerical flux of the approximate Riemann solver type, high-order non-oscillatory reconstructions, proper discretization of the source term and suitable numerical

boundary conditions. We present the model and use HLL type approximate Riemann solver to define our first-order accurate finite volume scheme. We also use suitable ENO-WENO type reconstructions to obtain formal second-order accuracy. The source term is discretized in a standard way. We introduce novel Neumann type boundary conditions that are stable, maintain mass balance, are computationally cheap and reduce reflections at the top boundary. Some of the results of this paper (the model included magnetic fields) were presented in a recent paper [33]. However, the high-order extensions and specific form of boundary conditions are new.

6.2 The model

The idealized stellar atmosphere (ignoring magnetic fields) is modeled by the Euler equations of gas dynamics, together with the gravitational source terms. For simplicity, we consider a two dimensional domain and the equations take the form,

$$\begin{aligned} \rho_t + (\rho u)_x + (\rho v)_z &= 0, \\ (\rho u)_t + (\rho u^2 + p)_x + (\rho uv)_z &= 0, \\ (\rho v)_t + (\rho uv)_x + (\rho v^2 + p)_z + (\rho uv)_z &= -\rho g, \\ E_t + ((E+p)u)_x + ((E+p)v)_z &= -\rho v g, \end{aligned} \tag{6.2.1}$$

where ρ is the density, p is the pressure, $\mathbf{u} = \{u, v\}$ is the velocity field and g is the constant acceleration due to gravity. In addition, the energy E is given by the ideal gas equation of state,

$$E = \frac{p}{\gamma - 1} + \frac{1}{2}\rho(u^2 + v^2), \tag{6.2.2}$$

where γ is the gas constant. Note that x- denotes the horizontal direction and z- denotes the vertical direction in the above model. Introducing the vector of unknowns $U = \{\rho, \rho u, \rho v, E\}$, (6.2.1) can be written in the following compact form,

$$U_t + f(U)_x + h(U)_z = S(U), \tag{6.2.3}$$

where the fluxes f, h and source S can be identified from (6.2.1). Note that (6.2.3) represents a system of two-dimensional balance laws. Denoting the direction Jacobians as $(A, B) = (\partial_U f, \partial_U h)$, a simple direct calculation ([50]) shows that the eigenvalues of A are $u, u, u \pm a$ and the eigenvalues of B are $v, v, v \pm a$ where a is the sound speed given by

$$a = \sqrt{\frac{\gamma p}{\rho}}.$$

Hence, the system (6.2.3) is hyperbolic. Furthermore, the characteristic fields are either genuinely non-linear or linearly degenerate. We consider (6.2.1) in the domain $[0, X] \times [0, Z]$ where X and Z are positive numbers. Next, we specify steady states (stationary solutions) that are of interest as they will serve as a background for the propagation of waves.

Hydrodynamic steady state.

We assume that the atmosphere is assumed to be steady by setting the velocity field $\mathbf{u}$ to zero. With this ansatz the pressure and the density have to satisfy the following ordinary differential equation

$$\frac{\partial p}{\partial z} = -\rho g. \tag{6.2.4}$$

We look for solutions of (6.2.4) satisfying $p(x,z) = c\rho(x,z)$ for some constant c and for all x and z, which amounts to assuming an isothermal atmosphere. This is a reasonable approximation since we are interested in simulating the region of the stellar atmosphere where the temperature remains approximately constant. Substituting this into (6.2.4) leads to the following hydrodynamic steady state,

$$u = 0, \quad v = 0, \quad \rho(x,z) = \rho_0 e^{-\frac{z}{H}}, \quad p(x,z) = p_0 e^{-\frac{z}{H}}. \tag{6.2.5}$$

where the scale height H is given by $H = \frac{p_0}{g\rho_0}$ and p_0 and ρ_0 are the values of the pressure and density at the bottom boundary of the domain.

6.3 Finite Volume schemes

We consider (6.2.3) in the domain $[0, X] \times [0, Z]$. We divide this uniformly into $I \times K$ cells (or control volumes), and define $x_i = -\Delta x/2 + i\Delta x$, $i = 0, \ldots, I+1$, and $z_k = -\Delta z/2 + k\Delta z$, $k = 0, \ldots, K+1$, so that $z_{k+1/2} = k\Delta z$. Let $I_{i,k}$ denote the control volume $[x_{i-1/2}, x_{i+1/2}) \times [z_{k-1/2}, z_{k+1/2})$. The cell average of the vector of conserved variables at any time t over the cell $I_{i,k}$ is given by $U_{i,k}(t)$. Then, a standard finite volume scheme ([50]) in semi-discrete form is given by,

$$\begin{aligned} \frac{d}{dt}U_{i,k} &= \mathcal{F}\left(U_{i-1,k}, U_{i,k-1}, U_{i,k}, U_{i+1,k}, U_{i,k+1}\right), \\ &= -\frac{1}{\Delta x}\left(F_{i+1/2,k} - F_{i-1/2,k}\right) - \frac{1}{\Delta z}\left(H^n_{i,k+1/2} - H^n_{i,k-1/2}\right) + S(U_{i,k}), \end{aligned} \tag{6.3.1}$$

where we have suppressed the time dependence of all the quantities and the numerical fluxes are functions of the neighboring cell averages, i.e.,

$$F_{i+1/2,k} = F\left(U_{i,k}, U_{i+1,k}\right), \quad H_{i,k+1/2} = H\left(U_{i,k}, U_{i,k+1}\right).$$

These numerical fluxes should be such that $F(A,B)$ is an approximation to the solution at $x = 0$ of the Riemann problem in the x-direction for (6.2.1). To be concrete, if U satisfies

$$U_t + f(U)_x = 0, \quad U(x,0) = \begin{cases} U_L & x < 0, \\ U_R & x > 0, \end{cases} \tag{6.3.2}$$

then $F(U_L, U_R) \approx f(U(0,t))$. The numerical flux $H(U_L, U_R)$ is defined analogously.

The key issue is to determine the numerical fluxes $F_{i+1/2,k}$ and $H_{i,k+1/2}$. As stated before, we will use the following approximate Riemann solver to define the numerical fluxes.

6.3.1 HLL Solver

Approximate Riemann solvers are approximate solutions of the Riemann problem (6.3.2) that approximate the full Riemann structure by a lower number of moving discontinuities. The simplest approximate Riemann solver is the two-wave HLL ([50]) solver where we approximate the full Riemann solution using two moving discontinuities (waves). Let $U_{L,R}$ and $f_{L,R}$ denote the left and right state and flux respectively. If the speed of the two waves are s_L and s_R then the constant state in between these waves, U_* will be determined from conservation by

$$f_R - f_* = s_R\left(U_R - U_*\right), \quad f_* - f_L = s_L\left(U_* - U_L\right),$$

where f_* denotes the numerical flux between these two waves. Solving the above equations yields

$$U_* = \frac{f_R - f_L - s_R U_R + s_L U_L}{s_L - s_R}, \quad f_* = \frac{s_R f_L - s_L f_R + s_L s_R (U_R - U_L)}{s_R - s_L}. \tag{6.3.3}$$

Then, the numerical flux can be written as

$$F^{\text{hll2}}(U_L, U_R) = \begin{cases} f_L & \text{if } s_L \geq 0, \\ f_* & \text{if } s_L < 0 < s_R, \\ f_R & \text{if } s_R \leq 0. \end{cases} \tag{6.3.4}$$

It remains to define the waves speeds s_L and s_R, and we do this as described in [28]. Let $\bar{U} = (U_L + U_R)/2$ be the arithmetic average of the states, then the wave speeds are given by

$$s_L = \min\{u_L - a_L, \bar{u} - \bar{a}\}, \quad s_R = \max\{u_R + a_R, \bar{u} + \bar{a}\}, \tag{6.3.5}$$

where $\bar{u}$ and $\bar{a}$ are the normal velocity and the sound speed of $A(\bar{U})$ respectively. This solver only approximates the outermost (fast) waves of the Riemann solution. This implies that the solver can be dissipative at approximating contact discontinuities. However, the solver is stable, i.e, it is proved to have positive pressures and densities (see [28]). We focus on this simple solver for the rest of this paper for the simplicity of presentation. We emphasize that less dissipative solvers like the HLL three-wave solver and the linearized Roe solver can also be used. Similarly one can define the numerical flux $H_{i,k+1/2}$ by using a HLL solver corresponding to the z- direction.

6.3.2 High-Order schemes

The above finite volume scheme (6.3.1) is restricted to first-order of accuracy in space. We can recover higher order of spatial accuracy by using fairly standard non-oscillatory piecewise polynomial reconstructions by the ENO ([40]) or WENO ([72]) procedure. We provide a very brief outline of these procedures below for the sake of completeness.

ENO procedure:

We will approximate the cell-average in the cell $I_{i,k}$ by a piecewise linear function. For simplicity, we consider interpolation in the x-direction only. Using the three neighboring cell averages $U_{i-1,k}, U_{i,k}, U_{i+1,k}$, we compute the differences $U^R_{i,k} = U_{i+1,k} - U_{i,k}$ and $U^L_{i,k} = U_{i,k} - U_{i-k}$. Using the above differences, we compute,

$$D^x U_{i,k} = \frac{M(U^L_{i,k}, U^R_{i,k})}{\Delta x},$$

where the non-linear function M simply selects the state that has the least absolute value of both states. Thus, we select the smoothest available stencil for reconstruction in this procedure. Using the above, we compute a piecewise linear reconstruction in the x-direction and denote it as

$$p^x_{i,k} = U_{i,k} + D^x U_{i,k}(x - x_i).$$

Similarly, we can compute a piecewise linear function in the z-direction $p^z_{i,k}$ by considering the cell-averages $U_{i,k}, U_{i,k-1}, U_{i,k+1}$ and repeating the ENO procedure outlined above. We use the tensor product of $p^x_{i,k}$ and $p^z_{i,k}$ and denote $p_{i,k}$ as the second-order accurate piecewise bilinear reconstruction in the cell $I_{i,k}$. One can similarly obtain higher-order ENO reconstructions by considering wider stencils and selecting the one with the most *smoothness*.

WENO procedure:

Another alternative to the ENO reconstruction is the WENO reconstruction. In this procedure, we use both $U^L_{i,k}$ and $U^R_{i,k}$ (defined above) to define the following gradient,

$$\bar{D}^x_{i,k} = \frac{1}{\Delta x}(\alpha^x_{i,k} U^L_{i,k} + (1 - \alpha^x_{i,k}) U^R_{i,k}),$$

where the weight $\alpha^x_{i,k}$ is chosen to in-order to ensure that the stencil which is smoother has more weight. The details of the choice of WENO weights can be found in [S] and we omit them due to space constraints. Note that in the WENO procedure, the linear reconstruction uses information from both stencils and hence, one can in principle recover third-order of accuracy for smooth solutions. We then use $\bar{D}^x_{i,k}$ to define the piecewise linear approximation,

$$p^x_{i,k} = U_{i,k} + \bar{D}^x U_{i,k}(x - x_i).$$

The above procedure can be repeated in the z-direction and the resulting tensor product is used to define a bi-linear approximation $p_{i,k}$ in the cell $I_{i,k}$.

Denote the following,

$$UE_{i,k} = p_{i,k}(x_{i+1/2}, y_k), \quad UW_{i,k} = p_{i,k}(x_{i-1/2}, y_k),$$
$$UN_{i,k} = p_{i,k}(x_i, y_{k+1/2}), \quad US_{i,k} = p_{i,k}(x_i, y_{k-1/2}).$$

where $p_{i,k}$ is defined by either the ENO or the WENO procedure. Then, the finite volume scheme (6.3.1) is formally second-order accurate if we re-define the numerical fluxes as

$$F_{i+1/2,k} = F(UE_{i,k}, UW_{i+1,k}), \quad H_{i,k+1/2} = H(UN_{i,k}, US_{i,k+1}).$$

6.3.3 Time stepping

The above scheme (6.3.1) is semi-discrete and we need to use a suitable time-stepping routine. For the first-order spatial approximation, we use the standard forward-Euler time stepping,

$$U_{i,k}^{n+1} = U_{i,k}^{n} + \Delta t^n \mathcal{F}_{i,k}^{n},$$

where $\mathcal{F}$ is the right-hand side of (6.3.1) and Δt^n is the time-step at the n-th time level. For the second-order schemes, we use the second-order strong-stability preserving Runge-Kutta time stepping,

$$\begin{aligned} U_{i,k}^{*} &= U_{i,k}^{n} + \Delta t^n \mathcal{F}_{i,k}^{n}, \quad U_{i,k}^{**} = U_{i,k}^{*} + \Delta t^n \mathcal{F}_{i,k}^{*}, \\ U_{i,k}^{n+1} &= \frac{1}{2}(U_{i,k}^{n} + U_{i,k}^{**}). \end{aligned}$$

The time step is determined by a standard CFL condition.

6.3.4 Source discretization:

In (6.3.1), the source is disrectized by an explicit evaluation, even for the second-order accurate schemes. Note that this retains the overall second-order accuracy of the entire scheme. This choice works well in practice. However, one can use more sophisticated discretizations of the source term based on a fractional steps method. One such choice in [33] led to a scheme which was still provably positive in the presence of sources.

6.3.5 Boundary conditions:

We use periodic boundary conditions in the x-direction. Note that the second-order schemes require two rows of ghost cells and the periodic boundary conditions can be easily used to specify them in the horizontal direction. The top boundary is artificial and we need non-reflecting boundary conditions there. The simplest choice is to use standard Neumann-type boundary conditions by setting the ghost cell values as

$$U_{i,K+1}^{n+1} = U_{i,K}^{n+1}, \quad \forall i,$$

Similarly, we can specify the ghost cell value $U_{i,K+2}^{n+1}$ as $U_{i,K-1}^{n+1}$ for second-order schemes. This choice is naive as it doesn't preserve the delicate mass balance in (6.2.5) and leads to mass leaking out of the top boundary and the resulting numerical errors are unacceptably large.

An alternative Neumann-type balanced boundary condition was first proposed in [33]. The ghost cell values were specified as,

$$\begin{aligned} \rho_{i,K+1}^{n+1} &= \rho_{i,K+1}^{0}, \quad P_{i,K+1}^{n+1} = P_{i,K+1}^{0}, \quad \forall i \\ u_{i,K+1}^{n+1} &= u_{i,K}^{n+1}, \quad v_{i,K+1}^{n+1} = v_{i,K}^{n+1}. \end{aligned} \tag{6.3.6}$$

Analogously, we can define the ghost cell values in the outermost layer for second-order schemes. The above conditions imply that ρ and P in the ghost cells are set to their

initial values. This step ensures mass balance across the boundary. Furthermore, we put Neumann boundary conditions for the velocity which should minimize reflections when waves from the interior reach the top boundary. However, as shown in [33], the numerical errors were still large on account of reflections at the top boundary.

In-order to further minimize reflections and maintain mass balance, we take advantage of the structure of the steady state (6.2.5) and define the following extrapolated ghost cell values,

$$\begin{aligned} &\rho_{i,K+1}^{n+1} = \rho_{i,K}^{n+1} e^{-\frac{\Delta z}{H}}, \quad P_{i,K+1}^{n+1} = P_{i,K}^{n+1} e^{-\frac{\Delta z}{H}}, \quad \forall i, \\ &u_{i,K+1}^{n+1} = u_{i,K}^{n+1}, \quad v_{i,K+1}^{n+1} = v_{i,K}^{n+1}. \end{aligned} \tag{6.3.7}$$

In this case, we are extrapolating the steady state values of the density and pressure to the ghost cells. This should maintain mass-balance and handle small perturbations of the steady state (6.2.5). A Neumann-type boundary condition is used for the velocity field. For second order schemes, we specify the following values in the outermost ghost cell layer,

$$\begin{aligned} &\rho_{i,K+2}^{n+1} = \rho_{i,K-1}^{n+1} e^{-\frac{3\Delta z}{H}}, \quad P_{i,K+2}^{n+1} = P_{i,K-1}^{n+1} e^{-\frac{3\Delta z}{H}}, \quad \forall i, \\ &u_{i,K+2}^{n+1} = u_{i,K-1}^{n+1}, \quad v_{i,K+2}^{n+1} = v_{i,K-1}^{n+1}. \end{aligned} \tag{6.3.8}$$

Numerical boundary conditions at the bottom boundary can be defined analogously. Another possible choice of boundary conditions are the characteristic-type balanced boundary conditions proposed in [33]. We refer the reader to this paper for details about these boundary conditions. The description of the finite volume schemes is complete with the specification of boundary conditions.

6.4 Numerical Experiments

We test the schemes on a set of numerical experiments in this section. We have the following combinations of solvers and boundary conditions: first-order HLL solver with the fixed-Neumann boundary condition (6.3.6) and forward Euler time stepping (denoted as HLLFN), first-order HLL solver with the extrapolated-Neumann boundary condition (6.3.7) and forward Euler time stepping (denoted as HLLEN), second-order ENO-type HLL solver with the extrapolated-Neumann boundary condition (6.3.7),(6.3.8) and Runge-Kutta time stepping (denoted as ENOEN) and second-order WENO-type HLL solver with the extrapolated-Neumann boundary condition (6.3.7),(6.3.8) and Runge-Kutta time stepping (denoted as WENOEN). For the sake of comparison, we will also present results computed with the first-order HLL solver with the balanced characteristic boundary conditions of [33] and forward Euler time stepping (denoted as HLLCB).

6.4.1 Hydrodynamics: steady state

We consider (6.2.1) in $[0, 4] \times [0, 1]$. The initial conditions are given by the hydrodynamic steady state (6.2.5) with the scale height $H = 0.158$, initial pressure $p_0 = 1.13$ and gravitational constant $g = 2.74$. The computation is carried up to time $t = 2$. Our aim is to ensure that the steady state (6.2.5) is preserved by our schemes to a high degree of accuracy. The numerical errors in L^1 for the pressure and the acoustic Mach number in

the vertical direction on a series of meshes are presented in Table 6.4.1. The errors are calculated with respect to the exact solution which is given by the steady state (6.2.5) in this case. The table clearly shows that the schemes preserve the steady state quite

Errors in the Mach number

Mesh size	$HLLFN$	$HLLEN$	$ENOEN$
200x50	$1.0e-1$	$1.5e-2$	$5.1e-3$
400x100	$5.2e-2$	$3.4e-3$	$1.4e-3$
800x200	$2.1e-2$	$8.1e-4$	$3.7e-4$
16000x400	$8.6e-3$	$1.9e-4$	$9.4e-5$

Relative errors in p

Mesh size	$HLLFN$	$HLLEN$	$ENOEN$
200x50	$8.6e-1$	$11.9e-1$	$2.2e-3$
400x100	$4.4e-1$	$4.4e-1$	$1.1e-4$
800x200	$2.0e-1$	$1.9e-1$	$8.9e-5$
1600x400	$9.0e-2$	$9.0e-2$	$3.8e-5$

Table 6.4.1: Scaled L^1 errors for the $HLLFN$, $HLLEN$ and $ENOEN$ at the hydrodynamic steady state for $t = 2$.

well even though they are not well-balanced in design. The errors are low and converge to zero at the expected rates. The use of extrapolated boundary conditions (6.3.7) leads to an order of magnitude lower errors in the velocity as shown by the lower errors with the HLLEN scheme than the HLLFN scheme although the difference in pressure errors is negligible. Furthermore, the second-order ENOEN scheme is much more accurate than the first-order schemes particularly at preserving pressure. The gain in resolution by using second-order schemes is about two orders of magnitude more than the first-order schemes. The WENO based WENOEN scheme gave similar results to the ENOEN scheme and we omit them in the table.

6.4.2 Wave propagation:

We use the same domain as in the previous experiment. The propagation of waves is initiated by sending in a sinusoidal (in time) sequence of waves from the bottom boundary and letting them propagate across the domain and (hopefully) exit at the top. The waves are modeled by the following boundary conditions for the normal velocity at the bottom,

$$u^{3,n+1}_{i,-1} = c \sin\left(6\pi t^{n+1}\right) \chi_{[1.85,1.95]} \tag{6.4.1}$$

Hence, we model the bottom boundary as a localized piston in the interval $[1.85, 1.95]$ sending in sinusoidal waves. These waves move up the domain and are modified by the flow equations. We start by comparing different boundary conditions at the top boundary and show the velocity v at time $t = 1.8$ on a 400×100 mesh with the HLLFN, HLLCB and HLLEN schemes in figure 6.4.1. The figure clearly shows that the HLLEN scheme resolves the wave propagation far better than the HLLFN and HLLCB. The magnitude of reflections generated using the extrapolated boundary conditions (6.3.7) is much lower than those generated using the fixed boundary conditions (6.3.6). More surprisingly, the extrapolated boundary conditions also lead to lower reflections than

the characteristic type boundary conditions proposed in [33]. Considering the fact that the extrapolated boundary conditions are computationally cheaper than characteristic type boundary conditions clearly suggests them to be well suited for numerical wave propagation. Further evidence of the robustness of this approach is provided in figure 6.4.2 where we compare the HLLEN, ENOEN and WENOEN schemes at the same mesh resolution. The second-order schemes are hardly distinguishable from each other but lead to sharper wave fronts compared to the first-order HLLEN scheme. All the three schemes based on the extrapolated boundary conditions resolve the curved wave-fronts quite well and the magnitude of the numerical reflections from the top boundary is quite low.

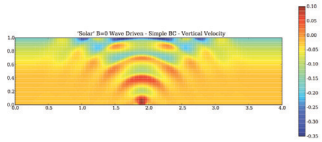

(a) HLLFN

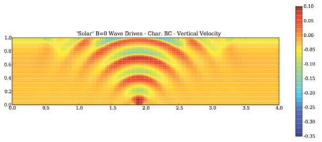

(b) HLLCB

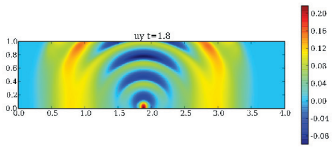

(c) HLLEN

Figure 6.4.1: Approximate v obtained the three first-order schemes and different boundary conditions on a 400×100 mesh at time $t = 1.8$.

To summarize, we model wave propagation in stellar atmospheres numerically by solving the Euler equations with source terms. Finite volume schemes based on HLL solvers and ENO-WENO second order interpolation was found to be robust and accurate at computing the waves. The key ingredient was a proper choice of non-reflecting and balanced Neumann type extrapolated boundary conditions. The schemes, particularly at second-order resolve both the steady states and the propagating waves quite accurately. The model considered needs to be extended by adding magnetic fields. The presence of magnetic fields complicates the entire design framework and has been simulated in [33] with first-order schemes. We will extend the new boundary conditions and high-order schemes to stratified magneto-atmospheres in a forthcoming paper.

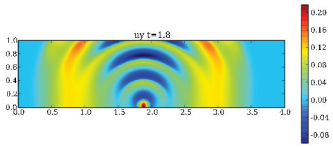

(a) HLLEN

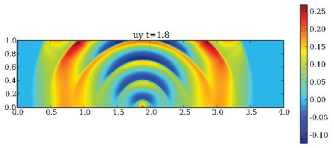

(b) ENOEN

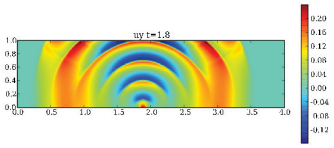

(c) WENOEN

Figure 6.4.2: Approximate v obtained from the three schemes with extrapolated boundary conditions (6.3.7) and different order on a 400×100 mesh at time $t = 1.8$.

7

High order well balanced finite volume schemes for simulating wave propagation in stratified magnetic atmospheres

F. G. Fuchs, A. D. McMurry, S. Mishra, N.H. Risebro, K. Waagan
preprint

Dedicated with appreciation to Prof. Ragnar Winther on his 60th Birthday.

Keywords: Conservation laws, MHD, Divergence constraint, Upwinded Source terms

Abstract

Wave propagation in idealized stellar atmospheres is modeled by the equations of ideal MHD, together with the gravity source term. The waves are modeled as small perturbations of isothermal steady states of the system. We consider a formulation of ideal MHD based on the Godunov-Powell form, with an embedded potential magnetic field appearing as a coefficient. The equations are discretized by finite volume schemes based on approximate Riemann solvers of the HLL type and upwind discretizations of the Godunov-Powell source terms. Local hydrostatic reconstructions and suitable discretization of the gravity source term lead to a well-balanced scheme, i.e., a scheme which exactly preserves a discrete version of the relevant steady states. Higher order of accuracy is obtained by employing suitable minmod, ENO and WENO reconstructions, based on the equilibrium variables, to construct a well-balanced scheme. The resulting high order well-balanced schemes are validated on a suite of numerical experiments involving complex magnetic fields. The schemes are observed to be robust and resolve the complex physics well.

7.1 Introduction

The problem of modeling wave propagation in idealized stellar atmospheres has received considerable attention in the solar physics and astrophysics communities in recent years (see [69, 18] and references therein). A typical situation of interest is to model how convection generated waves from the inner layers of the sun transport and deposit energy in the overlaying chromospheric and coronal plasmas. The waves interact with complex

magnetic fields generated by the plasma and these interactions affect the qualitative as well as quantitative features of the energy transfer.

In [69, 18], these complex phenomena were modeled in terms of the equations of Magnetohydrodynamics (MHD) in two space dimensions, together with a gravitational source term given by

$$\begin{aligned}
\rho_t + \operatorname{div}(\rho \mathbf{u}) &= 0, \\
(\rho \mathbf{u})_t + \operatorname{div}\left(\rho \mathbf{u} \otimes \mathbf{u} + \left(p + \frac{1}{2}\left|\bar{\mathbf{B}}\right|^2\right) I - \bar{\mathbf{B}} \otimes \bar{\mathbf{B}}\right) &= -\rho g \mathbf{e}_2, \\
\bar{\mathbf{B}}_t + \operatorname{div}\left(\mathbf{u} \otimes \bar{\mathbf{B}} - \bar{\mathbf{B}} \otimes \mathbf{u}\right) &= 0, \\
E_t + \operatorname{div}\left(\left(E + p + \frac{1}{2}\left|\bar{\mathbf{B}}\right|^2\right)\mathbf{u} - \left(\mathbf{u} \cdot \bar{\mathbf{B}}\right)\bar{\mathbf{B}}\right) &= -\rho g \left(\mathbf{u} \cdot \mathbf{e}_2\right), \\
\operatorname{div}(\bar{\mathbf{B}}) &= 0,
\end{aligned} \tag{7.1.1}$$

where ρ is the density, $\mathbf{u} = \{u_1, u_2, u_3\}$ and $\bar{\mathbf{B}} = \{\bar{B}_1, \bar{B}_2, \bar{B}_3\}$ are the velocity and magnetic fields respectively, p is the thermal pressure, g is constant acceleration due to gravity , $\mathbf{e}_2$ represents the unit vector in the vertical (y-) direction. E is the total energy, for simplicity determined by the ideal gas equation of state:

$$E = \frac{p}{\gamma - 1} + \frac{1}{2}\rho\left|\mathbf{u}\right|^2 + \frac{1}{2}\left|\bar{\mathbf{B}}\right|^2, \tag{7.1.2}$$

where $\gamma > 1$ is the adiabatic gas constant. The above equations represent the conservation of mass, momentum and energy and the Magnetic induction equations for the evolution of the magnetic field. The momentum conservation is affected by the Lorentz force due to the magnetic field and by the gravitational force. The total energy is the sum of the energy due to the pressure and the kinetic and magnetic energies. The gravitational potential energy is modeled by the source term on the right hand side of the energy equation. The divergence constraint on the magnetic field reflects the fact that magnetic monopoles have not been observed in nature.

The above equations (7.1.1) posses a rich variety of steady states that are of interest in modeling wave propagation. Two interesting steady states considered in [69, 18] and in a recent paper [33] are given as follows.

Hydrodynamic steady state

This steady state assumes that the velocity $\mathbf{u}$ and magnetic field $\bar{\mathbf{B}}$ are set to zero. Furthermore, we are interested in chromospheric plasmas where the temperature is approximately constant ([18]) and one can assume that the atmosphere is isothermal. A simple calculation ([33]) with the above assumptions leads to the following steady state:

$$\mathbf{u} \equiv \mathbf{0}, \quad \bar{\mathbf{B}} \equiv \mathbf{0}, \quad \rho(x, y) = \rho_0 e^{-y/H}, \quad p(x, y) = p_0 e^{-y/H}. \tag{7.1.3}$$

where the scale height H is given by $H = p_0/g\rho_0$ and p_0 and ρ_0 are the values of the pressure and density at the bottom boundary of the domain. Note that the hydrostatic balance due to gravity implies that the pressure and the density decay exponentially in the vertical direction. Hence, very low pressures and densities can be found at the top of the domain of interest.

Magnetic steady state

The hydrodynamic steady state assumes that the magnetic field is zero. Any realistic description of solar plasmas cannot ignore the effect of magnetic field since it plays a crucial role in the energy transfer ([18]). Steady states with a magnetic field are easy to determine once the momentum balance in (7.1.1) is rewritten as

$$(\rho \mathbf{u})_t + \operatorname{div}(\rho \mathbf{u} \otimes \mathbf{u} + pI) = \operatorname{curl}(\bar{\mathbf{B}}) \times \bar{\mathbf{B}} - \rho g \mathbf{e}_2.$$

The above equation displays the role of the Lorentz force explicitly in the momentum balance. Under the assumption that the velocity field is set to zero, the following magnetic steady states are easy to obtain,

$$\begin{aligned} \mathbf{u} \equiv \mathbf{0}, \quad \operatorname{div}(\bar{\mathbf{B}}) \equiv \mathbf{0}, \quad \operatorname{curl}(\bar{\mathbf{B}}) \equiv 0, \\ \rho(x,y) = \rho_0 e^{-y/H}, \quad p(x,y) = p_0 e^{-y/H}. \end{aligned} \tag{7.1.4}$$

The above conditions require that the magnetic field is both divergence free and curl free. It is easy to obtain closed form solutions of such magnetic fields in terms of harmonic functions ([33] and in section 7.2). Note that the conditions on steady magnetic fields are quite general and imply that there is a rich variety of magnetic steady states (7.1.4).

The usual method in modeling waves is to consider them as small perturbations of the above steady states. The equations (7.1.1) are supplemented with the steady states (7.1.3), (7.1.4) as initial conditions. Since, we are interested in a small part of the solar atmosphere, periodic boundary conditions are imposed in the horizontal (x-) direction. The waves are pushed into the domain by imposing suitable inflow boundary conditions at the bottom boundary. One expects the wave forms to be distorted due to interactions with the magnetic field and the action of gravity. The distorted waves exit the domain through the top boundary. The top boundary is an artificial boundary and suitable numerical boundary conditions need to be imposed in order to ensure that the waves exit the domain without large reflections.

Equations of form (7.1.1) are examples of systems of balance laws (conservation laws with source terms). Solutions of such equations develop discontinuities such as shock waves and contact discontinuities, even for smooth initial data. Hence, solutions have to be considered in the weak sense. The MHD equations are hyperbolic but not strictly hyperbolic, since different characteristic speeds can coincide.

If the eigenvectors of the Jacobian matrix of the flux functions are to be used in computations, then these must be suitably scaled (see [68, 12] for detailed descriptions). The structure of discontinuities of the MHD equations is quite complicated as the flux functions are non-convex ([79]).

We remark that (even in one space dimension) global existence and uniqueness results have not been obtained at the current time.

Hence, numerical simulations of these equations is the main tool of study and analysis. Finite volume methods ([50]) are among the most popular tools for discretizing non-linear balance laws like (7.1.1). The computational domain is divided into control volumes or cells. The method consists of discretizing an integral version of a balance law like (7.1.1) over each cell to obtain a time update of the cell averages of the unknown. The key step

in the update is to determine numerical fluxes by solving local Riemann problems at each cell interface (along the normal direction). The source term in the balance law (7.1.1) can be discretized in several ways. Higher order accuracy in space can be obtained by using non-oscillatory piecewise polynomial reconstructions like the MUSCL ([81]), ENO ([40]) and WENO ([72]) reconstructions. High order temporal accuracy is obtained by using strong stability preserving Runge Kutta methods ([37]).

Finite volume schemes for ideal MHD equations have undergone considerable development in the last fifteen years. In one space dimension, finite volume schemes for MHD equations include the linearized solvers developed in [68, 24]. Other schemes are the non-linear HLL type solvers designed in [53, 36, 59, 20, 21, 32] and other references therein. The linearized Roe-type solvers are less dissipative than the HLL type solver but can lead to unphysical negative densities and pressures. The non-linear HLL type solvers like the ones designed in [36, 59, 20] are proved to preserve positive densities and pressures. Comparisons between different approximate Riemann solvers are performed in papers like [33, 73, 58].

In one space dimension, the divergence constraint in (7.1.1) implies that the normal magnetic field is constant in space. This information is used in the design of some of the above approximate Riemann solvers. However, the nature of MHD equations in multi space dimensions is different. The divergence constraint in several dimensions does not imply that the normal magnetic field is constant. Hence, it is not straightforward to extend one dimensional MHD schemes to several dimensions.

It is also difficult to satisfy the divergence constraint itself. Standard schemes may not preserve the constraint in a discrete manner and divergence errors are speculated to lead to numerical instabilities and unphysical oscillations ([80]). Several methods have been designed to deal with the divergence constraint in MHD codes. Popular choices include the projection method, in which the magnetic field is projected unto a zero divergence field by solving an elliptic equation at each time step ([22]), a method which is computationally expensive. A cheaper alternative is the parabolic cleaning method of [55] and [27]. Another popular method of handling the divergence constraint is the use of staggered grids to ensure that a particular form of discrete divergence is zero. Several versions of staggered grid methods exist, and an incomplete list includes those developed in [11, 26, 30, 54, 71, 70, 73, 78, 80] and other references therein. A possible disadvantage of staggered grid methods is the complexity of the book-keeping at the code level, leading to overheads in parallelizing the code. It is also more difficult to obtain numerical stability for these schemes, since some of the theoretical basis of finite volume schemes is lost.

A different divergence cleaning procedure was presented in [65, 66] where a slightly different form of the ideal MHD equations (with a source term proportional to divergence) was discretized. This form, also called the *Godunov-Powell* form happens to be symmetrizable ([35]) and Galilean invariant, while the standard form (7.1.1) is neither symmetrizable nor Galilean invariant. Furthermore, in the Godunov-Powell form divergence errors are transported out of the domain with the flow ([65]). Similar ideas were presented in [27]. A possible pitfall of this procedure was pointed out in recent papers [31, 32]. Examples were presented to argue that the Godunov-Powell form needs to be discretized in a suitable manner for numerical stability. Various upwind discretizations of a partial form of the Godunov-Powell source term were proposed recently in [20, 83, 32].

The Godunov-Powell form makes it mathematically feasible to deal with data not satisfying the divergence constraint. Hence, it allows constructing one-dimensional schemes that immediately extend to accurate and remarkably robust multidimensional schemes, as carried out by the authors in [34] (see also [83]). The method involved designing suitable three- and five wave HLL type solvers and discretizing the Godunov-Powell source term in an upwind manner. The source discretization involved utilizing the structure of the approximate Riemann solver. Positivity preserving high order ENO and WENO reconstructions were also proposed. The resulting schemes were high order accurate and robust in computations, particularly on very fine meshes. The numerical schemes designed in [34] constitute an attractive framework for robust simulations of models involving MHD equations.

In order to extend existing finite volume methods for the ideal MHD equations to the balance law (7.1.1), we need to discretize the terms due to gravity in a suitable manner. The resulting scheme should be able to handle very low pressures and densities (see the exponential structure in (7.1.4)) at the top of the domain. Furthermore, waves are very small perturbations of the steady states (7.1.3), (7.1.4), and a robust scheme approximating (7.1.1) must preserve discrete versions of the steady states (7.1.3), (7.1.4) to a reasonable degree of accuracy, so that waves can be resolved. Another hurdle is the issue of suitable numerical boundary conditions at the top boundary. This boundary condition must ensure mass balance and low reflections.

A recent paper [33] illustrated some of the problems in extending existing finite volume methods to simulate wave propagation involving models like (7.1.1). In [33], the gravity source term was discretized by a fractional steps method ([50]) and characteristic type boundary conditions ([63, 75]) were used at the top boundary. However, these methods led to significant numerical instabilities and large boundary reflections, particularly on problems with strong magnetic fields. In fact, *none* of the schemes considered in [33] were stable on wave propagation problems with strong magnetic fields. The lack of robust finite volume schemes preserving discrete steady states was a persistent problem.

Finite volume methods which preserve steady states in balance laws are called *well-balanced*. Many balance laws like shallow water equations with bottom topography ([52]) and Euler equations for gas flows in nozzles ([49]) involve balance laws with interesting steady states. Well-balanced schemes for the shallow water equations with topography have been designed in many recent papers including [52, 7, 60, 61, 25] and other references therein. Well-balanced schemes for nozzle flows are considered in [48, 49] among others. The most popular form of well-balancing a scheme is to use local *hydrostatic* reconstructions. A different approach is considered in [46]. To the best of our knowledge, no well-balanced schemes for simulating wave propagation in stratified atmospheres has been designed, even in the absence of magnetic fields.

The aim of this paper is to design a robust finite volume scheme to simulate waves modeled as perturbations of steady states (7.1.3), (7.1.4) in the balance law (7.1.1). Our approach consists of the following ingredients,

- We follow the approach of [74, 66] and consider a modified formulation of the balance law (7.1.1). The modified form includes the Godunov-Powell source term discussed earlier. It also considers an embedded steady magnetic field like (7.1.4) and solves for perturbations of the magnetic field as a coefficient. This approach is motivated

by the fact that we are interested in small perturbations of the steady magnetic field (7.1.4).

- The resulting modified MHD system is discretized by a finite volume method, similar to the schemes of [34]. The numerical fluxes are calculated by a suitable three wave approximate Riemann solver of the HLL type. The Godunov-Powell term is discretized in an upwind fashion. Minmod, ENO and WENO reconstructions are used to obtain higher order accuracy.

- A novel form of well balancing is designed by using suitable local hydrostatic reconstructions in the numerical fluxes. The gravity source term is also well-balanced. Novel piecewise linear reconstructions are proposed to obtain a second-order accurate well-balanced scheme.

- Well-balanced Neumann type boundary conditions are proposed to reduce reflections and ensure stability at the top boundary. These conditions are very similar to the extrapolated Neumann boundary conditions of [33].

The above ingredients are combined to obtain robust well-balanced high order finite volume schemes for wave propagation in stratified magneto-atmospheres. The schemes are tested on a suite of numerical experiments including perturbations of hydrodynamic steady states (7.1.3). However, the main interest is to study wave propagation as perturbations of the magnetic steady states (7.1.4). We consider realistic magnetic fields and simulate wave propagation. The numerical results illustrate both accuracy and stability of the schemes. The schemes are employed to describe complex physical phenomena accompanying wave propagation. Particular attention is paid to examine the role of magnetic fields in influencing waves. The numerical results show qualitative agreement with the ones presented in [18], and demonstrate considerable improvements over the results of [18] with respect to modeling very small perturbations of steady states, long time integration and interaction of waves with the top boundary.

The remaining part of the paper is organized as follows: in Section 7.2, we describe a modified formulation of (7.1.1). The high order accurate well-balanced schemes are presented in Section 7.3. In Section 7.4, we present various numerical experiments demonstrating the computational efficiency of the schemes. We describe some of the complex physical phenomena underlying wave propagation in this section. Contents of the papers are summarized in Section 7.5.

7.2 The Model

Deriving the ideal MHD equations with gravity (7.1.1) from the first principles without explicitly using the divergence constraint results in the following semi-conservative *Godunov-Powell* form of the equations, (see [34] for a detailed derivation in the absence

of gravity),

$$\begin{aligned}
\rho_t + \operatorname{div}(\rho\mathbf{u}) &= 0,\\
(\rho\mathbf{u})_t + \operatorname{div}\left(\rho\mathbf{u}\otimes\mathbf{u} + \left(p + \frac{1}{2}\left|\bar{\mathbf{B}}\right|^2\right) I - \bar{\mathbf{B}}\otimes\bar{\mathbf{B}}\right) &= -\bar{\mathbf{B}}(\operatorname{div}\bar{\mathbf{B}}) - \rho g\mathbf{e}_2,\\
\bar{\mathbf{B}}_t + \operatorname{div}(\mathbf{u}\otimes\bar{\mathbf{B}} - \bar{\mathbf{B}}\otimes\mathbf{u}) &= -\mathbf{u}(\operatorname{div}\bar{\mathbf{B}}),\\
\bar{E}_t + \operatorname{div}\left(\left(E + p + \frac{1}{2}\left|\bar{\mathbf{B}}\right|^2\right)\mathbf{u} - (\mathbf{u}\cdot\bar{\mathbf{B}})\bar{\mathbf{B}}\right) &= -(\mathbf{u}\cdot\bar{\mathbf{B}})(\operatorname{div}\bar{\mathbf{B}}) - \rho g\left(\mathbf{u}\cdot\mathbf{e}_2\right).
\end{aligned} \tag{7.2.1}$$

The system is coupled with an ideal gas equation of state (7.1.2) and all the quantities in (7.2.1) are as defined before. The difference between the standard form (7.1.1) and the Godunov-Powell form (7.2.1) are the explicitly $\operatorname{div}\bar{\mathbf{B}}$-dependent source terms in (7.2.1). Taking divergence on both sides of (7.2.1), we obtain

$$(\operatorname{div}\bar{\mathbf{B}})_t + \operatorname{div}\left(\mathbf{u}\left(\operatorname{div}\bar{\mathbf{B}}\right)\right) = 0. \tag{7.2.2}$$

Hence, initial divergence free fields remain divergence free under time evolution in (7.2.1). Furthermore, the Godunov-Powell system is Galilean invariant ([66]) and symmetrizable ([35]). Hence, our starting point will be the Godunov-Powell form (7.2.1) instead of the standard form (7.1.1).

Motivated by our interest in modeling wave propagation as perturbations of steady states (7.1.3), (7.1.4), we consider a further modification of the system (7.2.1). Assume that there exist a magnetic field $\tilde{\mathbf{B}}$ satisfying the following assumptions,

$$\tilde{\mathbf{B}}_t = 0, \quad \operatorname{div}(\tilde{\mathbf{B}}) = 0, \text{ and } \operatorname{curl}(\tilde{\mathbf{B}}) = 0. \tag{7.2.3}$$

Specific examples of such fields will be given in the sequel. Next, we define perturbations $\mathbf{B}$ about this potential field $\tilde{\mathbf{B}}$ by,

$$\mathbf{B} = \bar{\mathbf{B}} - \tilde{\mathbf{B}}.$$

We plug in the above form in (7.2.1) and after some calculations (see [66]), we obtain the following modified system,

$$\begin{aligned}
&\rho_t + \operatorname{div}(\rho\mathbf{u}) = 0,\\
&(\rho\mathbf{u})_t + \operatorname{div}\left(\rho\mathbf{u}\otimes\mathbf{u} + \left(p + \frac{1}{2}|\mathbf{B}|^2 + \tilde{\mathbf{B}}\cdot\mathbf{B}\right) I - \mathbf{B}\otimes\mathbf{B} - \tilde{\mathbf{B}}\otimes\mathbf{B} - \mathbf{B}\otimes\tilde{\mathbf{B}}\right)\\
&\qquad\qquad = -\left(\mathbf{B} + \tilde{\mathbf{B}}\right)(\operatorname{div}\mathbf{B}) - \rho g\mathbf{e}_2,\\
&\mathbf{B}_t + \operatorname{div}\left(\mathbf{u}\otimes\mathbf{B} - \mathbf{B}\otimes\mathbf{u} + \mathbf{u}\otimes\tilde{\mathbf{B}} - \tilde{\mathbf{B}}\otimes\mathbf{u}\right) = -\mathbf{u}(\operatorname{div}\mathbf{B}),\\
&E_t + \operatorname{div}\left(\left(E + p + \frac{1}{2}|\mathbf{B}|^2 + \mathbf{B}\cdot\tilde{\mathbf{B}}\right)\mathbf{u} - (\mathbf{u}\cdot\mathbf{B})\mathbf{B} - \left(\mathbf{u}\cdot\tilde{\mathbf{B}}\right)\tilde{\mathbf{B}}\right)\\
&\qquad\qquad = -(\mathbf{u}\cdot\mathbf{B})(\operatorname{div}\mathbf{B}) - \rho g\left(\mathbf{u}\cdot\mathbf{e}_2\right),
\end{aligned} \tag{7.2.4}$$

where $E = \frac{p}{\gamma-1} + \frac{1}{2}|\mathbf{B}|^2 + \frac{1}{2}\rho|\mathbf{u}|^2$. The variable of interest is now the perturbed magnetic field $\mathbf{B}$ and the background magnetic field $\tilde{\mathbf{B}}$ satisfying (7.2.3) appears as a coefficient in the above equations.

Remark 7.2.1. The only assumptions used in deriving (7.2.4) are given by (7.2.3). In particular, no linearization assumptions were made nor was any condition imposed on the magnitude of **B**. Hence, the above equations (7.2.4) can be thought of as another equivalent form of the MHD equations with gravity (7.1.1).

We will discretize the above equations (7.2.4) in the remaining part of this paper. Writing (7.2.4) explicitly in two space dimensions results in

$$\mathbf{U}_t + (\mathbf{f}(\mathbf{U}, \tilde{\mathbf{B}})_x + \mathbf{g}(\mathbf{U}, \tilde{\mathbf{B}})_y = \mathbf{s}^1(\mathbf{U}, \tilde{\mathbf{B}}) + \mathbf{s}^2(\mathbf{U}, \tilde{\mathbf{B}}) + \mathbf{s}^g(\mathbf{U}), \tag{7.2.5}$$

where

$$\mathbf{U} = \{\rho, \rho u_1, \rho u_2, \rho u_3, B_1, B_2, B_3, E\}$$

is the vector of conserved variables and $\tilde{\mathbf{B}} = \{\tilde{B}_1, \tilde{B}_2, \tilde{B}_3\}$ is any background magnetic field defined by (7.2.4). The above form clearly illustrates that the fluxes and the Godunov-Powell source term depend on the coefficient $\tilde{B}$. Hence, (7.2.5) is an example of a balance law with spatially varying coefficients. Such equations have many interesting properties (see [56]) for a detailed exposition). The fluxes in (7.2.5) are given by

$$\mathbf{f} = \begin{pmatrix} \rho u_1 \\ \rho u_1^2 + \pi_1 - \frac{B_1^2}{2} - \tilde{B}_1 B_1 \\ \rho u_1 u_2 - B_1 B_2 - \tilde{B}_1 B_2 - B_1 \tilde{B}_2 \\ \rho u_1 u_3 - B_1 B_3 - \tilde{B}_1 B_3 - B_1 \tilde{B}_3 \\ 0 \\ u_1 \left(B_2 + \tilde{B}_2\right) - u_2 \left(B_1 + \tilde{B}_1\right) \\ u_1 \left(B_3 + \tilde{B}_3\right) - u_3 \left(B_3 + \tilde{B}_3\right) \\ (E + \pi_1) u_1 - u_1 \frac{B_1^2}{2} - \left(B_1 + \tilde{B}_1\right)(u_2 B_2 + u_3 B_3) \end{pmatrix},$$

$$\mathbf{g} = \begin{pmatrix} \rho u_2 \\ \rho u_1 u_2 - B_1 B_2 - \tilde{B}_1 B_2 - B_1 \tilde{B}_2 \\ \rho u_2^2 + \pi_2 - \frac{B_2^2}{2} - \tilde{B}_2 B_2 \\ \rho u_2 u_3 - B_2 B_3 - \tilde{B}_2 B_3 - B_2 \tilde{B}_3 \\ 0 \\ u_2 \left(B_2 + \tilde{B}_2\right) - u_2 \left(B_2 + \tilde{B}_2\right) \\ u_2 \left(B_3 + \tilde{B}_3\right) - u_3 \left(B_3 + \tilde{B}_3\right) \\ (E + \pi_2) u_2 - u_2 \frac{B_2^2}{2} - \left(B_2 + \tilde{B}_2\right)(u_2 B_2 + u_3 B_3) \end{pmatrix}, \tag{7.2.6}$$

where we have defined

$$\pi_1 = p + \frac{B_2^2 + B_3^2}{2} + B_2 \tilde{B}_2 + B_3 \tilde{B}_3, \quad \pi_2 = p + \frac{B_1^2 + B_3^2}{2} + B_1 \tilde{B}_1 + B_3 \tilde{B}_3. \tag{7.2.7}$$

Similarly, the Godunov-Powell source terms in (7.2.1) can be written explicitly as

$$\mathbf{s}^1 = \begin{pmatrix} 0, \\ -\left(\frac{B_1^2}{2}\right)_x - \tilde{B}_1 (B_1)_x \\ -\left(B_2 + \tilde{B}_2\right)(B_1)_x \\ -\left(B_3 + \tilde{B}_3\right)(B_1)_x \\ -u_1 (B_1)_x \\ -u_2 (B_1)_x \\ -u_3 (B_1)_x \\ -u_1 \left(\frac{B_1^2}{2}\right)_x - (u_2 B_2 + u_3 B_3)(B_1)_x \end{pmatrix}, \quad \mathbf{s}^2 = \begin{pmatrix} 0, \\ -\left(B_1 + \tilde{B}_1\right)(B_2)_y \\ -\left(\frac{B_2^2}{2}\right)_y - \tilde{B}_2 (B_2)_y \\ -\left(B_3 + \tilde{B}_3\right)(B_2)_y \\ -u_1 (B_2)_y \\ -u_2 (B_2)_y \\ -u_3 (B_2)_y \\ -u_2 \left(\frac{B_2^2}{2}\right)_y - (u_1 B_1 + u_3 B_3)(B_2)_y \end{pmatrix} \tag{7.2.8}$$

Note that we have used the chain rule $B_1(B_1)_x = (\frac{B_1^2}{2})_x$ as well as a similar rule for the product $B_2(B_2)_y$. While true for smooth solutions, this formula may no longer hold when the magnetic field has discontinuities. However, choosing this definition of the non-conservative product was found to be robust in practice (see [34]).

Finally, the gravitational source term is given by

$$\mathbf{s}^g = \{0, 0, -\rho g, 0, 0, 0, 0, -\rho u_2 g\}. \tag{7.2.9}$$

Considering the primitive variables $\mathbf{V} = \{\rho, \mathbf{u}, \mathbf{B}, p\}$, we can write (7.2.5) in the quasilinear form

$$\mathbf{V}_t + A\mathbf{V}_x + B\mathbf{V}_y = \tilde{\mathbf{S}},$$

where $(A, B) = (\partial_{\mathbf{U}}\mathbf{f}, \partial_{\mathbf{U}}\mathbf{g})$ are the flux Jacobians. Set $\bar{\mathbf{B}} = \mathbf{B} + \tilde{\mathbf{B}}$, denoting the sound speed $a^2 = \frac{\gamma p}{\rho}$ and $b_{1,2,3} = \frac{\bar{\mathbf{B}}_{1,2,3}}{\sqrt{\rho}}$, $b^2 = b_1^2 + b_2^2 + b_3^2$, $b_\perp^2 = b_2^2 + b_3^2$, the eigenvalues of A are calculated (see [66]) as

$$\begin{aligned} &\lambda_1 = u_1 - c_f, \quad \lambda_2 = u_1 - b_1, \quad \lambda_3 = u_1 - c_s, \quad \lambda_4 = u_1, \\ &\lambda_5 = u_1, \quad \lambda_6 = u_1 + c_s, \quad \lambda_7 = u_1 + b_1, \quad \lambda_8 = u_1 + c_f, \end{aligned} \tag{7.2.10}$$

where c_f, c_s are given by

$$c_f^2 = \frac{1}{2}\left(a^2 + b^2 + \sqrt{(a^2 + b^2)^2 - 4a^2 b_1^2}\right), \quad c_s^2 = \frac{1}{2}\left(a^2 + b^2 - \sqrt{(a^2 + b^2)^2 - 4a^2 b_1^2}\right).$$

The waves corresponding to λ_1, λ_8 are termed as fast waves, ones corresponding to λ_3, λ_6 as slow waves, those corresponding to λ_2, λ_7 as Alfvén waves and the wave associated with $\lambda_{4,5}$ is a contact or shear wave. Note that the coefficient $\tilde{\mathbf{B}}$ enters into the expressions of the eigenvalues. The eigenvalues of B (in the y-direction) are analogously defined.

7.2.1 Steady states

As in the introduction, we assume that $\mathbf{u} \equiv 0$ and that $\tilde{\mathbf{B}}$ satisfies the potential field assumptions (7.2.3). Furthermore if the perturbation $\mathbf{B} \equiv 0$ and an isothermal atmosphere

is assumed, i.e, $p = C\rho$ for some constant C, then simple calculations (see [33]) lead to the following steady states of (7.2.4),

$$\mathbf{u} = 0, \quad \mathbf{B} = 0, \quad \rho(x, y) = \rho_0 e^{-y/H}, \quad p(x, y) = p_0 e^{-y/H}. \tag{7.2.11}$$

where the scale height H is given by $H = p_0/g\rho_0$ and p_0 and ρ_0 are the values of the pressure and density at the bottom boundary of the domain. Observe that the above steady state is not necessarily hydrodynamic, since only the perturbation $\mathbf{B}$ is assumed to be zero. The magnetic field is manifest in (7.2.4) through the background field $\tilde{\mathbf{B}}$.

Hydrodynamic steady state

So far, the background field $\tilde{\mathbf{B}}$ only satisfies (7.2.3). Specific solutions of the assumptions (7.2.3) lead to a classification of possible steady states. The simplest solution of (7.2.3) is given by

$$\tilde{\mathbf{B}} \equiv 0. \tag{7.2.12}$$

The steady state (7.2.11) together with zero background field (7.2.12) is called the hydrodynamic steady state. It is equivalent to the hydrodynamic steady state (7.1.3) of (7.1.1).

Magnetic steady states

Non-trivial solutions of (7.2.3) lead to interesting magnetic steady states. Note that solutions of (7.2.3) can be characterized by vector harmonic functions. We use the following Fourier expansion of vector harmonic functions (see also [33]),

$$B_1(x, y) = \sum_{k=0}^{M} f_k \sin\left(\frac{2k\pi x}{X}\right) e^{-\frac{2\pi k y}{X}}, \quad B_2(x, y) = \sum_{k=0}^{M} f_k \cos\left(\frac{2k\pi x}{X}\right) e^{-\frac{2\pi k y}{X}}, \quad B_3(x, y) \equiv 0, \tag{7.2.13}$$

where the f_k's are Fourier coefficients corresponding to the background magnetic field at the bottom of the domain and M is total number of Fourier modes. Note that the above field (7.2.13) can be quite complicated with a large number of modes. However, even more general solutions of (7.2.3) can be found, particularly those with non-zero B_3. We restrict ourselves to fields of the form (7.2.13) in our numerical simulations. The steady state (7.2.11) with a background field like (7.2.13) is called a magnetic steady state.

Remark 7.2.2. A big advantage of using the modified formulation (7.2.4) is that it allows for a unified treatment of steady states. Observe that all isothermal steady states of (7.2.4) are given by (7.2.11). The difference between individual steady states lies in the choice of the background field $\tilde{\mathbf{B}}$. This enables us to use a single characterization of isothermal steady states and design well-balanced schemes which preserve them.

7.3 Numerical Schemes

For notational simplicity, we focus on the MHD equations (7.2.1) in two space dimensions. The extension to three space dimensions is straightforward. We approximate (7.2.5) in

a domain $\mathbf{x} = (x, y) \in [X_l, X_r] \times [Y_b, Y_t]$. For simplicity, the domain is discretized by a uniform grid in both directions with the grid spacing Δx and Δy. We set $x_i = X_l + i\Delta x$ and $y_j = Y_b + j\Delta y$. The indices are $0 \le i \le N_x$ and $0 \le j \le N_y$. Set $x_{i+1/2} = x_i + \Delta x/2$ and $y_{j+1/2} = y_j + \Delta y/2$, and let $I_{i,j} = [x_{i-1/2}, x_{i+1/2}) \times [y_{j-1/2}, y_{j+1/2})$ denote a typical cell. The cell average of the unknown state vector $\mathbf{W}$ (approximating $\mathbf{U}$) over $I_{i,j}$ at time t^n is denoted $\mathbf{W}^n_{i,j}$.

7.3.1 First order schemes

A standard finite volume scheme (first-order in both space and time) (see [50]) is obtained by integrating the balance law (7.2.5) over the cell $I_{i,j}$ and the time interval $[t^n, t^{n+1})$ with $t^{n+1} = t^n + \Delta t^n$, where the time-step Δt^n is determined by a suitable CFL condition. The resulting fully-discrete form of the scheme is

$$\mathbf{W}^{n+1}_{i,j} = \mathbf{W}^n_{i,j} - \frac{\Delta t^n}{\Delta x}(\mathbf{F}^n_{i+1/2,j} - \mathbf{F}^n_{i-1/2,j}) - \frac{\Delta t^n}{\Delta y}(\mathbf{G}^n_{i,j+1/2} - \mathbf{G}^n_{i,j-1/2}) + \Delta t^n(\mathbf{S}^{1,n}_{i,j} + \mathbf{S}^{2,n}_{i,j} + \mathbf{S}^{g,n}_{i,j}). \tag{7.3.1}$$

The numerical fluxes $\mathbf{F}$, $\mathbf{G}$ and discretized sources $\mathbf{S}^1$, $\mathbf{S}^2$ and $\mathbf{S}^g$ are specified in the following sections.

Numerical flux and Godunov-Powell source in the x-direction

As in [34], we determine the numerical flux $\mathbf{F}^n_{i+1/2,j}$ and the source term $\mathbf{S}^{1,n}_{i,j}$ from the (approximate) solution of the following Riemann problem

$$\mathbf{W}_t + \mathbf{f}\left(\mathbf{W}, \tilde{\mathbf{B}}_M\right)_x = \mathbf{s}^1\left(\mathbf{W}, \tilde{\mathbf{B}}_M, \mathbf{W}_x\right), \quad \mathbf{W}(x,0) = \begin{cases} \mathbf{W}_L & x < 0, \\ \mathbf{W}_R & x > 0, \end{cases} \tag{7.3.2}$$

where $\mathbf{f}$ and $\mathbf{s}^1$ are defined in (7.2.6) and (7.2.8) respectively. The Riemann initial data in terms of primitive variables are

$$\mathbf{V}_L = \{\rho^n_{i,j}, \mathbf{u}^n_{i,j}, \mathbf{B}^n_{i,j}, p^n_{i,j}\}, \quad \mathbf{V}_R = \{\rho^n_{i+1,j}, \mathbf{u}^n_{i+1,j}, \mathbf{B}^n_{i+1,j}, p^n_{i+1,j}\}. \tag{7.3.3}$$

The data $\mathbf{W}_L, \mathbf{W}_R$ (in terms of conservative variables) is easily obtained from the primitive variables. The coefficient $\tilde{\mathbf{B}}_M$ in (7.3.2) is given by the average,

$$\tilde{\mathbf{B}}_M = \tilde{\mathbf{B}}_{i+1/2,j} = \frac{\tilde{\mathbf{B}}_{i,j} + \tilde{\mathbf{B}}_{i+1,j}}{2}. \tag{7.3.4}$$

Hence, we stagger the coefficient $\tilde{\mathbf{B}}$ in defining the approximate Riemann solver. This approach is a popular discretization of balance laws with coefficients ([45]) and results in a simplification of the Riemann problem.

The HLL three wave solver

There are eight possible waves in the exact solution of the Riemann problem (7.3.2). We will approximate these eight waves with three waves, i.e, two representing the outermost

fast waves and a middle wave approximating the material contact discontinuity. This approximate solution and fluxes for (7.3.2) are given by

$$\mathbf{W}^{H_3} = \begin{cases} \mathbf{W}_L & \text{if } \frac{x}{t} \le s_L, \\ \mathbf{W}_L^* & \text{if } s_L < \frac{x}{t} < s_M, \\ \mathbf{W}_R^* & \text{if } s_M < \frac{x}{t} < s_R, \\ \mathbf{W}_R & \text{if } s_R \le \frac{x}{t}, \end{cases} \qquad \mathbf{F}^{H_3}\left(\mathbf{W}_L, \mathbf{W}_R, \tilde{\mathbf{B}}_M\right) = \begin{cases} \mathbf{F}_L & \text{if } \frac{x}{t} \le s_L, \\ \mathbf{F}_L^* & \text{if } s_L < \frac{x}{t} < s_M, \\ \mathbf{F}_R^* & \text{if } s_M < \frac{x}{t} < s_R, \\ \mathbf{F}_R & \text{if } s_R \le \frac{x}{t}. \end{cases} \tag{7.3.5}$$

Note that we do not enforce $\mathbf{F} = \mathbf{f}(\mathbf{W}, \tilde{\mathbf{B}}_M)$. The reason is that we allow π_1 of (7.2.7) to be a free variable, hence taking the role of the relaxation pressure in [20]. For consistency we have to set $\pi_1 = p + \frac{B_2^2+B_3^2}{2} + B_2\tilde{B}_2 + B_3\tilde{B}_3$ in $\mathbf{F}_L$ and $\mathbf{F}_R$. The outer wave speeds s_L and s_R model the fast magneto-sonic waves and are defined as in [36, 28], i.e.,

$$s_L = \min\left\{u_{1L} - c_{fL},\ \bar{u}_1 - \bar{c}_f\right\}, \quad s_R = \max\left\{u_{1R} + c_{fR},\ \bar{u}_1 + \bar{c}_f\right\}, \tag{7.3.6}$$

where $\bar{u}_1$ and $\bar{c}_f$ are the normal velocity and the fast wave speed of the Jacobian matrix $A((\mathbf{W}_L + \mathbf{W}_R)/2)$ respectively. This choice is important for numerical stability and accuracy.

In order to describe the solver, we need to determine the speed of the middle wave s_M and the intermediate states $\mathbf{W}_L^*, \mathbf{W}_R^*$. The middle wave models a material contact discontinuity. Hence, the velocity field and the tangential magnetic fields are assumed to be constant across the middle wave. This allows us to define $\mathbf{u}^* = \mathbf{u}_L^* = \mathbf{u}_R^*$, $B_2^* = B_{2L}^* = B_{2R}^*$ and $B_3^* = B_{3L}^* = B_{3R}^*$. As in [34], the normal magnetic field B_1 is not assumed to be constant but jumps only across the middle wave (modeling the linear degenerate "divergence wave" implied by (7.2.2)), and B_1 is constant across the outer waves. The only difference between the solver designed here and the three wave solver described in [34] is the fact that we include a coefficient $\tilde{\mathbf{B}}_M$ in our expressions and we must account for it in the conservation relations below.

We impose local conservation across each wave to determine the various states. Local conservation across the outermost waves means that

$$s_L\mathbf{W}_L^* - \mathbf{F}_L^* = s_L\mathbf{W}_L - \mathbf{F}_L, \text{ and } s_R\mathbf{W}_R - \mathbf{F}_R = s_R\mathbf{W}_R^* - \mathbf{F}_R^*. \tag{7.3.7}$$

Conservation across the middle wave s_M involves taking the source term $\mathbf{s}^1$ in (7.3.2) into account. The conservation relation reads

$$s_M\mathbf{W}_R^* - s_M\mathbf{W}_L^* = \mathbf{F}_R^* - \mathbf{F}_L^* + \mathbf{s}^{1,*} \tag{7.3.8}$$

where

$$\mathbf{s}^{1,*} = \begin{pmatrix} 0 \\ -\frac{B_{1R}^2 - B_{1L}^2}{2} - \tilde{B}_{1M}\left(B_{1R} - B_{1L}\right) \\ -\left(B_2^* + \tilde{B}_{2M}\right)\left(B_{1R} - B_{1L}\right) \\ -\left(B_3^* + \tilde{B}_{3M}\right)\left(B_{1R} - B_{1L}\right) \\ -\mathbf{u}^*\left(B_{1R} - B_{1L}\right) \\ -u_1^*\frac{B_{1R}^2 - B_{1L}^2}{2} - \left(u_2^*B_2^* + u_3^*B_3^*\right)\left(B_{1R} - B_{1L}\right) \end{pmatrix}. \tag{7.3.9}$$

This amounts to integrating the source $\mathbf{s}^1$ in (7.3.2) across the wave fan as described in the next section. The above expression follows from the assumption that B_1 jumps only across the middle wave while the velocity field and the tangential components of the magnetic field remain constant.

For any middle speed s_M, a straightforward application of the conservation relations (7.3.7) determines unique values of ρ^*_θ given by

$$\rho^*_\theta = \rho_\theta \frac{u_{1\theta} - s_\theta}{s_M - s_\theta}, \quad \theta \in \{L, R\} \tag{7.3.10}$$

Using conservation across all the three waves (adding (7.3.7) and (7.3.8)) results in the global conservation relation,

$$\mathbf{F}_R - \mathbf{F}_L = s_R \mathbf{W}_R - s_L \mathbf{W}_L + (s_M - s_R)\mathbf{W}^*_R + (s_L - s_M)\mathbf{W}^*_L + \mathbf{s}^{1,*}. \tag{7.3.11}$$

We can use the intermediate density states (7.3.10) and global conservation (7.3.11) to obtain

$$s_M = u^*_1 = \frac{\pi_{1R} - \pi_{1L} + \rho_R u_{1R}(u_{1R} - s_R) - \rho_L u_{1L}(u_{1L} - s_L)}{\rho_R(u_{1R} - s_R) - \rho_L(u_{1L} - s_L)}.$$

Similarly, one uses local conservation (7.3.7) across the two outer waves to obtain the intermediate "relaxed" pressures,

$$\pi^*_{1\theta} = \pi_{1\theta} + \rho_\theta(u_{1\theta} - s_\theta)(u_{1\theta} - s_M), \tag{7.3.12}$$

for $\theta \in \{L, R\}$. Note that conservation across the middle wave automatically implies that $\pi^*_{1L} = \pi^*_{1R}$, and that (7.3.12) confirms this assertion. The next step is to determine the tangential velocity and magnetic field. Using global conservation across the wave fan (7.3.11), we obtain that the intermediate values u^*_σ and B^*_σ satisfy the following two linear equations,

$$\alpha u^*_\sigma - \beta B^*_\sigma = c_\sigma, \quad -\beta u^*_\sigma - \zeta B^*_\sigma = d_\sigma, \quad \sigma \in \{2, 3\},$$

where

$$\begin{aligned}
c_\sigma &= \rho_R u_{\sigma R}(u_{1R} - s_R) - \rho_L u_{\sigma L}(u_{1L} - s_L) \\
&\quad - (B_{1R}B_{\sigma R} - B_{1L}B_{\sigma L}) - \tilde{B}_{1M}(B_{\sigma R} - B_{\sigma L}), \\
d_\sigma &= B_{\sigma R}(u_{1R} - s_R) - B_{\sigma L}(u_{1L} - s_L) \\
&\quad - (B_{1L}u_{\sigma L} - B_{1R}u_{\sigma R}) + \tilde{B}_{\sigma M}(u_{1R} - u_{1L}) - \tilde{B}_1(u_{\sigma R} - u_{\sigma L}), \\
\alpha &= \rho_R(u_{1R} - s_R) - \rho_L(u_{1L} - s_L), \\
\zeta &= s_R - s_L, \\
\beta &= B_{1R} - B_{1L}.
\end{aligned} \tag{7.3.13}$$

Solving the linear system (7.3.13), the intermediate tangential components of velocity and magnetic field are obtained as

$$u^*_\sigma = \frac{\zeta c_\sigma - \beta d_\sigma}{\alpha\zeta + \beta^2}, \quad B^*_\sigma = \frac{-\alpha d_\sigma - \beta c_\sigma}{\alpha\zeta + \beta^2}. \tag{7.3.14}$$

Remark 7.3.1. In general, the denominator; $\alpha\zeta + \gamma^2$, in (7.3.14) can become small, leading to a degeneracy in the states. A simple calculation shows that $\alpha\zeta + \gamma^2 \neq 0$ if $(\rho_R c_f^R + \rho_L c_f^L)(s_R - s_L) > (B_{1R} - B_{1L})^2$. This condition can be ensured by "widening" the wave fan slightly by modifying the fast wave speeds in (7.3.6). The resulting conditions are

$$s_R \geq u_{1R} + \frac{1}{2}(\max((u_{1L} - u_{1R}), 0)) + \tilde{c}_{fR}, \quad s_L \leq u_{1L} - \frac{1}{2}(\max((u_{1L} - u_{1R}), 0)) - \tilde{c}_{fL}, \tag{7.3.15}$$

where

$$\tilde{c}_{f\theta}^2 = \frac{\gamma p_\theta}{\rho_\theta} + \frac{\bar{B}_{1\theta}^2}{\rho_\theta}(1+\epsilon) + \frac{\bar{B}_{2\theta}^2 + \bar{B}_{3\theta}^2}{\rho_\theta} + \sqrt{(\frac{\gamma p_\theta + |\bar{\mathbf{B}}|_\theta^2}{\rho_\theta})^2 - 4\frac{\gamma p_\theta \bar{B}_{1\theta}^2}{\rho_\theta^2}}, \quad \theta \in \{L, R\},$$

for some small positive ϵ and $\bar{B}_{\sigma\theta} = B_{\sigma\theta} + \tilde{B}_{\sigma M}$ with $\sigma \in \{1, 2, 3\}$. Using the conditions (7.3.15) to widen the wave fan ensures that the denominator $\alpha\zeta + \beta^2$ is never zero and the states are well defined.

Finally, the intermediate total energy states are determined by local conservation relations (7.3.7)

$$\begin{aligned} E_\theta^* = \frac{1}{s_M - s_\theta}\Big(& E_\theta\,(u_{1\theta} - s_\theta) + \pi_{1\theta} u_{1\theta} - \pi_{1\theta}^* s_M + \frac{B_{1\theta}^2}{2}\,(u_{1\theta} - s_M) \\ & + \Big(B_{1\theta} + \tilde{B}_{1M}\Big)\,(B_{2\theta} u_{2\theta} + B_{3\theta} u_{3\theta} - B_{2\theta}^* u_{2\theta}^* - B_{3\theta}^* u_{3\theta}^*)\Big), \end{aligned}$$

for $\theta \in \{L, R\}$. Hence, all the intermediate states are determined explicitly. The intermediate fluxes are obtained in terms of the intermediate states by local conservation (7.3.7),

$$\mathbf{F}_L^* = \mathbf{F}_L + s_L(\mathbf{W}_L^* - \mathbf{W}_L), \quad \mathbf{F}_R^* = \mathbf{F}_R + s_R(\mathbf{W}_R^* - \mathbf{W}_R).$$

Combining the above expressions for the states and the fluxes, we write down our explicit flux formula for the three-wave solver as

$$\mathbf{F}_{i+1/2,j}^{H_3} = \begin{cases} \mathbf{F}_{i,j} & , \text{ if } s_{L,i+1/2,j} > 0, \\ \mathbf{F}_{i,j}^* & , \text{ if } s_{L,i+1/2,j} \leq 0 \wedge s_{M,i+1/2,j} \geq 0, \\ \mathbf{F}_{i+1,j}^* & , \text{ if } s_{M,i+1/2,j} < 0 \wedge s_{R,i+1/2,j} \geq 0, \\ \mathbf{F}_{i+1,j} & , \text{ if } s_{R,i+1/2,j} < 0. \end{cases} \tag{7.3.16}$$

Note that this may be discontinuous at $s_{M,i+1/2,j} = 0$ according to (7.3.8). Hence our choice of $\mathbf{F}^{H_3}$ in that case is merely a convention. It is the proper addition of the source term which ensures that the scheme is continuous.

Discretization of the Godunov-Powell source term

In this section we explain (7.3.8), and specify the discrete source $\mathbf{S}_{i,j}^{1,n}$ in (7.3.1). The discrete source must be consistent with the Godunov-Powell source term in x-direction $\mathbf{s}^1(\mathbf{W}, \tilde{\mathbf{B}}, \mathbf{W}_x)$. It will be determined from our solution of the Riemann problem (7.3.2)

along the x-direction at the cell interfaces $(x_{i+1/2}, y_j)$. The HLL three wave approximate Riemann solver of the previous section provide us with the assumptions we need: The normal magnetic field jumps only across the contact-discontinuity modeled by the middle wave, while the velocity field and the tangential components of the magnetic field are constant across the middle wave.

We follow the presentation in [34] and let T be a quantity that is constant with value T^* across the middle wave, then

$$(TB_x^1)(x,t) = T^*(B_{1R} - B_{1L})\delta(x + tu_1^*), \tag{7.3.17}$$

where δ denotes the Dirac delta function. If we assume that $|u_1^*|\,\Delta t^n \leq \Delta x$, integrating TB_x^1 over $(0, \Delta t^n) \times (-\Delta x, 0)$ yields

$$\frac{1}{\Delta x}\int_0^{\Delta t^n}\int_{-\Delta x}^{0} TB_x^1 dxdt = \Delta t^n T^* \frac{B_{1R} - B_{1L}}{\Delta x}\mathbf{1}_{\{u_1^*<0\}}, \tag{7.3.18}$$

where $\mathbf{1}_A$ denotes the characteristic function of the set A. Integration over $(0, \Delta t^n) \times (0, \Delta x)$ leads to

$$\frac{1}{\Delta x}\int_0^{\Delta t^n}\int_{0}^{\Delta x} TB_x^1 dxdt = \Delta t^n T^* \frac{B_{1R} - B_{1L}}{\Delta x}\mathbf{1}_{\{u_1^*>0\}},$$

under the same restriction, $|u_1^*|\,\Delta t^n \leq \Delta x$. Similarly, by again using the assumption that B_1 jumps only across the contact and T remains constant across it, we obtain that

$$\frac{1}{\Delta x}\int_0^{\Delta t^n}\int_{-\Delta x}^{0} T\left(\frac{B_1^2}{2}\right)_x dxdt = \Delta t^n T^* \frac{B_{1R}^2 - B_{1L}^2}{2\Delta x}\mathbf{1}_{\{u_1^*<0\}},$$

and

$$\frac{1}{\Delta x}\int_0^{\Delta t^n}\int_{0}^{\Delta x} T\left(\frac{B_1^2}{2}\right)_x dxdt = \Delta t^n T^* \frac{B_{1R}^2 - B_{1L}^2}{2\Delta x}\mathbf{1}_{\{u_1^*>0\}}. \tag{7.3.19}$$

Hence, we can derive (7.3.8) from (7.3.18)-(7.3.19) by observing that we must have

$$\mathbf{s}^{1,*} = \int_{t^n}^{t^{n+1}}\int_{-\Delta x}^{\Delta x} \mathbf{s}^1\left(\mathbf{W}^{H_3}, \tilde{\mathbf{B}}_M, \mathbf{W}_x^{H_3}\right) dxdt.$$

The final scheme is defined by evolving the piecewise constant function $\mathbf{W}_{i,j}$ according to the approximate Riemann solver (7.3.5), and then taking the cell average of the conserved quantities. Hence, the scheme is determined by (7.3.7)-(7.3.8), yielding (7.3.16), and

$$\mathbf{S}_{i,j}^{1,n} = \mathbf{s}_{i-1/2,j}^{1,*}\mathbf{1}_{\{(s_{M,i-1/2,j}\geq 0)\}} + \mathbf{s}_{i+1/2,j}^{1,*}\mathbf{1}_{\{(s_{M,i+1/2,j}<0)\}}, \tag{7.3.20}$$

where $\mathbf{s}_{i\pm1/2,j}^{1,*}$ is defined in (7.3.9). For the case that $s_{M,i+1/2,j} = 0$ our choice here was dictated by our choice in (7.3.16). Integration along the y-direction is taken care of by the midpoint rule.

We emphasize that the discrete Godunov-Powell source term in each cell consists of contributions from Riemann solutions at the bordering interfaces and depends on the sign

of the middle wave at each interface. Thus, the Godunov-Powell source term is suitably upwinded. Note that assuming the normal magnetic field B_1 to be constant for the whole domain leads to the source term being zero. This approach follows [34],[20] and is very different from the usual centered discretization of the Godunov-Powell source term ([66] and other references therein).

Thus, we have completed the descriptions of the numerical fluxes $\mathbf{F}$ and the source $\mathbf{S}^1$ in (7.3.1).

Remark 7.3.2. The above fluxes and sources are designed using a three wave solver. An alternative would be to design a five wave solver like in [59],[34]. This solver models Alfvén waves in addition to the outer most fast waves and the contact discontinuity. We can follow the steps of [33] to design a five wave solver for (7.3.2) by taking into account contributions of the coefficient $\tilde{\mathbf{B}}$.

Fluxes and sources in the y-direction

The numerical flux $\mathbf{G}$ and discrete Godunov-Powell source term $\mathbf{S}^2$ in (7.3.1) are similarly described in terms of the following Riemann problem

$$\mathbf{W}_t + \mathbf{g}(\mathbf{W}, \tilde{\mathbf{B}}_m)_y = \mathbf{s}^2(\mathbf{W}, \tilde{\mathbf{B}}_m, \mathbf{W}_y), \quad \mathbf{W}(y,0) = \begin{cases} \mathbf{W}_B & y < 0, \\ \mathbf{W}_T & y > 0, \end{cases} \tag{7.3.21}$$

where $\mathbf{g}, \mathbf{s}^2$ are defined in (7.2.6) and (7.2.8) respectively. The natural way to specify initial data $\mathbf{W}_{T,B}$ in the above problem is to use the states $\mathbf{W}_B = \mathbf{W}^n_{i,j}$ and $\mathbf{W}_T = \mathbf{W}^n_{i,j+1}$. However, this approach leads to a scheme that does not preserve discrete versions of the interesting steady states (7.2.11). Therefore we must design suitable fluxes in order to design well-balanced schemes.

Local Hydrostatic reconstructions

Instead of just using the cell averages below and above the interface as data in (7.3.21), we utilize the special structure of the isothermal steady states (7.2.11) and perform a local hydrostatic reconstruction inside the cell, i.e., we observe that the pressure and density at steady state (7.2.11) have an exponentially decaying profile. We use the same structure locally inside a cell to define

$$\mathbf{V}_B = \{\rho^{n,-}_{i,j+1/2}, \mathbf{u}^n_{i,j}, \mathbf{B}^n_{i,j}, p^{n,-}_{i,j+1/2}\}, \quad \mathbf{V}_T = \{\rho^{n,+}_{i,j+1/2}, \mathbf{u}^n_{i,j+1}, \mathbf{B}^n_{i,j+1}, p^{n,+}_{i,j+1/2}\}, \tag{7.3.22}$$

where the reconstructed density and pressure are given in terms of extrapolated cell averages by

$$\begin{aligned} \rho^{n,-}_{i,j+1/2} &= \rho^n_{i,j} e^{\frac{-\Delta y}{2H^n_{i,j}}}, \quad p^{n,-}_{i,j+1/2} = p^n_{i,j} e^{\frac{-\Delta y}{2H^n_{i,j}}}, \\ \rho^{n,+}_{i,j+1/2} &= \rho^n_{i,j+1} e^{\frac{\Delta y}{2H^n_{i,j+1}}}, \quad p^{n,+}_{i,j+1/2} = p^n_{i,j} e^{\frac{\Delta y}{2H^n_{i,j+1}}}, \end{aligned} \tag{7.3.23}$$

with the local scale height $H^n_{i,j} = \frac{p^n_{i,j}}{/}(g\rho^n_{i,j})$. The above sub-cell hydrostatic reconstruction has been inspired by the approach of [7] to design well-balanced schemes for the shallow

water equations with bottom topography. It involves using the steady state density and pressure (7.2.11) to define the reconstructed densities and pressures at the cell edges in the y-direction.

The data $\mathbf{W}_B$ and $\mathbf{W}_T$ (in terms of conservative variables) are easily obtained from the primitive variables $\mathbf{V}_B$, $\mathbf{V}_T$. The coefficient $\tilde{\mathbf{B}}_m$ in (7.3.21) is given by the average,

$$\tilde{\mathbf{B}}_m = \tilde{\mathbf{B}}_{i,j+1/2} = \frac{\tilde{\mathbf{B}}_{i,j} + \tilde{\mathbf{B}}_{i,j+1}}{2}. \tag{7.3.24}$$

Hence, we stagger the coefficient $\tilde{\mathbf{B}}$ in defining the approximate Riemann solver as in the previous section.

An approximate Riemann solution of the problem (7.3.2) in terms of the HLL three wave solver of the previous section is easily obtained by repeating the approach of describing the solver in the x-direction. This can be used to describe the flux $\mathbf{G}$ and source $\mathbf{S}^2$. Note that the difference between the design of the fluxes and Godunov-Powell sources in the x- and the y-directions is due to the use of local hydrostatic reconstructions of the density and the pressure in the y-direction.

Discretization of the gravitational source term

We need to discretize the gravity source term to define $\mathbf{S}^g$ in (7.3.1). Instead of using a simple evaluation of the gravity term (it does not involve any derivatives) inside each cell, we follow an approach suggested in [7] for shallow water equations with topography to define

$$\mathbf{S}^{g,n}_{i,j} = \left\{ 0, 0, \frac{p^{n,-}_{i,j+1/2} - p^{n,+}_{i,j-1/2}}{\Delta y}, 0, 0, 0, 0, -\rho^n_{i,j} u^n_{2,i,j} g \right\}. \tag{7.3.25}$$

where $p^{n,-}_{i,j+1/2}, p^{n,+}_{i,j-1/2}$ are defined in (7.3.23). We will prove that this discretization of the gravity source term is consistent, and that it ensures well-balancing of the scheme.

Boundary conditions:

In order to complete our description of the scheme (7.3.1), we need to specify boundary conditions in both directions. As mentioned before, we use periodic boundary conditions in the horizontal x-direction by setting,

$$\mathbf{W}^n_{0,j} = \mathbf{W}^n_{N_x,j}, \quad \mathbf{W}^n_{N_x+1,j} = \mathbf{W}^n_{1,j}. \tag{7.3.26}$$

In the vertical y-direction, we use the following balanced Neumann type boundary conditions,

$$\mathbf{W}^n_{i,0} = \mathbf{W}^n_{i,1} e^{\frac{\Delta y}{H_i}}, \quad \mathbf{W}^n_{i,N_y+1} = \mathbf{W}^n_{i,N_y} e^{-\frac{\Delta y}{H_i}}. \tag{7.3.27}$$

This completes the description of the first order scheme (7.3.1). Some properties of this scheme are summarized in the theorem below,

Theorem 7.3.1. *Consider the scheme* (7.3.1) *approximating the system* (7.2.5). *This scheme has the following properties,*

(i.) The scheme (7.3.1) *is consistent with* (7.2.4)*, and it is first order accurate in both space and time (for smooth solutions).*

(ii.) The scheme (7.3.1) *is well-balanced and preserves discrete versions of the steady state* (7.2.11)*, i.e, given data satisfying*

$$\mathbf{u}^n_{i,j} = 0, \quad \mathbf{B}^n_{i,j} = 0, \quad \rho^n_{i,j} = \rho^0_{i,j} e^{\frac{-y_j}{H}}, \quad p^n_{i,j} = p^0_{i,j} e^{\frac{-y_j}{H}}, \tag{7.3.28}$$

and any background field $\tilde{\mathbf{B}}$*, then the numerical update* $\mathbf{W}^{n+1}_{i,j}$ *is*

$$\mathbf{W}^{n+1}_{i,j} \equiv \mathbf{W}^n_{i,j}.$$

Proof. We start by proving consistency of (7.3.1). The flux $\mathbf{F}$ and discrete source $\mathbf{S}^1$ are clearly consistent. Observe from (7.3.23) that $(\rho^{n,\pm}_{i,j+1/2}, p^{n,\pm}_{i,j+1/2}) \to (\rho^n_{i,j}, p^n_{i,j})$ as $\Delta y \to 0$. Hence, $\mathbf{G}$ and $\mathbf{S}^2$ are also clearly consistent. The consistency of the gravitational source term $\mathbf{S}^g$ in (7.3.25) is a consequence of the following elementary identity,

$$\frac{p^{n,-}_{i,j+1/2} - p^{n,+}_{i,j-1/2}}{\Delta y} = -g\rho^n_{i,j} \frac{e^{\frac{\Delta y}{2H^n_{i,j}}} - e^{\frac{-\Delta y}{2H^n_{i,j}}}}{\frac{\Delta y}{H^n_{i,j}}} = -g\rho^n_{i,j} + O(\Delta y^2). \tag{7.3.29}$$

In fact, (7.3.29) shows that the gravity source term $\mathbf{S}^g$ in (7.3.25) is in fact second order accurate. The first-order accuracy of (7.3.1) is very easy to check.

To prove that scheme (7.3.1) is well-balanced, we observe that the data (7.3.28) are constant in the x-direction. Therefore, the flux differences $F^n_{i+1/2,j} - F^n_{i-1/2,j}$ are zero for $1 \le i \le N_x$ and for all j (including the boundaries). The source terms $\mathbf{S}^1$ and $\mathbf{S}^2$ are zero because $\mathbf{B}^n_{i,j} = 0$ for all i, j (including the boundaries).

Insert the data (7.3.28) into (7.3.23) and we obtain,

$$\rho^{n,-}_{i,j+1/2} = \rho^n_{i,j} e^{\frac{-\Delta y}{2H}} = \rho^0_{i,j} e^{\frac{-y_j}{H}} e^{\frac{-\Delta y}{2H}} = \rho^0_{i,j} e^{\frac{-y_j}{H}} e^{\frac{-\Delta y}{H}} e^{\frac{\Delta y}{2H}} = \rho^n_{i,j+1} e^{\frac{\Delta y}{2H}} = \rho^{n,+}_{i,j+1/2}.$$

A similar calculation holds for the pressure. Consequently for all i, j (including the boundaries),

$$\begin{aligned} \rho^{n,-}_{i,j+1/2} &= \rho^{n,+}_{i,j+1/2}, \quad & \mathbf{u}^n_{i,j} &= \mathbf{u}^n_{i,j+1} = 0 \\ p^{n,-}_{i,j+1/2} &= p^{n,+}_{i,j+1/2}, \quad & \mathbf{B}^n_{i,j} &= \mathbf{B}^n_{i,j+1} = 0. \end{aligned} \tag{7.3.30}$$

Hence the numerical flux $\mathbf{G}$ is

$$\mathbf{G}^n_{i,j+1/2} = \mathbf{g}\left(\rho^n_{i,j+1/2}, 0, 0, p^n_{i,j+1/2}, \rho^n_{i,j+1/2}, 0, 0, p^n_{i,j+1/2}, \tilde{\mathbf{B}}_{i,j+1/2}\right)$$

and by consistency of the flux in (7.2.6), we have

$$\mathbf{G}^n_{i,j+1/2} = \mathbf{G}(\rho^n_{i,j+1/2}, 0, 0, p^n_{i,j+1/2}, \tilde{\mathbf{B}}_{i,j+1/2}) = (0, 0, p_{i,j+1/2}, 0, 0, 0, 0, 0), \tag{7.3.31}$$

Similarly an explicit evaluation of the gravity source term (7.3.25) yields,

$$\mathbf{S}^{g,n}_{i,j} = \left\{0, 0, \frac{p^n_{i,j+1/2} - p^n_{i,j-1/2}}{\Delta y}, 0, 0, 0, 0, 0\right\}.$$

Therefore combining the above two expressions, we obtain

$$\frac{\mathbf{G}^n_{i,j+1/2} - \mathbf{G}^n_{i,j-1/2}}{\Delta y} = \mathbf{S}^{n,g}_{i,j} \quad \text{for all } i \text{ and } j.$$

Using the above identity in (7.3.1) and the fact that flux differences in the x-direction and the Godunov-Powell source terms vanish leads to

$$\mathbf{W}^{n+1}_{i,j} \equiv \mathbf{W}^n_{i,j}.$$

Hence, the scheme (7.3.1) is well balanced with respect to the discrete steady state (7.3.28). □

Remark 7.3.3. It is important that the scheme produces positive states, i.e., states with positive values of density and pressure. For zero gravity and a constant $\tilde{\mathbf{B}}$, the positivity conditions of [83] (see also [15]) apply. They amount to ensuring that the state $3\mathbf{W}^n_{i,j} - \mathbf{W}^{n,-}_{i,j+1/2} - \mathbf{W}^{n,+}_{i,j-1/2}$ is positive. In our case this means that $3 - 2\cosh(\Delta y/(2H_{i,j})) > 0$, which holds as long as the local scale height $H_{i,j}$ is reasonably resolved. For general $\tilde{\mathbf{B}}$ the techniques of [83] do not apply unless we include some form of Godunov-Powell source contribution from $\tilde{\mathbf{B}}$. However, we want to avoid such a contribution for the sake of well-balancing, and in practice it should be quite small for smooth $\tilde{\mathbf{B}}$. Finally, when gravity is added, density trivially remains positive, while we expect pressure to remain positive at resolved scale heights.

7.3.2 The second order scheme

The finite volume scheme (7.3.1) is first order accurate in both space and time. For practical applications, we need higher order of accuracy. We will design a finite volume scheme based on (7.3.1) which is second order accurate in both space and time. At any time t, given the cell averages $\mathbf{W}_{i,j}(t)$, the semi-discrete form of this scheme is given by

$$\frac{d}{dt}\mathbf{W}_{i,j} = \boldsymbol{\mathcal{F}}_{i,j} = -\frac{1}{\Delta x}(\tilde{\mathbf{F}}_{i+1/2,j} - \tilde{\mathbf{F}}_{i-1/2,j}) - \frac{1}{\Delta y}(\tilde{\mathbf{G}}_{i,j+1/2} - \tilde{\mathbf{G}}_{i,j-1/2}) + \tilde{\mathbf{S}}^1_{i,j} + \tilde{\mathbf{S}}^2_{i,j} + \mathbf{S}^g_{i,j}. \tag{7.3.32}$$

The numerical fluxes $\mathbf{F}, \mathbf{G}$ and the sources $\tilde{\mathbf{S}}^1, \tilde{\mathbf{S}}^2$ are defined below.

It is standard (see [50]) to replace the piecewise constant approximation $\mathbf{W}_{i,j}$ with a non-oscillatory piecewise linear reconstruction in-order to obtain second-order spatial accuracy. There are a variety of reconstructions including the popular TVD-MUSCL limiters [81], ENO reconstruction [40] and WENO reconstruction [72]. The ENO and WENO reconstructions can be extended to even higher orders of accuracy.

A standard reconstruction is performed in terms of the conservative variables $\mathbf{W}$. However, such a reconstruction may not preserve discrete steady states like (7.2.11). Hence, we introduce a novel reconstruction procedure (see [7, 60] for well-balanced reconstructions of shallow water equations with topography) based on the following *equilibrium* variables,

$$\mathbf{R}_{i,j} = \{\mathbf{L}\rho_{i,j}, \mathbf{u}_{i,j}, \mathbf{B}_{i,j}, \mathbf{L}p_{i,j}\}, \tag{7.3.33}$$

where

$$\mathbf{L}\rho_{i,j} = \log(\rho_{i,j}), \quad \mathbf{L}p_{i,j} = \log(p_{i,j}).$$

Next, we use the equilibrium variables in each cell to define non-oscillatory slopes inside each cell by the following procedures,

Minmod Reconstruction (MM)

Given the cell averages $\mathbf{W}_{i,j}$, we calculate the equilibrium variables $\mathbf{R}_{i,j}$ defined in (7.3.33). Define the Minmod-differences in each direction as

$$\begin{aligned} D^x\mathbf{R}_{i,j} &= \text{minmod}(\mathbf{R}_{i+1,j} - \mathbf{R}_{i,j}, \mathbf{R}_{i,j} - \mathbf{R}_{i-1,j}), \\ D^y\mathbf{R}_{i,j} &= \text{minmod}(\mathbf{R}_{i,j+1} - \mathbf{R}_{i,j}, \mathbf{R}_{i,j} - \mathbf{R}_{i,j-1}) \end{aligned} \tag{7.3.34}$$

where

$$\text{minmod}(a,b) = \frac{1}{2}(\text{sgn}(a) + \text{sgn}(b))\min(|a|,|b|).$$

Note that the limiting is performed componentwise.

ENO Reconstruction

Given the cell averages $\mathbf{W}_{i,j}$, calculate the equilibrium variables $\mathbf{R}_{i,j}$ by (7.3.33). Define the ENO-differences in each direction as

$$D^x\mathbf{R}_{i,j} = \begin{cases} \mathbf{R}_{i+1,j} - \mathbf{R}_{i,j} & \text{if } \Gamma^x_{i,j} \le 1, \\ \mathbf{R}_{i,j} - \mathbf{R}_{i-1,j} & \text{otherwise,} \end{cases} \quad D^y\mathbf{R}_{i,j} = \begin{cases} \mathbf{R}_{i,j+1} - \mathbf{R}_{i,j} & \text{if } \Gamma^y_{i,j} \le 1, \\ \mathbf{R}_{i,j} - \mathbf{R}_{i,j-1} & \text{otherwise,} \end{cases} \tag{7.3.35}$$

where

$$\Gamma^x_{i,j} = \frac{|\psi(\mathbf{V}_{i+1,j}) - \psi(\mathbf{V}_{i,j})|}{|\psi(\mathbf{V}_{i,j}) - \psi(\mathbf{V}_{i-1,j})|}, \qquad \Gamma^y_{i,j} = \frac{|\psi(\mathbf{V}_{i,j+1}) - \psi(\mathbf{V}_{i,j})|}{|\psi(\mathbf{V}_{i,j}) - \psi(\mathbf{V}_{i,j-1})|},$$

for some function ψ called the global smoothness indicator. Here $\mathbf{V}$ denotes the primitive variables $\mathbf{V}_{i,j} = \{\rho_{i,j}, \mathbf{u}_{i,j}, \mathbf{B}_{i,j}, p_{i,j}\}$. We use $\psi(\mathbf{V}) = \rho + \mathbf{B}^2$. This choice of ψ is just one possibility and other choices can be made. However, this choice is quite robust in practice (see [34]). Note that for a piecewise linear reconstruction, the ENO procedure reduces to providing a limiter for the slopes in each direction.

WENO procedure

As an alternative to the above reconstruction, consider the following cell-differences

$$\begin{aligned} D^x\mathbf{R}_{i,j} &= \left(\omega^x_{i,j}\left(\mathbf{R}_{i+1,j} - \mathbf{R}_{i,j}\right) + \left(1 - \omega^x_{i,j}\right)\left(\mathbf{R}_{i,j} - \mathbf{R}_{i-1,j}\right)\right), \\ D^y\mathbf{R}_{i,j} &= \left(\omega^y_{i,j}\left(\mathbf{R}_{i,j+1} - \mathbf{R}_{i,j}\right) + \left(1 - \omega^y_{i,j}\right)\left(\mathbf{R}_{i,j} - \mathbf{R}_{i,j-1}\right)\right), \end{aligned} \tag{7.3.36}$$

where the weights are given by,

$$\begin{aligned} \omega^x_{i,j} &= \frac{a^0_{i,j}}{a^0_{i,j} + a^1_{i,j}}, \quad a^0_{i,j} = \frac{1}{3(\epsilon + \beta^{x,0}_{i,j})}, \quad a^1_{i,j} = \frac{2}{3(\epsilon + \beta^{x,1}_{i,j})}, \\ \omega^y_{i,j} &= \frac{b^0_{i,j}}{b^0_{i,j} + b^1_{i,j}}, \quad b^0_{i,j} = \frac{1}{3(\epsilon + \beta^{y,0}_{i,j})}, \quad b^1_{i,j} = \frac{2}{3(\epsilon + \beta^{y,1}_{i,j})}, \end{aligned}$$

where ϵ is a small positive number, and the parameters are given by

$$\beta^{x,0}_{i,j} = (\psi(\mathbf{V}_{i+1,j}) - \psi(\mathbf{V}_{i,j}))^2, \quad \beta^{x,1} = (\psi(\mathbf{V}_{i,j}) - \psi(\mathbf{V}_{i-1,j}))^2,$$
$$\beta^{y,0}_{i,j} = (\psi(\mathbf{V}_{i,j+1}) - \psi(\mathbf{V}_{i,j}))^2, \quad \beta^{y,1} = (\psi(\mathbf{V}_{i,j}) - \psi(\mathbf{V}_{i,j-1}))^2,$$

and the indicator function ψ is defined above. The WENO reconstruction leads to a third-order accurate approximation.

Remark 7.3.4. The above procedures do not necessarily lead to schemes that preserve positive pressure. A provably positive scheme, at least for constant $\tilde{\mathbf{B}}$, can be obtained with the framework outlined in recent papers [83, 34] with suitable modifications. We did not observe problems with positivity in our numerical simulations in this paper. One stabilizing factor was the use of logarithms of the pressure and density in the reconstruction, which automatically ensures positivity of the reconstructed pressure and density. Hence, we omit details of positivity preserving modifications here and refer the reader to [83, 34] for details.

All the above procedures supply slopes $D^x\mathbf{R}_{i,j}$ and $D^y\mathbf{R}_{i,j}$ and can be used to define the following reconstructed piecewise linear function is each cell $I_{i,j}$ denoted by

$$\overline{\mathbf{R}}_{i,j}(x,y) = \mathbf{R}_{i,j} + \frac{1}{\Delta x} D^x\mathbf{R}_{i,j}(x - x_i) + \frac{1}{\Delta y} D^y\mathbf{R}_{i,j}(y - y_j). \tag{7.3.37}$$

where the gradients $D^{x,y}$ may be defined by the minmod (7.3.34), ENO (7.3.35) or WENO (7.3.36) procedures. The reconstructed primitive variables are obtained from the reconstructed equilibrium variables by the following simple transformation,

$$\mathbf{V}_{i,j}(x,y) = \left\{ e^{\mathbf{L}\rho_{i,j}(x,y)}, \mathbf{u}_{i,j}(x,y), \mathbf{B}_{i,j}(x,y), e^{\mathbf{L}p_{i,j}(x,y)} \right\}.$$

Hence, the reconstruction procedure outlined here entails taking a logarithm of the pressure and density, reconstruct in these variables and transforming back via an exponential to obtain the reconstructed primitive variables. The conservative variables can be trivially obtained from the primitive variables and are denoted by the piecewise linear function $\mathbf{W}_{i,j}(x,y)$.

Define the point values,

$$\mathbf{W}^E_{i,j} = \mathbf{W}_{i,j}(x_{i+1/2}, y_j), \qquad \mathbf{W}^W_{i,j} = \mathbf{W}_{i,j}(x_{i-1/2}, y_j),$$
$$\mathbf{W}^N_{i,j} = \mathbf{W}_{i,j}(x_i, y_{j+1/2}), \qquad \mathbf{W}^S_{i,j} = \mathbf{W}_{i,j}(x_i, y_{j+1/2}).$$

We use these point values to define the numerical fluxes by

$$\tilde{\mathbf{F}}_{i+1/2,j} = \mathbf{F}\left(\mathbf{W}^E_{i,j}, \mathbf{W}^W_{i+1,j}, \tilde{\mathbf{B}}_{i+1/2,j}\right), \qquad \tilde{\mathbf{G}}_{i,j+1/2} = \mathbf{G}\left(\mathbf{W}^N_{i,j}, \mathbf{W}^S_{i,j+1}, \tilde{\mathbf{B}}_{i,j+1/2}\right),$$

where $\mathbf{F}$,and $\mathbf{G}$ are given by the three wave solver of the previous section. The value of the staggered coefficient $\tilde{\mathbf{B}}$ is given by a simple evaluation,

$$\tilde{\mathbf{B}}_{i+1/2,j} = \tilde{\mathbf{B}}(x_{i+1/2}, y_j), \quad \tilde{\mathbf{B}}_{i,j+1/2} = \tilde{\mathbf{B}}(x_i, y_{j+1/2}).$$

The above choice ensures second-order accuracy for smooth (say C^2) coefficients $\tilde{\mathbf{B}}$. In case the coefficient is not smooth enough, or given by cell averages, we can reconstruct the coefficient on a staggered mesh. A crucial difference between the first order and the second order fluxes is the definition of $\mathbf{G}$. In the first order scheme, hydrostatic reconstructions (7.3.23) were used to define the flux in the y-direction. The piecewise linear reconstruction in terms of the equilibrium variables (7.3.33) automatically ensures local hydrostatic balance and further modification of the reconstructed densities and pressures is unnecessary.

Similarly, the second-order source terms can be calculated as

$$\mathbf{S}^1_{i,j} = \mathbf{s}^{1,*}_{i-1/2,j}\mathbf{1}_{\{s_{M,i-1/2,j}\geq 0\}} + \mathbf{s}^{1,*}_{i+1/2,j}\mathbf{1}_{\{s_{M,i+1/2,j}<0\}},$$

where $\mathbf{s}^{1,*}_{i+1/2,j}$ is defined as in (7.3.9), but with the values $\mathbf{W}_{i,j}$ and $\mathbf{W}_{i+1,j}$ replaced by $\mathbf{W}^E_{i,j}$ and $\mathbf{W}^W_{i+1,j}$ and a second order equivalent value of coefficient $\tilde{\mathbf{B}}$. The source $\mathbf{S}^2_{i,j}$ in the y-direction is defined analogously. Observe that for smooth solutions, the discretized source $\mathbf{S}^1_{i,j}$ vanishes to truncation order with $(B^E_1)_{i,j} - (B^W_1)_{i+1,j}$. Hence, we need to add an extra term for second-order consistency. However, this term should vanish when $\mathbf{S}^1_{i,j}$ becomes significant at jumps (see e.g., [7] for an analogous situation). We suggest the following simple modification,

$$\tilde{\mathbf{S}}^1_{i,j} = \mathbf{S}^1_{i,j} + \begin{pmatrix} 0 \\ \mathbf{B}_{i,j} + \tilde{\mathbf{B}}_{i,j} \\ \mathbf{u}_{i,j}\cdot\mathbf{B}_{i,j} \\ \mathbf{u}_{i,j} \end{pmatrix} \frac{1}{\Delta x} D^x B^1_{i,j}.$$

The term $\tilde{\mathbf{S}}^2_{i,j}$ in the y-direction is defined analogously. A similar form of the discrete source was found to be very stable in [83]. Note that $\tilde{\mathbf{S}}^{1,2}_{i,j}$ are consistent second-order discretizations of the Godunov-Powell source terms $\mathbf{s}^{1,2}$. A similar form of the discrete source was found to be very stable in [83, 34]. Note that $\tilde{\mathbf{S}}^{1,2}_{i,j}$, are consistent second-order discretizations of the Godunov-Powell source terms $\mathbf{s}^{1,2}$.

The gravity source term $\mathbf{S}^g_{i,j}$ is defined by (7.3.23) and (7.3.25) (omitting the n-superscript in (7.3.25) for compatibility of notation). Note that (7.3.29) established that the source term (7.3.25) is second-order accurate.

Boundary conditions for the second order scheme

The boundary is treated in the following way. We need to specify two layers of ghost cells in each direction for a second order scheme. We have periodic boundary conditions in the x-direction, i.e., for $1 \leq j \leq N_y$ we have

$$\mathbf{W}_{0,j} = \mathbf{W}_{N_x,j}, \quad \mathbf{W}_{-1,j} = \mathbf{W}_{N_x-1,j}, \quad \mathbf{W}_{N_x+1,j} = \mathbf{W}_{1,j}, \quad \mathbf{W}_{N_x+2,j} = \mathbf{W}_{2,j} \qquad (7.3.38)$$

In the y-direction, we use extrapolated Neumann boundary conditions. In terms of the equilibrium variables, where $\mathbf{L}\rho_{i,j} = \log(\rho_{i,j})$ and $\mathbf{L}p_{i,j} = \log(p_{i,j})$, we take

$$\begin{aligned} \mathbf{L}\rho_{i,d} &= \mathbf{L}\rho_{i,1} + \frac{(1+d)\Delta y}{H_{i,1}}, & \mathbf{L}\rho_{i,Ny+1+d} &= \mathbf{L}\rho_{i,Ny} - \frac{(1+d)\Delta y}{H_{i,Ny}} \\ \mathbf{u}_{i,d} &= \mathbf{u}_{i,1+d}, & \mathbf{u}_{i,Ny+1+d} &= \mathbf{u}_{i,Ny-d} \\ \mathbf{L}p_{i,d} &= \mathbf{L}_{i,1} + \frac{(1+d)\Delta y}{H_{i,1}}, & \mathbf{L}p_{i,N_y+1+d} &= \mathbf{L}p_{i,N_y} - \frac{(1+d)\Delta y}{H_{i,N_y}} \\ \mathbf{B}_{i,d} &= \mathbf{B}_{i,1+d}, & \mathbf{B}_{i,N_y+1+d} &= \mathbf{B}_{i,N_y-d}, \end{aligned} \tag{7.3.39}$$

for $1 \leq i \leq N_x$ and $d \in \{0, 1\}$ in order to define all the values in the ghost cells. This amounts to using the extrapolated Neumann type boundary conditions of [33] for the primitive variables.

Time Stepping

The standard scheme for a first order approximation in time is the forward Euler time stepping, formally written

$$\mathbf{W}_{i,j}^{n+1} = \mathbf{W}_{i,j}^{n} + \Delta t^n \boldsymbol{\mathcal{F}}_{i,j}^{n}$$

where $\boldsymbol{\mathcal{F}}_i^n$ is defined in (7.3.32). For second-order schemes, we use the second-order strong-stability preserving Runge-Kutta (SSP) time stepping (see [37])

$$\begin{aligned} \mathbf{W}_{i,j}^{*} &= \mathbf{W}_{i,j}^{n} + \Delta t^n \boldsymbol{\mathcal{F}}_{i,j}^{n}, \\ \mathbf{W}_{i,j}^{**} &= \mathbf{W}_{i,j}^{*} + \Delta t^n \boldsymbol{\mathcal{F}}_{i,j}^{*}, \\ \mathbf{W}_{i,j}^{n+1} &= \frac{1}{2}(\mathbf{W}_{i,j}^{n} + \mathbf{W}_{i,j}^{**}). \end{aligned}$$

The time step is determined by a standard CFL condition.

The properties of the second-order scheme are summarized in the theorem below,

Theorem 7.3.2. *Consider the scheme* (7.3.32) *approximating the system* (7.2.5). *This scheme has the following properties,*

(i.) The scheme (7.3.32) *is consistent with* (7.2.5) *and is second-order accurate.*

(ii.) The scheme (7.3.32) *is well-balanced and preserves a discrete version of the steady state* (7.2.11)*, i.e, given data satisfying*

$$\mathbf{u}_{i,j} = 0, \quad \mathbf{B}_{i,j} = 0, \quad \rho_{i,j} = \rho_{i,j}^0 e^{\frac{-y_j}{H}}, \quad p_{i,j} = p_{i,j}^0 e^{\frac{-y_j}{H}}, \quad \textit{for all } i \textit{ and } j, \tag{7.3.40}$$

and any background field $\tilde{\mathbf{B}}$*, then the approximate solutions computed by* (7.3.32) *satisfy,*

$$\frac{d}{dt}\mathbf{W}_{i,j} \equiv 0, .$$

for all i *and* j.

Proof. The proof of consistency and second order accuracy is a straightforward consequence of the design of the scheme (7.3.32) and can be easily checked. We prove the well-balancing property. Assume that the data satisfies (7.3.40), then observe that the data is constant along the x-direction. This implies that

$$\tilde{\mathbf{F}}_{i+1/2,j} - \tilde{\mathbf{F}}_{i-1/2,j} \equiv 0,$$

for all i and j. Furthermore $\mathbf{u}_{i,j}, \mathbf{B}_{i,j} \equiv 0$ implies that

$$D^x\mathbf{u}_{i,j}, D^y\mathbf{u}_{i,j}, \quad D^x\mathbf{B}_{i,j}, D^y\mathbf{B}_{i,j} \equiv 0,$$

for all i and j. This is true for the minmod, ENO and WENO reconstructions. Therefore all the reconstructed values of $\mathbf{u}$ and $\mathbf{B}$ are zero and the source terms $\tilde{\mathbf{S}}^1$ and $\tilde{\mathbf{S}}^2$ are zero for all i and j. A straightforward application of (7.3.40) leads to the following,

$$\begin{aligned} D^x\mathbf{L}\rho_{i,j} \equiv 0, \quad D^x\mathbf{L}p_{i,j} \equiv 0, \\ D^y\mathbf{L}\rho_{i,j} \equiv \frac{-\Delta y}{H}, \quad D^y\mathbf{L}p_{i,j} \equiv \frac{-\Delta y}{H}, \end{aligned}$$

The above is true for all the three reconstructions, i.e, minmod (7.3.34), ENO (7.3.35) or WENO (7.3.36) reconstructions. Consequently, a simple calculation leads to the following reconstructed density and pressure,

$$\begin{aligned} \bar{\rho}_{i,j}(x,y) &= \rho_0 e^{-y_j/H} e^{-(y-y_j)/H}, \\ \bar{p}_{i,j}(x,y) &= p_0 e^{-y_j/H} e^{-(y-y_j)/H}. \end{aligned} \tag{7.3.41}$$

Hence, we can define $\rho_{i,j+1/2}$ and $p_{i,j+1/2}$ by

$$\begin{aligned} \rho^N_{i,j} = \rho^S_{i,j+1} = \rho_{i,j+1/2} &= \rho_0 e^{-y_j/H} e^{\frac{-\Delta y}{2H}}, \\ p^N_{i,j} = p^S_{i,j+1} = p_{i,j+1/2} &= p_0 e^{-y_j/H} e^{\frac{-\Delta y}{2H}}, \end{aligned} \tag{7.3.42}$$

for all i and j. From consistency of the numerical flux, we obtain

$$\tilde{\mathbf{G}}_{i,j+1/2} = \mathbf{G}(\rho^E_{i,j}, 0, 0, p^E_{i,j}, \rho^W_{i,j+1}, 0, 0, p^W_{i,j+1}, \tilde{\mathbf{B}}_{i,j+1/2}) = \mathbf{g}(\rho^E_{i,j}, 0, 0, p^E_{i,j}),$$

and using (7.3.42), we obtain

$$\tilde{\mathbf{G}}_{i,j+1/2} = (0, 0, p_{i,j+1/2}, 0, 0, 0, 0, 0). \tag{7.3.43}$$

Similarly an explicit evaluation of the gravitational source term in this case yields,

$$\mathbf{S}^g_{i,j} = \left\{ 0, 0, \frac{p_{i,j+1/2} - p_{i,j-1/2}}{\Delta y}, 0, 0, 0, 0, 0 \right\}.$$

where using (7.3.23) leads to a value of $p_{i,j+1/2}$ defined in (7.3.42).

Therefore combining the above two expressions, we obtain

$$\frac{\tilde{\mathbf{G}}_{i,j+1/2} - \tilde{\mathbf{G}}_{i,j-1/2}}{\Delta y} = \mathbf{S}^g_{i,j}.$$

Using the above identity in (7.3.32) and the fact that both flux differences in the x-direction and the Godunov-Powell source terms vanish, leads to

$$\frac{d}{dt}\mathbf{W}_{i,j} \equiv 0,$$

for all i and j. Note that the reconstruction in equilibrium variables was absolutely essential in the above proof. □

7.4 Wave propagation: Numerical experiments

We test the first order (7.3.1) and second order (7.3.32) schemes on a suite of numerical experiments. For the sake of comparison, we consider an *unbalanced* version of the first order scheme similar to (7.3.1) based on the HLL three wave solver and upwind discretization of the Godunov-Powell source terms. This scheme does not use local hydrostatic reconstructions of density and pressure (7.3.23) and discretizes gravity by the simpler form

$$\tilde{\mathbf{S}}^g_{i,j} = \{0, 0, 0, -\rho_{i,j} g, 0, 0, 0, -\rho_{i,j} u_{2,i,j} g\}\,. \tag{7.4.1}$$

Similarly, we consider a second-order version of the above *unbalanced* scheme based on a WENO reconstruction in the conservative variables, as opposed to the equilibrium variables of the scheme (7.3.32). Hence, we test the following five schemes:

H_3	First order *unbalanced* HLL three wave solver,
$H_{3\mathrm{WB}}$	well-balanced version of H_3 (7.3.1),
$H_{3\mathrm{WB}}M$	second order well-balanced HLL three-wave solver (7.3.32) with Minmod reconstruction (7.3.34),
H_3W	second order *unbalanced* HLL three-wave solver with WENO reconstruction
$H_{3\mathrm{WB}}W$	second order well-balanced HLL three wave solver (7.3.32) with WENO reconstruction (7.3.36).

The results with a well-balanced ENO scheme were very similar on most problems to either the $H_{3\mathrm{WB}}M$ scheme or the $H_{3\mathrm{WB}}W$ scheme and we omit them from the following presentation. The first order schemes are evolved with a CFL number of 0.45 and the second order schemes use a CFL number of 0.9. In all our computations we set $\gamma = 5/3$.

Regarding the measurement of errors, if we have a reference solution available, then we define the relative error as

$$100 \times \frac{\|\alpha - \alpha_{\mathrm{ref}}\|}{\|\alpha_{\mathrm{ref}}\|},$$

where α is (a component of) the numerical approximation and α_{ref} is (the same component of) the reference solution, and $\|\cdot\|$ is some (usually L^1) norm.

7.4.1 Hydrodynamics: steady state

We begin with a numerical experiment with zero background magnetic field $\tilde{\mathbf{B}}$. This idealized stellar atmosphere is modeled by a two dimensional spatial domain of $[0, 4]\times[0, 1]$.

The initial conditions are given by the hydrodynamic steady state (7.2.11) and $\tilde{\mathbf{B}} \equiv 0$ with a scale height of $H = 0.158$, initial pressure $p_0 = 1.13$ and gravitational constant $g = 2.74$. The parameters are chosen to approximate the dimensional parameters used in [18]. The simulation is carried out up to a time of $t = 1.8$. Here we will compare the performance of our schemes in preserving the steady state (7.2.11) to the *unbalanced* version of these schemes. Our interest is measuring errors in preserving the steady state with respect to both the pressure (density) and the velocity. We compute relative percentage errors in pressure by

$$100 \times \frac{\|p - p_{\text{ref}}\|_{L^1}}{\|p_{\text{ref}}\|_{L^1}},$$

where p_{ref} is simply the steady state pressure (7.2.11). It is harder to compute relative errors in the velocity as the steady state velocity is $\mathbf{u} \equiv 0$. However, the velocity can be compared to the sound speed $a = \sqrt{\gamma p/\rho}$. Note that the steady state sound speed is a constant given by $a = \sqrt{\gamma g H}$ where g and H are the acceleration due to gravity and the scale height. A simple calculation with the constants considered here lead to $a = 0.85$. Therefore, we measure velocity errors by the following,

$$100 \times \frac{\|u_2\|_{L^1}}{a},$$

where we choose the velocity component u_2 for convenience. The numerical errors in L^1 for the pressure and the velocity (as calculated above) on a series of meshes are presented in Table 7.4.1. From this table, we see that using the *unbalanced* schemes H_3 and H_3W

% L^1-error in p	H_3	H_3W	$H_{3\text{WB}}$	$H_{3\text{WB}}M$	$H_{3\text{WB}}W$
100x25	4.9e+2	8.2e+0	7.0e-13	1.1e-12	1.6e-13
200x50	1.6e+2	1.1e+0	3.7e-14	7.2e-14	5.7e-14
400x100	6.7e+1	1.4e-1	4.8e-13	4.3e-13	2.7e-13
800x200	3.0e+1	1.7e-2	6.4e-13	7.1e-13	3.1e-13

% L^1-error in u_2	H_3	H_3W	$H_{3\text{WB}}$	$H_{3\text{WB}}M$	$H_{3\text{WB}}W$
100x25	2.8e+1	9.7e-1	7.0e-13	1.1e-12	1.6e-13
200x50	1.5e+1	1.3e-1	3.7e-14	7.2e-14	5.7e-14
400x100	7.6e+0	1.7e-2	4.8e-13	4.3e-13	2.7e-13
800x200	2.4e+0	2.1e-3	6.4e-13	7.1e-13	3.1e-13

Table 7.4.1: Percentage relative L^1 errors in p and u_2 for different schemes on different meshes. Left: un-balanced schemes, right: well-balanced schemes

leads to errors in preserving the steady state pressure and velocity although they converge to zero when the mesh is refined. The first order H_3 scheme has large errors and the rate of convergence is one. The WENO based H_3W does a much better job with respect to steady state errors and the observed rate of convergence is close to 3 . However, the errors (even with WENO scheme) are too large to allow for computations of very small steady state perturbations.

On the other hand, the well-balanced schemes perform much better. As proved in theorems 7.3.1, 7.3.2, the well-balanced schemes preserve the steady state up to machine

precision for both first and second order schemes. This experiment serves to illustrate the constrast between *unbalanced* schemes are their well-balanced counterparts.

7.4.2 Hydrodynamics: Wave propagation

The next step is to simulate hydrodynamic wave propagation. The computational domain is the same as in the previous experiment. The propagation of waves is initiated by sending in a sinusoidal (in time) sequence of waves from the bottom boundary, and letting them propagate across the domain and exiting at the top. The initial data is the hydrodynamic steady state (7.2.11) (with the background magnetic field $\tilde{\mathbf{B}} \equiv 0$). The waves are modeled by the following boundary conditions for the normal velocity at the bottom,

$$u^{2,n}_{i,\{0,-1\}} = c \sin\left(6\pi t^n\right) \mathbf{1}_{\{[1.85,1.95]\}} \tag{7.4.2}$$

Hence, we model the bottom boundary as a localized piston in the interval $[1.85, 1.95]$.

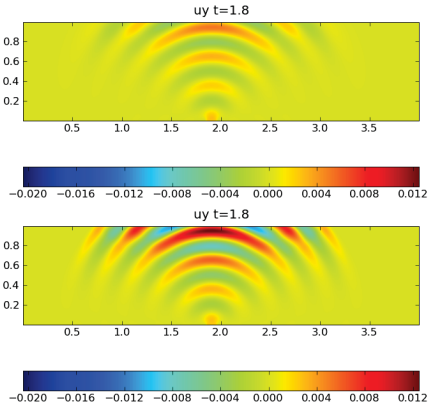

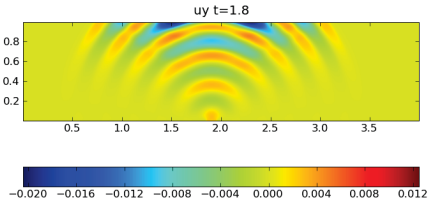

Figure 7.4.1: The vertical velocity u^2 at $t = 1.8$ at a mesh resolution of 800×200 points for $c = 3.0e^{-3}$. Top left: $H_{3\text{WB}}$, top right: $H_{3\text{WB}}M$, left: $H_{3\text{WB}}W$.

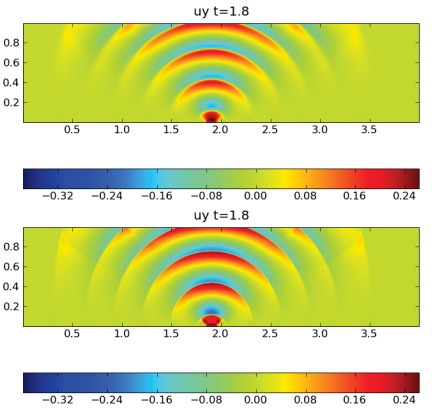

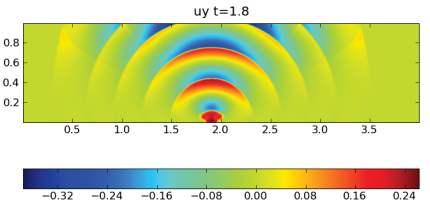

Figure 7.4.2: The vertical velocity u^2 at $t = 1.8$ at a mesh resolution of 800×200 points for $c = 3.0e^{-1}$. Top left: $H_{3\text{WB}}$, top right: $H_{3\text{WB}}M$, left: $H_{3\text{WB}}W$.

These waves move up through the domain and are modified by the flow equations and the action of gravity. We perform two different tests for this model. In the first one, we send in very small perturbations ($c = 3.0e^{-3}$). This test serves to illustrate the well-balancing properties of the schemes. Figure 7.4.1 shows u_2 at time $t = 1.8$ for the small wave perturbations ($c = 3.0e^{-3}$) for a 800×200 mesh. The first order $H_{3\text{WB}}$ scheme is very dissipative. There is a tremendous difference between the first order scheme and the second order schemes. Additionally, we observe that the WENO scheme, (being formally third-order accurate) shows better accuracy than the Minmod reconstruction. Observe from Table 7.4.1 that the steady state velocity errors with the unbalanced H_3 and H_3W are either of the same order or orders of magnitude greater than the perturbations and it was not possible to resolve these very small waves for any of the *unbalanced* schemes. This illustrate the computational efficiency of well-balanced schemes in resolving small perturbations of the steady state.

Now, we increase the amplitude of the waves introduced at the bottom boundary (7.4.2) by two orders of magnitude with $c = 0.3$. In figure 7.4.2 we present the results for the first and second order well-balanced schemes ($H_{3\text{WB}}$, $H_{3\text{WB}}M$, $H_{3\text{WB}}W$). We can see that the waves are resolved very well and there is a clear improvement in resolution from first to second order schemes. Furthermore, the WENO scheme has better resolution than the Minmod scheme. The features are resolved quite well by the minmod and the WENO schemes. There was a small amount of reflections from the top boundary. However, the errors were quite small and did mnot affect the quality of the approximation in the interior.

7.4.3 Magneto-Hydrodynamics: steady state

A realistic model of the solar atmosphere must account for the magnetic field. We begin considering magnetic fields by a test case that illustrates the performance of different schemes in preserving a magnetic steady state of of the form (7.2.4). As in the previous numerical experiment, the computational domain is $[0, 4] \times [0, 1]$. We consider the steady state (7.2.11) but a non-trivial background magnetic field $\mathbf{B}$. The background magnetic field is given by an expression of the form (7.2.13) in terms of a Fourier expansion. The Fourier coefficients are listed below, (The X in (7.2.13) is in this case is equal to 4.)

$$\begin{aligned}\mathbf{FR} = \{f_0, f_1, \ldots, f_{14}\} = \\ \big\{&0.552802906842, -0.696736253842, 0.908809914778, -0.813921192337, 0.360524088458, \\ &0.115217242296, -0.281974513346, 0.143723957761, 0.049431756210, -0.110095259045, \\ &0.053464228949, 0.011695376102, -0.028284735991, 0.013116555865, 0.001434008866\big\}.\end{aligned} \tag{7.4.3}$$

Note that the above magnetic field is quite complicated. It is designed to approximate a perturbed Gaussian magnetic field considered in [18]. This experiment was also considered in a recent paper [33]. The results of [33] indicated that it was much harder to compute steady states like (7.2.11) with magnetic field given by (7.2.13). In fact, all the finite volume schemes (with different combinations of boundary conditions) considered in [33] crashed on this problem. Hence, it is very interesting to see how the well-balanced schemes perform on this test case.

We compute with the three well-balanced schemes i.e, $H_{3\text{WB}}$, $H_{3\text{WB}}M$ and $H_{3\text{WB}}W$, and for the sake of comparison, we also compute with the two *unbalanced* schemes until $t = 1.8$ on a sequence of meshes. The relative percentage errors in L^1 (as calculated in Numerical experiment 7.4.1) for both the pressure and the velocity are given in table 7.4.2. The table clearly shows that the well-balanced schemes preserve the steady state

% L^1-error in p	H_3	H_3W	$H_{3\text{WB}}$	$H_{3\text{WB}}M$	$H_{3\text{WB}}W$
100x25	3.5e+2	6.3e+0	9.8e-20	2.5e-18	7.9e-17
200x50	1.2e+2	8.2e-1	1.6e-18	3.6e-18	4.1e-16
400x100	4.9e+1	1.0e-1	2.8e-18	3.5e-18	2.6e-15
800x200	2.2e+1	1.3e-2	4.6e-18	1.4e-17	2.0e-14

% L^1-error in u_2	H_3	H_3W	$H_{3\text{WB}}$	$H_{3\text{WB}}M$	$H_{3\text{WB}}W$
100x25	2.0e+1	6.9e-1	7.0e-13	1.1e-12	1.6e-13
200x50	9.8e+0	8.6e-2	3.7e-14	7.2e-14	5.7e-14
400x100	4.8e+0	1.0e-2	4.8e-13	4.3e-13	2.7e-13
800x200	2.4e+0	1.3e-3	6.4e-13	7.1e-13	3.1e-13

Table 7.4.2: Percentage relative L^1 errors in p and u_2 for different schemes on different meshes. Left un-balanced schemes. Right well-balanced schemes

to machine precision whereas the *unbalanced schemes* lead to relatively large errors. The errors in both sets of schemes are comparable to the errors in preserving the hydrodynamic steady state (see table 7.4.1). Hence, it is not possible to use *unbalanced schemes* for approximating very small perturbations of steady states.

7.4.4 Wave propagation: Effect of the magnetic field

This test case is set up to illustrate the transition from hydrodynamics to MHD by observing the effect that magnetic fields have on wave propagation. The computational domain is $[0, 2] \times [0, 1]$ with the initial data corresponding to the steady state (7.2.11). The waves are modeled by the following boundary conditions for the normal velocity at the bottom,

$$u^{2,n}_{i,\{0,-1\}} = c \sin\left(6\pi t^n\right) \chi_{[0.95,1.05]}, \tag{7.4.4}$$

with $c = 3e^{-1}$. We consider the simple homogenous background field $\tilde{\mathbf{B}}$ given by

$$\tilde{B}_2 = \mu, \quad \tilde{B}_1 = \tilde{B}_3 = 0. \tag{7.4.5}$$

with a constant μ that we vary between each experiment. A crucial parameter is the plasma β given by

$$\beta = \frac{2p}{\mathbf{B}^2}. \tag{7.4.6}$$

The parameter β measures the relative strength of the thermal pressure to the magnetic field and is crucial in determining the dynamics of the plasma. We show results on a 400×200 mesh at time $t = 0.54$, computed with the $H_{3\text{WB}}W$ scheme in figure 7.4.3.

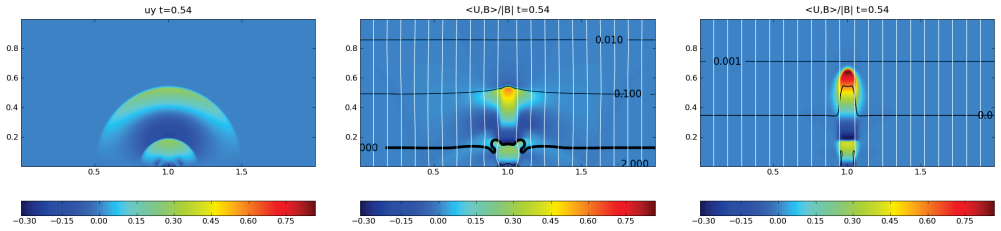

Figure 7.4.3: Results for the simple magnetic field (7.4.5) with the WENO reconstruction at $t = 0.54$ on a 400×200 mesh. The magnetic field-lines are in white and the β-lines are in black. The figures show the velocity in the direction of the magnetic field. The magnetic field strength increases from left to right: left: $\mu = 0$, center: $\mu = 1$, right: $\mu = 5$.

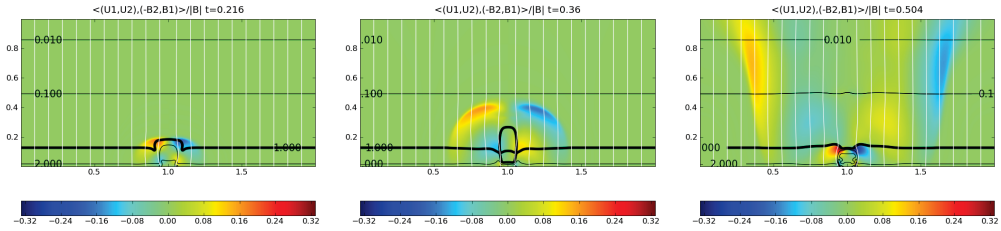

Figure 7.4.4: Velocity perpendicular to the magnetic field for the simple magnetic field (7.4.5) with $\mu = 1$ and with the WENO reconstruction at different times on a 400×200 mesh. The magnetic field lines are white and the isolines of β black. Left:$t = 0.216$, center: $t = 0.36$, right: $t = 0.50$.

Three different values of $\mu = 0, 1, 5$ are chosen to illustrate of the effect of increasing the magnetic field strength. The magnetic field lines are shown in white and the β isolines are shown in black. The figure clearly illustrates the role of the magnetic field. For $\mu = 0$ (hydrodynamics), the waves radiate outward as they are bent by gravity. Before discussing the numerical results for the configurations with magnetic fields, we describe some terminology: the waves corresponding to the eigenvalues $\lambda_{1,8}$ in (7.2.10) are called *fast waves*. Similarly, waves corresponding to the eigenvalues $\lambda_{3,6}$ are called *slow waves*. Clearly, the fast waves have much higher speed than the slow waves. Furthermore, the plasma velocity in the direction of the magnetic field only shows the presence of slow waves ([18]) whereas the velocity in the direction perpendicular to the magnetic field shows both fast as well as slow waves. In a stratified magneto-atmosphere (see the structure of (7.2.11), (7.2.13) and (7.4.3)), the pressure and the density decay exponentially with height whereas the magnetic field (at least its constant mode) remains approximately constant. Hence, a pressure dominated flow (with $\beta \gg 1$) at the bottom of the domain can change into a magnetically dominated flow (with $\beta \ll 1$) near the top of the domain. This implies that gas pressure and magnetic fields play different roles in different parts of the domain. Furthermore, the region $\beta \approx 1$ is very interesting in nature, since $\beta = 1$

corresponds to the well known *triple point* of MHD ([17]). This region is characterized by the fact that the fast and slow (also the Alfvén) eigenvalues almost coincide. The brief description above (a more detailed one can be found in [18]) serves to illustrate the complexity of the physics underlying wave propagation in stellar atmospheres, and the considerable numerical challenges that must be overcome to model this.

In Figure 7.4.3 we present the velocity in the direction of the magnetic field. Given the planar magnetic field (7.4.5), this reduces to the velocity in y-direction. For $\mu = 1$, the magnetic field compresses the wave and its outward radial spread is reduced considerably. This should be contrasted with the hydrodynamic case. The compression increases considerably by increasing the magnetic field strength to $\mu = 5$. In this case, the velocity is completely focused by the magnetic field. This example clearly shows the role of the magnetic field in focusing waves.

Another significant feature is the role of the plasma β. The triple line $\beta = 1$ serves to convert fast waves into a combination of fast and slow waves ([18]). This phenomenon is illustrated in Figure 7.4.4 where the velocity in the direction perpendicular to the magnetic field (the velocity in x-direction for this planar magnetic field) is shown. We show the results with the WENO scheme on a 400×200 mesh and with $\mu = 1$ at three different times. This particular magnetic field is chosen because it has a $\beta = 1$ isoline lying within the computational domain. Thus, this example shows the effect of both the gas pressure as well as the magnetic field. As soon as a fast wave hits the $\beta = 1$ isoline, mode conversion takes place and it is converted into a combination of fast and slow waves. Furthermore, the decreasing values of β imply that velocity of the fast waves increases quite rapidly and the fast waves get accelerated after crossing the $\beta = 1$ isoline. The acceleration in the low β region forces the fast waves to turn towards the high β region near the top boundary. This *turning* behavior is demonstrated quite well in right most panel of Figure 7.4.4 and is physical ([18]). The above results show that there are many interesting physical effects accompanying wave propagation in the presence of magnetic fields.

7.4.5 Wave propagation: Weak magnetic fields

The above numerical experiment sets the stage for introducing more complicated background magnetic fields. We consider (7.2.4) with the steady state (7.2.11) as the initial data. The background magnetic field $\tilde{\mathbf{B}}$ is given in terms of the expansion (7.2.13) with Fourier coefficients given by the vector $\mathbf{FR}/3$ where $\mathbf{FR}$ is defined in (7.4.3). This magnetic field is called *weak* in analogy with the terminology in [18]. The computational domain is $[0, 4] \times [0, 1]$.

We use the well-balanced schemes to compute to above configuration with two different perturbations. First, we consider a very weak perturbation of type (7.4.2) with magnitude $c = 3e^{-3}$. This test illustrates the well-balancing of the schemes. The results with all the three schemes $H_{3\mathrm{WB}}$, $H_{3\mathrm{WB}}M$ and $H_{3\mathrm{WB}}W$ on a 800×200 mesh at time $t = 0.9$ are presented in Figure 7.4.5. We show both the component of the velocity field parallel to the magnetic field and the component perpendicular to it. Observe that all the three schemes are able to capture the small perturbations. This is quite challenging as the schemes need to preserve the steady state (7.2.11) with this complex magnetic field to machine

precision in order to capture these small waves. The figure shows that the WENO scheme is most accurate and the first order scheme is most dissipative. Furthermore, the complex

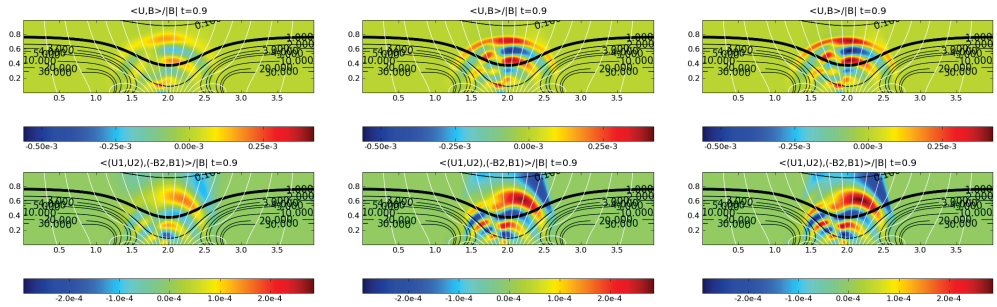

Figure 7.4.5: Results for the weak magnetic background with small wave perturbations ($c = 3e^{-3}$) at $t = 0.9$ on a 800×200 mesh. The magnetic field lines are shown in white and the isolines of β in black. The top row shows the speed in the direction of the magnetic field lines and the bottom row shows the speed perpendicular to the magnetic field lines. Left column: $H_{3\mathrm{WB}}$, middle column: $H_{3\mathrm{WB}}M$, right column: $H_{3\mathrm{WB}}W$.

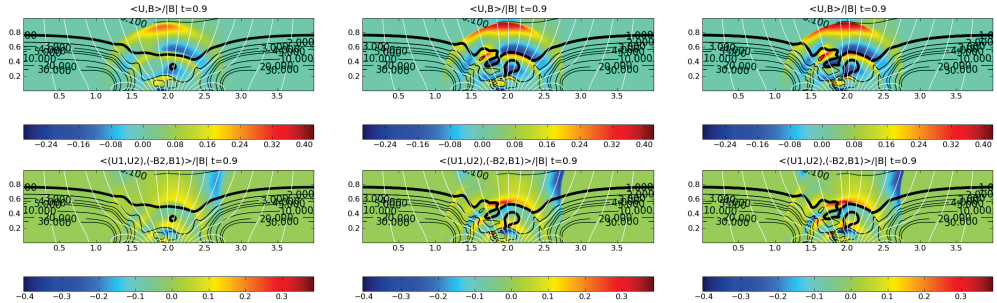

Figure 7.4.6: Results for the weak magnetic background at $t = 0.9$ on a 800×200 mesh for $c = 3e^{-1}$. The magnetic field lines are shown in white and the isolines for β in black. The top row shows the speed in the direction of the magnetic field lines and the bottom row shows the speed perpendicular to the magnetic field lines. Left column: $H_{3\mathrm{WB}}$, middle column: $H_{3\mathrm{WB}}M$, right column: $H_{3\mathrm{WB}}W$.

physics is nicely resolved by all the three schemes. The velocity in the direction of the magnetic field shows the presence of the slow waves whereas the perpendicular component shows both fast and slow waves (observe that the leading fast wave has already reached the boundary at this time instant whereas the leading slow wave is still quite far from the top boundary). Note that the $\beta = 1$ isoline is at the center of the domain. The mode conversion described in the previous experiment is quite clearly seen.

A second set of computations with the above configuration involves a much stronger perturbation of the type (7.4.2) with magnitude $c = 3e^{-1}$. Thus the perturbation is two

orders of magnitude greater than the one considered before. The results with all the three schemes at time $t = 0.9$ are shown in Figure 7.4.6. The results are obtained on a 800×200 mesh. The qualitative features shown in Figure 7.4.6 are similar to those presented in Figure 7.4.5. The main differences are: the fast waves are much faster now and are exiting the top boundary at this instant of time. The turning behavior of the fast waves is quite pronounced. Another difference in this case is the observation that the magnetic field is being distorted quite strongly by the wave. This is to be expected as the magnetic field is not very strong and the waves have reasonably large magnitude. Note that the slow waves continue to spread radially outward as the magnetic field is not strong enough to focus them. At the level of schemes, all the three schemes resolve the complex physics quite well and allow us to deduce quantitative as well as qualitative conclusions on the nature of the wave propagation.

7.4.6 Wave propagation: Strong magnetic fields

We consider the same configuration as in the previous experiment. However, we increase the strength of the background magnetic field (7.2.13) by considering Fourier coefficients given by (7.4.3). Thus, the strength of the magnetic field is increased three times compared with the previous numerical experiment. This field is called the *strong* magnetic field. We begin with a very small perturbation of the type (7.4.2) with $c = 3e^{-3}$ to test the well-balancing properties of the schemes. The parallel and perpendicular components (to the direction of the magnetic field) of the velocity field at a resolution of 800×200 points are shown in Figure 7.4.7. All the three schemes are able to capture the small perturbations quite accurately. The first order scheme is dissipative, but the minmod and WENO schemes compute much sharper wave fronts. Furthermore, there are considerable differences in the behavior of the waves compared with the numerical experiment with a weaker magnetic field. The waves in direction of the magnetic field are much more focused by the magnetic field. This is to be expected as the magnetic field is stronger (see Figure 7.4.3 for the planar magnetic field case). Also the fast waves are considerably faster in this case since β decays much faster, given the stronger magnetic field. Hence, the maximum eigenvalues in (7.2.10) corresponding to the fast waves are larger. Consequently, the turning of the fast waves at the top boundary is more pronounced. The accurate numerical resolution of the complex phenomena with very small amplitudes illustrates the robustness of the well-balanced schemes. We consider the same configuration as above but increase the perturbation (7.4.2) by two orders of magnitude with $c = 3e^{-1}$. The results are shown in Figure 7.4.8. The results are qualitatively similar to those observed in Figure 7.4.7. The fast waves travel even faster now and the turning at the top boundary is more pronounced. Furthermore, the turned fast waves hit the $\beta = 1$ isoline and are converted into slow waves. These slow waves are visible in the right hand side of the domain as very small waves in the direction parallel to the magnetic field.

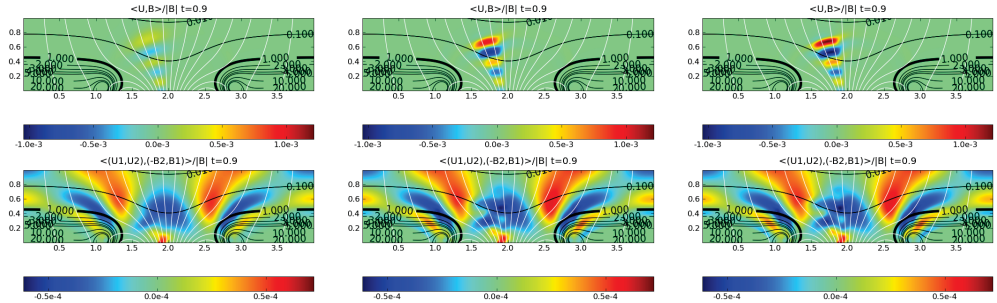

Figure 7.4.7: Results for the strong magnetic background with small wave perturbations ($c = 3e^{-3}$) at $t = 0.9$ on a 800×200 mesh. The magnetic field-lines are shown in white and the β-lines in black. The top row shows the speed in the direction of the magnetic field-lines and the bottom row shows the speed perpendicular to the magnetic field-lines. left column: $H_{3\mathrm{WB}}$, middle column: $H_{3\mathrm{WB}}M$, right column: $H_{3\mathrm{WB}}W$.

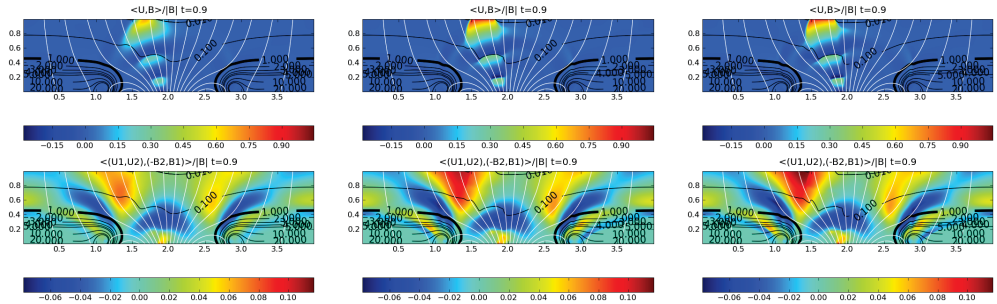

Figure 7.4.8: Results for the strong magnetic background at $t = 0.9$ on a 800×200 mesh for $c = 3e^{-1}$. The magnetic field lines are shown in white and the isolines of β in black. The top row shows the speed in the direction of the magnetic field lines and the bottom row shows the speed perpendicular to the magnetic field lines. Left column: $H_{3\mathrm{WB}}$, middle column: $H_{3\mathrm{WB}}M$, right column: $H_{3\mathrm{WB}}W$.

7.5 Conclusion

We consider numerical simulations of wave propagation in an idealized stellar atmosphere. The model consists a reformulated ideal MHD system based on the Godunov-Powell form, together with an embedded steady magnetic field. The resulting equations are balance laws with gravity source terms and background magnetic fields playing the role of coefficients. The system possesses interesting isothermal steady states. Waves are modeled as small perturbations of these steady states.

The system is simulated by finite volume schemes based on HLL three wave approximate Riemann solvers and upwind discretizations of the Godunov-Powell source term. The scheme is well-balanced by using local hydrostatic reconstructions of the density and pressure and a suitable discretization of the gravity source term. Second-order accurate schemes are designed by considered suitable minmod and WENO reconstructions. The reconstructions are performed in terms of *equilibrium* variables to ensure well-balancing.

The resulting schemes are high-order accurate, stable and well-balanced. They are validated on a large suite of numerical experiments. The underlying physical phenomena are quite complex and involve multiple scales and parameters. The schemes perform very well and are able to resolve very small perturbations as well as the complex phenomena to a high degree of accuracy.

Future projects include employing the schemes of the paper on more realistic three dimensional configurations with background magnetic fields and perturbations derived from observed data. Additional physical effects need to be included in order to increase the range of application of the models considered here. We plan to consider non-isothermal steady states, and to add effects of radiation in order to model stellar atmospheres in a more realistic manner. Such extensions will be considered in forthcoming papers.

Bibliography

[1] http://history.nasa.gov/SP-402/p2.htm

[2] http://www.nasa.gov/worldbook/sun_worldbook.html

[3] http://en.wikipedia.org/wiki/Sun.

[4] http://ircamera.as.arizona.edu/NatSci102/lectures/sun.htm

[5] http://upload.wikimedia.org/wikipedia/commons/8/89/Solar_internal_structure.svg

[6] http://commons.wikimedia.org/wiki/File:Solarmap.png

[7] E. Audusse, F. Bouchut, M. O. Bristeau, R. Klien and B. Perthame. A fast and stable well-balanced scheme with hydrostatic reconstruction for shallow water flows. *SIAM. Jl. Sci. Comp,* 25 (6), 2004, 2050 - 2065.

[8] D. S. Balsara. Linearized formulations of the Riemann problem for adiabatic and isothermal hydrodynamics. *Astrophys. Jl. Suppl.,* 116, 119, 1998.

[9] D. S. Balsara. Total Variation diminshing algorithms for adiabatic and isothermal hydrodynamics. *Astrophys. J., suppl.,* 116, 133, 1998.

[10] D.S. Balsara and J. W. Kim. An intercomparison between divergence cleaning and staggered mesh formulations for numerical magneto-hydrodynamics. *Astrophys. J.,* 602, 1079-1090, 2004.

[11] D. S. Balsara and D. Spicer. A staggered mesh algorithm using high order Godunov fluxes to ensure solenoidal magnetic fields in magnetohydrodynamic simulations. *J. Comp. Phys.*, 149(2):270-292, 1999.

[12] T. J. Barth. Numerical methods for gas dynamics systems. *In An introduction to recent developments in theory and numerics for conservation laws*, D. Kröner, M. Ohlberger, C. Rohde (eds), Springer, 1999.

[13] S. Benzoni-Gavage and D. Serre. *Multidimensional hyperbolic partial differential equations*. Oxford Mathematical Monographs. The Clarendon Press Oxford University Press, Oxford, 2007. First-order systems and applications.

[14] C. Berthon. Why the MUSCL-Hancock scheme is L^1-stable *Numer. Math.*, 104, 27-46, 2006.

[15] Christophe Berthon. Stability of the MUSCL Schemes for the Euler Equations, *Commun. Math. Sci.*, 3(2):133-157, 2005.

[16] N. Besse and D. Kröner. Convergence of the locally divergence free discontinuous Galerkin methods for induction equations for the 2D-MHD system. *M2AN Math. Model. Num. Anal* 39(6):1177-1202, 2005.

[17] D. Biskamp. Nonlinear magnetohydrodynamics. *Cambridge monographs on plasma physics*, Cambridge university press, 1993.

[18] T. J. Bogdan *et al.* Waves in the magnetized solar atmosphere II: Waves from localized sources in magnetic flux concentrations. *Astrophys. Jl,* 599, 2003, 626 - 660.

[19] F. Bouchut. Entropy satisfying flux vector splittings and kinetic BGK models. *Numer. Math.* 94 (4), (2003) 623-672

[20] F. Bouchut, C. Klingenberg and K. Waagan. A multi-wave HLL approximate Riemann solver for ideal MHD based on relaxation I- theoretical framework. *Numer. Math.*, 108 (1), 7-42, 2007.

[21] F. Bouchut, C. Klingenberg and K. Waagan. A multi-wave HLL approximate Riemann solver for ideal MHD based on relaxation II- Numerical experiments. *Preprint, 2008.*

[22] J. U. Brackbill and D. C. Barnes. The effect of nonzero Div(B) on the numerical solution of the magnetohydrodynamic equations. *J. Comp. Phys.*, 35:426-430, 1980.

[23] M. Brio and C. C. Wu. An upwind differencing scheme for the equations of ideal MHD. *J. Comp. Phys,* 75 (2), 1988, 400 - 422.

[24] P. Cargo and G. Gallice. Roe matrices for ideal MHD and systematic construction of Roe matrices for systems of conservation laws. *J. Comp. Phys,* 136 (2), 1997, 446 - 466.

[25] M. Castro, J. M. Gallardo, C Parés. High order finite volume schemes based on reconstruction of states for solvving hyperbolic systems with non-conservative products. *Math. Comp.,* 75, 2006, 1103-1134.

[26] W. Dai and P. R. Woodward. A simple finite difference scheme for multi-dimensional magnetohydrodynamic equations. *J. Comp. Phys.*, 142(2):331-369, 1998.

[27] A. Dedner, F. Kemm, D. Kröner, C. D. Munz, T. Schnitzer and M. Wesenberg. Hyperbolic divergence cleaning for the MHD equations. *J. Comp. Phys.,* 175, 645-673, 2002.

[28] B. Einfeldt. On the Godunov type methods for gas dynamics. *SIAM. J. Num. Anal.*, 25 (2), 1988, 294 - 318.

[29] B. Engquist and A. Majda. Absorbing boundary conditions for the numerical simulation of waves. *Math. Comp.* 31, 1977, 629 - 651.

[30] C. Evans and J. F. Hawley. Simulation of magnetohydrodynamic flow: a constrained transport method. *Astrophys. J.*, 332:659, 1998.

[31] F. Fuchs, K. H. Karlsen, S. Mishra and N.H. Risebro. Stable upwind schemes for the Magnetic Induction equation. *Preprint, Math. Model. Num. Anal,* to appear.

[32] F. Fuchs, S. Mishra and N. H. Risebro. Splitting based finite volume schemes for the ideal MHD equations. *J. Comp. Phys.,* 228 (3), 2009, 641-660.

[33] F. Fuchs, A. D. McMurry, S. Mishra, N. H. Risebro and K. Waagan. Finite volume schemes for wave propagation in stratified magneto-atmospheres. *Preprint 2008.*, Submitted, available from folk.uio.no/siddharm/art26.pdf

[34] F. Fuchs, A. D. McMurry, S. Mishra, N. H. Risebro and K. Waagan. Approximate Riemann solver based high-order finite volume schemes for the Godunov-Powell form of ideal MHD equations in multi-dimensions. *Preprint 2008.*, Submitted, available from folk.uio.no/siddharm/art32.pdf

[35] S. K. Godunov. The symmetric form of magnetohydrodynamics equation. *Num. Meth. Mech. Cont. Media*, 1:26-34, 1972.

[36] K. F. Gurski. An HLLC-type approximate Riemann solver for ideal Magneto-hydro dynamics. *SIAM. J. Sci. Comp.*, 25(6), 2004, 2165-2187.

[37] S. Gottlieb, C. W. Shu and E. Tadmor. High order time discretizations with strong stability property. *SIAM. Review,* 43, 2001, 89 - 112.

[38] A. Harten. High resolution schemes for hyperbolic conservation laws. *Jl. Comput. Phys.* 49, 1983, 357-393.

[39] A. Harten and J. M. Hyman. Self adjusting grid methods for one-dimensional hyperbolic conservation laws. *J. Comput. Phys.*, 50, 1983, 235-269.

[40] A. Harten, B. Engquist, S. Osher and S. R. Chakravarty. Uniformly high order accurate essentially non-oscillatory schemes. *J. Comput. Phys.*, 1987, 231-303.

[41] A. Harten, P. D. Lax and B. Van Leer. On upstream differencing and Godunov type schemes for hyperbolic conservation laws. *SIAM Rev.,* 25 (1), 1983, 35-61.

[42] T. J. R Hughes, L. P. Franca and M. Mallet. A new finite element formulation for CFD I: symmetric forms of the compressible Euler and Navier-Stokes equations and the second law of thermodynamics. *Comp. Meth. Appl. Mech. Engg.*, 54, 1986, 223 - 234.

[43] J. D. Jackson. Classical Electrodynamics, Wiley, 3rd Edition, 1999.

[44] V. Jovanovic and C. Rohde. Finite volume schemes for Friedrichs systems in multiple space dimensions: a priori and a posteriori error estimates. *Num. Meth. PDEs*, 21(1):104-131, 2005.

[45] K. H. Karlsen, S. Mishra and N.H. Risebro. Semi-Goudunov schemes for systems of conservation laws. *Ap. Num. Math.,* To appear, 2009.

[46] K. H. Karlsen, S. Mishra and N.H. Risebro. A new class of well-balanced schemes for conservation laws with source terms, *Math. Comp.,* 78 (265), 2009, 55-78.

[47] S. Karni. Far field filtering operators for suppresion of reflections from artificial boundaries. *SIAM Jl. Num. Anal.* 33 (3), 1996, 1014 - 1047.

[48] D. Kröner and M. D. Thanh. Numerical solutions to compressible flows in a nozzle with variable cross section. *SIAM. J. Numer. Anal.,* 43 (2) (2005), 796 - 824.

[49] P. G. LeFloch and M .D. Thanh. The Riemann problem for fluid flows in a nozzle with discontinuous cross-section. *Commun. Math. Sci.,* 1 (4), 2003, 763-797.

[50] R. J. LeVeque. Finite volume methods for hyperbolic problems. *Cambridge university press,* Cambridge, 2002.

[51] R. J. LeVeque. Wave propagation algorithms for multi-dimensional hyperbolic systems, *J. Comp. Phys.,* 131, 327-353, 1997.

[52] R. J. LeVeque. Balancing source terms and flux gradients in high-resolution Godunov methods: The quasi-steady wave-propagation algorithm *J. Comput. Phys.*, 146, 346 - 365, 1998.

[53] T. J. Linde. *A three adaptive multi fluid MHD model for the heliosphere.* Ph.D thesis, University of Michigan, Ann-Arbor, 1998.

[54] P. Londrillo, L. del Zanna. On the divergence-free condition in Godunov-type schemes for ideal magnetohydrodynamics: the upwind constrained transport method. *J. Comput. Phys.* 195, 17-48, 2004.

[55] B. Marder A method for incorporating Gauss' law into electromagnetic pic codes. *J. Comput. Phys.*, 68 (1), 48-55, 1987.

[56] S. Mishra. Analysis and Numerical Approximation of Conservation laws with discontinuous coefficients.
Ph.D thesis, IISc, Bangalore, India, 2005, 260 pp.

[57] S. Mishra and E. Tadmor, Constraint preserving schemes using potential-based fluxes. III. Genuinely multi-dimensional central schemes for MHD equations. *Preprint,* 2009.

[58] A. Mignone et. al. Pluto: A numerical code for computational astrophysics. *Astrophys. J. Suppl.*, 170, 2007, 228 - 242.

[59] T. Miyoshi and K. Kusano. A multi-state HLL approximate Riemann solver for ideal magneto hydro dynamics. *J. Comp. Phys.* 208 (1), 2005, 315 - 344.

[60] S. Noelle, N. Pankratz, G. Puppo and J. Natvig. Well-balanced finite volume schemes of arbitrary order of accuracy for shallow water flows. *Journal of Computational Physics*, 213, 474-499, 2006.

[61] S. Noelle, N. Pankratz, G. Puppo and J. Natvig. Well-balanced finite volume schemes of arbitrary order of accuracy for shallow water flows. *Journal of Computational Physics*, 213, 474-499, 2006.

[62] B. Perthame and C. W. Shu. On positivity preserving finite volume schemes for Euler equations. *Numer. Math.,* 73 (1), 119 - 130, 1996.

[63] T. J. Poinsot and S. K. Lele. Boundary conditions for direct simulations of compressible viscous flows. *J. Comp. Phys.* 101, 1992, 104 - 129.

[64] G. K. Parks, Physics of Space Plasmas: An Introduction, Addition-Wesley, 1991.

[65] K. G. Powell. An approximate Riemann solver for magneto-hydro dynamics (that works in more than one space dimension). Technical report, 94 -24, ICASE, Langley, VA, 1994.

[66] K. G. Powell, P. L. Roe. T. J. Linde, T . I. Gombosi and D . L. De zeeuw, A solution adaptive upwind scheme for ideal MHD. J. Comp. Phys, 154(2), 284 - 309, 1999

[67] P. L. Roe. Approximate Riemann solvers, parameter vectors and difference schemes. *J. Comput. Phys.* 43, 1981, 357-372.

[68] P. L. Roe and D. S. Balsara. Notes on the eigensystem of magnetohydrodynamics. *SIAM. J. Appl. Math.*, 56 (1), 1996, 57 - 67.

[69] C. S. Rosenthal *et al.* Waves in the magnetized solar atmosphere I: Basic processes and internetwork oscillations. *Astrophys. Jl,* 564, 2002, 508 - 524.

[70] J. Rossmanith. A wave propagation method with constrained transport for shallow water and ideal magnetohydrodynamics. Ph.D thesis, University of Washington, Seattle, 2002.

[71] D. S. Ryu, F. Miniati, T. W. Jones and A. Frank. A divergence free upwind code for multidimensional magnetohydrodynamic flows. *Astrophys. J.*, 509(1):244-255, 1998.

[72] C. W. Shu and S. Osher. Efficient implementation of essentially non-oscillatory schemes - II, *J. Comput. Phys.*, 83, 1989, 32 - 78.

[73] J. M. Stone et. al. Athena: A new code for astrophysical MHD. *Astrophys. J. Suppl.*, to appear. Preprint availabe on url:http://arxiv.org/abs/0804.0402.

[S] C. W. Shu. ENO and WENO schemes for hyperbolic conservation laws. *NASA ICASE reprort no. 97-65*, 1997.

[74] T. Tanaka. Finite volume TDV scheme on an unstructured grid system for three-dimensional simulations of inhomogenous system including strong background potential field. *J. Comput. Phys.,* 111, 1994, 381.

[75] K. W. Thompson. Time dependent boundary conditions for hyperbolic systems. *J. Comp. Phys.*, 68, 1987, 1 - 24.

[76] E. F. Toro. *Riemann solvers and Numerical Methods for Fluid Dynamics.* Springer Verlag, Berlin, 1997.

[77] M. Torrilhon and M. Fey. Constraint-preserving upwind methods for multidimensional advection equations. *SIAM. J. Num. Anal.*, 42(4):1694-1728, 2004.

[78] M. Torrilhon. Locally divergence preserving upwind finite volume schemes for magnetohyrodynamic equations. *SIAM. J. Sci. Comp.*, 26(4):1166-1191, 2005.

[79] M. Torrilhon. Uniqueness conditions for Riemann problems of ideal Magnetohydrodynamics. J. Plasma. Phys., 69 (3), 253-276, 2003.

[80] G. Tóth. The Div(B)=0 constraint in shock capturing magnetohydrodynamics codes. *J. Comp. Phys.*,161:605-652, 2000.

[81] B. Van Leer. Towards the ultimate conservative difference scheme. V. *J. Comp. Phys.*, 32, 101-136, 1979.

[82] J-P. Vila and P. Villedeau. Convergence of explicit finite volume scheme for first order symmetric systems. *Numer. Math.*, 94:573-602, 2003.

[83] K. Waagan. A positive MUSCL-Hancock scheme for ideal MHD. *Preprint, 2008.*